

**MULTIPLICITY AND TRANSVERSE  
MOMENTUM DISTRIBUTIONS  
OF CHARGED PARTICLES IN PROTON-ANTIPROTON  
COLLISIONS AT  $\sqrt{s}=630$  AND 1800 GEV**

**June, 1988**

**MAKI SEKIGUCHI**

Submitted in partial fulfillment of the requirements for  
the Degree of Doctor of Science  
in the Doctoral program in  
University of Tsukuba

## Abstract

We have measured the multiplicity and transverse momentum distributions of charged particles produced in proton-antiproton collisions at center of mass energies of 630 and 1800 GeV. This is the first measurement of this kind at the center of mass of 1800 GeV, which is the highest energy available today. Data are obtained for the pseudorapidity  $|\eta| \leq 3.0$  and for the transverse momentum down to 50 MeV/c. The number of events analyzed is  $2.7 \times 10^3$  for 630 GeV and  $2.5 \times 10^4$  for 1800 GeV.

The experiment has been performed at the Fermi National Accelerator Laboratory in Batavia, Illinois, U.S.A., utilizing the world largest Tevatron accelerator. Particles from  $\bar{p}p$  collisions are detected by the CDF (Collider Detector at Fermilab). We trigger the  $\bar{p}p$  events with scintillation counters which detect charged particles produced at small polar angles with respect to the beam axis. This trigger introduces the least biases and is sensitive to nearly 60% of the total cross section.

The number and direction of charged particles are measured with the Vertex Time Projection Chamber (VTPC) surrounding the beam pipe and mounted along the beam direction ( $z$  direction). The VTPC is a set of eight time projection chambers, each of which has two of 15.25 cm long drift volumes divided by a central high voltage grid. A proportional chamber is located at the end of each drift space and has 24 sense wires radially (in  $r$ ) and three rows of pads behind the sense wires. The inner and outer radii of the VTPC are 6.5 and 21 cm, respectively. The VTPC extends to  $z = \pm 145$  cm in the beam direction. The  $rz$  trajectories of charged particles are given by the sense wire position and drift time measurements with time-to-digital converters. The information on the azimuthal direction is obtained by measuring the center of gravities of induced charge distributions on the pads with flash analog-to-digital converters. Using 1.5 Tesla axial magnetic field, the transverse momentum of charged particles is measured with the VTPC (transverse momentum from 0.05 to 1.0 GeV/c) and complementarily with the Central Tracking

Chamber (transverse momentum  $\geq 0.5$  GeV/c), which is an axial drift chamber surrounding the VTPC.

To raw data, we apply event selection criteria based upon the number and direction of reconstructed tracks and the time-of-flight data from the trigger counters. The track selection is based on how well they point to the primary vertex. The track reconstruction efficiency has been obtained by a hand-scan and Monte Carlo simulation. The corrections to the data include the effects of particle decays and conversions, track selection, chamber inefficiencies, and reconstruction inefficiency for very low transverse momentum.

We have studied the charged particle density per unit pseudorapidity ( $dN/d\eta$ ). The charged particle densities obtained at our energies are consistent with the extrapolation based on other experiments at center of mass energies of 200, 546, and 900 GeV. The charged particle density at  $\eta = 0$  for 1.8 TeV  $\bar{p}p$  is observed to be  $4.15 \pm 0.26$  (non single diffractive) showing an 27% increase compared to that for 630 GeV.

The charged multiplicity distributions are fitted to a negative binomial function resulting in a  $\chi^2/NDF$  of 57.3/40 at  $\sqrt{s} = 630$  GeV and 396/62 at  $\sqrt{s} = 1.8$  TeV.

To study the multiplicity distribution, we used the KNO  $\psi$  distribution in which  $\langle n \rangle P(n)$  is plotted against  $n/\langle n \rangle$ , where  $\langle n \rangle$  is the average charged multiplicity,  $n$  is the charged multiplicity, and  $P(n)$  is the probability density. Our  $\psi$  distribution at  $\sqrt{s} = 630$  GeV and UA5  $\psi$  distribution at  $\sqrt{s} = 546$  GeV agree very well. We have observed possible structures (bumps) in the shape of the KNO distribution as the energy goes to 1.8 TeV GeV. The multiplicity has also been studied for different  $|\eta|$  ranges of  $\leq 1.0$ ,  $\leq 2.0$ , and  $\leq 3.0$ . For a fixed energy, the shape of the KNO distribution is flatter for smaller range of  $|\eta|$ .

We have observed the flattening of the transverse momentum ( $p_t$ ) spectra with the colliding energy. The spectra are well fitted to a function  $1/(p_t + a)^m$ , where

$m$  decreases from  $8.89 \pm 0.02$  to  $8.28 \pm 0.02$  as the energy goes from 630 to 1800 GeV with a fixed  $a$  of 1.30. The average transverse momentum has been measured to be  $0.432 \pm 0.004$  GeV/ $c$  at 630 GeV and to increase to  $0.495 \pm 0.014$  GeV/ $c$  at 1.8 TeV.

The  $dN/d\eta$  obtained by this experiment at  $\sqrt{s} = 1.8$  TeV is about 5% larger than  $dN/d\eta$  theoretically predicted by a Dual Parton Model for  $\sqrt{s} = 2$  TeV. This model is based on the constituent quark-gluons and on the low  $Q^2$  calculation of the QCD. According to this model, a hadronic collision produces a system in which a large number of quarks and gluons are interacting strongly, which later on fragment into hadrons. This model describes the experimental data at lower energy fairly well.

## Acknowledgements

I would like to thank my advisor Prof. K. Takikawa for his excellent guidance and encouragement throughout my thesis work. His advices with many good questions have improved my research abilities. I have learned from his careful and deep research thinking.

I would also like to thank Prof. K. Kondo for his providing relaxed atmosphere in our laboratory and for his encouragement. His positive attitude toward physics research has always been a great help.

I wish to express the deepest appreciation to Dr. R. Kephart and Dr. M. Binkley, who have been my coworkers and advisors for four years at Fermilab, giving me an opportunity to work on the vertex time projection chamber with their excellent guidance and encouragement. From them, I have learned countless of things necessary to build and test chambers and electronics, and have learned how to run experiments and to pursue research. My present career would not have been possible without them.

My deep thanks go to other coworkers and friends, Rick Snider and Toshihiro Mimashi. It has always been pleasure to work with them.

I wish to express thanks to Dr. A. Tollestrup and Dr. R. Schwitters, spokesmen of the CDF collaboration, for their administrative work and valuable suggestions on the detector development and physics analysis.

I thank Dr. A. Para for his valuable ideas, suggestions, and encouragement when analyzing data and working on the software development. His ideas are simple and very effective and his suggestions and encouragement have been a great help to reach physics goals.

The construction of the tracking chambers was possible only with outstanding and excellent engineers, Serge Palanque from Saclay and Don Tousignant at Fermilab with good hard-working technicians, Eric Eros and Jim Welch.

I thank Ray Yarema, Tom Zimmerman, and Arran King for their work on the chamber electronics. It has always been educational to work with them.

Dr. J. Patrick has developed micro codes for our scanner processors and maintained their hardware by his priceless hard work. We would not have been able to do data taking without his effort.

Dr. C. N. Holmes has provided software tools to test our chambers and electronics and has tested TDC's. I would also like to thank her for providing data and histograms of the magnetic field measurements. Her kindness and hospitality are my appreciation.

A development of very fast graphic display by Dr. G. W. Foster has accelerated our work on developing the track reconstruction software. We have saved a lot of time by using his display software. I would also like to thank him for his valuable suggestions on both hardware and software.

I thank Aesook Byon for her providing results of the CTC transverse momentum spectra. Her patient work as a graduate student has always been a great encouragement to me.

I would like to thank Dr. Y. Takaiwa for his developing a Monte Carlo event generator. His simple and effective software has been an advantage for studying the systematic corrections to our results.

I wish to thank Dr. G. P. Yeh for his work on the event selection and on a part of the track reconstruction program. I also thank Dr. J. Freeman for his developing and maintaining the CDF detector simulation package. A deep thanks go to Dr. P. Berge for his developing the CTC reconstruction code and his patient work as a software librarian. It has been a great opportunity to receive suggestions from Dr. M. Atac, Dr. R. W. Kadel, Dr. S. Kim, Martin H. Schub, Dr. T. Yamanouchi, and Dr. J. Yoh. It is a pleasure to have discussions with them.

Carol Picciolo is our proud secretary who works very hard for our collaboration.

We have been enjoying and appreciating relaxed and friendly atmosphere created by her.

I thank Kazuko Kumashiro for her secretary work at University of Tsukuba and her maintaining my graduate status.

I have been getting a valuable help from Trang Nguyen to solve the problems with the LaTeX text processing throughout my thesis work. She also kindly provided some TeX macros for my thesis.

My status at Fermilab has been maintained by a hard work of the personnel administrator Borys Jurkiw. I would also like to thank Dr. K. Stanfield who is the head of the research division at Fermilab and Dr. L. Lederman who is the director of the Fermilab. Dr. M. Mishina and Kyoko Kunori have always been giving priceless support to the Japanese group at Fermilab.

The success of this CDF experiment is the results of hard and patient work of many collaborators. I wish to thank all of them (appendix A).

Finally, I would like to thank my family and my grandfather for their constant support and encouragement during the long period from nursery school through graduate school, without which none of this would have been possible.

This work was supported by the U.S. Department of Energy; U.S. National Science Foundation; A. P. Sloan Foundation; Istituto Nazionale di Fisica Nucleare; Ministry of Education, Science and Culture of Japan; and Nihon Ikuei-kai.



# Contents

<b>1</b>	<b>Introduction</b>	<b>1</b>
1.1	Characteristics of multiparticle production	2
1.2	Theoretical models	4
<b>2</b>	<b>Apparatus</b>	<b>7</b>
2.1	Tevatron Beam	7
2.2	Collider Detector	9
2.3	Vertex Time Projection Chamber system	11
2.3.1	VTPC construction	13
2.3.2	VTPC operation	14
2.3.3	VTPC wire electronics	15
2.3.4	VTPC pad electronics	16
2.4	Amount of materials in the tracking system	18
2.5	Uniformity of magnetic field	19
2.6	Trigger System	21
2.6.1	Beam-Beam Counter	21
2.6.2	Trigger logic	23
2.7	Data Acquisition	24
2.7.1	Overview	24
2.7.2	Acquisition for VTPC	25
<b>3</b>	<b>Track Reconstruction and Performance</b>	<b>27</b>

3.1	VTPC reconstruction	27
3.1.1	Reconstruction with TDC data	27
3.1.2	Reconstruction with pad FADC data	33
3.1.3	Reconstruction with wire FADC data	36
3.2	VTPC systematics and alignment	36
3.2.1	Systematics with TDC data	36
3.2.2	Systematics with pad FADC data	37
3.3	VTPC chamber performance	38
3.4	VTPC reconstruction efficiency	40
<b>4</b>	<b>Analysis</b>	<b>43</b>
4.1	Monte Carlo event simulation	44
4.2	Track Selection	45
4.3	Corrections to charged multiplicity	48
4.3.1	Loss of very low $p_t$ tracks	48
4.3.2	Loss of tracks near the radial board	49
4.3.3	Loss of tracks by the vertex cut	49
4.3.4	Effects of materials	50
4.3.5	Effects of particle decay	50
4.3.6	Overall efficiency	51
4.3.7	Trigger bias	51
4.3.8	Track density dependence of efficiency	53
4.4	Correction to low $p_t$ spectrum	55
4.5	Event Selection	56
4.5.1	Criteria	56
4.5.2	Efficiency	57
<b>5</b>	<b>Results and Discussions</b>	<b>59</b>

<b>CONTENTS</b>	<b>9</b>
5.1 Pseudorapidity distribution . . . . .	59
5.1.1 Uncorrected results . . . . .	59
5.1.2 Corrected data . . . . .	61
5.1.3 Multiplicity dependence . . . . .	62
5.2 Multiplicity distributions . . . . .	62
5.2.1 Uncorrected distributions . . . . .	62
5.2.2 Corrected multiplicity distributions . . . . .	63
5.3 Transverse momentum spectra . . . . .	66
5.4 Average transverse momenta . . . . .	67
<b>6 Conclusions</b>	<b>71</b>
<b>A The CDF Collaboration</b>	<b>245</b>
<b>B Negative Binomial Distribution</b>	<b>247</b>
<b>D <math>E \times B</math> effect on the drift direction</b>	<b>251</b>
<b>E VTPC detector simulation</b>	<b>253</b>
<b>F VTPC wire systematics</b>	<b>257</b>
<b>G VTPC pad systematics</b>	<b>263</b>
<b>H Trajectory of charged particle</b>	<b>281</b>
<b>I Statistical hydrodynamic model</b>	<b>287</b>
<b>J Dual parton model</b>	<b>289</b>
<b>K Feynman scaling</b>	<b>291</b>

# Chapter 1

## Introduction

This article describes the first measurements of the charged multiplicity and transverse momentum distributions in the  $\bar{p}p$  collisions at a center of mass energy of 630 and 1800 GeV. This energy (1800 GeV) was as twice as high compared to that in the previous experiments and is the highest energy available today.

The high energy hadron-hadron collision produces a large number of particles inelastically. The collision at a center-of-mass energy of several hundreds GeV, for instance, produces 25-30 of charged particles on the average and occasionally more than 100 [1]. The number of charged particles is normally counted by mean of tracking detectors. Although such inelastic interactions attribute about 80% (non-diffractive and diffractive) of total cross section [2,3], the underlining physics process is not perfectly understood and there is no theoretical model which everyone approves. Our new measurements of the charged multiplicity and transverse momentum distributions at 1.8 TeV has extended the knowledge of the hadron-hadron collision and hopefully will provide the clues to understand the underling physics.

This chapter describes the already known characteristics of the multiparticle production in the hadron-hadron collision followed by the brief description of present theoretical models.

### 1.1 Characteristics of multiparticle production

It was more than 30 years ago that the multiparticle productions were first observed in the high energy nucleon-nucleon collisions in cosmic ray experiments [4,5,6,7]. These were well before the development of the gauge field theory and the quark model. Emulsion chambers were exposed at high altitude (20-30 Km) with balloons to record the collisions of the primary cosmic rays. The energy of the studied collisions was  $10^{12}$ eV to  $10^{14}$ eV in the laboratory frame. For a proton-(anti)proton system, this corresponds to a center-of-mass energy of 50-500 GeV, which is calculated using a Lorentz invariant  $s$ :

$$s \equiv (P_{1\mu} + P_{2\mu})(P_1^\mu + P_2^\mu) \quad (1.1)$$

$$= (2E_C)^2 \quad (1.2)$$

$$= 2mc^2(mc^2 + E_L) \simeq 2mc^2 E_L \quad (1.3)$$

where  $P_{1\mu} + P_{2\mu}$  is the sum of particle four-momenta,  $E_C$  is the particle energy at the center-of-mass frame,  $E_L$  is the incident particle energy at the laboratory frame and  $m$  is the particle mass. Accelerators available at that time produced much lower energies ( $E_L \sim 10$  GeV at Dubna). For the proton-nucleon collisions, the results of such cosmic ray experiments [9][10][11] showed:

1. The average multiplicity  $\langle n_{ch} \rangle$  increased slowly as the energy increased.  $\langle n_{ch} \rangle$  per nucleon was about 10 for  $\sqrt{s} \sim 20$  GeV and about 20 for  $\sqrt{s} \sim 200$  GeV.
2. The average transverse momentum  $\langle p_t \rangle$  (respect to the direction of incident particles) was 0.4-0.5 GeV/c. The energy dependence of  $\langle p_t \rangle$  was not apparent.

There were difficulties to make more detail investigations with the cosmic experiments. The energy of incident particles could not be determined well and tar-

get nucleons were not well defined. Statistics were also very limited. More than ten years after, when man-made machines reached at  $\sqrt{s} > \sim 10$  GeV, the significant progress started. Some distinct characteristics of the charged multiplicity in proton-proton or proton-antiproton collisions have been revealed by the experiments at CERN ISR ( $\sqrt{s} = 30$ -60 GeV) and SPS ( $\sqrt{s} = 200$ -900 GeV). (It should be noted that such progresses would not have been possible without the use of the collider accelerators.) The followings are the known characteristics of charged particle production in the hadron-hadron collisions.

### 1. Average multiplicity

The average charged multiplicity  $\langle n_{ch} \rangle$  increases from 10 to 20 as  $\sqrt{s}$  increases from 20 GeV to 200 GeV. It grows as  $\ln s$  or  $s^*$ . Figure 1.1 shows this energy dependence [1, 13] for non-single diffractive events. The solid curve on the plot is:

$$\langle n_{ch} \rangle = 1.97 + 0.21 \times \ln s + 0.148 \times \ln^2 s \quad (1.4)$$

and the dashed curve is:

$$\langle n_{ch} \rangle = -7.5 + 7.6 \times s^{0.124} \quad (1.5)$$

A simple extrapolation to  $\sqrt{s} = 1.8$  TeV would expect  $\langle n_{ch} \rangle$  to be 40.

### 2. Particle density

The spatial distribution of charged particles is measured as a pseudorapidity distribution. The pseudorapidity  $\eta$  is:

$$\eta \equiv -\ln \tan \theta/2 \quad (1.6)$$

where  $\theta$  is the polar angle between the production direction of a particle and an incident proton direction.  $\eta = 1.0, 2.0$  and  $3.0$  correspond to approximately  $40^\circ, 14^\circ$  and  $5^\circ$ , respectively. Figure 1.2 shows the pseudorapidity distributions ( $dN/d\eta(\eta) = (1/\sigma)(d\sigma/d\eta)$ ) for various  $\sqrt{s}$ 's from 53 GeV to 900 GeV [14].

### 3. Multiplicity distribution

The experimental results [15][16][17] show the multiplicity distribution is well fitted to a negative binomial distribution:

$$P(n_{ch}) = \frac{(n_{ch} + k - 1)!}{n_{ch}!(k - 1)!} \left| \frac{\langle n_{ch} \rangle / k}{1 + \langle n_{ch} \rangle / k} \right|^{n_{ch}} \frac{1}{(1 + \langle n_{ch} \rangle / k)^k} \quad (1.7)$$

where  $\langle n_{ch} \rangle$  (the average charged multiplicity) and  $k$  are free parameters<sup>1</sup>. Figure 1.4 shows the experimental data and fitting to the negative binomial distribution. Equation 1.7 becomes the Bose-Einstein distribution when  $k = 1.0$  and the Poisson distribution when  $1/k = 0.0$ . The physical meaning of the negative binomial distribution is discussed in § 5.2.2.

### 4. Average transverse momentum

The transverse momentum  $p_t$  is the momentum component perpendicular to the beam axis or to the incident proton direction. The average  $p_t$ ,  $\langle p_t \rangle$ , has a small energy dependence. Figure 1.6 [24] shows a plot of  $\langle p_t \rangle$  against  $\sqrt{s}$ . At  $\sqrt{s} = 20$  GeV,  $\langle p_t \rangle$  is 0.330 GeV/c and increases to 0.450 GeV/c at  $\sqrt{s} = 900$  GeV.  $\langle p_t \rangle$  is also found to be larger for the larger particle density. Figure 1.7 shows the particle density (average  $dN/d\eta$  or  $dN/dY$  in an event) dependence of  $\langle p_t \rangle$  at  $\sqrt{s} = 540$  GeV [25]. It increases rapidly from 0.35 to 0.45 GeV/c as the average  $dN/d\eta$  increases from  $\sim 1$  to 7.5. For the larger particle density,  $\langle p_t \rangle$  becomes rather flat and increases only slowly.

## 1.2 Theoretical models

There are two successful models of the multiparticle production, the Statistical Hydrodynamic Model (SHM) and the Dual Parton Model (DPM). According to SHM model [26]-[33] in the hadron-hadron collision, the valence quarks fly away and leave a system with some fraction ( $\sim 50\%$ ) of the initial energy-momentum. (See

<sup>1</sup>The mathematical meaning of the negative binomial distribution is described in appendix B

figures 1.8a-c.) In the system, many quarks and gluons are excited by the energy resulting in a statistical system — the system size  $\gg$  the mean free path and the number of particles  $\gg 1$ . The physical quantities are calculated by the classical statistical treatment of the system with a relativistic hydrodynamic equation. The prediction by SHM describes the experimental results fairly well up to  $\sqrt{s} = 546$  GeV. DPM is based on the  $1/N_{of\ degree\ of\ freedom}$  expansion of QCD (or equivalently the Pomeron expansion of QCD) and the constituent quark model [37,38]. This models also describes experimental results fairly well up to  $\sqrt{s} = 546$  GeV. More detail of these models are described in appendix I (SHM) and appendix J (DPM). We compare our results on  $dN/d\eta$  at  $\sqrt{s} = 1.8$  TeV to that predicted by DMP, which is the only prediction available at this time.

a beam crossing occurred every 7  $\mu\text{sec}$ . The luminosity of the collision is given by:

$$\mathcal{L} = f \cdot n \cdot \frac{N_p \cdot N_{\bar{p}}}{A} \text{ cm}^{-2}\text{sec}^{-1}, \quad (2.1)$$

where

- $f$  : frequency of bunch circulation =  $(1/21) \times 10^6 \text{ sec}^{-1}$ ,
- $n$  : number of (anti)proton bunches in the storage ring = 3,
- $N_p$  : number of protons in a bunch,
- $N_{\bar{p}}$  : number of antiprotons in a bunch,
- $A$  : beam-beam cross section ( $\text{cm}^2$ ).

For one of typical runs with  $\mathcal{L} = 3.2 \times 10^{28} \text{ cm}^{-2}\text{sec}^{-1}$ ,  $N_p$  was  $4.7 \times 10^{10}$ ,  $N_{\bar{p}}$  was  $2.4 \times 10^9$ , and  $A$  was  $5.0 \times 10^{-4} \text{ cm}^2$ . The Tevatron peak luminosity during the run is shown in figure 2.1, in which each point represents a separate  $\bar{p}p$  store. At the end of the period, the peak luminosity reached  $1.2 \times 10^{29} \text{ cm}^{-2}\text{sec}^{-1}$ . The integrated luminosity in  $\text{nb}^{-1}$  ( $1 \text{ b} = 10^{-24} \text{ cm}^2$ ) is shown in figure 2.2, where solid squares represent the luminosity delivered by the accelerator and open squares represent the luminosity with which we recorded  $\bar{p}p$  collisions on magnetic tape. The total integrated luminosity logged on tape was about  $34 \text{ nb}^{-1}$ . The integrated luminosity we used for our analysis was approximately  $1 \mu\text{b}^{-1}$ .

The colliding energies (in  $\sqrt{s}$ ) of the Tevatron have been calibrated to be [47]:

- $631.4 \pm 0.6 \text{ GeV}$  for the nominal 630 GeV energy
- $1803.0 \pm 1.8 \text{ GeV}$  for the nominal 1.8 TeV energy

The Tevatron beam had some undesirable characteristics. First, the bunch size along the beam direction was finite resulting in an unnegligible timing jitter. These caused the collision positions smeared around a nominal position with a width of 30-40 cm in rms. In order to calculate physics quantities such as the pseudorapidity

## Chapter 2

# Apparatus

The experiment was performed at the Fermi National Accelerator Laboratory (Fermilab) in Batavia, Illinois, U.S.A. using the Tevatron accelerator/collider which gave proton-antiproton collisions at a center-of-mass energy of 1.8 TeV. We detected particles produced by the collisions with the Collider Detector at Fermilab (CDF). The CDF detector consisted of (1) tracking chambers, (2) calorimeters, (3) muon chambers, (4) trigger counters, and (5) a 1.5 Telsa superconducting solenoid magnet. For this article, we used the data from the Vertex Time Projection Chamber (VTPC) which was one of the tracking chambers closely surrounding the beam pipe. The VTPC had a large angular coverage ( $-3.5 \leq \eta \leq 3.5$ ) and a low mass construction, which were both desirable for our study. The  $\bar{p}p$  collision events were triggered by the Beam-Beam Counters (BBC) which were located close to the beam pipe in the forward and backward region. The data were taken with a FASTBUS based acquisition system, sent to a VAX785 host computer, and written on magnetic tape. The data used for this article were taken during the 1987 run (from February 1st to May 11th).

### 2.1 Tevatron Beam

The Tevatron accelerator produced proton-antiproton collisions with the highest energy available today (1.8 TeV). Protons and antiprotons were bunched such that

or the transverse momentum, we determined the collision position on an event-by-event basis using the Vertex Time Projection Chambers (VTPC) (described in §3.1.1). Figure 2.3 shows a typical distribution of the collision points given by the VTPC. The rms width of the distribution is approximately 35 cm for this particular Tevatron store. Second, the beam bunch normally carried undesirable secondary peaks along the beam direction. The collisions occurred at such secondary peaks were rejected by the timing requirement for trigger counter signals (described in §2.6.2).

## 2.2 Collider Detector

The Collider Detector at Fermilab (CDF) [48] is divided into a central part and a forward/backward part (from now on, forward also means backward) based on their angular coverage and construction as shown in figure 2.4. The central part covers  $10^\circ \leq \theta \leq 170^\circ$  and the forward covers  $2^\circ \leq \theta \leq 10^\circ$  and  $170^\circ \leq \theta \leq 178^\circ$ , where  $\theta$  is the polar angle with respect to the beam axis. The total coverage is more than 98% of  $4\pi$  solid angle. Figure 2.5 shows a vertical cut of one half of the CDF. There are four types of detector components and a solenoid magnet (from the nominal collision point to outside):

### ♣ Tracking system ♣

- ⊙ Vertex Time Projection Chamber (VTPC) [49]:  $5^\circ \leq \theta \leq 175^\circ$
- ⊙ Central Tracking Chamber (CTC) [50]:  $20^\circ \leq \theta \leq 160^\circ$
- ⊙ Forward Tracking Chamber (FTC) [51]:  $2^\circ \leq \theta \leq 10^\circ$ ,  $170^\circ \leq \theta \leq 178^\circ$

The tracking system is a set of drift chambers which record tracks of charged particles and measure their momenta. They are located in the innermost of the CDF detector in order to minimize particle conversions and multiple scatterings by materials. The detail of the VTPC is described in §2.3.

### ♣ Superconducting solenoid magnet ♣

The superconducting magnet [52] is 3 m in diameter by 5 m long, and produces a 1.5 Tesla field coaxial with the beam. The return path of its magnetic flux is formed by the iron in the endplug/wall calorimeters and the iron return yoke. The uniformity of the magnetic field is described in §2.5.

### ♣ Trigger counters ♣

The Beam-Beam Counters (BBC) [74] are used in order to trigger  $\bar{p}p$  collision events. They consist of a set of scintillation hodoscopes surrounding the beam pipe in front of the forward calorimeter. The angular coverage was  $0.32^\circ \leq \theta \leq 4.47^\circ$  and  $175.53^\circ \leq \theta \leq 179.68^\circ$ . The detail of BBC is described in §2.6.

### ♣ Calorimeter system ♣

- ⊙ Central electromagnetic[53]/hadron[54] and wall hadron[54] :  $30^\circ \leq \theta \leq 150^\circ$
- ⊙ End plug electromagnetic[55]/hadron[56] :  $10^\circ \leq \theta \leq 30^\circ$  and  $150^\circ \leq \theta \leq 170^\circ$
- ⊙ Forward electromagnetic[57]/hadron[58] :  $2^\circ \leq \theta \leq 10^\circ$  and  $170^\circ \leq \theta \leq 178^\circ$

The calorimeter system measures the energies of charged and neutral particles except for muons and neutrinos. The calorimeters consist of sandwiches of (a) radiator plates (materials such as iron or lead) and (b) sampling layers such as scintillation counters or gas proportional tubes. The electromagnetic parts use lead plates as their radiators and the hadron parts use iron plates. We use scintillation counters as samplers for the central and wall calorimeter for which photomultiplier tubes are located outside of the magnetic field. In the plug and forward region, the gas proportional tubes are used. Table 2.1 [59]

summarizes the characteristics of the calorimeters.

#### ♣ Muon detection system ♣

⊙ Central muon detector [60] :  $56^\circ \leq \theta \leq 124^\circ$

⊙ Forward muon detector [61]:  $2^\circ \leq \theta \leq 17^\circ$  and  $163^\circ \leq \theta \leq 178^\circ$

The muon detectors identify muons. They are located behind the hadron calorimeters so that particles other than muons were absorbed before the detection. The central muon detector is four planes of drift tubes. The forward muon detector consists of two magnetized steel toroids between three sets of drift chambers.

Figure 2.6 indicates the CDF coordinate system. The  $z$  axis is parallel to the beam axis and its direction is along the proton beam direction.  $\theta$  is the polar angle with respect to the proton beam or the  $z$ -axis. The  $x$  axis is horizontal and the  $y$  axis is vertical, forming a right-handed coordinate with the  $z$  axis. The nominal collision point is at the origin ( $x = y = z = 0$ ).  $\phi$  is the azimuthal angle on the  $xy$ -plane, starting  $\phi = 0$  at  $y = 0/x > 0$  and increasing toward  $y > 0/x = 0$ . Finally the radius  $r$  is defined to be  $\sqrt{x^2 + y^2}$ .

The following sections describe the details of the VTPC and the BBC which we used to study the charged multiplicity and the average transverse momentum.

## 2.3 Vertex Time Projection Chamber system

The Vertex Time Projection Chamber (VTPC) system was a set of eight mini time-projection-chambers surrounding the beam pipe and mounted along the beam direction. Two of such chambers are shown in figure 2.7. The VTPC covered a volume which was 2.9 m long in the beam direction and 6.5 cm to 21 cm in radius. Time-projection chambers<sup>1</sup> had been chosen because 1) they had a relatively large

<sup>1</sup>The principle of the time-projection chamber can be found in reference [62].

gas volume which minimized the mass of the material in the tracking system, 2) they provided easy pattern recognition (no left-right ambiguities), and 3) they provided a three dimensional view of tracks which was necessary to separate many charged tracks (30-100) in an event. The VTPC provided:

1. Determination of the collision vertices along the beam axis. The distribution of the vertex was a Gaussian with a typical rms width of 30-40 cm. The location of the vertex gave (a) a correction in calculating quantities such as transverse momenta/energies and (b) the starting point for the offline event reconstruction.
2. Measurement of charged multiplicity. By counting the number of tracks, we obtained quantities such as the average charged multiplicity for a very wide polar angle range ( $5^\circ \leq \theta \leq 175^\circ$ ).
3. Measurement of low transverse momentum. With the inner radius of 6.5 cm, charged tracks with  $p_t$  as low as 50-75 MeV/c were reconstructed. This was complement to the CTC which measured  $p_t > 400$  MeV/c. The VTPC  $p_t$  resolution was limited to  $0.3-0.4 \cdot p_t$  GeV/c.
4. Tracking in the plug/forward region. The VTPC provided the charged particle identification (over neutral ones) for  $5^\circ \leq \theta \leq 10^\circ$  with the FTC information and for  $10^\circ \leq \theta \leq 20^\circ$  where only the limited number of CTC hits were available.
5. Identification of multiple collisions in the same beam crossing. At a luminosity of  $10^{30} \text{ cm}^{-2}\text{sec}^{-1}$  with a six bunch mode which is the design goal of the Tevatron, 7.5% of collisions contain multiple collisions. At a luminosity of  $10^{28} \text{ cm}^{-2}\text{sec}^{-1}$  with a three bunch mode, which was our condition, only 0.15% of collisions contain multiple collisions.



### 2.3.1 VTPC construction

Since the VTPC was located inside the CDF central and forward tracking chambers, it was extremely important to minimize the effective thickness of the chamber in radiation lengths.<sup>2</sup> The materials used in constructing the VTPC were chosen with particular emphasis toward low mass and long radiation length. The mechanical structure of the VTPC consisted mainly of such light-nuclei materials as Rohacell foam [66], Kapton film [67], and epoxy-fiber laminates employing either glass or graphite fibers. The basic technique was to use a core of lightweight foam covered with a strong skin. This construction put the denser material where it contributes most to the moment of inertia and therefore provided the best stiffness-to-mass ratio. The use of graphite fibers was particularly effective since they had excellent strength, a high modulus of rigidity, and a long radiation length.

The VTPC system consisted of eight double-drift-space time projection chambers. Figure 2.7 shows two of the VTPC modules. Each of the eight octagonal VTPC modules had a central high voltage grid that divided it into two 15.25 cm long drift regions.<sup>3</sup> The cathode high voltage grids were located at the both ends of drift region and produced the necessary electric fields in the drift region together with the central grid. The drift region was cylindrically surrounded by the inner and outer field cages to shape the electric fields.

The ionized electrons drifted away from the center grid until they passed through a cathode grid and entered one of two proportional chamber endcaps. Each endcap was divided into octants, with 24 sense wires and 24 cathode pads in each octant. Figure 2.8 shows the construction of the endcap proportional chamber. As viewed from the drift region, it consisted of a cathode grid followed by a plane of field shaping wires, a plane of sense wires, and a resistive ink cathode plane. The spacing

<sup>2</sup>The  $\bar{p}p$  collision produces an average of  $\sim 30$   $\gamma$ 's passing through the VTPC region.

<sup>3</sup>The Tevatron was eventually planned to be operated in six bunch mode with 3.5  $\mu\text{sec}$  between beam crossing. The 15.25 cm drift length was chosen so that the maximum drift time would be less than 3.5  $\mu\text{sec}$  at a certain condition of chamber operation.

between both field shaping wires and sense wires was 6.34 mm. The field shaping wires were offset by half wire spacing in  $r$  with respect to the sense wires. Three rows of pads were located behind the resistive cathode, separated by 150  $\mu\text{m}$  of epoxy-fiberglass (G-10). A pad covered 4.12 cm in  $r$  and  $\sim 1.4$  cm in  $r\phi$ . The active area of the chamber extended from about  $r = 7$  cm to 21 cm. The construction of the VTPC is summarized in table 2.2.

The arrival times of the electrons at the sense wires gave pictures of events in the  $rz$ -plane. In addition as shown in figure 2.9, the sense wires and pads in four endcaps were instrumented with an analog pulse height readout using Flash Analog to Digital Converters (FADCs), so that  $dE/dx$  and  $\phi$  information was available for particles produced in  $5^\circ \leq \theta \leq 25^\circ$  or  $155^\circ \leq \theta \leq 175^\circ$ . Adjacent modules had a relative rotation angle of  $\phi_{\text{rot}} = 11.3^\circ = \arctan(0.2)$  about the beam axis. For tracks passing through at least two modules, this relative rotation eliminated inefficiencies near octant boundaries and also provided  $\phi$  information from small angle stereo.

### 2.3.2 VTPC operation

The CTC inner wall was used as a VTPC gas vessel which was filled with argon (50%) / ethane (50%) at one atmospheric pressure. The central-grid voltage was  $-6.4$  KV and the cathode-grid voltage was  $-2.4$  KV, together producing a strength of electric field in the drift region of 256 V/cm. This resulted in a drift velocity of 4.3 cm/ $\mu\text{sec}$  giving a maximum drift time of 3.9  $\mu\text{sec}$ . The sense wires were held at 0 V while the field shaping wires were held at  $-1.6$  KV. The gain of the proportional chamber was  $\sim 2 \times 10^4$ . In order to compensate the heat generated by the preamplifiers (140 W total), we water-cooled ( $10^\circ\text{C}$ ) the cable-feed-through frames at both ends of the VTPC gas vessel. The frames were thermally coupled with the cables going to the VTPC modules. With this cooling system, we maintained the maximum temperature of  $37^\circ\text{C}$  and the minimum temperature of  $27^\circ\text{C}$  in the

VTPC gas vessel. Table 2.3 summarizes the operation of the VTPC. During the three months of operation, we did not have any high voltage problems nor broken sense wires.

### 2.3.3 VTPC wire electronics

The front-end electronics for the wire signals consisted of:

1. Preamplifiers mounted directly on the chambers
2. Amplifier-Shaper-Discriminator (ASD) cards located on the end-walls
3. Time-to-Digital Converters (TDCs) located in the counting room

In order to minimize the mass contribution, two important technologies were employed in building the preamplifier cards. One was the use of a custom integrated circuit by Fujitsu micro electronics [68]. The resulting chip (MB43458) contained four preamplifier channels on a single substrate. The other was the intense use of surface mount parts on very thin (0.625 mm) G-10 circuit board. One preamplifier card weighed only 10 g. After the preamplification, signals were carried outside of the VTPC gas vessel by 10 m long miniature coaxial cable. Each coax was 0.75 mm in diameter manufactured by Junkosha Co. Ltd. [63] giving the least amount of mass contribution than any other copper based coaxial cables. The ASD cards further amplified signals with appropriate shapings. The signals were then discriminated to produce time-over-threshold<sup>4</sup> signals which were sent to the TDCs through 61 m flat cables. (For the wire  $dE/dx$  measurement, the ASD also provided the analog signal outputs which were sent to FADCs.) The TDC was LeCroy 1879 TDC [70] which was a CCD-based TDC and had an internal data compaction circuit (takes 0.5 msec). One TDC count was 8 nsec corresponding to a drift distance of

<sup>4</sup>The time-over-threshold signal becomes 1 (or high level) when an analog signal exceeds a threshold. It maintains the level as long as the analog signal is higher than the threshold, and goes back to 0 when the analog signal goes below the threshold.

$320 \mu\text{m}$ . The maximum TDC count was 511 corresponding to 4,088 nsec in drift time which was long enough for the maximum drift time of  $3.9 \mu\text{sec}$ . Figure 2.10 shows a simplified schematic of the wire electronics. Table 2.4 summarizes the wire electronics.

### 2.3.4 VTPC pad electronics

The front-end electronics for pad signals consisted of:

1. Preamplifiers mounted directly on the chambers
2. Pulse-Amplifier-Shaper (PAS) cards located on the end-walls
3. Flash ADCs (FADCs) located in the counting room

The pad preamplifier was LeCroy HQV802, an FET input charge sensitive hybrid amplifier. It was custom packaged into a low mass plastic case (3.5 grams for eight channels). This device was selected because of its relatively low power consumption (60 mW per channel) and its low noise ( $\sim 1500$  electrons equivalent noise for a 200 nsec integration time). The preamplified signals were carried out by the miniature coax cables described above and arrived at the PAS cards. Each channel of the PAS consisted of a four stage semi-Gaussian integrator and an amplifier. A very narrow pulse at the PAS input became a 170 nsec wide (FWHM) pulse at the integrator. This integration reduced the high frequency noises that would otherwise be observed by the FADC sampling.<sup>5</sup>

The FADC system performed digitization of analog signals and compaction of the digitized data. The system consisted of (a) 32 FADC modules (768 channels) for the pad  $\phi$  measurement and 32 FADC modules (768 channels) for the wire  $dE/dx$  measurement, and (b) eight compaction modules which read and compacted the digitized data from the FADC modules.

<sup>5</sup>FADCs are voltage sampling devices and do not integrate charges as Charge Coupled Devices (CCDs) do. One FADC sampling typically takes only 50-200 psec. Without an integration, high-frequency noises in signals would be "properly" digitized.

A FADC module contained 24 channels in a single-width FASTBUS module. The analog signals from PAS cards were received by a line receiver and fed into an eight bit FADC chip (Sony CXA1016P). (The wire analog signals from ASD for the  $dE/dx$  measurement were also sent to another set of the FADCs). The digitized data from the FADC chip were continuously written into two random access memories until stop signals were issued at the end of the VTPC drift time. A single FADC module dissipated 77 W in total and could operate at clock speeds up to 35 MHz. For the data described in this article the FADC module was operated at a 10.6 MHz<sup>6</sup> sampling rate to reduce the total amount of data per event written on magnetic tape.

A compaction module read and compacted data from the FADC modules. Each compaction module was a single-width FASTBUS slave that communicated with eight FADC modules through a dedicated external bus. After the stop signal, the FADCs were read out and their data were compacted to form groups of FADC data which were above a programmable threshold and contiguous in time. Usually such a group was the result of one chamber pulse. Since the typical signal from the chamber was quite long (1-4  $\mu\text{sec}$ ), this compaction method eliminated redundant address/time information which otherwise would be assigned to each FADC sampling. There was only a single set of a channel address, a start time address and the number of samplings for each group. Such time-channel information was only 29% of the compacted data.<sup>7</sup> The compaction process required 500  $\mu\text{sec}$  per event.

A simplified schematic of the pad electronics is shown in figure 2.11. The pad electronics is summarized in table 2.5.

<sup>6</sup>We generated a FADC clock by using a Tevatron RF clock to synchronize the phase of collisions and FADC samplings. The RF clock frequency was 53 MHz, which was frequency-divided by five for FADCs.

<sup>7</sup>If data are compacted only by a conventional zero-suppression, time-channel information would occupy about 2/3 of data.

## 2.4 Amount of materials in the tracking system

The charged particles produced by the  $\bar{p}p$  collisions were first tracked by the Vertex Time Projection Chamber (VTPC) before the mass of material became significant to the particle conversions. (An average of  $\sim 30$  photons pass through the VTPC per event.) Any photon conversions which do occur in the VTPC can result in large local track density and can make pattern recognition and track reconstruction difficult or impossible. In addition, such conversions degrade the electron-identification capability of the experiment and the multiple Coulomb scattering adversely affects the CTC momentum resolution. As a result the materials used in constructing the VTPC were chosen with particular emphasis toward low mass and long radiation length. Figure 2.12 shows the average amount of material in radiation lengths which a particle originating at the center of the detector traverses before reaching the active volume of the VTPC (dotted line), after passing through the entire VTPC system (dot-dashed line), and before entering the active volume of the CTC or FTC (solid line).

The amount of material traversed is lowest over the angular region ( $50^\circ \leq \theta \leq 130^\circ$ ) covered by the CTC. Over this region a particle on average crosses less than 0.7% of a radiation length before it is tracked by the VTPC, and less than 3.2% before entering the CTC. The traversed mass distribution peaks between  $10^\circ$  to  $20^\circ$  with respect to each exiting beam with 4% of a radiation length before, and 22% after tracking by the VTPC in the worst region. However, in this angular range, the VTPC provides nearly all tracking information available. Thus the material after the VTPC active volume has a relatively small impact on other tracking systems. In the angular region covered by the FTC ( $2^\circ \leq \theta \leq 10^\circ$ ), the amount of material crossed by a particle passing through the VTPC drops to 5-10% of a radiation length. The discontinuities in the plot correspond to places where a new set of cables is added, or a new proportional chamber is traversed. The drop in effective

thickness below  $10^\circ$  is due to the fact that the signal cables exit the gas vessel at  $10^\circ$ , then pass between the CTC endplate and the end plug calorimeter system, away from the path of particles pointing at the FTC.

The material effect on the charged multiplicity was studied with a Monte Carlo program and described in 4.3.4.

## 2.5 Uniformity of magnetic field

The uniformity of the magnetic field in the tracking system was important for the momentum measurement and for linking tracks over different tracking chambers. The uniformity can be seen as variation in the  $z$  component of the magnetic field and as the radial component. The non uniformity of the  $z$  component could affect the momentum measurement with the VTPC and CTC, while the radial component could affect both the  $rz$  measurement and the momentum measurement with the VTPC. The geometrical relation between the magnet and the CTC/VTPC can be seen in figure 2.9. The magnet was 3 m in diameter and 5 m long surrounding the 3 m long CTC. Inside the CTC, the VTPC was 21 cm in diameter and 2.9 m long. The maximum  $z$  where the pad FADC read was installed was  $\pm 100$  cm. The magnetic field has been measured with nuclear magnetic resonance (NMR) probes and a set of three orthogonal search coils [72]<sup>a</sup>.

At  $z = 0$  cm, the variation in the  $z$ -component with  $\phi$  was less than 0.066% at  $r = 135$  cm. The averaged  $z$  component changed by 0.56 % — from 15155 gauss ( $r = 0$  cm) to 15240 gauss ( $r = 135$  cm). The average  $z$  component slowly decreases toward larger  $|z|$ . At  $r = 0$  cm, it decreased by 1.3%, 2%, and 3% at  $z = \pm 100, 120$ , and 140 cm, respectively, while at  $r = 135$  cm it decreased by 0.8% at  $z = 140$  cm.

The maximum radial component of the magnetic field at  $z = 0$  cm was 10 gauss (0.07% of the  $z$ -component) at  $r = 0$  cm and 50 gauss (0.3%) at  $r = 135$  cm. The

<sup>a</sup>The results presented here are taken from reference [72].

$z$  dependence of the radial component averaged over  $\phi$  is shown in figures 2.13a-b for  $r = 0$  cm and  $r = 135$  cm. The crosses are raw data and the open circles are after the alignment correction to the NMR probe. The curves are fittings based on the Maxwell equation [73]. At  $r = 0$  cm, the radial component is less than 10 gauss for  $|z| \leq 140$  cm, although at  $r = 135$  cm, the radial component increases to 120 gauss at  $z = -140$  cm or to 400 gauss at  $z = 140$  cm. These are 0.66% or 2.6 % of the  $z$  component.

The effect of the variation of the  $z$  component on the CTC momentum measurement is estimated to be an order of 1.0% at most ( $|z| \sim 100$  cm). The CTC  $p_t$  resolution ( $\Delta p_t/p_t$ ), calculated from the chamber spatial precision, is  $0.002 \cdot p_t$  GeV/c [50]. The variation of the  $z$  component can affect  $p_t$  *leg* 5 GeV/c. However, since the error in absolute value is smaller than  $5 \text{ GeV/c} \cdot 0.01 = 0.05 = 50 \text{ MeV/c}$ , this can hardly affect the actual momentum spectrum. This is also true for the VTPC momentum measurement which has a much worse resolution ( $\Delta p_t/p_t = 0.3-0.4 \cdot p_t \text{ GeV/c}$ ).

The radial component of the magnetic field can affect the  $rz$ -measurement and the momentum measurement with the VTPC. Using equation D.4 in appendix D with a radial component of 150 gauss, the radial drift velocity is calculated to be 0.45% of the longitudinal drift velocity. For the maximum drift distance of 15.25 cm, the maximum displacement due to this effect is thus  $15.25 \times 0.0045 = 0.069 \text{ cm} \approx 700 \mu\text{m}$ . The correction due to  $E \times B$  effects is important at large  $z$  ( $\sim 100$  cm). The displacement, however, is also caused by the misalignment of the VTPC module. The actual correction has been done as a part of the alignment correction, in which we did not separate the effects due to the radial component and the effect due to the misalignment. The maximum overall effect was  $\pm 400 \mu\text{m}$ .

## 2.6 Trigger System

### 2.6.1 Beam-Beam Counter

The  $\bar{p}p$  collisions were triggered by detecting particles in the forward and backward direction close to the beam pipe. We used the Beam-Beam Counters (BBC) [74][75], which were 2.5 cm thick SCSN-23 scintillation counters located at  $z = \pm 581$  cm from the nominal collision point, as shown in figure 2.14. The counters were arranged in quadrants, with four counters per quadrant, as shown in figure 2.15. The total number of the counters was therefore 16 in the forward direction and also 16 in the backward direction. In order to obtain a good timing accuracy, each end of the counter had a phototube connected to a mean timer. These 16 counters were divided into four types depending on the size of the counter and on the phototube attached, as shown in table 2.6. The counter extended from 3.3 cm to 47.0 cm in radius resulting in an angular coverage of  $0.317^\circ$  to  $4.47^\circ$ . This corresponded to 3.24 to 5.89 in pseudorapidity and a total pseudorapidity range of 2.65 on either side.

In order to estimate the cross section triggered by the BBC, the total cross section ( $\sigma_{tot}$ ) is break up into elastic ( $\sigma_{el}$ ), single diffractive ( $\sigma_{SD}$ ), double diffractive ( $\sigma_{DD}$ ), and hard core components (inelastic minus single/double diffractive). We used a Monte Carlo simulation which was based on the UA4/UA5 data [77] [78] and on the extrapolation to our energy region [76]. Estimations of each cross-section component are summarized in table 2.8. The BBC acceptance for each component at  $\sqrt{s} = 1.8$  TeV has been estimated as:

- 17% for single diffractive events,
- 71% for double diffractive events,
- 96% for non-diffractive events.

Using the estimated cross section in table 2.8 and the results from the Monte Carlo, the cross section triggered by the BBC at  $\sqrt{s} = 1.8$  TeV would be:

$$\sigma_{BBC} = 0.17\sigma_{SD} + 0.71\sigma_{DD} + 0.96\sigma_{ND} \quad (2.2)$$

$$= 2.6 \pm 0.9 + 2.9 \pm 0.7 + 38.6 \pm 5 \quad (2.3)$$

$$= 44 \pm 6 \text{ mb}, \quad (2.4)$$

where  $\sigma_{ND}$  is a non-diffractive cross section and equal to  $\sigma_{tot} - \sigma_{el} - \sigma_{SD} - \sigma_{DD}$ .

The BBC acceptance for  $\sqrt{s} = 630$  GeV was estimated to be:

- 11.6% for single diffractive events,
- 75.0% for double diffractive events,
- 93.8% for non-diffractive events,

The cross section triggered by the BBC at  $\sqrt{s} = 630$  GeV would be:

$$\sigma_{BBC} = 0.12\sigma_{SD} + 0.75\sigma_{DD} + 0.94\sigma_{ND} \quad (2.5)$$

$$= 1.2 \pm 0.4 + 1.9 \pm 0.5 + 31.9 \pm 4 \quad (2.6)$$

$$= 35 \pm 4 \text{ mb}, \quad (2.7)$$

The BBC acceptances and triggering cross sections are summarized in table 2.9. Figure 2.16 shows a block diagram of the BBC electronics. The analog signals from the phototubes were discriminated and sent to a latch system which allowed to setup an appropriate fast logic for event triggering (described in the next section). To allow the offline analysis (pulse height correction to TDC data) and an event selection, the discriminated signals were also sent to LeCroy Time to Digital Converters (TDCs) 2228A's, and the analog signals from the phototubes were sent to LeCroy Analog to Digital Converters (ADCs) 1885N's.

The timing resolution of the BBC has been measured by comparing the vertex position given by the BBC with the vertex position determined by the VTPC<sup>9</sup>.

<sup>9</sup>The VTPC  $z$  vertex resolution was better than 3 mm as described in §3.3.

Figure 2.17 shows the distribution of the difference between the two vertex positions. The FWHM of the distribution is about 9 cm corresponding to a timing resolution of 300 psec in FWHM.

### 2.6.2 Trigger logic

If a collision occurs at the center of the detector ( $z=0$ ), the resulting particles with  $v = c$  have the same time of flight (19.4 nsec) from the collision point to the forward or backward BBC. There were two kinds of background in such a trigger. One was collisions from secondary peaks (called "satellites") in the beam intensity, and the other was collisions between beam and gas (the vacuum in the beam pipe was  $10^{-9}$  to  $10^{-10}$  torr). Most of such backgrounds were rejected by requiring a timing gate to the forward-backward coincidence. Figure 2.18 is a timing diagram for  $\bar{p}p$  collisions and the background. The horizontal axis is the  $z$  position in unit flight time (nsec). The vertical axis is time in nsec. Two vertical lines at  $z = \pm 19.4$  nsec correspond to the BBC positions in the forward and backward directions. The diagonal bold lines correspond to proton and antiproton bunches. They collide at  $z = 0$  nsec at  $t = 0$  nsec. The four diagonal broken lines represent "satellites" prior to and after the proton or antiproton bunches. By setting a "beam-beam" gate at  $t = 20$  nsec with 15 nsec window (hatched areas), and requiring at least one BBC hits in each of the forward and backward counters, most of the background were rejected. The single beam-gas interaction, the "satellite"-satellite collision, or "satellite"-main collision is outside of this gate. The background events, which were not rejected by this gate, were rejected by the offline event selection (4.5 Event Selection).

## 2.7 Data Acquisition

### 2.7.1 Overview

The data acquisition system [79] is based upon the Fast-Bus (FASTBUS) [80] system which allows to correct a large amount of data (80-100 Kbytes) from the large number of front-end electronics (14 partitions —  $7.5 \times 10^4$  channels) in a limited time (1-2 sec). The data acquisition system forms a tree structure as shown in Figure 2.19. The bottom of the tree is independent FASTBUS crates (called crate segments) which include:

1. Front-end TDC/FADC modules for the tracking systems, with a *scanner-processor* [82] in each crate which reads and formats the data from the TDC and FADC compaction modules.
2. Interface modules to the calorimeter digitization system which is a separate analog-bus-based ADC/TDC system with its own data preprocessors [81].
3. CAMAC-FASTBUS interface for the trigger counters which use CAMAC TDCs and FASTBUS ADCs/latches. (The data is read by the scanner-processor through the interface.)

These "front-end" crates are connected to higher-level crates through which all the data from the lower level are read. The connection is made by the FAST-BUS modules called *segment interconnects* [83] through digital cable bus. All connections finally lead to the crate to which the host VAX785 is connected via an Unibus-Processor-Interface [84]. We also have three VAX750s for test and calibration purpose.

During the 1987 run, the number of the front-end FASTBUS crates was approximately 20 and the typical acquisition rate was 0.6 Hz with the data from all detector components. The typical amount of the data was 60 Kbytes for the BBC trigger.

### 2.7.2 Acquisition for VTPC

The data acquisition cycle is initiated by a module called *trigger supervisor* [79] which starts sending "clear and strobe" signals to the front-end electronics. The TDC and FADC-compaction modules does not start compacting data with the clear-and-strobe signals, although stop signals to TDCs/FADCs are generated at the end of the VTPC drift time. When an event is accepted by the BBC trigger logic, the trigger-supervisor stops the clear-and-strobe signals and sends a "start scan" signals to all the scanner processors. This starts the data compaction in TDCs and FADC compaction modules and the following reading/formatting in the scanner processors. When the scanner processors finish, they send "done" signals back to the trigger supervisor which then sends an "event ready" signal to the host VAX. The host VAX reads the data from each scanner processor through the FASTBUS network.

During the 1987 run, we had two scanner processors each of which read 24 TDCs, and one scanner processor which read eight FADC compaction modules. The typical amount of the data was 10 Kbytes from the TDCs and 11 Kbytes from the FADCs with the BBC trigger. The data transfer rate between these modules and the scanner processors was approximately 32 bits/250 nsec. The scanner processors reordered the TDC data by channel number and TDC count within each channel and added pointers to the first word of each octant data block. It took about 0.6 msec to transfer data and 12.6 msec to formatting data for a typical event. For the FADC data, which were already compacted, the scanner processor only added the similar pointers. It took about 0.6 msec to transfer data and 2 msec to add the pointers for a typical event. Table 2.7 summarizes the VTPC data acquisition.

## Chapter 3

# Track Reconstruction and Performance

Tracks in the VTPC were first reconstructed in the  $rz$  plane with TDC data. Since the apparent curvatures of tracks in the  $rz$  plane were small, tracks were easily recognized. The  $\phi$  or  $\phi$ /curvature information were then added by using the FADC data from the pads, followed by the  $dE/dx$  calculation using the FADC data from the sense wires. The efficiency of the reconstruction has been studied by a hand-scan of reconstructed events. In this chapter we also describe the systematics and performance of the VTPC chamber using reconstructed data.

### 3.1 VTPC reconstruction

#### 3.1.1 Reconstruction with TDC data

The reconstruction with TDC data takes four steps (figure 3.1), (1) vertex determination, (2) spiral filtering, (3) stiff tracks reconstruction, and (4) weak or low- $p_t$  track reconstruction. The following paragraphs describe each step of the reconstruction in order.

#### *Vertex determination*

The purpose of the vertex determination is to find where each  $\bar{p}p$  collision occurred along the beam axis because the Tevatron had smeared collision points with a rms width of 30-40 cm. Segments of tracks are found in each VTPC octant (octant segments) by requiring at least three consecutive TDC hits. Figure 3.2 shows such octant segments with raw data points. (A part of the figure is shown magnified in figure 3.3.) The horizontal axis is the  $z$  axis and the vertical axis is the sense wire position measured from the beam axis. Each solid lined square box represents a VTPC module boundary divided into two drift spaces by the dotted line corresponding to the high voltage screen. Four octants in the same  $z$  location are superimposed on the upper half, while the other four octants on the lower half. The aspect ratio of the figure is distorted; the overall horizontal and vertical lengths correspond to 2.8 m and 42 cm, respectively. The numbers and small segments surrounding the module line represents the pseudorapidities. Using a drift velocity obtained by the method described in next section, the TDC leading edge data (hits) are translated into  $z$  coordinates and plotted as dots. The very short horizontal lines by the dots indicate pulse widths obtained from the trailing-edge time minus the leading-edge time. The straight lines connecting these dots are the octant segments having  $rz$  slopes and intercepts in  $z$ . On the  $z$  axis, there are dots representing the  $z$  intercepts of the segments. We then find a cluster of the  $z$  intercepts which corresponded to the vertex position indicated by a cross in the figure. For the events that do not have any octant segments found, we use the vertex positions obtained by the BBC time of flight.

The vertex determination required about 0.2 sec of VAX 8800 CPU time per event on average. The vertex location obtained in this step was also used by the other CDF analyses.



### *Spiral filtering*

In the VTPC, we had a background of spiral tracks. They were due in part to the primary particles coming back into the VTPC volume ( $p_t < 350 \text{ MeV}/c$ ) and in part to nonprimary particles coming from very forward/backward directions. In order to have the following steps of the reconstruction work properly, it was important to eliminate such spiral tracks.

In this process, the three consecutive TDC hits are found at inner, middle, and outer radius of each octant as seed hits, requiring hits to be aligned on a straight line and pointing away from the vertex. We require these seeds to be pointing more than 15 cm away from the vertex with  $\cot \theta \leq 4.0$ . The seeds are then extended to become tracks by finding more TDC hits in the other octants. The program which find such TDC hits from the seed hits (a *TDC-hit-search program*) is the same program used to reconstruct nonspiral tracks and is described in the fourth paragraph. We accept a spiral track if it has at least four TDC hits and if the final fit to straight line satisfies the above vertex-away criterion. Figure 3.4 shows reconstructed spirals. The figure is again the  $rz$  view of the VTPC, where the TDC hits associated with the reconstructed spirals (lines) are marked by "+". The spirals appearing on the lower right half have TDC hits only at outer radius, indicating that these came from the forward or backward direction and were not associated with the primary particles. The other spirals that have TDC hits in full radius may be the low  $p_t$  primary particles coming back into the VTPC volume.

The spiral reconstruction took typically 0.4 sec of VAX 8800 CPU time depending on the amount of backgrounds which varied run by run. The TDC hits used by the reconstructed spirals were marked and not used in the following reconstruction steps.

### *Stiff track reconstruction*

In the third step, relatively *stiff* or non-low- $p_t$  tracks are reconstructed by a *histogramming method* assisted by the TDC-hit-search program. Since such a track appears as a good straight line in the  $rz$  plane, all the associated TDC hits (points in  $rz$  plane) have almost the same pseudorapidities with respect to the vertex, and form a clear peak when histogrammed as a function of the pseudorapidity. Figure 3.5 shows such a histogram with a bin width of 0.01 in pseudorapidity. Spikes in the histogram corresponds to tracks coming from the vertex. The hits associated with each peaks are then fit to a straight line. This histogramming and fitting are done separately for two sets of VTPC modules (module number 0/2/4/6 and 1/3/5/7 from  $-z$  to  $+z$ ) — the modules in each set having no relative  $\phi$  rotation with respect to each other. This procedure eliminates the need to translate sense wire positions (the local  $y$  coordinates) into cylindrical coordinates in order to find tracks. If a track goes across the two module sets, the two resulting track segments are merged into a single track. At the same time, using the relative  $\phi$  rotation between the two module sets, the  $\phi$  position at the module boundary is obtained by combining the fit parameters in the individual module sets. If a track does not have more than 90% of TDC hits expected geometrically, the TDC-hit-search program (described in next paragraph) is invoked to attempt to find the rest of the TDC hits. In this case, the hits already found are used as seed hits. Figure 3.6 shows the tracks reconstructed in this step with raw data hits, and figure 3.7 shows the same reconstructed event with each  $\phi$  slice separately.

The TDC data associated with reconstructed tracks were marked and not used in the next step. The average CPU time for this step was about 1.6 seconds on VAX 8800.

### *Weak or low $p_t$ track reconstruction*

At this point, unreconstructed tracks are weak tracks which go close the radial boards, not-well separated tracks due to near-by tracks, or low  $p_t$  tracks. These tracks are reconstructed with the TDC-hit-search method. The hit-search starts by using a single TDC hit (a seed hit) in the outermost sense wires and proceeds to search toward the inner sense wires. The reason to start with the outermost wires is that tracks which are very close to other tracks can be better separated at the outer radius than at the inner radius. Using the vertex location obtained in the first step, we calculate the expected TDC value and width on the next sense wire. Since the sense wire separation is small (6.33 mm in local  $y$ ), such a calculation is adequate to find a next hit even for low  $p_t$  tracks. If there is an actual hit with the TDC value and width consistent with the expected one, the hit is added to the seed hits. If there are more than one seed hit, those are fitted to a straight line with a vertex constraint in order to find a next hit. No more than the nearest seven seed hits ( $|\cot \theta| < 1.5$ ) or five seed hits ( $|\cot \theta| \geq 1.5$ ) are used in this fit in order to follow a low  $p_t$  track which have curvature. If the fitting can not be consistent to the vertex location, the vertex constraint is taken out to allow secondary tracks to be reconstructed. When the next hit is expected be in the next module, the TDC data in three sense wires around the nominal one are investigated. This takes care of the transition between modules which have a relative  $\phi$  rotation. If a TDC hit is not found in next sense wire as expected, the program creates a "virtual" hit with the expected TDC value and added to the seed hits. When the number of the consecutive virtual hits exceeds a certain value (4-8 depending on the polar angle and on the number of real hits found so far), the virtual hits are dropped and the search is switched to the octant in the next  $\phi$  slice. If more than two real hits are found after switching the  $\phi$  slice, the program begins a "backward search" to make

sure these new hits do not belong to another track. The backward search, with those newly found hits as seed hits, does exactly the same thing as the forward search except that the search proceeds toward the outer radius. If the backward search find additional hits consistent to another track, or if the forward search accumulates more virtual hits than the limit, the search switches to another  $\phi$  slice. The search for each track would be terminated when it reaches the innermost sense wire or no real hits are found in the two neighboring  $\phi$  slices. If the search find at least four real hits on consecutive wires, they are accepted as a track. The all TDC data associated with an accepted track are flagged and are not used in the subsequent hit-searches. After using all the TDC hits in the all outermost sense wires as seed hits, the hit-search uses hits from the next inner sense wires as seed hits. The fully reconstructed tracks after this step are shown in figure 3.8 and each  $\phi$  slice is shown in figure 3.9 separately. The average CPU time for this reconstruction step was 0.6 sec on VAX 8800.

As already mentioned, The TDC-hit-search program was also used in the spiral filtering and stiff track reconstruction. For spiral filtering which uses sets of three TDC hits as seed hits, the vertex constrain is removed and switching between  $\phi$  slices is prohibited to minimize the CPU time. For the stiff track reconstruction, the TDC hits found by the histogramming method are used as seed hits. In this case the hit-search proceeded toward both the inner and outer radius. The total average CPU time for the reconstruction of TDC data was 2.8 sec on VAX 8800.

The fraction of tracks reconstructed in each step shows the characteristics of each reconstruction. On the average, 30% of tracks were reconstructed by the stiff track reconstruction without a help of the hit-search program and 48% of tracks were reconstructed with the help of the hit-search program. The last step of the reconstruction — the hit-search program, took care of the rest of tracks (22%). (All percentages shown here were after applying a track selection described in next chap-

ter.) By using a single track simulation where particles were generated uniformly in  $\eta$  and randomly in  $\phi$ , the ratios of tracks reconstructed in each step were found to be functions of the track  $p_t$ . Table 3.1 summarizes the ratios for the different track  $p_t$ . As the track  $p_t$  become smaller, more tracks are found in the later reconstruction steps. For tracks with  $p_t = 800 \text{ MeV}/c$ , for instance, the histogramming method found 79% of tracks, the histogramming with hit-search method found 17% of tracks, and the hit-search method found 4% of tracks, while for  $p_t = 100 \text{ MeV}/c$ , the ratios changed to 24%, 54%, and 22%, respectively. The  $\eta$  distribution of tracks reconstructed in each step have also been studied with real  $\bar{p}p$  data. Figures 3.10, 3.11, and 3.12 show the  $\eta$  distributions of the track reconstructed by the histogramming method, the histogramming + hit-search method, and the hit-search method, respectively. These are after track selection. The tracks found by the histogramming method alone are seen more in smaller  $|\eta|$  than in larger  $|\eta|$ . The  $\eta$  distribution with the histogramming + hit-search shows the opposite characteristics. This is because the apparent curvature in the  $rz$  plane is larger for larger  $|\eta|$  with a fixed  $p_t$ . The  $\eta$  distribution with the hit-search method shows sharp peaks around  $|\eta| = 3.3$ . This is because the tracks with that  $|\eta|$  exited the VTPC modules with TDC hits only 4-10 sense wires and were not easily found by the histogramming method.

### 3.1.2 Reconstruction with pad FADC data

After finding tracks with the TDC data, we used the FADC data from the pads in order to obtain complete the three-dimensional information including the particle transverse momenta. An example of the FADC raw data is shown in figure 3.13, which indicates the three dimensional prospect of the VTPC pads with raw FADC data in an octant. The vertical axis is the radius  $r$  and  $\phi$  increases counter clockwise around the beam axis which is below outside of the picture. Each pad row is drawn as a plane at inner, middle, and outer radius. (The actual pad had a fan shape as shown in figure 2.7. The edges of the three pad rows have the same  $\phi$  coordinates.)

The axis perpendicular to the  $r\phi$  plane corresponding to the  $z$  coordinate or the drift time  $t$ . On each pad, the FADC raw data are shown on each pad as a function of  $t$  with the height corresponding to FADC counts. The rms width of the induced charge distribution was typically one pad spacing (1.5 cm in  $r\phi$ ) and therefore there were typically three pads receiving significant induced charges for a track. This example shows that two tracks went through this octant. One track, at larger  $\phi$  (left hand side), entered into the middle row at late  $t$  and exited from the outer row at early  $t$ . Another track, at smaller  $\phi$  (right hand side), entered into the inner row at late  $t$  and exited from the middle row in early  $t$ .

The flow of the pad FADC reconstruction is shown in figure 3.14. The reconstruction starts with finding peaks in the induced charge distributions. The peaks are searched in each pad row in every FADC time slice of  $\Delta t = 94 \text{ nsec}$  in the all octants where the TDC  $rz$  tracks are found. After the raw FADC data are converted into calibrated data by subtracting pedestals and applying electronic gain corrections, the  $\phi$  position of each peak is determined by fitting a Gaussian to the measured charge distribution. The  $z$  positions are obtained from the FADC time bin numbers. Approximately 20% of peaks are not isolated and results in multiple peaks. We use an iteration program to separate such multiple peaks. The zeroth-approximations of height, width, and position of each peaks are first obtained by fitting a Gaussian to the distribution around a peak pretending each peak is independent. Next, the contribution from all other peaks are subtracted using the approximated heights, widths, and positions of the other peaks. We obtain better parameters by fitting a Gaussian to this peak after the subtraction. These better parameters are then used for the next subtraction. The program repeats 5-20 time of this process depending on the number of degrees of freedom. (The parameters converges faster with more number of degrees of freedom.)

The FADC data are now translated into the points on the  $z\phi$  plane where the

primary tracks are easily recognizable straight lines with small  $d\phi/dz$  slopes. These lines are usually well separated in one of the three measured coordinates. In each pad raw, the points associated with a single track segment are a group of points which are located contiguously in both  $z$  and  $\phi$ . We find such groups of points by a two-dimensional histogram method. The points are filled into the  $z\phi$  histogram weighted by the peak heights of the induced charge distributions. Examples of such two-dimensional histograms are shown in figures 3.15a-c. The histograms are filled the  $z\phi$  points obtained from the raw data shown in figure 3.13 for each pad raw. The bin width of the histogram is two FADC time bins in  $z$  (188 nsec in drift time or 0.79 cm in  $z$ ) and 0.022 radian ( $1.25^\circ$ ) in  $\phi$  for all pad raws. The program makes the projection of this histogram first onto the  $\phi$  axis on which an track segment appears as a peak for non-low  $p_t$  track or a broad peak for low  $p_t$  track. All the points in a found peak are then used to make a projected histogram onto the  $z$  axis. This is to separate two different track segments which have about the same  $\phi$  but are located in different  $z$ . The points associated with a single track segment appears as a group of contiguous points in this  $z$ -projected histogram. If the program find such a group, it is recognized as a track segment, and the points in the group are taken out from the original two-dimensional histogram. The next process starts with remaking the  $\phi$ -projected histogram. This process continues until all points in the two-dimensional histogram are removed.

The segments are then matched with tracks found in the  $rz$  wire reconstruction. From the  $rz$  track parameters ( $z_0$  and  $\cot\theta$ ), the expected  $z$  position and  $z$  length of the track segment are geometrically calculated for each pad raw. The pad  $z\phi$  segments which satisfies the expected  $z$  position and  $z$  length are searched in each raw. After finding all  $z\phi$  segments for the  $rz$  track, all points associated with the segments are fitted to a straight line in the  $z\phi$  space. This fit combines with the  $rz$  information yields complete three dimensional tracks.

### 3.1.3 Reconstruction with wire FADC data

## 3.2 VTPC systematics and alignment

We observed several systematic effects which required corrections in the reconstruction. Proper treatment of the effects was essential to ensure good tracking efficiency when linking tracks across the chamber boundaries and the transverse momentum measurement. Since the effect and amounts of the systematics appeared differently in the  $rz$  plane (the TDC reconstruction) and in the  $z\phi$  plane (the FADC reconstruction), we employed different methods.

### 3.2.1 Systematics with TDC data

We have observed the following systematic effects with the TDC data:

1. Chamber misalignment
2.  $E \times B$  effect due to the misalignment
3. Apparent shift in track position as a function of polar angle
4. Apparent shift of track position due to diffusion effect
5. Variation in drift velocity due to pressure and temperature variation

The effects on the TDC data appeared as 1) discontinuities of track segments at octant or module boundary and as 2) deviation of the track intercept from the primary vertex in  $z$ . Requiring the continuity at the chamber boundaries and the agreement between the intercept and the vertex, several systematic effects were studied and the corrections were obtained by a most likelihood method. The detail of the wire systematic study is described in appendix F.

### 3.2.2 Systematics with pad FADC data

We have observed the following systematic effects on the pad FADC data:

1. Chamber misalignment
2.  $E \times B$  effect due to the misalignment
3. Apparent shift of  $\phi$  position near octant boundary
4. Deviation of induced charge distribution from a Gaussian

The systematic effects on the pad data were studied by using the CTC tracks because they had good uniform  $\phi$  precision ( $\sim 250 \mu\text{m}$ ) with much less systematic and misalignment effects [50]. We selected relatively high quality CTC tracks which had at least 30 axial layer hits and 12 stereo layer hits with  $p_t \geq 0.8 \text{ GeV}/c$ . The FADC raw data were translated into the  $z\phi$  hits as described in section 3.1.2. The expected positions of the pad hits were calculated from the CTC track parameters. If the pad hits were found within one pad width ( $4.5^\circ$ - $7.5^\circ$  depending on the raws) and if they were near the expected  $z$  position, the hits were used to calculate the deviations from the CTC tracks. We defined the deviation as:

$$\Delta\phi = \phi_{VTPC} - \phi_{CTC}, \quad (3.1)$$

or

$$\Delta r_\phi = r \cdot (\phi_{VTPC} - \phi_{CTC}), \quad (3.2)$$

where  $r$  is a radius calculated from the CTC track parameters,  $\phi_{VTPC}$  is the  $\phi$  position of each pad hit, and  $\phi_{CTC}$  is the expected  $\phi$  position of tracks at  $r$  calculated from the CTC track parameters (See figure 3.16). We observed the systematics by looking at the distribution of  $\Delta r_\phi$ .

Most of the effects were approximately independent. For instance, the effects of the radial board were smeared over when we studied the other effects. The  $E \times B$

effects were extracted by comparing  $\Delta r_\phi$  at the short drift distance to that at the long drift distance to be independent of other effects. Figure 3.17-3.18 show the distribution of  $\Delta\phi$  for two of the VTPC modules. Since the distributions include  $\Delta\phi$  for all  $\phi$  direction, the overall shift of the peak position, which is nearly zero in figure 3.17 and about 10 mrad in figure 3.18, is the relative  $\phi$  rotation between the CTC and the VTPC modules caused by the misalignment. The detail description and discussion can be seen in appendix G. Here, we would like to show only one example. Most of the misalignment effects agreed with alignment survey data.

### 3.3 VTPC chamber performance

For tracks near  $\theta = 90^\circ$  (i.e., parallel to the sense wire plane) the longitudinal diffusion of electrons dominated the measured resolution. For tracks highly inclined with respect to the wire plane, different effects dominated at different drift distances. Ionization fluctuations dominated the resolution for short drift distances and the transverse diffusion dominated for long drift distances. We have been studying hit-residuals from the fitted straight line. The  $z$  resolution is defined to be the rms width of the residual distribution. Figure 3.20 shows the  $z$  resolution averaged over the drift length as a function of polar angle  $\theta$ . For  $90^\circ$  tracks the resolution was  $420 \mu\text{m}$ , rising to  $1100 \mu\text{m}$  at  $11^\circ$ . Figure 3.21 shows the  $z$  resolution squared as a function of the drift distance for  $90^\circ$  tracks. This plot is expected to be approximately linear because the longitudinal diffusion fluctuations scale as the square root of the drift distance. The line superimposed on the plot represents the best fit to the data. The position resolution near the sense wires was about  $200 \mu\text{m}$ , while the resolution for the longest drift times was about  $550 \mu\text{m}$ .

To study the vertex resolution, we used the impact parameter  $b$  of a track which is defined by:

$$b = (z_{\text{track}} - z_{\text{vertex}}) \cdot \sin \theta, \quad (3.3)$$

where  $z_{\text{track}}$  is the  $z$  intercept of a track and  $z_{\text{vertex}}$  is the event vertex. Figure 3.22 shows the distribution of the impact parameters for a few hundred  $\bar{p}p$  events. The rms width of the distribution is about 0.3 cm.

Multiple track separation in  $z$  was determined primarily by the pulse width of signals from a single track. At  $90^\circ$ , the pulse width for a track corresponded to about 0.5 cm of drift length. For smaller angles, the effective pulse width was  $W_s \cdot \cot \theta + 0.5$  cm, where  $W_s$  is the wire spacing and equaled to 0.634 cm. For instance, the width is 1.6 cm for  $\theta = 30^\circ$  and farther increases to 4.1 cm for  $\theta = 10^\circ$ .

The chamber precision in  $\phi$  has been studied by looking at the residual distribution of the pad data. For a given FADC sampling, the  $\phi$  residual from the fitted line in the  $z\phi$  plane was calculated for isolated tracks. The  $\phi$  residual was converted into  $r\phi$  residual using the  $r$  information of the track. Figure 3.19 shows the  $r\phi$  residual distribution per FADC sampling averaged over the drift length. The distribution is fitted to a Gaussian with a  $\sigma$  of 418  $\mu\text{m}$ . The residual  $\sigma$  was about 350  $\mu\text{m}$  per sampling for a very short drift length ( $\sim 1$ -2 cm) and 400-450  $\mu\text{m}$  per sampling for a larger drift length. There were 40 FADC samplings made on a track that extended across the full 15.25 cm drift region. Since the shaped-pulse width from the PAS was about 200 nsec in FWHM, there were correlations in successive FADC samplings whose rate was 94 nsec. The number of independent measurements was typically about 15 with 40 successive samplings. The overall chamber precision was therefore of order 100  $\mu\text{m}$ .

The VTPC  $p_t$  resolution has been studied by comparing VTPC  $p_t$  and CTC  $p_t$  for the same tracks. The procedure we took was the same ones used for the pad systematic study. Since the CTC had more than 100 times higher  $p_t$  resolution, this gave a good measurement of the VTPC  $p_t$  resolution. The  $p_t$  resolution is defined

as:

$$\Delta = \frac{|p_{t\text{VTPC}} - p_{t\text{CTC}}|}{p_{t\text{CTC}}}, \quad (3.4)$$

where  $p_{t\text{VTPC}}$  and  $p_{t\text{CTC}}$  are the transverse momenta measured by the VTPC and CTC, respectively. Figures 3.23-3.24 show the distribution of  $\Delta$  for different radial spans of tracks,  $5.0 \text{ cm} \leq \Delta r \leq 10 \text{ cm}$  and  $10.0 \text{ cm} \leq \Delta r \leq 15 \text{ cm}$ . (Since the pad FADC were not installed in all modules, the radial span where the  $\phi$  measurement was available differed track by track.) The rms of  $\Delta$  is approximately  $0.5 (\text{GeV}/c)^{-1}$  for the small  $\Delta r$  and  $0.3 (\text{GeV}/c)^{-1}$  for the large  $\Delta r$ . Deterioration of the  $p_t$  resolution for smaller  $\Delta r$  is due to the fact that the  $p_t$  resolution is proportional to  $1/\Delta r^2$ . The  $p_t$  resolution by the pads was thus typically  $0.3$ - $0.5 \cdot p_t$  in rms, where  $p_t$  is in  $\text{GeV}/c$ .

The efficiency of the pad data has been studied with reconstructed CTC tracks. We counted the number of FADC samplings which gave  $\phi$  positions in the expected road determined by a CTC track. The probability that there were one or more such FADC samplings is plotted as a function of  $\phi$  in figure 3.25. The inefficiency at every  $45^\circ$  was due to the chamber inefficiency near the octant radial board boundary. A depression around  $\phi = 0$ , where the last  $\phi$  slice is located, is due the buffer overflow in the scanner processor. Figure 3.26 shows the probability that there were more than two such FADC samplings. Similarity between figure 3.25 and figure 3.26 indicates that there were at least three FADC samplings in most of the cases. This was due to the fact that the signals from the pads were shaped so that the minimum pulse width was about 200 nsec in FWHM compared to the FADC sampling rate of 94 nsec.

### 3.4 VTPC reconstruction efficiency

The efficiency of the track reconstruction has been studied by hand-scanning for about 200 events with about 6000 tracks. Tracks were first reconstructed by the

computer program. Scanners then checked the results by mean of graphic terminals. If the track which should have been reconstructed by the program do not present, the scanners interactively reconstructed the tracks. If the tracks reconstructed by the program is created from the junk TDC hits (mostly from spirals), the tracks were deleted. If the two track segments which belongs to the same track were not merged together by the program, the scanners created a single track by merging the segments. The events with a vertex position of  $-31 \text{ cm} < z < -3 \text{ cm}$  or  $3 \text{ cm} < z < 31 \text{ cm}$  were selected in order to keep the geometrical acceptance to be 100 % for  $-3 \leq \eta \leq 3$  and to avoid the chamber gap around  $z=0$ . After the scanning, we applied a track selection described in the next chapter and calculated the reconstruction efficiency. Figures 3.27 shows the reconstruction efficiency as a function of  $\eta$ . The efficiency is symmetric for  $+\eta$  and  $-\eta$ . The maximum overefficiency is about 105-107% at  $\eta = \pm 2.5$ . We see the reconstruction has an least efficiency of about 100% at  $\eta = 0$  and 3.0.

This study tells only the efficiency for the average  $p_t$  and multiplicity. The  $p_t$  dependence and multiplicity dependence of the reconstructed efficiency has been studied by using a Monte Carlo program and described in the next chapter.

## Chapter 4

### Analysis

After VTPC tracks were reconstructed, we selected tracks coming from primary vertices by a method described in §4.2). The selected samples of tracks still contained some nonprimary tracks. These were:

- Converted particles (mostly  $\gamma \rightarrow e^+e^-$ ) due to materials,
- Charged particles produced by decays of neutral particles such as  $K_S^0$ 's.

On the other hand, there were some losses of primary tracks due to:

- Track selection itself,
- Inefficiency of the reconstruction for very low  $p_t$  tracks ( $< 50\text{-}75\text{ MeV}/c$ ),
- Inefficiency of the reconstruction for very high multiplicity events,
- Inefficiency of the chambers near the octant boundaries (radial boards).

The amounts of background and lost tracks were determined by a Monte Carlo simulation, as described in section 4.3. An event selection program was then applied in order to distinguish  $\bar{p}p$  collisions from background events such as beam-gas interactions. Section 4.5 describes the event selection criteria and the efficiency. The correction to the low  $p_t$  spectrum has been studied separately because it required a different correction. This is described in section 4.4.

#### 4.1 Monte Carlo event simulation

Our Monte Carlo  $\bar{p}p$  event simulation was based upon the extrapolation of CERN-ISR and -SPS data to  $\sqrt{s} = 1.8\text{ TeV}$ . The extrapolation was obtained by fitting the energy dependence of the charged multiplicity and the  $p_t$  spectrum. The followings are some of the extrapolated quantities:

- average charged multiplicity = 36.2 for  $-5 < \eta < 5$ ,
- KNO distribution,
- $dN/d\eta$  ( = 4.1 at  $\eta = 0$  ),
- $p_t$  distribution (  $\langle p_t \rangle = 560\text{ MeV}/c$  ).

Figure 4.1 shows the  $dN/d\eta$  from the Monte Carlo simulation at  $\sqrt{s} = 1.8\text{ TeV}$  (circles) with UA5 data at  $\sqrt{s} = 546$  and  $900\text{ GeV}$  [14]. Although the simulated  $dN/d\eta$  is flatter than the real  $dN/d\eta$ , overall behavior is satisfactory. The KNO  $\psi$  at  $\sqrt{s} = 1.8\text{ TeV}$  from the simulation is shown in figure 4.2 with UA5 data at  $\sqrt{s} = 546\text{ GeV}$  [1]. Both are for  $|\eta| \leq 3$ . The multiplicity distribution used in the simulation is based on the experimental data for full  $\eta$  range, and is fixed for all  $\eta$  regions. The actual data, however, have slightly different distributions in different  $\eta$  regions. This difference is shown in the figure. Figure 4.3 shows the  $p_t$  spectrum (  $1/\sigma(d\sigma/dp_t^2)$  ) at  $1.8\text{ TeV}$  from the simulation with the actual CDF CTC and UA1 data. Circles are the simulated data, the dashed line is a fit to the CTC measurement at  $1.8\text{ TeV}$  [86] and the dotted line is a fit to the UA1 data [87]. The agreement between the CTC fit and the simulation is quite good. The minimum  $p_t$  generated in the simulation was  $30\text{ MeV}/c$ .

The VTPC detector simulation consisted of two parts, (1) a TDC leading edge simulation and (2) a wire/pad pulse height simulation. The TDC leading edge simulation translated  $z$ -positions of sense wire hits into TDC counts using the chamber



characteristics and systematics obtained from the actual data (described in section 3.2). In the pulse height simulation, the wire/pad pulse height distribution was generated according to the  $dE/dx$  distribution measured experimentally. The integrated pulse heights were then calculated based on time constants of the electronics and on the time window of TDC or FADC samplings. For TDC data, the time-over-threshold method was applied to these simulated pulses to derive TDC trailing edges and multiple hits. For pad signals, the fractions of charge received by each pad were calculated depending on the area of the pad and on the distance of the pad from the sense wire hit. The details of the VTPC simulation and its comparisons to the actual data are described in appendix E *VTPC detector simulation*.

## 4.2 Track Selection

Reconstructed tracks contained nonprimary tracks such as converted particles due to materials, decayed particles from strange particles, and low momentum spiral tracks. We selected tracks depending on how well they pointed back to the primary vertex to eliminate these nonprimary tracks (the vertex cut method). We define:

$$Z_{off} \equiv (Z_{track} - Z_{event}) / \sqrt{(\Delta Z_{track})^2 + (\Delta Z_{event})^2}, \quad (4.1)$$

where

- $Z_{track}$  :  $z$ -intercept of a track,
- $Z_{event}$  : Vertex position in  $z$ ,
- $\Delta Z_{track}$  : Error in  $Z_{track}$ ,
- $\Delta Z_{event}$  : Error in  $Z_{event}$ .

$Z_{track}$  and  $\Delta Z_{track}$  were calculated by a track fitting program. A track was fitted to a straight line by a least- $\chi^2$  method with the following two errors added in quadrature:

1. Error due to the diffusion effects: From the chamber systematic study, this was estimated to be:

$$\Delta z = 0.04 \cdot \sqrt{1 + \cot^2 \theta} \text{ cm}. \quad (4.2)$$

2. Error due to the track curvature: The helical trajectory of a primary track on the  $rz$ -plane is (a proof in appendix H):

$$z = z_0 + 2R_{cv} \cot \theta \cdot \arcsin \left( \frac{r}{2R_{cv}} \right), \quad (4.3)$$

where  $R_{cv}$  is a curvature radius and  $z_0$  is a  $z$  intercept. The deviation from the assumed linear trajectory ( $z = z_0 + \cot \theta \cdot y$ , where  $y$  is the octant  $y$ -coordinate) is:

$$\Delta z = \cot \theta \cdot (2R_{cv} \arcsin \left( \frac{r}{2R_{cv}} \right) - y). \quad (4.4)$$

We used  $2R_{cv} = 177.6$  cm corresponding to an average  $p_t$  of 400 MeV/c. The  $r$  in equation 4.4 was not always known because we needed both  $\phi_0$  ( $\phi$  at  $r = 0$ ) and  $2R_{cv}$  of each track to calculate  $r$  from an octant  $y$ -coordinate. The  $\phi$  calculated from the stereo method was reliable only for relatively high  $p_t$  tracks ( $> 1.2$  GeV/c) and the  $\phi_0$ /curvature obtained from the pads were available for only fraction ( $\sim 1/4$ ) of tracks. The error due to this uncertainty was estimated by inserting the following relation into equation 4.4:

$$r = y / \cos \phi_{local}, \quad (4.5)$$

where  $y$  is the octant  $y$ -coordinate and  $\phi_{local}$  is the local  $\phi$ -coordinate ( $=0^\circ$  at an octant center and  $=22.5^\circ$  at the octant boundary) which is a function of  $r$ ,  $\phi_0$ , and  $R_{cv}$ . We used an average value of  $\cos \phi_{local} = 0.9745$ . The error  $\Delta z$  by equation 4.4 increases as  $r$  increases and is proportional to  $\cot \theta$ : for instance, it is 1.0 mm for  $r = 6.5$  cm /  $\cot \theta = 1$  and increases to 6.0 mm at  $r = 21$  cm.

To calculate  $Z_{event}$  and  $\Delta Z_{event}$ , the tracks that formed a cluster in the  $Z_{track}$  distribution were selected.  $Z_{event}$  was calculated from  $Z_{track}$ 's and  $\Delta Z_{tracks}$ 's of those tracks as well as  $\Delta Z_{event}$  from  $\Delta Z_{track}$ 's. Figure 4.4 shows the distribution of  $Z_{off}$  for actual  $\bar{p}p$  events. The figure is the superimpose of three plots,  $Z_{off}$  for  $0 \leq |\eta| < 1$ ,  $1 \leq |\eta| < 2$ , and  $2 \leq |\eta| \leq 3$ . There are no significant differences among three  $\eta$  ranges, which indicates we would not distort the  $dN/d\eta$  distribution by the track selection. The FWHM of the distribution is approximately 2.4 which is consistent with an ideal case of 2.3. The track selection was  $|Z_{off}| \leq 4.0$  as indicated by arrows. Figure 4.5 shows a comparison of  $Z_{off}$  for real data with that for simulated data. The solid line is for the real data, the dashed line is for the simulation with the material effects (conversion and scattering) and decays. The histograms are normalized by the number of events. The width is slightly narrower for the simulated data. Figure 4.6 shows the effects of materials and decays. The solid line is the simulated  $Z_{off}$  distribution with these effects turned on and the dashed line is the simulated distribution without these effects. The histograms are again normalized by the number of events. They affect not only tails but rather the overall distribution. Although we selected tracks by  $|Z_{off}| \leq 4.0$  (a "nominal" cut), a "tight" cut ( $|Z_{off}| \leq 3.0$ ) and a "loose" cut ( $|Z_{off}| \leq 6.0$ ) have also been studied.

We did not select tracks by a TDC-hit occupancy or TDC-hit efficiency because there were some primary tracks with low occupancies. The occupancy is defined as:

$$Occupancy \equiv \frac{N_{fnd}}{N_{exp}}, \quad (4.6)$$

where  $N_{fnd}$  is the number of TDC hits found in a track, and  $N_{exp}$  is the number of geometrically expected TDC hits for the track. There were tracks which went close to the VTPC radial board leaving no TDC hits in some sense wires. There were also some two closely associated tracks which were not well separated resulting in low occupancies. Figure 4.7 shows the occupancy distributions after the track selection for real (solid line) and simulated (dashed line) data. The histograms are

normalized by the number of events. Multiple peaks in the distributions are due to the fact that the maximum number of wires is 24. The shapes of the distributions are quite similar for the real and simulated data. The average occupancy was 0.82 for the read data and 0.86 for the simulated data. The fraction of tracks which have the occupancy less than 0.5 is approximately 10%. The low occupancies for such tracks prevented us from distinguishing nonprimary tracks by looking at the starting position of track segments.

### 4.3 Corrections to charged multiplicity

The corrections to the charged multiplicity due to the various effects were obtained using the Monte Carlo program. The Monte Carlo program could turn on/off the effects such as conversions/scatterings by materials or particle decays. After reconstructing simulated events and applying the track selection, we compared the  $dN/d\eta$  with the effect turned on to that with the effect turned off. The net difference is expected not to be too sensitive to the detail of the Monte Carlo simulation. We did not have an acceptance correction because we required the event vertex position to be  $-31 \text{ cm} \leq z \leq -3 \text{ cm}$  or  $3 \text{ cm} \leq z \leq 31 \text{ cm}$  throughout the analysis. This kept the geometrical acceptance to be 100% for  $-3 \leq \eta \leq 3$ .

#### 4.3.1 Loss of very low $p_t$ tracks

There was a loss of tracks with very low  $p_t$  ( $< 50\text{-}75 \text{ MeV}/c$ ) due to the inefficiency of the VTPC reconstruction. This has been studied with a single particle simulation. For each event,  $\pi^+$  with a fix  $p_t$  was generated randomly in  $\phi$  and uniformly in  $\eta$ . After the reconstruction and the track selection, the efficiencies were obtained by comparing  $dN/d\eta$ 's for low  $p_t$  to  $dN/d\eta$  for  $p_t = 9 \text{ GeV}/c$ . Figure 4.8 shows the ratio of  $dN/d\eta$  for  $p_t = 50 \text{ MeV}/c$  to that for  $p_t = 9 \text{ GeV}/c$ . The efficiency in  $|\eta| < 1$  is below 50%, while the efficiency is 70-80% for larger  $|\eta|$ . Figure 4.9 shows

the ratio for  $p_t = 100$  MeV/c. The efficiency is more uniform and approximately 80%. We studied the efficiency up to  $p_t = 300$  MeV/c and made a sum of weighted efficiencies using the UA1  $p_t$  spectrum. Figure 4.10 shows the net efficiency plotted against  $|\eta|$ . The net effect of low  $p_t$  particles is 5% at most. For  $|\eta| > 1$ , a slight overefficiency is seen because the VTPC reconstruction occasionally breaks a single low  $p_t$  tracks into two separate segments, resulting in a double-counting.

#### 4.3.2 Loss of tracks near the radial board

The charged particles which passed close to the VTPC radial boards resulted in some inefficiency. In order to simulate this effect, the chamber gain near the radial board was obtained by studying the minimum ionizing. Figure 4.11 shows the ratios of  $dN/d\eta$  with the radial board effects turned on to  $dN/d\eta$  with the effects turned off. In the figure, circles are with the nominal vertex cut, triangles are with the loose vertex cut, and rectangles are with the tight vertex cut. The loss of tracks is about 2% in  $|\eta| > 1$  where a particle goes through at least two VTPC modules rotated in  $\phi$  to each other to reduce the effects of the radial boards. It increases to 4-5% in  $|\eta| < 1$  where a particle has more chance to go through only one VTPC module.

#### 4.3.3 Loss of tracks by the vertex cut

Because of the finite vertex resolution of a track, we had a loss of the primary tracks in the process of the track selection. We used the Monte Carlo simulation in which all tracks were the primary ones — no effects of materials, decays, nor radial-boards. The change in  $dN/d\eta$  with different vertex cuts is therefore only due to the loss of the primary tracks. We compared  $dN/d\eta$  with various vertex cuts to  $dN/d\eta$  with a very loose ( $Z_{off} \leq 8$ ) vertex cut. The very loose cut was applied to avoid the double-counting of low  $p_t$  spiral tracks. The ratios of  $dN/d\eta$  are shown in figure 4.12. The loss by the loose cut is about 1% independent of  $\eta$ . The discontinuities are seen at

$|\eta| = 1.4$  and  $2.2$  for the nominal and tight cuts. This indicates that tracks fitted by the stereo method over more than one VTPC module has a larger pointing power.

#### 4.3.4 Effects of materials

We simulated all possible electromagnetic and hadronic interactions ( $dE/dx$ , scatterings, and conversions) to neutral/charged particles for all materials inside of the VTPC system. The most dominant contribution was the  $e^+/e^-$  conversions from photons which were the decay products of  $\pi^0$ 's. The decay  $\pi^0 \rightarrow \gamma\gamma$  has a branching ratio of 98.8 % with  $c\tau = 2.5 \times 10^{-6}$  cm [85]. According to the Monte Carlo simulation, one event has on average about 30 photons relatively uniformly in  $|\eta| < 3$ . This corresponds to 5 photons per unit  $\eta$ . For  $|\eta| < 1.5$  where the amount of the materials before the VTPC active volume was 0.5-1.0% of radiation length (figure 2.12), the number of converted  $e^+/e^-$ 's per unit  $\eta$  would be  $2 \times 5 \times (1 - e^{-0.005 \times 7/9}) = 0.05$  to  $2 \times 5 \times (1 - e^{-0.01 \times 7/9}) = 0.1$ . The number of  $e^+/e^-$ 's would increase to 0.6 per unit  $\eta$  at  $|\eta| = 3$  where the amount of the material traversed was 6% of radiation length. Approximately 3/4 of the converted tracks, however, did not make contribution because of the track selection (the vertex cut). Figure 4.13 shows the ratios of the  $dN/d\eta$  with the effects turned on to that with the effects turned off (both are after the track selection is applied). Circles are with the nominal vertex cut, triangles are with the loose vertex cut, and rectangles are with the tight vertex cut. The maximum contribution is about 5 % at  $|\eta| = 1.0$  and 2.7. Some primary tracks (5%) are lost around  $\eta = 0$  because of the conversions.

#### 4.3.5 Effects of particle decay

Some particles such as  $K_S^0$  ( $c\tau = 2.675$  cm) decay into charged particles before entering the VTPC detector volume contributing to the charged multiplicity. Figure 4.14 shows the simulated distribution of radius  $r$  of charged particle production. A large peak at  $r = 0$  indicates primary particles and a tail indicates decay secondaries.

Since the vertex cut can not be very effective for secondaries originated close to  $r = 0$ , this makes the largest correction among the all effects. Figure 4.15 shows the ratios of  $dN/d\eta$  with the particle decay turned on to  $dN/d\eta$  with the decay turned off. In the figure, circles are with the nominal cut, triangles are with the loose cut, and rectangles are with the tight cut. The contribution from decays is maximum (12-15%) at  $|\eta| \sim 2$ , while as low as 5% in  $|\eta| < 1$ .

#### 4.3.6 Overall efficiency

We have obtained an overall efficiency (or overall-correction<sup>-1</sup>) by comparing the  $dN/d\eta$  input of the Monte Carlo and the reconstructed  $dN/d\eta$  with the detector simulation which include all possible effects described above. This also includes the reconstruction efficiency. Figure 4.16 shows the ratios of  $dN/d\eta$  as the Monte Carlo input to the reconstructed  $dN/d\eta$  for three vertex cuts. The curves are drawn by a computer such that they connect each data point smoothly. The overall efficiency is more than 90% and less than 110% with the nominal vertex cut for  $|\eta| \leq 3.0$ . The vertex cuts make approximately less than 5% differences in the efficiency. (The efficiencies are tabulated in table 4.1.)

#### 4.3.7 Trigger bias

The event sample triggered by the Beam-Beam Counters (BBC) is a mixture of single diffractive, double diffractive, and non diffractive events. The fraction of diffractive events often depends on  $\sqrt{s}$  or the experimental apparatus. It is therefore useful to estimate the physical quantities for pure non diffractive events or for non single diffractive events.

According to the Monte Carlo simulation, the fraction of single diffractive event is estimated to be  $3.4 \pm 1.2\%$  at  $\sqrt{s} = 630$  GeV, and increases to  $5.9 \pm 2.2\%$  at  $\sqrt{s} = 1.8$  TeV (§2.6 and table 2.9). On the other hand, the estimated BBC acceptance at  $\sqrt{s} = 1.8$  TeV is 71% and 96% for double diffractive and non diffractive events,

respectively. (See figure 4.17.) Since the BBC acceptance for single diffractive events is mere 17%, it is not unnatural to assume that the missed 4% of non diffractive events or missed 21% of double diffractive events are “single diffractive like” events. We may estimate the effects of missing parts of non diffractive and double diffractive events by studying the single diffractive events.

Figure 4.18 shows the  $dN/d\eta$  for single diffractive events generated by a Monte Carlo simulation [76]. The  $dN/d\eta$  is relatively flat ( $\sim 1$ ) and slowly increases toward the large  $\eta$ . The  $dN/d\eta$  is shown in figure 4.19, where  $dN/d\eta$  is approximately 2. We may conclude that the missing parts of events have an average charged particle density of  $\sim 1$  and the triggered single diffractive events or double diffractive events have an average charged particle density of  $\sim 2$ . Let the average charged density of triggered non diffractive events be  $x$ . At  $\sqrt{s} = 1.8$  TeV assuming an average charged density of  $\sim 4$  for the BBC-triggered events, we have:

$$4 = 2 \times 0.059 + 2 \times 0.066 + x \times 0.877. \quad (4.7)$$

$x$  is 4.28. The averaged charged density of non diffractive (ND) events (triggered + untriggered) is:

$$B = x \times 0.96 + 1 \times 0.04 = 4.15. \quad (4.8)$$

This is  $\sim 4\%$  higher than the average charged density with the BBC trigger. The average charged density of non single diffractive (NSD) events is:

$$C = \frac{1}{40.2 + 4.2} (B \times 40.2 + (2 \times 0.71 + 1 \times 0.29) \times 4.2) = 3.92. \quad (4.9)$$

$C$  is  $\sim 2\%$  smaller than  $B=4$ .

The BBC acceptances and triggering cross sections at  $\sqrt{s} = 630$  GeV are illustrated in figure 4.20 for various processes. Assuming an average charged density of 3 ( $|\eta| \leq 3$ ) and using the same argument, the average charged density for pure non diffractive events is estimated to be 2.97 (1% smaller than 3). The averaged

charged density for pure non single diffractive events is estimated to be 2.89 (4% smaller than 3).

The effects of single or double diffractive events to the charged multiplicity is small. The KNO plots of simulated single and double diffractive events at  $\sqrt{s} = 1.8$  TeV are shown in figures 4.21 and 4.22. The distributions are maximum at  $n = 1$  and rapidly decrease exponentially. Therefore most of the effects to the actual KNO plot is limited to the smallest  $n/\langle n \rangle$ .

### 4.3.8 Track density dependence of efficiency

The reconstruction efficiency depended on the number of the tracks in an event. We have obtained this dependence by comparing the number of reconstructed tracks to the number of generated tracks in the simulation which generated the number of tracks uniformly from 1 to 150. Figure 4.23 is a scatter plot where the number of generated track is plotted against:

$$\Delta N_{trk} = N_{rec} - N_{gen}, \quad (4.10)$$

where  $N_{rec}$  is the number of reconstructed tracks after the track selection applied, and  $N_{gen}$  is the number of generated tracks. The pseudorapidity range was  $|\eta| \leq 3.0$ . The average of  $\Delta N_{trk}$  is shown in figure 4.24 as a function of  $N_{gen}$ . The error bars are statistical ones and the curve is the fit to a function:

$$\Delta N_{trk} = p1 \cdot N_{gen} + p2 \cdot N_{gen}^2 + p3 \cdot N_{gen}^3, \quad (4.11)$$

where

$$p1 = -1.0E-2 \pm 1.6E-2,$$

$$p2 = -6.6E-4 \pm 3.8E-4,$$

$$p3 = -6.1E-6 \pm 2.6E-6,$$

$$\text{with } \chi^2/NDF = 27.7/25.$$

The errors of the fit parameters are for the values which make  $\chi^2$  increase by one. The three straight lines in the figure indicate the loss of tracks at constant rates of 5%, 10%, and 20%. The loss is less than 5% for  $N_{gen} \leq 20$  and increases to 10% at  $N_{gen} = 80$ . The loss becomes more than 20% for  $N_{gen} \geq 130$ . The correction to the actual  $\bar{p}p$  events has been done event-by-event basis by translating the number of reconstructed tracks to the corrected number of tracks by using the fit obtained above. In order to avoid binning effects<sup>1</sup>, a non-integer value is divided into two integers with proper weights. For instance, if the corrected number of tracks is 10.2, 0.8 is filled into a bin for 10 and 0.2 is filled into a bin for 11. This does not cause any distortions because the width or structure of the distribution is much larger than the bin width. The number of tracks in the limited eta ranges are scaled to the number of track for  $|\eta| \leq 3.0$  in order to obtain corrections. For example, if it is the number of tracks in  $|\eta| \leq 1.0$ , the number of tracks is multiplied by 3.0 to use the above results, and the after the correction, it is divided by 3.0. The amount of correction is not more than 20% and the difference in  $dN/d\eta$  for the different  $\eta$  is approximately 20%. This results in only 4% of errors which is quite small in terms of the scale of the KNO  $\psi$  distribution.

The rms width of  $\Delta N_{trk}$  is shown in figure 4.26 as a function of  $N_{gen}$ . The width increase from 1 to 3-4 for  $N_{gen} = 1$  to 60, while it does not increase proportional to  $N_{gen}$  for the larger  $N_{gen}$  and stays approximately at 4.

The track density dependence of efficiency has also been studied in three  $\eta$  regions,  $0.0 \leq |\eta| \leq 1.0$ ,  $1.0 \leq |\eta| \leq 2.0$ , and  $2.0 \leq |\eta| \leq 3.0$ . Figure 4.25 shows the averages of  $\Delta N_{trk}$  as a function of  $N_{gen}$  for the three  $\eta$  regions. The curves are fits to a function defined by equation 4.11. We tried the correction using these fits for each  $\eta$  region. The resulting corrected KNO distribution did not show the significant

<sup>1</sup>The corrected number of tracks is not integer. For instance, if the corrected number of tracks is 10.2, it may still filled in the same bin as 10.

difference from the case we used the same parameters for all  $\eta$  regions.

The effects of the material, decay, radial board, and track selection to the multiplicity distribution has been studied similar way as the effects to the  $dN/d\eta$ . The distribution was obtained for the simulations with all the effects turned on and turn off. The corrections were obtained by comparing the results. We fitted the distributions to the negative binomial function (equation 1.7) and compared two fit parameters,  $\langle n_{ch} \rangle$  and  $k$ . Table 4.2 shows the % increases of  $\langle n_{ch} \rangle$  with the various effects for  $|\eta| \leq 1.0$ ,  $\leq 2.0$ , and  $\leq 3.0$ . The average multiplicity increases by 7-8 % by the various effects. We did not see statistically significant changes in  $k$  by the effects.

## 4.4 Correction to low $p_t$ spectrum

We compared the  $p_t$  spectrum put in the Monte Carlo and that obtained by the VTPC pads with the simulated data. Figure 4.27 shows the  $p_t$  spectrum put into the Monte Carlo. The horizontal axis is the normalized invariant cross section. The errors are statistical. We tried the simulation with/without any effects such as the particle decay, conversion by the material, and the inefficiency near the radial board. The reconstructed  $p_t$  spectrum with the VTPC pads is shown in figure 4.28 which is without the effects. Comparing to figure 4.27, the reconstruction inefficiency for small  $p_t$  ( $< 100$  MeV/c) can be seen. Figure 4.29 shows the reconstructed  $p_t$  spectrum with all the effects which enhances the very low  $p_t$ . The inefficiency is compensated by the various effects and the spectrum agrees with the original  $p_t$  spectrum put into the simulation within the statistical error. We therefore do not apply corrections to the  $p_t$  spectrum obtained with the VTPC pads.

## 4.5 Event Selection

### 4.5.1 Criteria

The  $\bar{p}p$  collision events triggered by the beam-beam counters (BBC) contained background events which had to be eliminated by the offline analysis (the event selection). The event selection was based on (1) the reconstructed VTPC tracks, (2) the VTPC and BBC vertex position, and (3) the BBC in-time hits. An event was accepted as a  $\bar{p}p$  collision if any one of the following criteria was satisfied:

1. At least three primary VTPC tracks are found both in  $+\eta$  and in  $-\eta$ .

This is an "expected" topology for nondiffractive events. The primary tracks are the tracks coming from a primary vertex and selected by a track selection program described in § 4.2. Events with very low charged multiplicity can satisfy criterion 2 or/and 3.

2.  $|\text{VTPC } z \text{ vertex} - \text{BBC } z \text{ vertex}| \leq 20 \text{ cm}$   
and  $|\text{VTPC } z \text{ vertex}| \leq 120 \text{ cm}$   
and Number of BBC in-time hits  $\geq 1$  in both sides  
and No BBC hits in the beam-gas gate  
and At least five primary VTPC tracks  
and Number of TDC hits  $< 3200$  or  $< 50 \times (N \text{ of tracks}) + 1000$

The accuracy of the VTPC vertex was better than 3 mm in rms (figure 3.22 shows an impact parameter distribution with a rms spread of 3 mm.). The accuracy of BBC vertex was 4-5 cm in rms (figure 2.17). The cut value of 20 cm corresponds to about four standard deviations.

3. The number of in-time BBC hits  $\geq 3$  on both sides  
and No BBC hits in the beam-gas gate

and the number of VTPC TDC hits  $\leq 4000$

This criterion is for the low multiplicity events which do not have enough VTPC tracks to determine the VTPC vertex but enough in-time hits in the BBC. The maximum number of VTPC TDC hits is required to ensure that an event is not a beam-gas event which usually gives many junk hits in the VTPC with accidental in-time hits in the BBC.

### 4.5.2 Efficiency

The event selection had two types of failure; misidentifying non- $\bar{p}p$  events with  $\bar{p}p$  events (*ADD* case) and misidentifying  $\bar{p}p$  events with non- $\bar{p}p$  events (*LOSS* case). The *ADD* case has been studied by using Tevatron beam crossings with a proton bucket filled but an antiproton bucket empty ("p $\bar{p}$ -crossings"). This should give no  $\bar{p}p$  collisions but produce necessary backgrounds because the proton intensity was about 20 times higher than the antiproton intensity in the typical  $\bar{p}p$ -crossings. The *LOSS* case has been studied by scanning the events which did not pass the event selection for normal  $\bar{p}p$ -crossings. We used Tevatron stores which had same proton intensities in both p $\bar{p}$ -crossings and  $\bar{p}p$ -crossings.

For a certain 1.8 TeV Tevatron store, our data taking obtained 120 triggers from p $\bar{p}$ -crossings and 5081 triggers from  $\bar{p}p$ -crossings. Of the 120 non- $\bar{p}p$  events, one event passed the event selection. For the 5081 events, the event selection identified 4816 events as  $\bar{p}p$  events. A hand scanning was made for the rest of  $5081 - 4816 = 265$  events, 208 of which were found to be non- $\bar{p}p$  collisions. Using the fact that one p $\bar{p}$ -crossing event out of 120 passed the event selection, we expect that about  $1 \times (208/120) = 2$  events in the 4816 events are not real  $\bar{p}p$  collisions. The *ADD* case was therefore estimated to be  $2/4816 = 0.04\%$  of events passed. The remaining  $265 - 208 = 57$  events consisted of 21 proton-gas like events, 11 antiproton-gas

like events, 11 possible  $\bar{p}p$  collision events, and 14 events which were difficult to classify. Some of proton-gas-like events and antiproton-gas-like events could be real  $\bar{p}p$  collisions considering the ratio of proton intensity to antiproton intensity which was about 20. The *LOSS* case was therefore estimated to be no more than  $57/4816 = 1\%$ . We did the same study for a 630 GeV store which had a 10 times lower luminosity. With this store, the *ADD* case was about 0.3% and *LOSS* case was no more than 3%. These studies and results are summarized in table 4.3.

For 630 GeV data, we had 8514 of the actual event samples triggered by the BBC and 4546 events passed the event selection. For the analysis described in this article, we used 2778 of the passed events because of the event vertex restriction to maintain a perfect geometrical acceptance. For 1.8 TeV data, we had 42436 triggered events and 39825 passed the track selection. Among them, 25266 events were used for the analysis after applying the event vertex restriction. (See table 4.4 for a summary.)

## Chapter 5

### Results and Discussions

#### 5.1 Pseudorapidity distribution

##### 5.1.1 Uncorrected results

Uncorrected  $dN/d\eta$  's for  $\sqrt{s} = 1.8$  TeV are shown in figure 5.1 with three different track selections — the tight cut ( $|Z_{off}| \leq 3.0$ ), nominal cut ( $|Z_{off}| \leq 4.0$ ), and loose cut ( $|Z_{off}| \leq 6.0$ ). The error bars are statistical only. The difference in the vertex cut makes  $dN/d\eta$  change by 5-10%. Figure 5.2 shows the ratio of  $dN/d\eta$  with the loose cut to  $dN/d\eta$  with the nominal cut, and the ratio of  $dN/d\eta$  with the tight cut to  $dN/d\eta$  with the nominal cut. The error bars are purely statistical. The ratios change only 2-3% for different  $\eta$  's. The similar  $dN/d\eta$  plots and the ratios for  $\sqrt{s} = 630$  GeV are shown in figures 5.3 and 5.4.

The ratios of  $dN/d\eta$  for  $\sqrt{s} = 1.8$  TeV to  $dN/d\eta$  for  $\sqrt{s} = 630$  GeV are shown in figure 5.5. The ratio does not change for different tracks selections within statistical errors. This ratio of  $dN/d\eta$  at  $\sqrt{s} = 1.8$  TeV to that at 630 GeV is expected to be relatively independent of various corrections because the effects would cancel out. The systematics which can affect this ratio is only the event selection because the accelerator luminosity for two energies are more than 10 time different, resulting a different amount of background. According to the event selection study (section 4.5), the fractions of background events passed by the event selection were  $0.04 \pm 0.03\%$  for 1.8 TeV and  $0.3 \pm 0.2\%$ . This is negligible compared to the

statistical errors of the ratio — 1-2%. The fractions of real  $\bar{p}p$  event missed by the event selection were 1% and 3% for 1.8 TeV and 630 GeV, respectively, making 2% difference. Since the multiplicity of the events missed is not known, we quote this 2% as a systematic error. As shown in figure 5.5, the ratio increases for larger  $|\eta|$ . This is due to the increase in the width of the  $dN/d\eta$  distribution with the energy and can be understood in terms of the maximum rapidity:

$$Y_{max} = \frac{1}{2} \ln \frac{E_{max} + pz}{E_{max} - pz} \quad (5.1)$$

$$\sim \frac{1}{2} \ln \frac{2E_{max}}{m_\pi} \quad (5.2)$$

where we assume  $E_{max}$  is roughly proportional to  $\sqrt{s}$ . At  $\eta = 0$ , the increase of  $dN/d\eta$  from  $\sqrt{s} = 630$  GeV to 1.8 TeV is:

$$1.27 \pm 0.02 \text{ (statistical)} \pm 0.02 \text{ (systematical)} \\ \pm 0.03 \text{ (statistical + systematical)}$$

The ratios for other  $\eta$  's are listed in table 5.1. These ratios are shown to be unchanged after applying the various corrections. We can compare this ratio to the expected ratio obtained by the UA5 data at  $\sqrt{s} = 53, 200, 546$ , and 900 GeV. We<sup>1</sup> fit the UA5 NSD (Non-Single-Diffractive) data [14] to:

$$dN/d\eta(\eta = 0) = (-0.150 \pm 0.175) + (0.255 \pm 0.016) \cdot \ln s, \quad (5.3)$$

wherer  $s$  is in  $\text{GeV}^2$  with  $\chi^2/NDF = 6.7/2$  and to:

$$dN/d\eta(\eta = 0) = (0.864 \pm 0.064) \cdot s^{0.101 \pm 0.006}, \quad (5.4)$$

where  $s$  is in  $\text{GeV}^2$  with  $\chi^2/NDF = 2.4/2$ . In either case, the two fit parameters are highly correlated. The first fit results in a ratio ( $\sqrt{s} = 1800$  to 630 GeV) of 1.17

<sup>1</sup>A fit with UA5 data is published only for inelastic events.



and the second one results in 1.24. This indicates that our data with UA5 NSD data prefer the fit  $dN/d\eta(\eta = 0) = 0.864 \cdot s^{0.101}$ ; it may be indicating deviation from “ln  $s$  Physics”.

### 5.1.2 Corrected data

Figure 5.6 shows the corrected  $dN/d\eta$  at  $\sqrt{s} = 1.8$  TeV for three cases of track selection. The error bars in the figure are purely statistical. The corrections include (1) the reconstruction efficiency (section 3.4), (2) low  $p_t$  cut off (section 4.3.1), (3) the effect of materials (section 4.3.4), (4) particle decay (section 4.3.5), (5) inefficiency near the radial boards (section 4.3.2), and (5) the effect of track selection (section 4.3.3). The corrections were obtained for each vertex cut. The corrected  $dN/d\eta$  only differs by 1-4% for the different vertex cuts. This differences and the errors from the event selection (1% for 1.8 TeV and 3% for 630 GeV) are included into the systematic error. Tables 5.2 and 5.3 show the values of  $dN/d\eta$ ’s with statistical and systematic errors for  $\sqrt{s} = 630$  and 1800 GeV. The  $dN/d\eta$ ’s with the nominal vertex cut for  $\sqrt{s} = 630$  GeV and 1.8 TeV are shown in figure 5.7 with the statistical and the systematic errors. The UA5 data at  $\sqrt{s} = 546$  GeV and 900 GeV [14] are also shown. The consistency between our data and UA5 data is fairly good. The exception is our data at  $|\eta| = 2.75$ -3.00.

The  $dN/d\eta$ ’s at  $\eta = 0$  are:

$$3.12 \pm 0.07 \text{ (statistical)} \pm 0.17 \text{ (systematic)} \text{ at } 630 \text{ GeV,}$$

$$3.96 \pm 0.06 \text{ (statistical)} \pm 0.22 \text{ (systematic)} \text{ at } 1.8 \text{ TeV.}$$

The statistical errors at  $\sqrt{s} = 1.8$  TeV mostly originated from the statistical error of the Monte Carlo simulations, while the statistical errors at  $\sqrt{s} = 630$  GeV originated from both the real data and the Monte Carlo. Tables 5.2 and 5.3 shows all other values. The ratio of  $dN/d\eta$  at the two energies are unchanged after the corrections. The  $dN/d\eta$ ’s at  $\eta = 0$  are plotted against  $\sqrt{s}$  in figure 5.8 with UA5

NSD data [14]. The line or curve is a fitting with UA5 NSD data and our data. The dashed line is:

$$dN/d\eta(\eta = 0) = (-0.23 \pm 0.16) + (0.263 \pm 0.014) \cdot \ln s, \quad (5.5)$$

where  $s$  is in  $\text{GeV}^2$  and  $\chi^2/NDF$  is 8.1/4. The solid curve is:

$$dN/d\eta(\eta = 0) = (0.858 \pm 0.058) \cdot s^{0.1011 \pm 0.0056}, \quad (5.6)$$

where  $s$  is in  $\text{GeV}^2$  and  $\chi^2/NDF = 2.5/4$ . In either case, the two fit parameters are highly correlated. Our data with UA5 NSD data prefer  $a \cdot s^b$  to  $a + b \ln s$ .

Currently the prediction by the theoretical model (Dual Parton Model) is available for  $dN/d\eta$  at  $\sqrt{s} = 2.0$  TeV [38]. Figure 5.28 shows the comparison to our  $dN/d\eta$  at 1.8 TeV. The theoretical prediction for  $\sqrt{s} = 2$  TeV is  $\sim 5\%$  consistently lower than our data at  $\sqrt{s} = 1.8$  TeV. This is statistically significant disagreement.

### 5.1.3 Multiplicity dependence

We have studied the changes in the shape of  $dN/d\eta$  for different multiplicity ranges. Figures 5.9a-i show  $dN/d\eta$ ’s for different multiplicity ranges at  $\sqrt{s} = 1.8$  TeV. The multiplicity is corrected and for  $|\eta| \leq 3.0$ . The charged particles were more produced in the smaller  $|\eta|$  for higher multiplicity events. The same characteristics is seen at  $\sqrt{s} = 630$  GeV as shown in figures 5.10a-d and at  $\sqrt{s} = 546$  GeV by the UA5 experiment [1].

## 5.2 Multiplicity distributions

### 5.2.1 Uncorrected distributions

We first show the results on the charged multiplicity without any corrections. Figure 5.11 shows the uncorrected multiplicity distributions at  $\sqrt{s} = 630$  GeV for  $|\eta| \leq 1.0$ ,  $\leq 2.0$ , and  $\leq 3.0$ , while the multiplicity distributions at  $\sqrt{s} = 1.8$  TeV for  $|\eta| \leq$

1.0,  $\leq 2.0$ , and  $\leq 3.0$  are shown in figure 5.12. The error bars shown are only statistical ones. The curves are fittings to a negative binomial function (equation 1.7), which had two free parameters, the average multiplicity  $\langle n_{ch} \rangle$  and the  $k$  parameter. Table 5.7 shows the parameter values obtained by the fitting for the both energies. In the table,  $\chi^2/NDF$  for 1.8 TeV seem to be larger than that for 630 GeV. This might be because the number of  $\bar{p}p$  events analyzed is ten times larger for 1.8 TeV than for 630 GeV. The uncorrected multiplicity distributions do not fit very well to the negative binomial function. This becomes evident when we compare the UA5 KNO  $\psi$  distribution to our uncorrected ones, as shown in figure 5.13. (To obtain the KNO distribution, we used  $\langle n_{ch} \rangle$  given by the negative binomial fit.) Disagreements are seen for  $n/\langle n_{ch} \rangle \geq 3$  where the corrections become significant.

Some physics characteristics can be seen without the correction. Figures 5.14 and 5.15 show the KNO distributions for the different  $\eta$  ranges for  $\sqrt{s} = 630$  GeV and 1.8 TeV, respectively. The vertical axis is multiplies by 0.1 for  $|\eta| \leq 2.0$  and by 0.01  $|\eta| \leq 3.0$ . At both energies, in  $n/\langle n_{ch} \rangle \leq 1.5$ , the distribution is flatter for smaller  $\eta$  range. For instance, for  $|\eta| \leq 3.0$ ,  $\langle n_{ch} \rangle P(n)$  changes by a factor of  $\sim 8$  from  $n/\langle n_{ch} \rangle = 0.2$  to the peak of the distribution, while it changes only by a factor of  $\sim 2$  for  $|\eta| \leq 1.0$ . The same characteristics has been observed by the UA5 experiment [1] at  $\sqrt{s} = 546$  GeV.

### 5.2.2 Corrected multiplicity distributions

The correction to the charged distribution was based on the comparison of the number of reconstructed tracks to the number of generated tracks using the simulation, as described in § 4.3.8. Figure 5.16 shows the corrected multiplicity distributions at  $\sqrt{s} = 630$  GeV for  $|\eta| \leq 1.0$ ,  $\leq 2.0$ , and  $\leq 3.0$ , and the corresponding distributions at  $\sqrt{s} = 1.8$  TeV are shown in figure 5.17. (Tables 5.5 and 5.6 show the probability densities for each  $n_{ch}$  bin.) The vertical axis is the probability density and the horizontal axis is the charged multiplicity. The curves in the figures are the fits to a

negative binomial function. The fit parameters  $\langle n_{ch} \rangle$ 's and  $k$ 's are summarized in table 5.8. The fits with the distribution at  $\sqrt{s} = 630$  GeV are good. The  $\chi^2/NDF$ 's at  $\sqrt{s} = 1.8$  TeV is still not good after applying the correction. The multiplicity distribution for different  $\eta$  directions,  $0.0 \leq |\eta| \leq 1.0$ ,  $1.0 \leq |\eta| \leq 2.0$ , and  $2.0 \leq |\eta| \leq 3.0$  are shown in figures 5.18 ( $\sqrt{s} = 630$  GeV) and 5.19 ( $\sqrt{s} = 1.8$  TeV). The fit parameters are summarized in table 5.9.

The  $\langle n_{ch} \rangle$ 's obtained by the fit are plotted for  $|\eta| \leq 1.0$ ,  $\leq 2.0$ , and  $\leq 3.0$  as a function of  $\sqrt{s}$  in figure 5.20 with the value obtained by the UA5 experiment at  $\sqrt{s} = 546$  GeV. The increase in  $\langle n_{ch} \rangle$  from  $\sqrt{s} = 630$  GeV to 1.8 TeV is approximately 25%, 27%, and 30% for  $|\eta| \leq 1.0$ ,  $\leq 2.0$ , and  $\leq 3.0$ , respectively. This is consistent with the fact that the ratio of  $dN/d\eta$  at  $\sqrt{s} = 1.8$  TeV to that at  $\sqrt{s} = 630$  GeV increases in larger  $|\eta|$ .

The inverse values of parameter  $k$  ( $1/k$ ) for  $|\eta| \leq 1.0$ ,  $\leq 2.0$ , and  $\leq 3.0$  are plotted as a function of  $\sqrt{s}$  in figure 5.21 with the value obtained by the UA5 experiment at  $\sqrt{s} = 546$  GeV. The solid lines are:

$$1/k = a + b \cdot \ln s, \quad (5.7)$$

where the values of  $a$  and  $b$  for each  $|\eta|$  range are summarized in table 5.10. It is therefore a good approximation that  $1/k$  increases linearly with  $\ln s$  from  $\sqrt{s} = 546$  GeV to 1.8 TeV for  $|\eta| \leq$ . The slope (parameter  $b$ ) is nearly equal to all the  $\eta$  ranges.

Since  $\langle n_{ch} \rangle/k \gg 1$ , we can approximate the binomial function by:

$$\begin{aligned} \langle n_{ch} \rangle P(n_{ch}) &= \langle n_{ch} \rangle \frac{(n_{ch} + k - 1)!}{n_{ch}! (k - 1)!} \left( \frac{\langle n_{ch} \rangle / k}{1 + \langle n_{ch} \rangle / k} \right)^{n_{ch}} \frac{1}{(1 + \langle n_{ch} \rangle / k)^k} \\ &\Rightarrow \frac{k^k}{(k - 1)!} \left( \frac{n}{\langle n_{ch} \rangle} \right)^{k-1} e^{-k(\frac{n}{\langle n_{ch} \rangle})}. \end{aligned} \quad (5.8)$$

This means that if the KNO scaling is valid, the parameter  $k$  should be independent of the energy, which is not the case because the  $1/k$  increases roughly linearly

with  $\ln s$ . The slope of  $1/k$  is approximately 0.055 independent of the  $|\eta|$  range. This indicates that the KNO scaling is violated.

The corrected KNO  $\psi$  distributions have been obtained using  $\langle n_{ch} \rangle$  given by the negative binomial fit. Figure 5.22 shows the KNO  $\psi$  distribution at  $\sqrt{s} = 630$  GeV with the UA5 data at  $\sqrt{s} = 546$  GeV. The error bars in our data are statistical ones and the error bars in the UA5 data include both statistical and systematic errors. Both, for  $|\eta| \leq 3.0$ , agrees very well. The KNO  $\psi$  distribution at  $\sqrt{s} = 1.8$  TeV is shown in figure 5.23 again with the same UA5 data at  $\sqrt{s} = 546$  GeV. The error bars in our data are purely statistical. Two distributions agree well at  $n/\langle n \rangle > 2.0$ , while at smaller  $n/\langle n \rangle$ , some difference can be seen. Our 1.8 TeV  $\psi$  distribution has its peak at smaller  $n/\langle n \rangle$  compared to the  $\psi$  distributions at lower energies. This is consistent with the violation of the KNO scaling indicated by the change in the  $k$  parameter.

The corrected KNO distributions for the different  $|\eta|$  ranges are shown in figures 5.24 and 5.25 at  $\sqrt{s} = 630$  and 1800 GeV, respectively. As already shown in the uncorrected ones, the distribution are flatter for the smaller range of  $|\eta|$ . Figure 5.26 and 5.27 also show the KNO distributions for the different  $|\eta|$  regions (or directions),  $0.0 \leq |\eta| \leq 1.0$ ,  $1.0 \leq |\eta| \leq 2.0$  and  $2.0 \leq |\eta| \leq 3.0$ . Although the tendency is smaller than in the previous case, the KNO distribution is flatter in the smaller  $|\eta|$  region. (All data plotted in these figures are shown in tables 5.11 to 5.16.)

It was pointed out, more than ten years ago, that the negative binomial distribution gave an excellent account of hadron-hadron multiplicity data by some physicists [18,19,20]. The good agreements with the negative binomial function have been found in the wide range of the colliding energies (20-900 GeV in  $\sqrt{s}$ ). It is also reported that the agreements are found not only in  $\bar{p}p$  or  $pp$  collisions but also in  $\pi p$  collisions [21] and  $e^+/e^-$  collisions [22]. It seems that the negative

binomial distribution is the universal characteristics of the hadronization. There are, however, more than one way to arrive at equation 1.7 and the physics meaning of this distribution is controversial [23].

The negative binomial distribution occurs in the quantum optics, representing the distribution of photons from  $k$  independent sources. In the picture of the multiparticle production, the parameter  $k$  represents the number of sources or phase space cell [89]. The negative binomial arises from the convolution of  $k$  independent Poisson distributions. It is reasonable that  $k$  falls as the rapidity window is reduced as shown in the real data. As  $\sqrt{s}$  increases, however, since the rapidity range grows, one would naively expect the number of cells to increase, whereas in fact  $k$  falls with  $\sqrt{s}$ . It is also not obvious how to interpret non-integer values of  $k$ .

Another quantum statistical interpretation of the negative binomial distribution is in terms of partial stimulated emission [90]. Particles may be emitted either independently or the emission may be enhanced by the Bose-Einstein interference with particles already presented. The parameter  $k^{-1}$  is interpreted as the average fraction of the particles already present which stimulate the emission of an additional particle, therefore no problems with non-integer  $k$ . Since the Bose-Einstein interference works in short rapidity range, we expect  $k^{-1}$  to increase as the rapidity window become smaller or as the particle density increases with  $\sqrt{s}$ .

A different way to reach the negative binomial distribution is by the convolution of a Poisson with a logarithmic distribution. (A sort of cluster model [90].) Clusters are emitted with a Poisson distribution, while the number of particles into which each cluster decays is assumed to follow a logarithmic distribution.

### 5.3 Transverse momentum spectra

The  $p_t$  spectrum (invariant cross section) measured by the CTC is shown in figure 5.29 for  $|Y| \leq 1.0$ . We used the pion mass for all particles to calculate  $Y$ . The

shape of the inclusive cross section at 630 GeV agrees very well with the measurements of UA1[25] and UA2[92] at 546 GeV over the full range in  $p_t$  we present.

Figure 5.30 shows a comparison of inclusive cross sections measured at  $\sqrt{s}$  values from 27 to 1800 GeV. We find that the previously observed flattening in the shape of the  $p_t$  distribution with energy continues up to 1800 GeV.

Invariant cross sections were fitted with the functional form[25]:

$$E \frac{d^3\sigma}{d^3p} = \frac{A p_o^n}{(p_t + p_o)^n}. \quad (5.9)$$

The fit parameters  $A$ ,  $p_o$ ,  $n$ , and their statistical errors are given in table 5.17. Fitted curves are shown in figure 5.29. We find that  $p_o$  and  $n$  are highly correlated. When fitting the data with  $p_o$  fixed at 1.3 GeV/c, the power  $n$  decreases by 0.6 as the center-of-mass energy increases from 630 GeV to 1800 GeV. Our result at 630 GeV,  $n = 8.89 \pm 0.06$ , is in reasonable agreement with the UA1 result at 546 GeV,  $n = 9.14 \pm 0.02$  [25]. Results of the fits were stable against changes of the  $p_t$  range used in the fit as shown in table 5.17.

The  $p_t$  spectra measured by the VTPC pad are shown in figures 5.31, 5.32, and 5.33 for different rapidity ranges of  $0.0 \leq |Y| \leq 1.0$ ,  $1.0 \leq |Y| \leq 2.0$ , and  $2.0 \leq |Y| \leq 3.0$ , respectively. The vertical axis is the probability density of having  $p_t$  in GeV/c. The errors are statistical ones. The rapidity  $Y$  is calculated by assuming that all particles are charged pions. The  $p_t$  spectrum is the same for the different  $|Y|$  ranges within the statistical error. Figures 5.34 and 5.35 show the  $p_t$  spectra for  $|Y| \leq 3.0$  at  $\sqrt{s} = 630$  and 1800 GeV. The curves is  $(1 + (1.29)^{-1} p_t)^{-8.26}$  the fit obtained for the CTC data above  $p_t = 0.5$  GeV/c. There is no significant difference in the  $p_t$  spectrum at  $\sqrt{s} = 630$  and 1800 GeV below  $p_t = 500$  MeV/c.

## 5.4 Average transverse momenta

The determination of the mean value of transverse momentum  $\langle p_t \rangle$  with only the CTC relies on the extrapolation of the observed spectrum to  $p_t = 0$ . The error

in  $\langle p_t \rangle$  due to uncertainty in the shape of the spectrum at low  $p_t$  was reduced by using constraints from the measurement of  $dN/d\eta$  with the VTPC. By varying the functional form of the  $p_t$  spectrum for  $p_t < 0.5$  GeV/c with fixed  $dN/d\eta$ , the systematic error in  $\langle p_t \rangle$  was estimated to be  $\sim 0.003$  GeV/c. The results from VTPC  $dN/d\eta$  yields a ratio of  $dN/d\eta$  at 1800 GeV to that at 630 GeV of  $1.27 \pm 0.04$ . Interpolation of  $dN/d\eta$  measurements in the range 200 to 900 GeV [14] gives  $dN/d\eta$  of  $3.30 \pm 0.15$  at 630 GeV, in agreement with our VTPC results. Using these values we obtain:

$$\langle p_t \rangle = 0.432 \pm 0.004 \pm 0.020 \text{ GeV/c at 630 GeV,}$$

$$\langle p_t \rangle = 0.495 \pm 0.014 \pm 0.020 \text{ GeV/c at 1800 GeV.}$$

The estimated errors include uncertainties due to the extrapolation to low  $p_t$  and in the ratio of  $dN/d\eta$ . The 5% uncertainty in the value of  $dN/d\eta$  at 630 GeV gives an additional error of 0.020 GeV/c common to both values of  $\langle p_t \rangle$ .

The  $\langle p_t \rangle$ 's directly calculated from the CTC measurement ( $p_t \geq 0.5$  GeV/c) and VTPC measurement ( $0.5 \text{ GeV/c} \geq p_t \geq 0.05 \text{ GeV/c}$ ) are:

$$\langle p_t \rangle = 0.463 \pm 0.084 \text{ GeV/c at 630 GeV,}$$

$$\langle p_t \rangle = 0.499 \pm 0.008 \text{ GeV/c at 1800 GeV,}$$

where the errors are purely statistical. These agree with the results obtained by the indirect method within the errors. Figure 5.36 shows that  $\langle p_t \rangle$  grows significantly as a function of  $\sqrt{s}$  [25,93] in our energy domain, in agreement with the trend observed in cosmic ray interactions [91].

In thermodynamical models,  $\langle p_t \rangle$  is related to the temperature of the hadronic matter. Within this model, our results imply an increase of the temperature of the hadronic "fireball" from 0.15 GeV at ISR energies to 0.21 GeV at 1800 GeV.

The shape of the inclusive cross sections at large  $p_t$  agrees with qualitative expectations based on parton models and QCD. However, the theory currently does

not provide quantitative predictions for measurements such as this.

## Chapter 6

### Conclusions

We have made the first measurements of the multiplicity and transverse momentum distributions of charged particles produced in the  $\bar{p}p$  collisions at a center of mass energy of 1.8 TeV — the highest energy available today. We also made the measurements at a center of mass energy of 630 GeV in order to study the energy dependence and to check consistency with experiments at lower energies. The number of events analyzed was 2778 for 630 GeV and 25266 for 1.8 TeV. The pseudorapidity range covered was  $-3.0$  to  $3.0$  and the transverse momentum measured was down to 50 MeV/c. We triggered nearly 60% of the  $\bar{p}p$  total cross section with a least biased trigger formed from the scintillation counters. The main conclusions of this experiment are summarized as follows.

1. The charge density  $dN/d\eta$  at  $\eta = 0$  is  $2.95 \pm 0.3$  at  $\sqrt{s} = 630$  GeV and  $3.75 \pm 0.4$  at  $\sqrt{s} = 1.8$  TeV. The charge density increases by  $27 \pm 3\%$  as  $\sqrt{s}$  goes from 630 to 1800 GeV, preferring an energy dependence  $a \cdot s^b$  to  $a + b \ln s$ .
2. The increase in the charge density is larger for large  $|\eta|$ . For instance, at  $|\eta| = 3.0$ , it increases by  $33 \pm 1\%$  when  $\sqrt{s}$  goes from 630 to 1800 TeV. This is due to a growth in  $dN/d\eta$  width at  $\sqrt{s} = 1.8$  TeV compared at  $\sqrt{s} = 630$  GeV.

3. The KNO  $\psi$  distribution for  $|\eta| \leq 3.0$  at  $\sqrt{s} = 630$  GeV agrees very well with that at  $\sqrt{s} = 546$  GeV by the UA5 experiment. The multiplicity distribution at  $\sqrt{s} = 630$  GeV is well described by a negative binomial function.
4. At  $\sqrt{s} = 1.8$  TeV, the KNO  $\psi$  distribution shows a slight deviation from that at  $\sqrt{s} = 630$  GeV or 546 GeV. This is consistent with the KNO scaling violation. The KNO  $\psi$  distribution at  $\sqrt{s} = 1.8$  TeV indicates a possible structure. The fitting to a negative binomial function is not as good as the fitting at  $\sqrt{s} = 630$  GeV.
5. An average charged multiplicity obtained by the negative binomial fit for  $|\eta| \leq 3.0$  is  $19.8 \pm 0.2$  at  $\sqrt{s} = 630$  GeV and  $25.8 \pm 0.1$  at  $\sqrt{s} = 1.8$  TeV, showing a 30% increase.
6. The  $k$  parameter of the negative binomial fit is  $2.35 \pm 0.05$  at  $\sqrt{s} = 630$  GeV and decreases to  $2.08 \pm 0.01$  at  $\sqrt{s} = 1.8$  TeV. The  $1/k$  is well fitted to  $a + b \ln s$  with  $b$  approximately equal to 0.055 independent of the  $|\eta|$  range, indicating the violation of the KNO scaling.
7. The previously observed flattening in the shape of the  $p_t$  distribution with energy continues up to 1.8 TeV. The average transverse momentum is  $0.432 \pm 0.02$  GeV/c at  $\sqrt{s} = 630$  GeV and increases to  $0.498 \pm 0.008$  GeV/c at  $\sqrt{s} = 1.8$  TeV.

## Bibliography

- [1] G. J. Alner et al., Phys. Lett. 138B (1984) 304. UA5 collab.; Phys. Rep. 154 No.5 & 6 (1987) 247 contains all UA5 data upto 546 GeV.
- [2] R. Battiston et al., Phys. Lett. 117B (1982) 126, UA4 collab.
- [3] G. Arnison et al., Phys. Lett. 128B (1983) 336, UA1 collab.
- [4] H. L. Bradt, M. F. Kaplon and B. Peters, Phys. Rev., 76 (1949) 1735.
- [5] J. J. Lord, J. Fainberg, M. Schein, Phys. Rev., 80 (1950) 970.
- [6] Leprince-Ringuet, Bonsser, Fong, Jaundeav and Morellet, Comptes Rendus, 229 (1949) 163.
- [7] References in E. Lohrmann, Nuovo Cimento, 10 (1953) 127.
- [8] P. H. Fowler, Phil. Mag., 41 (1950) 169.
- [9] F. Brisbout, C. Dahanayke, A. Engler, Y. Fujimoto, D. H. Perkins, Phil. Mag. 1b (1956) 605.
- [10] O. Minakawa, Y. Nishimura, M. Tsuzuki, H. Yamanouchi, H. Aizu, H. Hasegawa, Y. Ishii, S. Tokunaga, Y. Fujimoto, S. Hasegawa, J. Nishimura, K. Niu, K. Nishikawa, K. Imaeda and M. Kezuno, Nuovo Cimento Suppl. 11 (1956) 125.
- [11] D. H. Perkins, *Progress in Elementary Particle and Cosmic Ray Physics* 259 Vol. V (North-Holland Publishing Company, Amsterdam, 1960) and references therein.
- [12] A. Breakstone et al., Phys. Rev. D30 (1984) 528, ABCDHW collab.
- [13] W. Thome et al., Nucl. Phys. B129 (1977) 365.
- [14] G. Alner et al., Z. Phys. 33C (1986) 1, UA5 collab.

- [15] G. Alner et al., Phys. Lett. 160B (1985) 193 & 199, UA5 collab.
- [16] G. Ekspog, Proceedings of the 6th International Conference on Physics in Collision, Chicago, 1986, page 19 and references therein.
- [17] P. Carlson, Proceedings of the XXIII International Conference on High Energy Physics, California, 1986, page 1346 and references therein.
- [18] A. Giovannini, Nuovo Cimento 15A (1973) 543, ibid 24 (1974) 421.
- [19] R. Knox, Phys. Rev. D10 (1974) 65.
- [20] N. Suzuki, Prog. Theor. Phys. 51 (1974) 51.
- [21] M. Adamus et al., Preprint HEN-273 (1986), NA22 collab.
- [22] M. Derrick et al., Phys. Lett. 168B (1986) 299, HRS collab.
- [23] P. Carruthers, Proceedings of Local Equilibrium in Strong Interaction Physics, Bad Honnef, Germany, 1984, page 390.
- [24] UA1 collab. presented by G. Ciapetti in Proceedings of a topical European meeting, Strasbourg, 1985, page 455.
- [25] G. Arnison et al., Phys. Lett. 118B (1982) 167, UA1 collab.
- [26] E. Fermi, Prog. Theor. Phys., 5 (1950) 570.
- [27] I. Y. Pomeranchuk, Dokl. Akad. Nauk SSSR 78 (1951) 889.
- [28] L. D. Landau, Izv. Akad. Nauk SSSR, Ser. Fiz., 17 (1953) 51.
- [29] S. Z. Belenki and L. D. Landau, Nuovo Cimento Suppl. 3, Serie X (1956) 15.
- [30] L. D. Landau and E. M. Lifshitz, Course of Theoretical Physics Vol. 6 (Fluid Mechanics), Pergamon, New York, 1959.

- [31] L. Van Hove and S. Pokorski, Nucl. Phys. B86 (1975) 243.
- [32] P. Carruthers and Minh Duong-Van, Phys. Rev. D28 (1983) 130.
- [33] R. M. Weiner, Proceedings of the 2nd International Workshop on Local Equilibrium in Strong Interaction Physics, New Mexico, 1986, page 106.
- [34] G. N. Fowler, E. M. Friedlander and M. Plumer and R. M. Weiner, Phys. Lett. 145B (1984) 407.
- [35] K. Wehrberger and R. M. Weiner, Phys. Rev. D31 (1985) 222.
- [36] E. V. Shuryak, Phys. Rep. 61 No.2 (1980) 71.
- [37] A. Capella and J. Tran Thanh Van, Z. Phys. C3 (1980) 330; Phys. Lett. 81B (1979) 68.
- [38] F. W. Bopp, P. Aurenche and J. Ranft, Phys. Rev. D33 (1986) 1867.
- [39] A. Capella and J. Tran Thanh Van, Phys. Lett. 93B (1980) 146.
- [40] A. Capella and A. Krzywicki, Phys. Rev. 18D (1978) 4120.
- [41] B. Andersson, G. Gustafson and C. Peterson, Nucl. Phys. B135 (1978) 273.
- [42] R. D. Field and R. P. Feynman, Nucl. Phys. B136 (1978) 1.
- [43] A. Capella and J. Tran Thanh Van, Phys. Lett. 114B (1982) 450.
- [44] A. Capella, A. Staar and J. Tran Thanh Van, Phys. Rev. D32 (1985) 2933.
- [45] R. P. Feynman, Phys. Rev. Letters 23 (1969) 1415.
- [46] Z. Koba, H. B. Nielsen and P. Olesen, Nucl. Phys. B40 (1972) 317.
- [47] R. Johnson, CDF Note No.664 April 1988.



- [48] F. Abe et al., Nucl. Instrum. Methods A271 (1988) 487; This is an overview of the detector and contains references to each detector. The more details of the CDF detector can be found in internal notes which can be obtained through the CDF Department, Mail Stop 223, Fermilab, P. O. Box 500, Batavia, Illinois 60510, U.S.A.
- [49] F. Snider et al., Nucl. Instrum. Methods A268 (1988) 75.
- [50] F. Bedeschi et al., Nucl. Instrum. Methods A268 (1988) 487.
- [51] M. Atac et al., Nucl. Instrum. Methods A269 (1988) 40.
- [52] H. Minemura et al., Nucl. Instrum. Methods A238 (1985) 18.
- [53] L. Balka et al., Nucl. Instrum. Methods A267 (1988) 272.
- [54] S. Bertolucci et al., Nucl. Instrum. Methods A267 (1988) 301.
- [55] Y. Fukui et al., Nucl. Instrum. Methods A267 (1988) 280.
- [56] W. Carithers et al., to be submitted to Nucl. Instrum. Methods A.
- [57] G. Brandenburg et al., Nucl. Instrum. Methods A267 (1988) 257.
- [58] S. Cihangir et al., Nucl. Instrum. Methods A267 (1988) 249.
- [59] M. Binkley, Precedings of the second Aspen Winter Particle Physics Conference, Aspen, Colorado, 1986, page 145.
- [60] G. Ascoli et al., Nucl. Instrum. Methods A268 (1988) 33.
- [61] K. Byrum et al., Nucl. Instrum. Methods A268 (1988) 46.
- [62] J. N. Marx and D. R. Nygren, Physics Today Vol. 31 No. 10 (1978) 46.
- [63] Junkosha Co., Ltd., Hanno Plant, 3-1 Ashikariba, Hanno-shi, Saitama-ken 357 Japan, Tel: 04297-3-2261, Telex: 2954185 JUN HP.

- [64] T. & B. /Ansley, 4371 Valley Blvd., Los Angeles, CA 90032
- [65] Hitachi Cable Ltd., Electronic Wire & Cable Design Dep., Hitaka Works, 5-1-1 Hitaka-cho, Hitachi-shi, Ibaraki-ken 319-14 Japan.
- [66] Rohacell foam is a rigid acrylic foam ( density = 0.05 g/cc) distributed by Cyro Industries, 25 Executive Blvd, P. O. Box 579, Orange, CT. 06477 Tel. (201)930-0100.
- [67] Kapton is a trademark for a polyimide film manufactured by DuPont de Nemours, E. I. , Co., Wilmington, Del. 19898.
- [68] Fujitsu Microelectronics Ltd., Solid State Department, 18-Mori Building, 2-3-13 Toranomon, Minato-ku, Tokyo, Japan.
- [69] R. J. Yarema et al.,IEEE Trans. Nucl. Sci. NS-33 (1986) 933.
- [70] LeCroy Research Systems Corp., 700 S. Main Street, Spring Valley, New York 10977.
- [71] R. A. Boie et al., IEEE Trans. Nucl. Sci. NS-28 (1981) 603.
- [72] R. Yamada et al., Fermilab TM-1369, November 1985.
- [73] C. N. Holmes, CDF Note No. 361, December 30, 1985.
- [74] H. Frish et al., CDF Note-250 (1984).
- [75] H. Frish et al., CDF Note-416 (1986).
- [76] T. M. Liss, CDF Note-552, September 1987.
- [77] M. Bozzo et al., Phys. Lett. 147B (1984) 392.
- [78] R. E. Ansorge et al., Z. Phys. C33 (1986) 175.

- [79] E. Barsotti et al., Nucl. Instrum. Metho. A269 (1988) 82.
- [80] U. S. NIM Committee, IEEE Standard FASTBUS Modular High Speed Data Acquisition and Control System, ANSI/IEEE-Std 960-1986, 1984.
- [81] G. Drake et al., Nucl. Instrum. Methods A269 (1988) 68.
- [82] H. Brafman et al., IEEE Trans. Nucl. Sci. NS-32 (1985) 336.
- [83] C. Swoboda et al., IEEE Trans. Nucl. Sci. NS-32 (1985) 1335.
- [84] M. Larwill et al., IEEE Trans. Nucl. Sci. NS-30 (1983) 4003.
- [85] Review of Particle Properties, M. Aguilar-Benitez et al., Phys. Lett. 111B (1982), Particle Data Group.
- [86] F. Abe et al., CDF-Note No.576 May 1988, submitted to Phys. Rev. Lett.
- [87] G. Arnison et al., Phys. Lett. 118B (1982) 167.
- [88] MB1 User's Guide, Y. Takaiwa, August 1987.
- [89] P. Carruthers and C. C. Shih Phys. Lett. 127B (1983) 242.
- [90] A. Giovannini and L. van Hove, Z. Phys. C33 (1986) 391
- [91] C. Lattes et al., Phys. Reports 65 (1980) 151.
- [92] M. Banner et al., Phys. Lett. 122B (1983) 322.
- [93] A. Rossi et al., Nucl. Phys. B84 (1975) 269 and references therein.
- [94] D. Antreasyan et al., Phys. Rev. D19 (1979) 764.
- [95] B. Alper et al., Nucl. Phys. B87 (1975) 19.

## Tables

$\sqrt{s}$ GeV	23.6	30.8	45.2	53.2	62.8	540
$\langle n_{ch} \rangle_{exp}$	$8.1 \pm 0.1$	$9.5 \pm 0.1$	$11.0 \pm 0.2$	$11.8 \pm 0.1$	$12.7 \pm 0.1$	$28.5 \pm 0.4$
$\langle n_{ch} \rangle_{SHM}$	8.8	9.5	11.1	11.9	12.7	27.6

Table 1.1: SHM prediction and experimental data for  $\langle n_{ch} \rangle$ . The theoretical value has one fit parameter and is normalized by the experimental data at  $\sqrt{s} = 62.8$  GeV.

EM Calorimetry Summary			
	Forward	End Plug	Central
Ang. range	2° to 10°	10° to 37°	37° to 90°
Towers in $\eta$	18	16	10
Tower size	$\Delta\eta \sim 0.1$ $\Delta\phi = 5^\circ$	$0.05 < \Delta\eta < 0.1$ $\Delta\phi = 5^\circ$	$0.087 < \Delta\eta < 0.13$ $\Delta\phi = 15^\circ$
Construction	Pb-gas tubes	Pb-gas tubes	Pb-scintillator
R.L. per layer	$0.9X_0$	$0.53X_0$	$0.6X_0$
Layers	15 15	5 24 5	31
R.L. per sect.	$13X_0$ $13X_0$	$2.7X_0$ $13X_0$ $2.7X_0$	$19X_0$
$\Delta E/E$	$\sim 27\%/\sqrt{E}$	$\sim 24\%/\sqrt{E}$	$\sim 14\%/\sqrt{E}$
Position resol.	2-4 mm	1-2 mm	1.5-3 mm

Hadron Calorimetry Summary				
	Forward	End Plug	End Wall	Central
Ang. range	2° to 10°	10° to 30°	30° to 45°	45° to 90°
Tower size	$\Delta\eta = 0.1$ $\Delta\phi = 5^\circ$	$\Delta\eta = 0.09$ $\Delta\phi = 5^\circ$	$0.08 < \Delta\eta < 0.12$ $\Delta\phi = 15^\circ$	$0.1 < \Delta\eta < 0.15$ $\Delta\phi = 15^\circ$
Construction	2 in. Fe + gas tubes	2 in. Fe + gas tubes	2 in. Fe + scintillator	1 in. Fe + scintillator
Layers	28	20	15	32
$\Delta E/E$	$\sim 125\%/\sqrt{E}$	$\sim 130\%/\sqrt{E}$	$\sim 14\%$ at 50 Gev	$\sim 70\%/\sqrt{E}$

Table 2.1: Summary of the CDF electromagnetic and hadron calorimetry (taken from reference [59]).

Dimensions	# modules	8
	Module Z-length	35.3 cm
	Modules Z-spacing	35.94 cm
	Total Z-length	287 cm
	Max. active radius:	21 cm
	Min. active radius:	6.5 cm
	Drift Length:	15.25 cm
End Caps	Sense Wires:	24 /octant 6.336 mm spacing 15 $\mu\text{m}$ gold-plated tungsten
	Field Wires:	24 /octant 63 $\mu\text{m}$ Copper/Beryllium
	Cathode Pads:	24 pads/octant, in 3 rows 4.12 cm in $r$ by $\approx 1.4$ cm in $r-\phi$
	Resistive ink:	10 M $\Omega$ /square
Field Cage	Material:	Kapton/Rohacell foam laminate epoxy/graphite-foam support frame
	Electrodes	3.175 mm overlapping strips on 2.38 mm centers
	Central grid	ss screen 50 $\mu\text{m}$ wires on 1000 $\mu\text{m}$ centers
	Cathode grid	ss screen 50 $\mu\text{m}$ wires on 500 $\mu\text{m}$ centers

Table 2.2: Summary of the VTPC construction.

<b>Magnetic Field</b>	$B_{axial}$	1.5 Tesla
	$B_{radial(max)}$	$< 1\% B_{axial}$
<b>Drift Field</b>	$E_{drift}$	256 V/cm
<b>Gas</b>	Argon-Ethane	50/50 at 1 atm.
	Drift velocity	43 $\mu\text{m/nsec}$
	Max. Temp.	37°C
	Min. Temp.	27°C
<b>Voltages</b>	Cathode	-2.5 kV
	Field Shaping	-1.6 kV
	Central grid	-6.4 kV
	Sense wire	Ground
	Chamber gain	$\sim 2 \times 10^4$
<b>Electronics</b>	# Wire channels	3072
	# Pad channels	768
	# $dE/dx$ channels	768

Table 2.3: Summary of the VTPC operation.

<b>Preamplifier</b>	Fujitsu MB43458	
	Circuit Package Technology # channels /chip Rise time $e^-$ equivalent noise Power consumption	Base-grounded amplifier 14 pin surface mount Analog master slice 4 20 nsec 10-90% 3000 $e^-$ 's (100 nsec gate) 25 mW /channel
<b>Preamp. card</b>	# channels additional circuit  Technology Card thickness Weight	24 Cross talk cancellation Protection diodes Surface mount 0.625 mm 10 gram
	<b>Coax cable</b> Junkosha miniature coax	
	# conductors Total length Dimension Impedance Rise time	25 10 m 0.80 mm thick, 25 mm wide 42 $\Omega$ 5 nsec 10-70%
	<b>ASD</b>	
	# channels /board Technology Amplifier Shaping  Discriminator	48 Surface mount NE529 700 nsec $RC$ pole-zero and 30 nsec integration LeCroy MVL407
	<b>TDC</b>	
	LeCroy FASTBUS 1897 Single width FASTBUS slave Multiple hit capability	
	Technology # channels/board Resolution Max. TDC counts Data compaction	CCD based pipe-line 96 8 nsec / TDC-count 511 no-hit chann. suppression

Table 2.4: Summary of the VTPC wire electronics.

Preamplifier	LeCroy HCV802	
	Circuit	FET input charge sensitive
	Package	12 pin DIP, 3.5 gram/package
	Technology	Hybrid
	# channels /pack.	8
	Rise time	20 nsec 10-90%
	$e^-$ equivalent noise	1500 $e^-$ 's (200 nsec gate)
Preamp. card	Power consumption	60 mW /channel
	# channels	24
	additional circuit	Protection diodes
	Technology	Surface mount
	Card thickness	0.625 mm
Coax cable	Weight	27 gram
	Junkosha miniature coax same ones as for wire	
PAS	# channels /board	48
	Technology	Surface mount
	Amplifier	NE529
	Shaping	400 nsec pole-zero and
		200 nsec FWHM integration (4-stage semi-Gaussian)
FADC	Single width FASTBUS board	
	Max. sampling rate	35 MHz (operated at 10.6 MHz)
	FADC chip	Sony CXA1016P (ECL)
	# channels/board	24
	Resolution	0.5-0.6 / 8 bit rms
	Linearity	0.5-0.6 / 8 bit rms
	Max.# time bins	255
	Power consumption	77 W /board
FADC compaction	Single width FASTBUS slave	
	Compaction algorithm	Time-clustering
	Compaction rate	25 MHz/ byte

Table 2.5: Summary of the VTPC pad electronics.

Counters			Phototube (Hamamatsu Photonics)		
Type	Width (cm)	Length (cm)	Type	Rise time (nsec)	Transit time (nsec)
0	3.13	12.92	R2083	1.3	14
1	6.07	25.06	R1828-01	1.3	28
2	11.76	48.87	R1828-01	1.3	28
3	22.70	93.98	R1828-01	1.3	28

Table 2.6: Beam-Beam Counters Specification.

TDC	
N of TDCs	48 (3072 chan.)
N of crates	2
N of scanners	2
Data size	total 10 Kbytes typical
Data Transfer rate in a crate	32 bits/250 nsec
Transfer time	0.6 msec typical
Formating	channel/TDC-count reordering and adding pointer
Formating time	12.6 msec typical
FADC	
N of FADCs	64 (1536 chan.)
N of compac. mod.	8
N of FADC crates	4
N of compac. crates	1
N of scanners	1
Data size	total 11 Kbytes typical
Data Transfer rate in a crate	32 bits/250 nsec
Transfer time	0.6 msec typical
Formating	adding pointers
Formating time	2 msec typical

Table 2.7: Summary of the VTPC data acquisition.

Component	$\sqrt{s} = 630 \text{ GeV}$	$\sqrt{s} = 1.8 \text{ TeV}$
$\sigma_{tot}$	$59.1 \pm 4.6 \text{ mb}$	$77 \pm 6 \text{ mb}$
$\sigma_{el}$	$12.7 \pm 1.1 \text{ mb}$	$17.6 \pm 1.6 \text{ mb}$
$\sigma_{SD}$	$10.0 \pm 3.3 \text{ mb}$	$15.0 \pm 5.0 \text{ mb}$
$\sigma_{DD}$	$2.5 \pm 0.6 \text{ mb}$	$4.2 \pm 1.0 \text{ mb}$
$\sigma_{ND}$	$33.9 \pm 4 \text{ mb}$	$40.2 \pm 5 \text{ mb}$

Table 2.8: Summary of estimated cross section for various components. The error resulted from the uncertainty in the total cross section and in the ratios  $\sigma_{xx}/\sigma_{tot}$ .

$\sqrt{s} = 630 \text{ GeV}$			
Component	Acceptance	Triggering $\sigma$	Fraction
Non diffractive	11.6%	$31.9 \pm 4 \text{ mb}$	91.1%
Double diffractive	75.0%	$1.9 \pm 0.4 \text{ mb}$	5.4%
Single diffractive	93.8%	$1.2 \pm 0.4 \text{ mb}$	3.4%
total	—	$35 \pm 4 \text{ mb}$	100%
$\sqrt{s} = 1.8 \text{ TeV}$			
Component	Acceptance	Triggering $\sigma$	Fraction
Non diffractive	17%	$38.6 \pm 5 \text{ mb}$	87.5%
Double diffractive	71%	$2.9 \pm 0.7 \text{ mb}$	6.6%
Single diffractive	96%	$2.6 \pm 0.9 \text{ mb}$	5.9%
total	—	$44 \pm 6 \text{ mb}$	100%

Table 2.9: Summary of the BBC acceptances and triggering cross section for various components. The error resulted from the uncertainty in the cross sections.

Particle $p_t$ (MeV/c)	50	100	200	300	500	800	9000	$\bar{p}p$ data
By histograming only	0.03	0.24	0.53	0.63	0.69	0.77	0.79	0.30
By histogram + hit-search	0.40	0.54	0.37	0.30	0.25	0.18	0.17	0.48
By hit-search only	0.57	0.22	0.10	0.07	0.06	0.05	0.04	0.22

Table 3.1: Fraction of tracks reconstructed by (1) the histograming method only, (2) histograming + hit-search method, and (3) hit-search method only for different track  $p_t$  's. We used a single particle simulation where particles were generated uniformly in  $\eta$  and randomly in  $\phi$ . For the smaller  $p_t$  's, the later steps of reconstruction found more tracks. The ratios for the real  $\bar{p}p$  data are also shown in the last column. All percentages were after applying a track selection (next chapter).

$ \eta $	Efficiency		
	Tight vertex cut	Nominal vertex cut	Loose vertex cut
0.00- 0.25	$0.957 \pm 0.015$	$0.996 \pm 0.016$	$1.045 \pm 0.016$
0.25- 0.50	$0.916 \pm 0.015$	$0.953 \pm 0.015$	$0.992 \pm 0.016$
0.50- 0.75	$0.899 \pm 0.015$	$0.947 \pm 0.015$	$1.000 \pm 0.016$
0.75- 1.00	$0.925 \pm 0.015$	$0.984 \pm 0.016$	$1.037 \pm 0.016$
1.00- 1.25	$0.942 \pm 0.015$	$1.009 \pm 0.016$	$1.070 \pm 0.017$
1.25- 1.50	$0.927 \pm 0.015$	$1.008 \pm 0.016$	$1.070 \pm 0.017$
1.50- 1.75	$0.978 \pm 0.016$	$1.046 \pm 0.016$	$1.102 \pm 0.017$
1.75- 2.00	$0.996 \pm 0.016$	$1.081 \pm 0.017$	$1.155 \pm 0.018$
2.00- 2.25	$0.953 \pm 0.015$	$1.043 \pm 0.016$	$1.106 \pm 0.017$
2.25- 2.50	$1.009 \pm 0.016$	$1.065 \pm 0.016$	$1.103 \pm 0.017$
2.50- 2.75	$1.026 \pm 0.016$	$1.088 \pm 0.017$	$1.137 \pm 0.017$
2.75- 3.00	$0.961 \pm 0.015$	$1.006 \pm 0.016$	$1.040 \pm 0.016$
3.00- 3.25	$0.850 \pm 0.014$	$0.873 \pm 0.014$	$0.888 \pm 0.015$

Table 4.1: Overall Efficiencies for three vertex cuts. The efficiency is the reconstructed  $dN/d\eta$  of the simulated data with all possible effects described in this chapter divided by the  $dN/d\eta$  put into the Monte Carlo, therefore also including the reconstruction efficiency.



$ \eta $ range	$\leq 1.0$	$\leq 2.0$	$\leq 3.0$
Increase of $\langle n_{ch} \rangle$ (%)	$8.5 \pm 1.2$	$7.6 \pm 1.0$	$7.1 \pm 1.0$

Table 4.2: Increase (%) of  $\langle n_{ch} \rangle$  due to the various effects for three  $|\eta|$  ranges. The errors are statistical ones.

### Run 7560A,B,C (1.8 TeV)

Luminosity =  $1.1 \times 10^{28}$

Crossing	$p$ inten	$\bar{p}$ inten	Trigger	Pass	Reject	Non- $\bar{p}p$	Other
A	$4.7 \times 10^{10}$	0	120	1	119	N/A	N/A
B	$4.7 \times 10^{10}$	$2.4 \times 10^9$	5081	4816	265	208	57

### Run 7536A,E,F (630 GeV)

Luminosity =  $0.7 \times 10^{27}$

Crossing	$p$ inten	$\bar{p}$ inten	Trigger	Pass	Reject	Non- $\bar{p}p$	Other
A	$4.0 \times 10^{10}$	0	707	3	704	N/A	N/A
B	$4.4 \times 10^{10}$	$1.4 \times 10^9$	2295	1283	1012	971	41

Table 4.3: Summary of event selection efficiency. N/A is *not applied*.

$\sqrt{s}$	No. of events triggered by BBC	No. of events passed event selec.	No. of events passed vertex selec.
630 GeV	8514	4546	2778
1.8 TeV	42436	39825	25266

Table 4.4: Summary of number of events used in the analysis. A cut has been applied on the  $z$  position of the primary vertex to insure a 100 % acceptance in the VTPC.

$ \eta $	With Nominal Cut	With Tight Cut	Width Loose Cut	Systematic
0.00-0.25	$1.268 \pm 0.020$	$1.259 \pm 0.021$	$1.262 \pm 0.019$	2 % for all $\eta$
0.25-0.50	$1.286 \pm 0.021$	$1.280 \pm 0.022$	$1.301 \pm 0.021$	
0.50-0.75	$1.253 \pm 0.020$	$1.243 \pm 0.021$	$1.280 \pm 0.020$	
0.75-1.00	$1.258 \pm 0.020$	$1.260 \pm 0.020$	$1.276 \pm 0.019$	
1.00-1.25	$1.304 \pm 0.020$	$1.300 \pm 0.021$	$1.304 \pm 0.019$	
1.25-1.50	$1.262 \pm 0.019$	$1.256 \pm 0.020$	$1.268 \pm 0.018$	
1.50-1.75	$1.285 \pm 0.019$	$1.285 \pm 0.020$	$1.280 \pm 0.018$	
1.75-2.00	$1.270 \pm 0.018$	$1.274 \pm 0.019$	$1.266 \pm 0.018$	
2.00-2.25	$1.301 \pm 0.019$	$1.300 \pm 0.020$	$1.313 \pm 0.019$	
2.25-2.50	$1.307 \pm 0.019$	$1.297 \pm 0.020$	$1.312 \pm 0.019$	
2.50-2.75	$1.319 \pm 0.019$	$1.325 \pm 0.020$	$1.322 \pm 0.019$	
2.75-3.00	$1.327 \pm 0.020$	$1.319 \pm 0.020$	$1.333 \pm 0.019$	

Table 5.1: Summary of ratios of  $dN/d\eta$  at  $\sqrt{s} = 1.8$  TeV to  $dN/d\eta$  at 630 GeV. The errors with various vertex cuts are statistical. The systematic error 2% ( $\sim 0.03$  in the absolute value) is due to the event selection. This systematic error does not depend on  $\eta$ .

$ \eta $	Tight cut	Nominal cut	Loose cut	Stati./Syste.	Ev. Selec.
0.00-0.25	$2.962 \pm 0.066$	$3.120 \pm 0.068$	$3.299 \pm 0.070$	0.182	3%
0.25-0.50	$2.815 \pm 0.065$	$2.958 \pm 0.067$	$3.074 \pm 0.068$	0.146	
0.50-0.75	$3.120 \pm 0.071$	$3.226 \pm 0.072$	$3.248 \pm 0.071$	0.096	
0.75-1.00	$3.215 \pm 0.072$	$3.298 \pm 0.072$	$3.324 \pm 0.071$	0.091	
1.00-1.25	$3.215 \pm 0.072$	$3.251 \pm 0.071$	$3.279 \pm 0.069$	0.079	
1.25-1.50	$3.440 \pm 0.076$	$3.423 \pm 0.074$	$3.438 \pm 0.072$	0.077	
1.50-1.75	$3.346 \pm 0.073$	$3.396 \pm 0.072$	$3.453 \pm 0.072$	0.090	
1.75-2.00	$3.393 \pm 0.073$	$3.444 \pm 0.072$	$3.484 \pm 0.071$	0.086	
2.00-2.25	$3.299 \pm 0.073$	$3.345 \pm 0.071$	$3.376 \pm 0.070$	0.082	
2.25-2.50	$3.287 \pm 0.071$	$3.338 \pm 0.070$	$3.413 \pm 0.070$	0.094	
2.50-2.75	$3.231 \pm 0.070$	$3.281 \pm 0.069$	$3.312 \pm 0.068$	0.080	0.090
2.75-3.00	$3.405 \pm 0.074$	$3.452 \pm 0.074$	$3.506 \pm 0.074$	0.090	

Table 5.2: Corrected  $dN/d\eta$  for  $\sqrt{s} = 630$  GeV with three vertex cuts. The errors with various vertex cuts are statistical ones. The systematic error is the center value with the loose cut minus that with the tight cut. Another 3% ( $\sim 0.1$  in  $dN/d\eta$ ) of systematic error is due to the event selection and is independent of  $\eta$ .

$ \eta $	Tight cut	Nominal cut	Loose cut	Stati./Syste.	Ev. Selec.
0.00-0.25	$3.729 \pm 0.061$	$3.955 \pm 0.064$	$4.162 \pm 0.066$	0.226	1%
0.25-0.50	$3.604 \pm 0.061$	$3.806 \pm 0.063$	$3.998 \pm 0.066$	0.207	
0.50-0.75	$3.879 \pm 0.066$	$4.043 \pm 0.068$	$4.157 \pm 0.068$	0.155	
0.75-1.00	$4.052 \pm 0.068$	$4.150 \pm 0.069$	$4.243 \pm 0.069$	0.118	
1.00-1.25	$4.181 \pm 0.070$	$4.239 \pm 0.070$	$4.276 \pm 0.069$	0.085	
1.25-1.50	$4.319 \pm 0.073$	$4.319 \pm 0.071$	$4.358 \pm 0.071$	0.076	
1.50-1.75	$4.300 \pm 0.071$	$4.363 \pm 0.071$	$4.419 \pm 0.071$	0.093	
1.75-2.00	$4.324 \pm 0.071$	$4.373 \pm 0.070$	$4.409 \pm 0.069$	0.083	
2.00-2.25	$4.289 \pm 0.072$	$4.351 \pm 0.071$	$4.433 \pm 0.071$	0.102	
2.25-2.50	$4.265 \pm 0.069$	$4.362 \pm 0.069$	$4.479 \pm 0.071$	0.128	
2.50-2.75	$4.281 \pm 0.070$	$4.328 \pm 0.069$	$4.379 \pm 0.069$	0.085	0.119
2.75-3.00	$4.489 \pm 0.074$	$4.582 \pm 0.075$	$4.673 \pm 0.075$	0.119	

Table 5.3: Corrected  $dN/d\eta$  for  $\sqrt{s} = 1.8$  TeV with three vertex cuts. The errors with various vertex cuts are statistical ones. The systematic error is the center value with the loose cut minus that with the tight cut. There is another systematic error of 1% ( $\sim 0.04$  in  $dN/d\eta$ ) due to the event selection and is independent of  $\eta$ .

$n_{ch}$	Probability Density		
	$ \eta  < 1.0$	$ \eta  < 2.0$	$ \eta  < 3.0$
0.50-2.50	$0.973E-01 \pm 0.442E-02$	$0.316E-01 \pm 0.245E-02$	$0.132E-01 \pm 0.137E-02$
2.50-4.50	$0.103E+00 \pm 0.459E-02$	$0.439E-01 \pm 0.288E-02$	$0.193E-01 \pm 0.189E-02$
4.50-6.50	$0.796E-01 \pm 0.400E-02$	$0.440E-01 \pm 0.288E-02$	$0.251E-01 \pm 0.207E-02$
6.50-8.50	$0.670E-01 \pm 0.367E-02$	$0.522E-01 \pm 0.314E-02$	$0.284E-01 \pm 0.229E-02$
8.50-10.50	$0.480E-01 \pm 0.310E-02$	$0.533E-01 \pm 0.317E-02$	$0.325E-01 \pm 0.245E-02$
10.50-12.50	$0.311E-01 \pm 0.250E-02$	$0.401E-01 \pm 0.275E-02$	$0.342E-01 \pm 0.252E-02$
12.50-14.50	$0.206E-01 \pm 0.203E-02$	$0.405E-01 \pm 0.276E-02$	$0.416E-01 \pm 0.278E-02$
14.50-16.50	$0.169E-01 \pm 0.184E-02$	$0.311E-01 \pm 0.242E-02$	$0.333E-01 \pm 0.249E-02$
16.50-18.50	$0.117E-01 \pm 0.153E-02$	$0.300E-01 \pm 0.238E-02$	$0.350E-01 \pm 0.255E-02$
18.50-20.50	$0.727E-02 \pm 0.121E-02$	$0.238E-01 \pm 0.212E-02$	$0.283E-01 \pm 0.229E-02$
20.50-22.50	$0.385E-02 \pm 0.870E-03$	$0.183E-01 \pm 0.180E-02$	$0.223E-01 \pm 0.204E-02$
22.50-24.50	$0.456E-02 \pm 0.960E-03$	$0.166E-01 \pm 0.177E-02$	$0.226E-01 \pm 0.205E-02$
24.50-26.50	$0.227E-02 \pm 0.675E-03$	$0.144E-01 \pm 0.165E-02$	$0.212E-01 \pm 0.198E-02$
26.50-28.50	$0.189E-02 \pm 0.582E-03$	$0.102E-01 \pm 0.136E-02$	$0.177E-01 \pm 0.181E-02$
28.50-30.50	$0.819E-03 \pm 0.406E-03$	$0.111E-01 \pm 0.144E-02$	$0.170E-01 \pm 0.178E-02$
30.50-32.50	$0.123E-02 \pm 0.496E-03$	$0.397E-02 \pm 0.864E-03$	$0.152E-01 \pm 0.186E-02$
32.50-34.50	$0.186E-03 \pm 0.183E-03$	$0.574E-02 \pm 0.104E-02$	$0.116E-01 \pm 0.146E-02$
34.50-36.50	$0.268E-03 \pm 0.232E-03$	$0.536E-02 \pm 0.101E-02$	$0.101E-01 \pm 0.137E-02$
36.50-38.50	$0.737E-03 \pm 0.385E-03$	$0.428E-02 \pm 0.868E-03$	$0.917E-02 \pm 0.130E-02$
38.50-40.50	$0.201E-03 \pm 0.201E-03$	$0.430E-02 \pm 0.909E-03$	$0.857E-02 \pm 0.126E-02$
40.50-42.50		$0.286E-02 \pm 0.738E-03$	$0.868E-02 \pm 0.127E-02$
42.50-44.50		$0.280E-02 \pm 0.726E-03$	$0.496E-02 \pm 0.958E-03$
44.50-46.50		$0.223E-02 \pm 0.648E-03$	$0.454E-02 \pm 0.917E-03$
46.50-48.50		$0.207E-02 \pm 0.623E-03$	$0.463E-02 \pm 0.926E-03$
48.50-50.50		$0.141E-02 \pm 0.510E-03$	$0.455E-02 \pm 0.918E-03$
50.50-52.50		$0.850E-03 \pm 0.400E-03$	$0.222E-02 \pm 0.642E-03$
52.50-54.50		$0.942E-03 \pm 0.421E-03$	$0.257E-02 \pm 0.690E-03$
54.50-56.50		$0.377E-03 \pm 0.266E-03$	$0.307E-02 \pm 0.754E-03$
56.50-58.50		$0.650E-03 \pm 0.352E-03$	$0.454E-02 \pm 0.918E-03$
58.50-60.50		$0.283E-03 \pm 0.231E-03$	$0.380E-02 \pm 0.840E-03$
60.50-62.50			$0.245E-02 \pm 0.674E-03$
62.50-64.50			$0.168E-02 \pm 0.559E-03$
64.50-66.50			$0.142E-02 \pm 0.513E-03$
66.50-68.50			$0.138E-02 \pm 0.505E-03$
68.50-70.50			$0.134E-02 \pm 0.496E-03$
70.50-72.50			$0.533E-03 \pm 0.314E-03$
72.50-74.50			$0.479E-03 \pm 0.296E-03$
74.50-76.50			$0.492E-03 \pm 0.302E-03$
76.50-78.50			$0.450E-03 \pm 0.304E-03$
78.50-80.50			$0.105E-03 \pm 0.140E-03$
80.50-82.50			$0.605E-03 \pm 0.335E-03$

Table 5.5: Corrected charged multiplicities at  $\sqrt{s} = 630$  GeV for three  $|\eta|$  ranges.

$n_{ch}$	Probability Density		
	$ \eta  < 1.0$	$ \eta  < 2.0$	$ \eta  < 3.0$
0.50-2.50	$0.767E-01 \pm 0.129E-02$	$0.224E-01 \pm 0.675E-03$	$0.762E-02 \pm 0.397E-03$
2.50-4.50	$0.893E-01 \pm 0.138E-02$	$0.324E-01 \pm 0.813E-03$	$0.127E-01 \pm 0.507E-03$
4.50-6.50	$0.753E-01 \pm 0.127E-02$	$0.428E-01 \pm 0.931E-03$	$0.189E-01 \pm 0.618E-03$
6.50-8.50	$0.581E-01 \pm 0.111E-02$	$0.431E-01 \pm 0.938E-03$	$0.241E-01 \pm 0.697E-03$
8.50-10.50	$0.453E-01 \pm 0.962E-03$	$0.416E-01 \pm 0.924E-03$	$0.273E-01 \pm 0.742E-03$
10.50-12.50	$0.350E-01 \pm 0.873E-03$	$0.370E-01 \pm 0.879E-03$	$0.291E-01 \pm 0.766E-03$
12.50-14.50	$0.281E-01 \pm 0.773E-03$	$0.329E-01 \pm 0.819E-03$	$0.300E-01 \pm 0.778E-03$
14.50-16.50	$0.222E-01 \pm 0.686E-03$	$0.283E-01 \pm 0.762E-03$	$0.291E-01 \pm 0.767E-03$
16.50-18.50	$0.169E-01 \pm 0.599E-03$	$0.259E-01 \pm 0.726E-03$	$0.242E-01 \pm 0.728E-03$
18.50-20.50	$0.120E-01 \pm 0.505E-03$	$0.234E-01 \pm 0.690E-03$	$0.237E-01 \pm 0.692E-03$
20.50-22.50	$0.103E-01 \pm 0.489E-03$	$0.210E-01 \pm 0.654E-03$	$0.216E-01 \pm 0.660E-03$
22.50-24.50	$0.773E-02 \pm 0.405E-03$	$0.195E-01 \pm 0.630E-03$	$0.199E-01 \pm 0.633E-03$
24.50-26.50	$0.550E-02 \pm 0.342E-03$	$0.184E-01 \pm 0.578E-03$	$0.190E-01 \pm 0.619E-03$
26.50-28.50	$0.433E-02 \pm 0.303E-03$	$0.147E-01 \pm 0.548E-03$	$0.177E-01 \pm 0.599E-03$
28.50-30.50	$0.307E-02 \pm 0.255E-03$	$0.130E-01 \pm 0.516E-03$	$0.173E-01 \pm 0.590E-03$
30.50-32.50	$0.210E-02 \pm 0.211E-03$	$0.114E-01 \pm 0.463E-03$	$0.148E-01 \pm 0.548E-03$
32.50-34.50	$0.176E-02 \pm 0.193E-03$	$0.106E-01 \pm 0.466E-03$	$0.140E-01 \pm 0.532E-03$
34.50-36.50	$0.131E-02 \pm 0.167E-03$	$0.812E-02 \pm 0.407E-03$	$0.131E-01 \pm 0.514E-03$
36.50-38.50	$0.822E-03 \pm 0.132E-03$	$0.792E-02 \pm 0.402E-03$	$0.111E-01 \pm 0.473E-03$
38.50-40.50	$0.563E-03 \pm 0.109E-03$	$0.727E-02 \pm 0.385E-03$	$0.113E-01 \pm 0.477E-03$
40.50-42.50	$0.309E-03 \pm 0.811E-04$	$0.500E-02 \pm 0.322E-03$	$0.074E-02 \pm 0.443E-03$
42.50-44.50	$0.174E-03 \pm 0.608E-04$	$0.471E-02 \pm 0.310E-03$	$0.045E-02 \pm 0.437E-03$
44.50-46.50	$0.103E-03 \pm 0.487E-04$	$0.463E-02 \pm 0.307E-03$	$0.088E-02 \pm 0.423E-03$
46.50-48.50	$0.669E-04 \pm 0.377E-04$	$0.428E-02 \pm 0.295E-03$	$0.730E-02 \pm 0.384E-03$
48.50-50.50	$0.607E-04 \pm 0.359E-04$	$0.331E-02 \pm 0.260E-03$	$0.792E-02 \pm 0.400E-03$
50.50-52.50	$0.213E-04 \pm 0.213E-04$	$0.306E-02 \pm 0.250E-03$	$0.615E-02 \pm 0.352E-03$
52.50-54.50	$0.189E-04 \pm 0.199E-04$	$0.237E-02 \pm 0.229E-03$	$0.517E-02 \pm 0.323E-03$
54.50-56.50	$0.239E-04 \pm 0.225E-04$	$0.200E-02 \pm 0.202E-03$	$0.575E-02 \pm 0.341E-03$
56.50-58.50		$0.201E-02 \pm 0.203E-03$	$0.526E-02 \pm 0.327E-03$
58.50-60.50		$0.130E-02 \pm 0.168E-03$	$0.450E-02 \pm 0.301E-03$
60.50-62.50		$0.136E-02 \pm 0.166E-03$	$0.464E-02 \pm 0.308E-03$
62.50-64.50		$0.101E-02 \pm 0.144E-03$	$0.386E-02 \pm 0.279E-03$
64.50-66.50		$0.923E-03 \pm 0.137E-03$	$0.392E-02 \pm 0.281E-03$
66.50-68.50		$0.763E-03 \pm 0.125E-03$	$0.334E-02 \pm 0.260E-03$
68.50-70.50		$0.583E-03 \pm 0.107E-03$	$0.313E-02 \pm 0.251E-03$
70.50-72.50		$0.504E-03 \pm 0.101E-03$	$0.266E-02 \pm 0.232E-03$
72.50-74.50		$0.338E-03 \pm 0.830E-04$	$0.220E-02 \pm 0.211E-03$
74.50-76.50		$0.202E-03 \pm 0.841E-04$	$0.234E-02 \pm 0.217E-03$
76.50-78.50		$0.882E-04 \pm 0.424E-04$	$0.199E-02 \pm 0.201E-03$
78.50-80.50		$0.177E-03 \pm 0.601E-04$	$0.189E-02 \pm 0.195E-03$
80.50-82.50		$0.113E-03 \pm 0.479E-04$	$0.149E-02 \pm 0.174E-03$
82.50-84.50		$0.302E-04 \pm 0.248E-04$	$0.126E-02 \pm 0.159E-03$
84.50-86.50			$0.121E-02 \pm 0.156E-03$
86.50-88.50		$0.408E-04 \pm 0.289E-04$	$0.111E-02 \pm 0.150E-03$
88.50-90.50		$0.408E-04 \pm 0.289E-04$	$0.901E-03 \pm 0.135E-03$
90.50-92.50		$0.204E-04 \pm 0.204E-04$	$0.103E-02 \pm 0.144E-03$
92.50-94.50		$0.499E-04 \pm 0.319E-04$	$0.621E-03 \pm 0.112E-03$
94.50-96.50		$0.726E-04 \pm 0.385E-04$	$0.478E-03 \pm 0.962E-04$
96.50-98.50		$0.286E-04 \pm 0.241E-04$	$0.460E-03 \pm 0.964E-04$
98.50-100.50		$0.122E-04 \pm 0.156E-04$	$0.307E-03 \pm 0.767E-04$
100.50-102.50			$0.563E-03 \pm 0.107E-03$
102.50-104.50			$0.286E-03 \pm 0.760E-04$
104.50-106.50			$0.208E-03 \pm 0.648E-04$
106.50-108.50			$0.199E-03 \pm 0.633E-04$
108.50-110.50			$0.178E-03 \pm 0.600E-04$
110.50-112.50			$0.166E-03 \pm 0.613E-04$
112.50-114.50			$0.157E-03 \pm 0.563E-04$
114.50-116.50			$0.709E-04 \pm 0.378E-04$
116.50-118.50			$0.111E-03 \pm 0.473E-04$
118.50-120.50			$0.834E-04 \pm 0.411E-04$
120.50-122.50			$0.172E-04 \pm 0.186E-04$
122.50-124.50			$0.731E-04 \pm 0.384E-04$
124.50-126.50			$0.460E-04 \pm 0.311E-04$
126.50-128.50			$0.260E-04 \pm 0.229E-04$
128.50-130.50			$0.547E-04 \pm 0.532E-04$
130.50-132.50			$0.260E-04 \pm 0.229E-04$
132.50-134.50			$0.144E-04 \pm 0.170E-04$

Table 5.6: Corrected charged multiplicities at  $\sqrt{s} = 1.8$  TeV for three  $|\eta|$  ranges.

$\sqrt{s}$	$ \eta  \leq$	$\chi^2/NDF$	$\langle n_{ch} \rangle$	$k$
630 GeV	1.0	24.3/15	$6.4 \pm 0.1$	$1.96 \pm 0.08$
	2.0	53.2/27	$13.4 \pm 0.2$	$2.22 \pm 0.08$
	3.0	57.3/40	$23.8 \pm 0.3$	$2.71 \pm 0.09$
1.8 TeV	1.0	160.7/21	$7.83 \pm 0.04$	$1.83 \pm 0.02$
	2.0	305.8/40	$16.77 \pm 0.07$	$2.07 \pm 0.02$
	3.0	396.5/62	$30.16 \pm 0.13$	$2.46 \pm 0.02$

Table 5.7: Summary of negative binomial fit parameters to uncorrected multiplicity distributions at  $\sqrt{s} = 630$  GeV and 1.8 TeV.

$\sqrt{s}$	$ \eta  \leq$	$\chi^2/\text{NDF}$	$\langle n_{ch} \rangle$	$k$
<b>546 GeV</b> UA5	1.0	41.8/27	$6.14 \pm 0.06$	$1.80 \pm 0.05$
	2.0	80.8/46	$12.8 \pm 0.1$	$2.12 \pm 0.05$
	3.0	78.7/59	$18.8 \pm 0.1$	$2.47 \pm 0.05$
<b>630 GeV</b>	1.0	22.1/18	$6.14 \pm 0.09$	$1.87 \pm 0.05$
	2.0	39.7/30	$13.0 \pm 0.1$	$2.02 \pm 0.05$
	3.0	55.4/42	$19.8 \pm 0.2$	$2.35 \pm 0.05$
<b>1.8 TeV</b>	1.0	156/26	$7.65 \pm 0.04$	$1.63 \pm 0.02$
	2.0	247/49	$16.50 \pm 0.06$	$1.86 \pm 0.01$
	3.0	353/68	$25.76 \pm 0.09$	$2.08 \pm 0.01$

Table 5.8: Summary of negative-binomial-fit parameters for corrected multiplicity distributions at  $\sqrt{s} = 630$  GeV and 1.8 TeV with UA5 data at  $\sqrt{s} = 546$  GeV. The errors in our data is statistical.

$\sqrt{s}$	$ \eta $	$\chi^2/\text{NDF}$	$k$
<b>630 GeV</b>	0.0-1.0	22.1/18	$1.87 \pm 0.05$
	1.0-2.0	23.0/16	$2.23 \pm 0.05$
	3.0-3.0	16.4/16	$2.61 \pm 0.02$
<b>1.8 TeV</b>	0.0-1.0	156/26	$1.63 \pm 0.02$
	1.0-2.0	173/28	$1.88 \pm 0.02$
	2.0-3.0	175/25	$2.11 \pm 0.02$

Table 5.9: Summary of negative-binomial-fit parameters for corrected multiplicity distributions at  $\sqrt{s} = 630$  GeV and 1.8 TeV. The errors in our data is the statistical.

	$a$	$b$	$\chi^2/\text{NDF}$
$ \eta  \leq 1.0$	$0.156 \pm 0.083$	$0.061 \pm 0.012$	1.9/1
$ \eta  \leq 2.0$	$0.165 \pm 0.057$	$0.050 \pm 0.008$	1.0/1
$ \eta  \leq 3.0$	$0.034 \pm 0.042$	$0.060 \pm 0.006$	1.1/1

Table 5.10: Summary of fit parameters for energy dependence of  $k$ . The fit is  $1/k = a + b \cdot \ln s$ .

$n/\langle n \rangle$	$\langle n \rangle P(n)$
0.08-0.38	$0.648E+00 \pm 0.294E-01$
0.38-0.68	$0.697E+00 \pm 0.305E-01$
0.68-0.98	$0.529E+00 \pm 0.266E-01$
0.98-1.28	$0.446E+00 \pm 0.244E-01$
1.28-1.58	$0.319E+00 \pm 0.207E-01$
1.58-1.88	$0.207E+00 \pm 0.166E-01$
1.88-2.18	$0.137E+00 \pm 0.135E-01$
2.18-2.48	$0.113E+00 \pm 0.123E-01$
2.48-2.78	$0.778E-01 \pm 0.102E-01$
2.78-3.08	$0.484E-01 \pm 0.804E-02$
3.08-3.38	$0.256E-01 \pm 0.585E-02$
3.38-3.68	$0.305E-01 \pm 0.639E-02$
3.68-3.98	$0.151E-01 \pm 0.449E-02$
3.98-4.28	$0.112E-01 \pm 0.387E-02$
4.28-4.58	$0.545E-02 \pm 0.270E-02$
4.58-4.88	$0.816E-02 \pm 0.330E-02$
4.88-5.18	$0.111E-02 \pm 0.122E-02$
5.18-5.48	$0.178E-02 \pm 0.154E-02$
5.48-5.78	$0.490E-02 \pm 0.256E-02$
5.78-6.09	$0.134E-02 \pm 0.134E-02$

Table 5.11: KNO distribution at  $\sqrt{s} = 630$  GeV for  $|\eta| \leq 1.0$ .

$n/\langle n \rangle$	$\langle n \rangle P(n)$
0.04-0.18	$0.444E+00 \pm 0.342E-01$
0.18-0.32	$0.613E+00 \pm 0.401E-01$
0.32-0.47	$0.614E+00 \pm 0.402E-01$
0.47-0.61	$0.729E+00 \pm 0.438E-01$
0.61-0.75	$0.744E+00 \pm 0.442E-01$
0.75-0.90	$0.560E+00 \pm 0.384E-01$
0.90-1.04	$0.565E+00 \pm 0.385E-01$
1.04-1.18	$0.434E+00 \pm 0.338E-01$
1.18-1.32	$0.419E+00 \pm 0.332E-01$
1.32-1.47	$0.333E+00 \pm 0.296E-01$
1.47-1.61	$0.255E+00 \pm 0.259E-01$
1.61-1.75	$0.232E+00 \pm 0.247E-01$
1.75-1.90	$0.201E+00 \pm 0.230E-01$
1.90-2.04	$0.142E+00 \pm 0.193E-01$
2.04-2.18	$0.154E+00 \pm 0.202E-01$
2.18-2.33	$0.554E-01 \pm 0.121E-01$
2.33-2.47	$0.802E-01 \pm 0.145E-01$
2.47-2.61	$0.749E-01 \pm 0.140E-01$
2.61-2.76	$0.598E-01 \pm 0.125E-01$
2.76-2.90	$0.612E-01 \pm 0.127E-01$
2.90-3.04	$0.404E-01 \pm 0.103E-01$
3.04-3.19	$0.391E-01 \pm 0.101E-01$
3.19-3.33	$0.311E-01 \pm 0.905E-02$
3.33-3.47	$0.289E-01 \pm 0.872E-02$
3.47-3.62	$0.197E-01 \pm 0.720E-02$
3.62-3.76	$0.119E-01 \pm 0.559E-02$
3.76-3.90	$0.132E-01 \pm 0.588E-02$
3.90-4.05	$0.526E-02 \pm 0.372E-02$
4.05-4.19	$0.920E-02 \pm 0.492E-02$
4.19-4.33	$0.395E-02 \pm 0.322E-02$
4.33-4.48	
4.48-4.62	$0.424E-02 \pm 0.334E-02$
4.62-4.76	$0.365E-02 \pm 0.310E-02$

Table 5.12: KNO distribution at  $\sqrt{s} = 630$  GeV for  $|\eta| \leq 2.0$ .

$n/\langle n \rangle$	$\langle n \rangle P(n)$
0.02-0.12	$0.281E+00 \pm 0.332E-01$
0.12-0.21	$0.410E+00 \pm 0.401E-01$
0.21-0.31	$0.490E+00 \pm 0.439E-01$
0.31-0.40	$0.602E+00 \pm 0.486E-01$
0.40-0.50	$0.689E+00 \pm 0.520E-01$
0.50-0.59	$0.725E+00 \pm 0.534E-01$
0.59-0.68	$0.886E+00 \pm 0.590E-01$
0.68-0.78	$0.706E+00 \pm 0.527E-01$
0.78-0.87	$0.743E+00 \pm 0.540E-01$
0.87-0.97	$0.600E+00 \pm 0.486E-01$
0.97-1.06	$0.474E+00 \pm 0.431E-01$
1.06-1.16	$0.479E+00 \pm 0.434E-01$
1.16-1.25	$0.450E+00 \pm 0.420E-01$
1.25-1.34	$0.375E+00 \pm 0.384E-01$
1.34-1.44	$0.361E+00 \pm 0.377E-01$
1.44-1.53	$0.323E+00 \pm 0.356E-01$
1.53-1.63	$0.245E+00 \pm 0.310E-01$
1.63-1.72	$0.214E+00 \pm 0.290E-01$
1.72-1.82	$0.194E+00 \pm 0.276E-01$
1.82-1.91	$0.182E+00 \pm 0.267E-01$
1.91-2.00	$0.184E+00 \pm 0.269E-01$
2.00-2.10	$0.105E+00 \pm 0.203E-01$
2.10-2.19	$0.962E-01 \pm 0.194E-01$
2.19-2.29	$0.980E-01 \pm 0.196E-01$
2.29-2.38	$0.964E-01 \pm 0.195E-01$
2.38-2.48	$0.472E-01 \pm 0.136E-01$
2.48-2.57	$0.545E-01 \pm 0.146E-01$
2.57-2.67	$0.651E-01 \pm 0.160E-01$
2.67-2.76	$0.963E-01 \pm 0.195E-01$
2.76-2.85	$0.806E-01 \pm 0.178E-01$
2.85-2.95	$0.519E-01 \pm 0.143E-01$
2.95-3.04	$0.357E-01 \pm 0.118E-01$
3.04-3.14	$0.300E-01 \pm 0.109E-01$
3.14-3.23	$0.292E-01 \pm 0.107E-01$
3.23-3.33	$0.283E-01 \pm 0.105E-01$
3.33-3.42	$0.113E-01 \pm 0.666E-02$
3.42-3.51	$0.101E-01 \pm 0.631E-02$
3.51-3.61	$0.104E-01 \pm 0.640E-02$
3.61-3.70	$0.106E-01 \pm 0.645E-02$
3.70-3.80	$0.223E-02 \pm 0.296E-02$
3.80-3.89	$0.128E-01 \pm 0.710E-02$
3.89-3.99	$0.681E-02 \pm 0.517E-02$
3.99-4.08	$0.000E+00 \pm 0.000E+00$
4.08-4.17	$0.000E+00 \pm 0.000E+00$
4.17-4.27	$0.422E-02 \pm 0.407E-02$
4.27-4.36	$0.364E-02 \pm 0.378E-02$

Table 5.13: KNO distribution at  $\sqrt{s} = 630$  GeV for  $|\eta| \leq 3.0$ .

$n/\langle n \rangle$	$\langle n \rangle P(n)$
0.06-0.30	$0.653E+00 \pm 0.107E-01$
0.30-0.54	$0.741E+00 \pm 0.114E-01$
0.54-0.78	$0.625E+00 \pm 0.105E-01$
0.78-1.02	$0.482E+00 \pm 0.922E-02$
1.02-1.27	$0.376E+00 \pm 0.815E-02$
1.27-1.51	$0.298E+00 \pm 0.725E-02$
1.51-1.75	$0.233E+00 \pm 0.641E-02$
1.75-1.99	$0.184E+00 \pm 0.570E-02$
1.99-2.23	$0.140E+00 \pm 0.497E-02$
2.23-2.47	$0.994E-01 \pm 0.419E-02$
2.47-2.71	$0.857E-01 \pm 0.389E-02$
2.71-2.95	$0.641E-01 \pm 0.336E-02$
2.95-3.19	$0.456E-01 \pm 0.284E-02$
3.19-3.43	$0.359E-01 \pm 0.252E-02$
3.43-3.68	$0.254E-01 \pm 0.212E-02$
3.68-3.92	$0.174E-01 \pm 0.175E-02$
3.92-4.16	$0.146E-01 \pm 0.160E-02$
4.16-4.40	$0.109E-01 \pm 0.139E-02$
4.40-4.64	$0.682E-02 \pm 0.110E-02$
4.64-4.88	$0.467E-02 \pm 0.908E-03$
4.88-5.12	$0.257E-02 \pm 0.673E-03$
5.12-5.36	$0.144E-02 \pm 0.505E-03$
5.36-5.60	$0.851E-03 \pm 0.388E-03$
5.60-5.84	$0.555E-03 \pm 0.313E-03$
5.84-6.09	$0.504E-03 \pm 0.298E-03$
6.09-6.33	$0.176E-03 \pm 0.176E-03$
6.33-6.57	$0.155E-03 \pm 0.165E-03$
6.57-6.81	$0.198E-03 \pm 0.187E-03$

Table 5.14: KNO distribution at  $\sqrt{s} = 1.8$  TeV for  $|\eta| \leq 1.0$ .



$\eta/(\pi)$	$(\eta)P(\eta)$
0.03-0.14	$0.397E+00 \pm 0.120E-01$
0.14-0.25	$0.575E+00 \pm 0.144E-01$
0.25-0.37	$0.754E+00 \pm 0.165E-01$
0.37-0.48	$0.745E+00 \pm 0.166E-01$
0.48-0.59	$0.742E+00 \pm 0.164E-01$
0.59-0.70	$0.672E+00 \pm 0.158E-01$
0.70-0.82	$0.583E+00 \pm 0.145E-01$
0.82-0.93	$0.508E+00 \pm 0.135E-01$
0.93-1.04	$0.459E+00 \pm 0.129E-01$
1.04-1.16	$0.414E+00 \pm 0.123E-01$
1.16-1.27	$0.372E+00 \pm 0.118E-01$
1.27-1.38	$0.345E+00 \pm 0.112E-01$
1.38-1.49	$0.290E+00 \pm 0.103E-01$
1.49-1.61	$0.262E+00 \pm 0.975E-02$
1.61-1.72	$0.231E+00 \pm 0.915E-02$
1.72-1.83	$0.205E+00 \pm 0.857E-02$
1.83-1.94	$0.189E+00 \pm 0.827E-02$
1.94-2.06	$0.144E+00 \pm 0.722E-02$
2.06-2.17	$0.141E+00 \pm 0.714E-02$
2.17-2.28	$0.129E+00 \pm 0.684E-02$
2.28-2.39	$0.904E-01 \pm 0.575E-02$
2.39-2.51	$0.837E-01 \pm 0.550E-02$
2.51-2.62	$0.672E-01 \pm 0.546E-02$
2.62-2.73	$0.759E-01 \pm 0.524E-02$
2.73-2.85	$0.588E-01 \pm 0.461E-02$
2.85-2.98	$0.543E-01 \pm 0.443E-02$
2.98-3.07	$0.458E-01 \pm 0.408E-02$
3.07-3.18	$0.355E-01 \pm 0.359E-02$
3.18-3.30	$0.357E-01 \pm 0.360E-02$
3.30-3.41	$0.245E-01 \pm 0.298E-02$
3.41-3.52	$0.248E-01 \pm 0.298E-02$
3.52-3.63	$0.160E-01 \pm 0.255E-02$
3.63-3.75	$0.164E-01 \pm 0.244E-02$
3.75-3.86	$0.135E-01 \pm 0.221E-02$
3.86-3.97	$0.999E-02 \pm 0.190E-02$
3.97-4.09	$0.895E-02 \pm 0.180E-02$
4.09-4.20	$0.599E-02 \pm 0.147E-02$
4.20-4.31	$0.358E-02 \pm 0.114E-02$
4.31-4.42	$0.157E-02 \pm 0.753E-03$
4.42-4.54	$0.314E-02 \pm 0.107E-02$
4.54-4.65	$0.200E-02 \pm 0.851E-03$
4.65-4.76	$0.535E-03 \pm 0.440E-03$
4.76-4.87	$0.000E+00 \pm 0.000E+00$
4.87-4.99	$0.724E-03 \pm 0.512E-03$
4.99-5.10	$0.724E-03 \pm 0.512E-03$
5.10-5.21	$0.362E-03 \pm 0.362E-03$
5.21-5.32	$0.865E-03 \pm 0.866E-03$
5.32-5.44	$0.129E-02 \pm 0.883E-03$
5.44-5.55	$0.507E-03 \pm 0.478E-03$
5.55-5.66	$0.217E-03 \pm 0.280E-03$

Table 5.15: KNO distribution at  $\sqrt{s} = 1.8$  TeV for  $|\eta| \leq 2.0$ .

$\eta/(\pi)$	$(\eta)P(\eta)$
0.03-0.09	$0.216E+00 \pm 0.110E-01$
0.09-0.16	$0.351E+00 \pm 0.140E-01$
0.16-0.24	$0.522E+00 \pm 0.171E-01$
0.24-0.31	$0.665E+00 \pm 0.192E-01$
0.31-0.38	$0.753E+00 \pm 0.203E-01$
0.38-0.45	$0.602E+00 \pm 0.211E-01$
0.45-0.53	$0.826E+00 \pm 0.215E-01$
0.53-0.60	$0.604E+00 \pm 0.212E-01$
0.60-0.67	$0.724E+00 \pm 0.201E-01$
0.67-0.74	$0.854E+00 \pm 0.191E-01$
0.74-0.82	$0.595E+00 \pm 0.182E-01$
0.82-0.89	$0.548E+00 \pm 0.175E-01$
0.89-0.96	$0.523E+00 \pm 0.171E-01$
0.96-1.03	$0.490E+00 \pm 0.165E-01$
1.03-1.11	$0.476E+00 \pm 0.163E-01$
1.11-1.18	$0.408E+00 \pm 0.151E-01$
1.18-1.25	$0.387E+00 \pm 0.147E-01$
1.25-1.32	$0.361E+00 \pm 0.142E-01$
1.32-1.40	$0.308E+00 \pm 0.131E-01$
1.40-1.47	$0.311E+00 \pm 0.132E-01$
1.47-1.54	$0.269E+00 \pm 0.122E-01$
1.54-1.61	$0.261E+00 \pm 0.121E-01$
1.61-1.69	$0.245E+00 \pm 0.117E-01$
1.69-1.76	$0.202E+00 \pm 0.106E-01$
1.76-1.83	$0.219E+00 \pm 0.110E-01$
1.83-1.90	$0.170E+00 \pm 0.972E-02$
1.90-1.98	$0.143E+00 \pm 0.891E-02$
1.98-2.05	$0.159E+00 \pm 0.940E-02$
2.05-2.12	$0.148E+00 \pm 0.901E-02$
2.12-2.19	$0.124E+00 \pm 0.831E-02$
2.19-2.27	$0.128E+00 \pm 0.844E-02$
2.27-2.34	$0.107E+00 \pm 0.771E-02$
2.34-2.41	$0.108E+00 \pm 0.778E-02$
2.41-2.48	$0.922E-01 \pm 0.717E-02$
2.48-2.55	$0.863E-01 \pm 0.693E-02$
2.55-2.63	$0.735E-01 \pm 0.640E-02$
2.63-2.70	$0.607E-01 \pm 0.582E-02$
2.70-2.77	$0.848E-01 \pm 0.600E-02$
2.77-2.84	$0.550E-01 \pm 0.543E-02$
2.84-2.92	$0.520E-01 \pm 0.536E-02$
2.92-2.99	$0.412E-01 \pm 0.479E-02$
2.99-3.06	$0.347E-01 \pm 0.440E-02$
3.06-3.13	$0.333E-01 \pm 0.430E-02$
3.13-3.21	$0.307E-01 \pm 0.413E-02$
3.21-3.28	$0.249E-01 \pm 0.372E-02$
3.28-3.35	$0.283E-01 \pm 0.397E-02$
3.35-3.42	$0.171E-01 \pm 0.309E-02$
3.42-3.50	$0.132E-01 \pm 0.271E-02$
3.50-3.57	$0.127E-01 \pm 0.266E-02$
3.57-3.64	$0.847E-02 \pm 0.217E-02$
3.64-3.71	$0.155E-01 \pm 0.294E-02$
3.71-3.79	$0.789E-02 \pm 0.210E-02$
3.79-3.86	$0.573E-02 \pm 0.179E-02$
3.86-3.93	$0.546E-02 \pm 0.175E-02$
3.93-4.00	$0.492E-02 \pm 0.166E-02$
4.00-4.08	$0.514E-02 \pm 0.169E-02$
4.08-4.15	$0.453E-02 \pm 0.159E-02$
4.15-4.22	$0.196E-02 \pm 0.104E-02$
4.22-4.29	$0.306E-02 \pm 0.130E-02$
4.29-4.37	$0.231E-02 \pm 0.113E-02$
4.37-4.44	$0.474E-03 \pm 0.314E-03$
4.44-4.51	$0.202E-02 \pm 0.106E-02$
4.51-4.58	$0.153E-02 \pm 0.459E-03$
4.58-4.66	$0.718E-03 \pm 0.832E-03$
4.66-4.73	$0.151E-02 \pm 0.917E-03$
4.73-4.80	$0.718E-03 \pm 0.632E-03$
4.80-4.87	$0.367E-03 \pm 0.470E-03$
4.87-4.95	$0.000E+00 \pm 0.000E+00$
4.95-5.02	$0.557E-03 \pm 0.557E-03$
5.02-5.09	$0.000E+00 \pm 0.000E+00$
5.09-5.16	$0.000E+00 \pm 0.000E+00$
5.16-5.24	$0.000E+00 \pm 0.000E+00$
5.24-5.31	$0.000E+00 \pm 0.000E+00$
5.31-5.38	$0.557E-03 \pm 0.557E-03$
5.38-5.45	$0.557E-03 \pm 0.557E-03$

Table 5.16: KNO distribution at  $\sqrt{s} = 1.8$  TeV for  $|\eta| \leq 3.0$ .

$\sqrt{s}$ (GeV)	Fit interval (GeV/c)	$A(10^{-24} \text{ cm}^2 \text{ GeV}^2 c^3)$	$p_0$	$n$	$\chi^2$	NDOF
1800	0.4-10.0	$0.45 \pm 0.01$	$1.29 \pm 0.02$	$8.26 \pm 0.08$	102	64
	0.5-10.0	$0.45 \pm 0.01$	$1.29 \pm 0.02$	$8.26 \pm 0.07$	90	62
	0.5- 5.0	$0.47 \pm 0.01$	$1.25 \pm 0.01$	$8.12 \pm 0.05$	86	59
630	0.4-4.0	$0.27 \pm 0.01$	$1.63 \pm 0.13$	$10.2 \pm 0.56$	32	33
1800	0.4-10.0	$0.45 \pm 0.01$	1.30 fixed	$8.28 \pm 0.02$	103	65
630	0.4-4.0	$0.33 \pm 0.01$	1.30 fixed	$8.89 \pm 0.06$	39	34
546(UA1)	0.3-2.0	$0.46 \pm 0.01$	1.30 fixed	$9.14 \pm 0.02$	29	32

Table 5.17: Fit Parameters of equation 5.9. The data is for  $|Y| \leq 1.0$ . Quoted errors are purely statistical.

# Figures

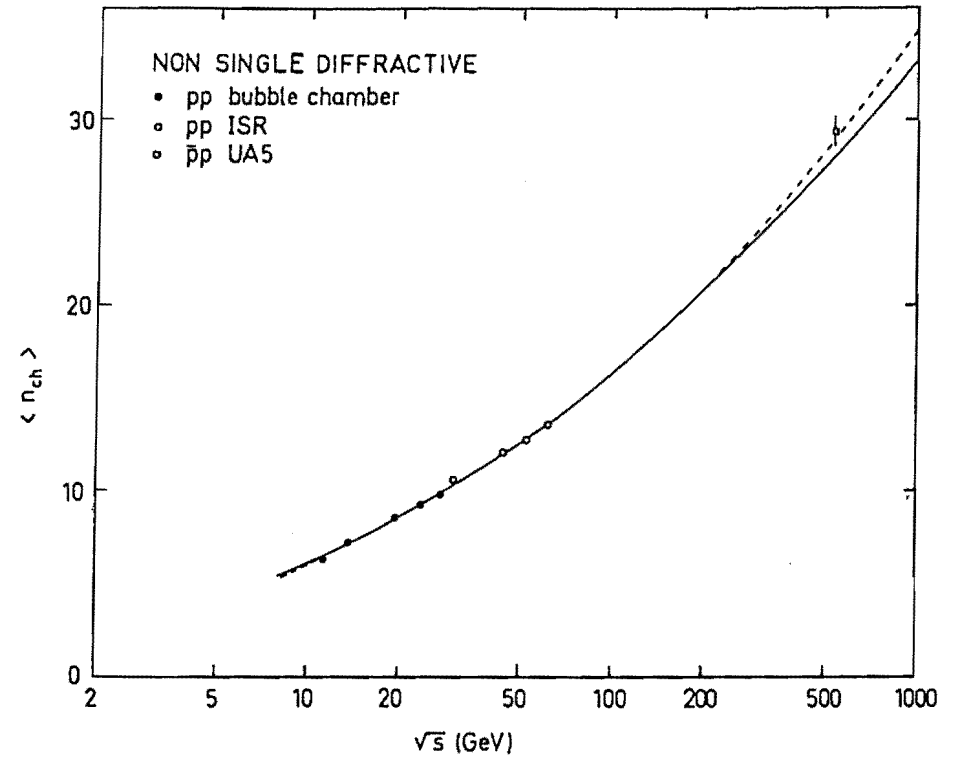


Figure 1.1: Average charged multiplicity vs Colliding energy. The average charged multiplicity (total  $\eta$  range) are for the non-single diffractive events. The solid curve is  $1.97 + 0.12 \times \ln(s) + 0.148 \times \ln^2(s)$  and the dashed curve is  $-7.5 + 7.6 \times s^{0.124}$ .

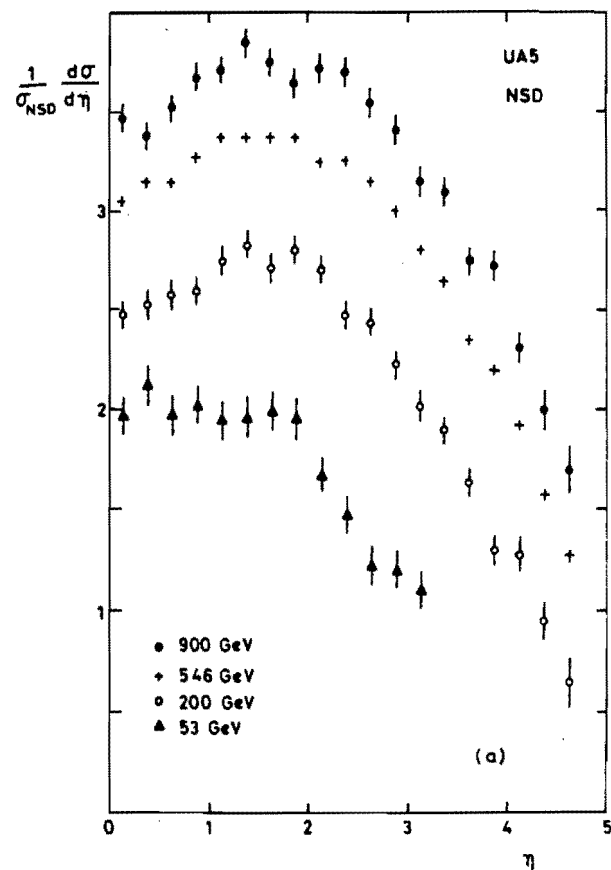


Figure 1.2: Charge multiplicity per pseudo-rapidity vs pseudo-rapidity. The non-single diffractive pseudorapidity distribution is plotted for  $\sqrt{s} = 53, 200, 546$  and  $900$  GeV. Peaks are seen around  $|\eta| 1.5-2.0$  for  $\sqrt{s} \geq 200$  GeV. The width of the distribution increases as the energy increases.

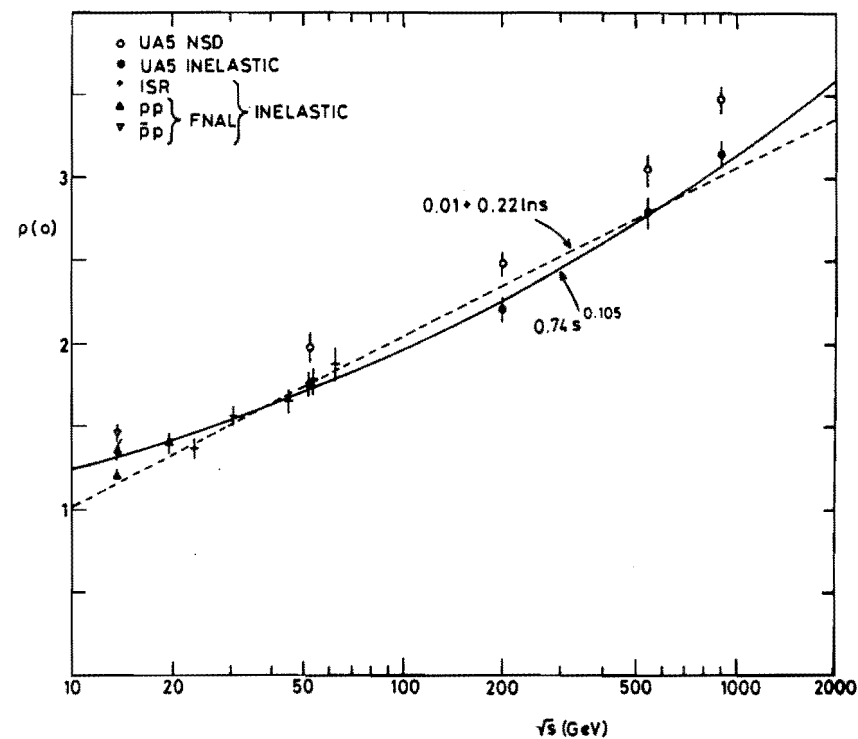


Figure 1.3:  $dN/d\eta$  at  $\eta = 0$  vs Colliding energy. It increases as  $\ln(s)$  or  $s^a$ . The curves are for the inelastic data. The extrapolation to  $1.8$  TeV would be around  $4.0$  for the non-single diffractive events.

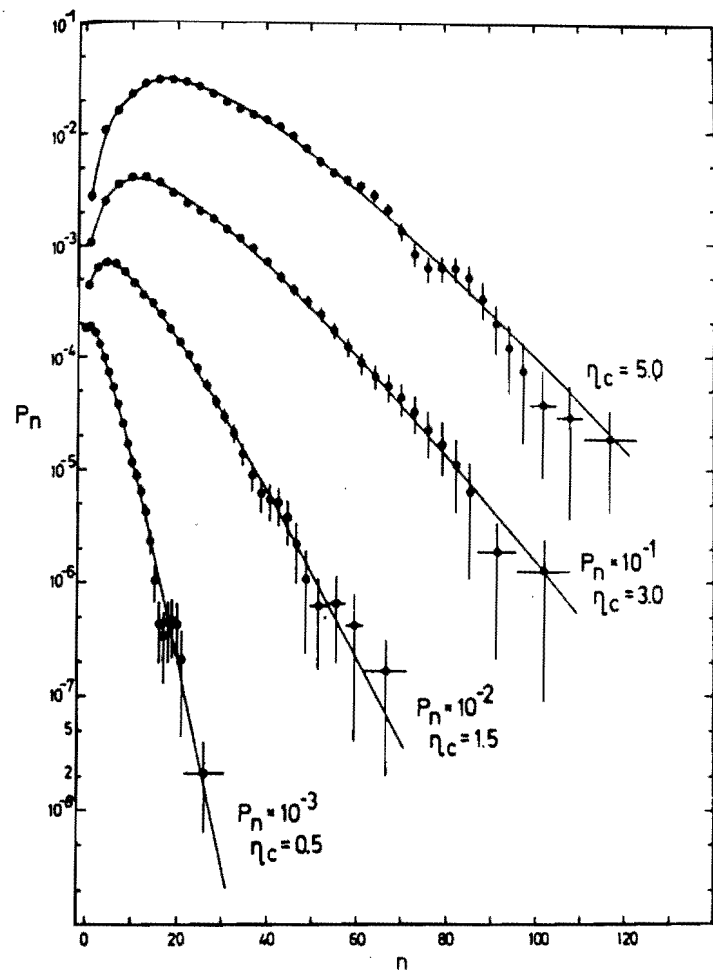


Figure 1.4: Multiplicity distributions and Negative Binomial fits. The charged distributions for the different  $|\eta|$  ranges ( $\leq 0.5$ ,  $\leq 1.5$ ,  $\leq 3.0$  and  $\leq 5.0$ ) at  $\sqrt{s} = 540$  GeV are plotted. The curves, which agree with the data well, are the fit to the negative binomial distribution.

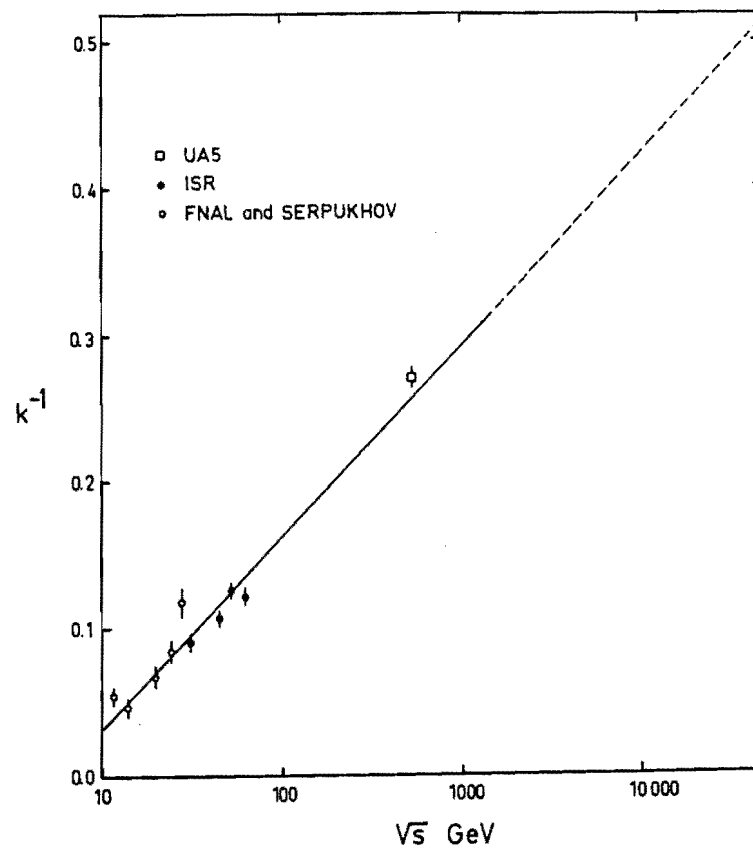


Figure 1.5: Energy dependence of fit parameter  $k$ .  $k^{-1}$  is plotted against the energy and scales almost linearly to  $\ln(s)$ . The line is  $k^{-1} = -0.098 + 0.0282 \times \ln(s)$ .

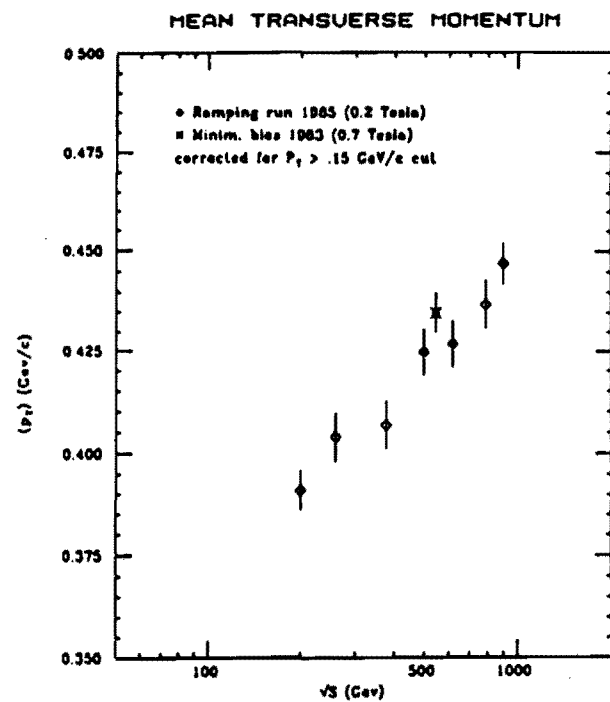
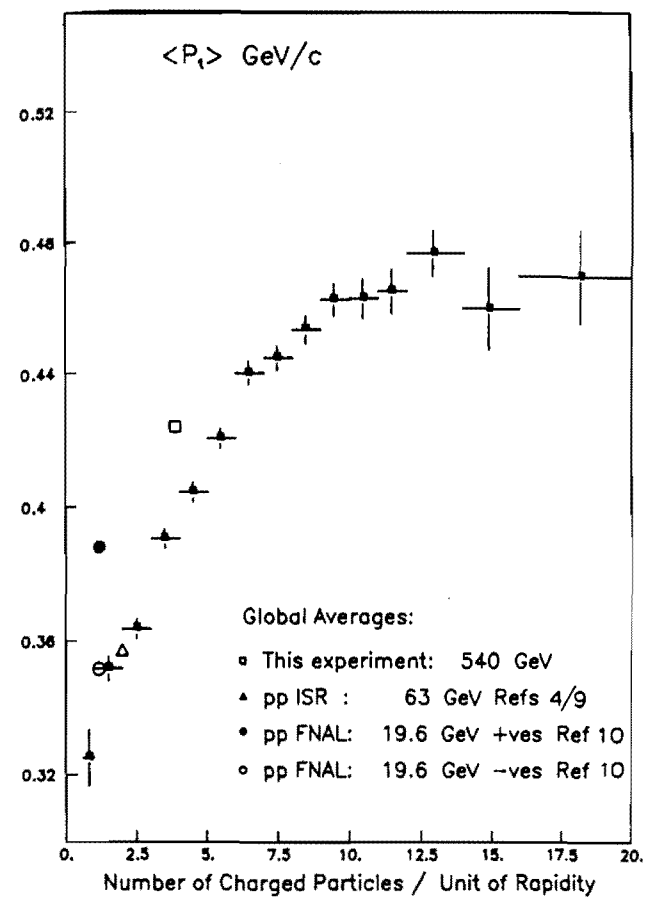


Figure 1.6: Average transverse momentum vs colliding energy.

Figure 1.7: Average transverse momentum vs charge density.  $\langle p_t \rangle$  increases rapidly up to  $dN/dY \sim 7$  and becomes flat for the larger charge density.

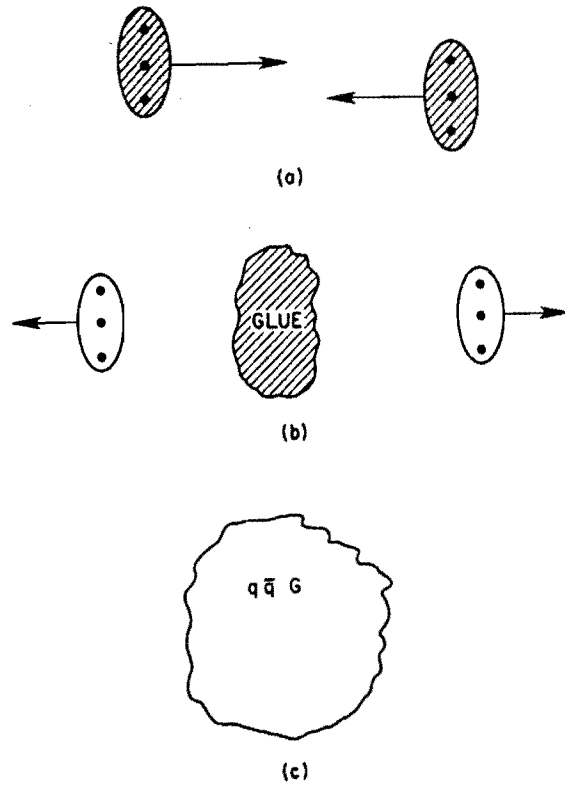


Figure 1.8: Formation of the statistical system. Two Lorentz contracted hadrons are shown in (a). The shading represents the preexisting glue and the dots represent the valence quarks. In (b) the valence quarks fly away and the glue is left. (c) suggests the excited statistical equilibrium which may be called a QCD plasma.

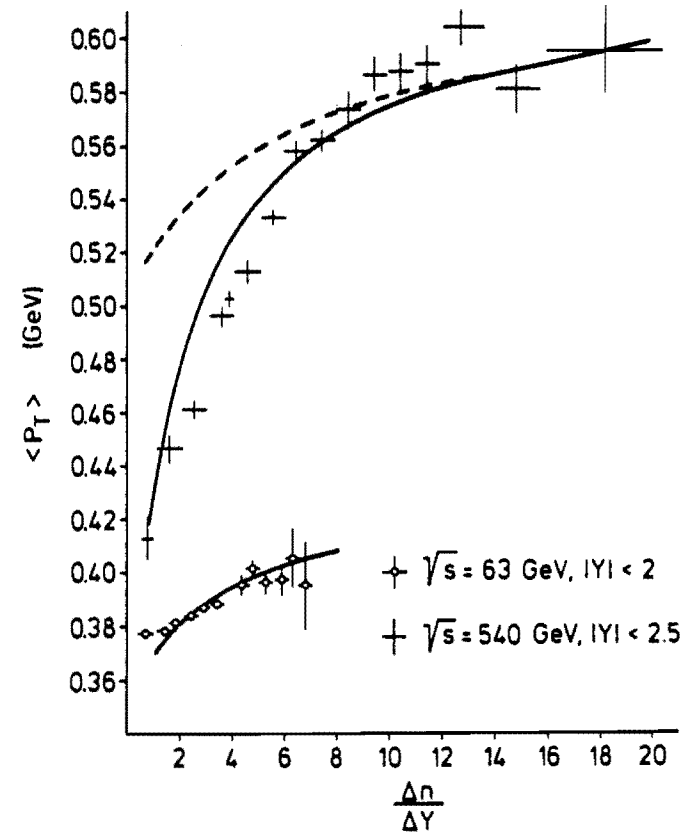


Figure 1.9: SHM fit and experimental data for  $\langle p_t \rangle$ . The solid lines are the theoretical functions with a single fit parameter for two energies. The dotted line is the theoretical curve but for the case that the KNO scaling is assumed.

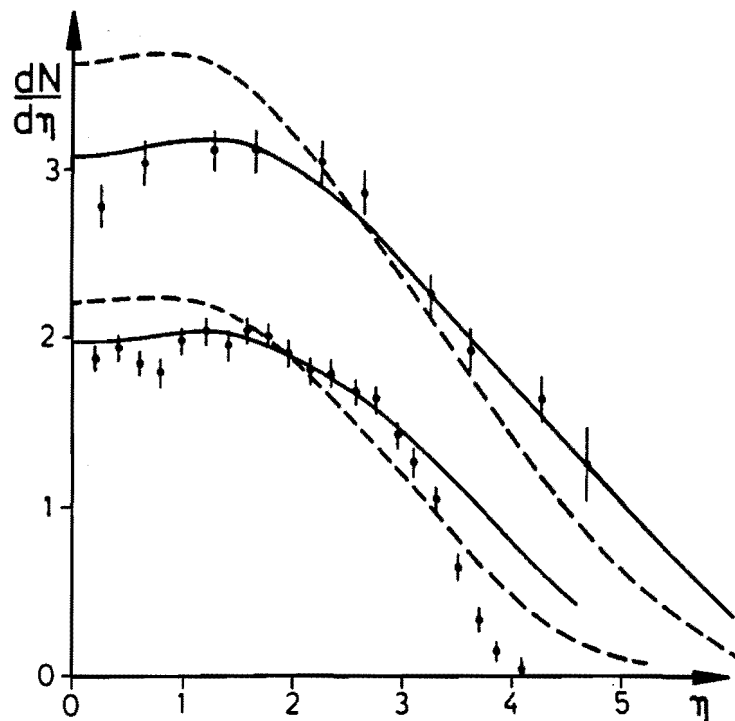


Figure 1.10: SHM prediction and experimental data for  $dN/d\eta$ . The solid lines are the SHM theoretical curves with a sound velocity of  $c/\sqrt{3}$ , while the dashed curves are for  $c/\sqrt{4}$ . The experimental data indicates the sound velocity is  $c/\sqrt{3}$  which is the case of the ideal relativistic QCD plasma.

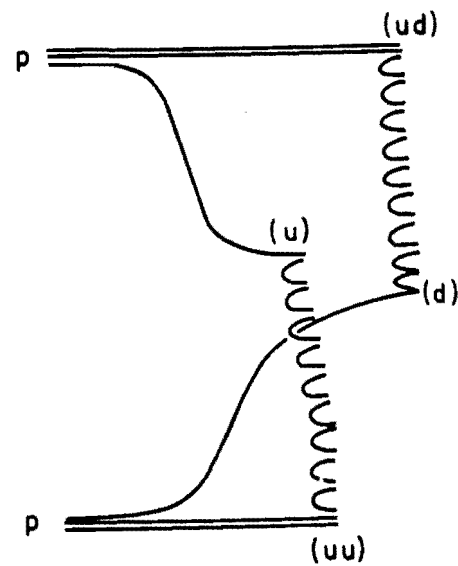


Figure 1.11: Dual Parton Model Diagram with two chains. Two incident protons are shown. One of the valence quarks is separated ("knock") in each proton. Two chains (corresponding to a single Pomeron exchange) are then formed. The fragmentation of each chain is independent.



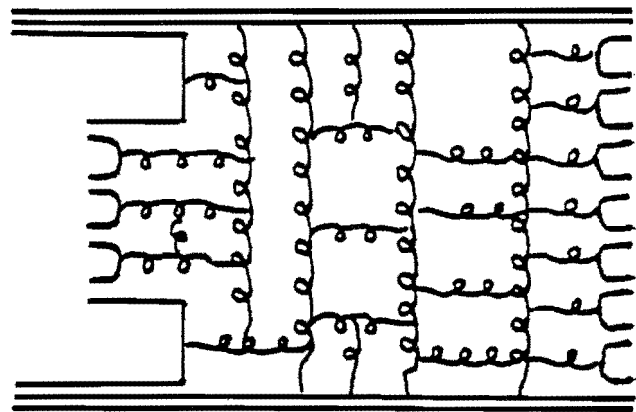
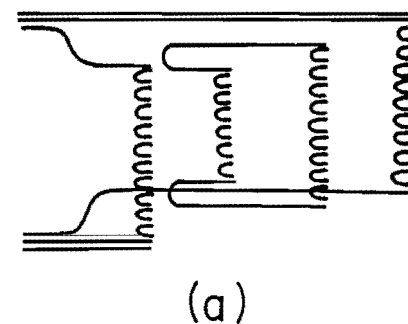
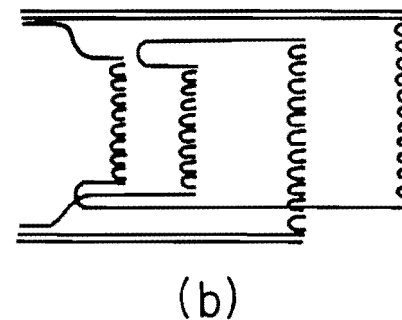


Figure 1.12: QCD representation of two DPM chains. This corresponds to many of strongly interacting gluons and quarks. Unlike the QED photon field, the gluon field is the non-abelian gauge field which directly interacts each other.



(a)



(b)

Figure 1.13: DPM Diagram with sea quark contributions. Any number of pairs of chains is possible. The contribution from such multiple chains (sea quark contribution) becomes significant for the energy larger than the ISR energy and is calculated according to the eikonal theory.

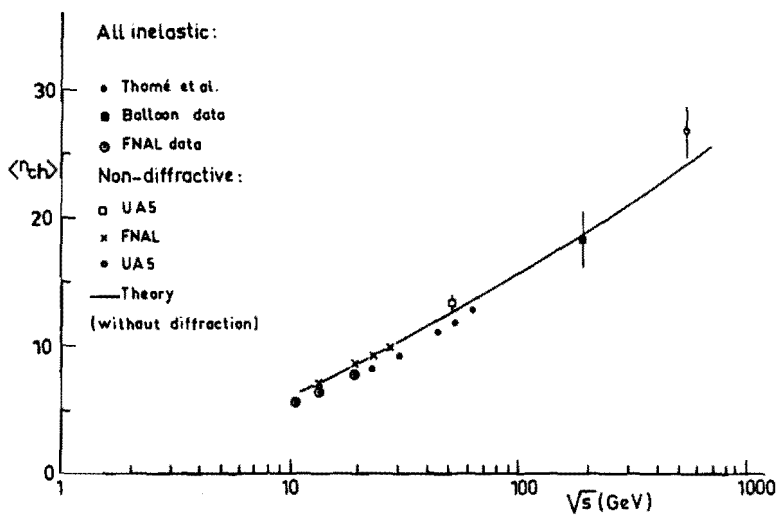


Figure 1.14:  $\langle n_{ch} \rangle$  with DPM and experimental data. The curve is the results from the DPM calculation for the non-diffractive case.

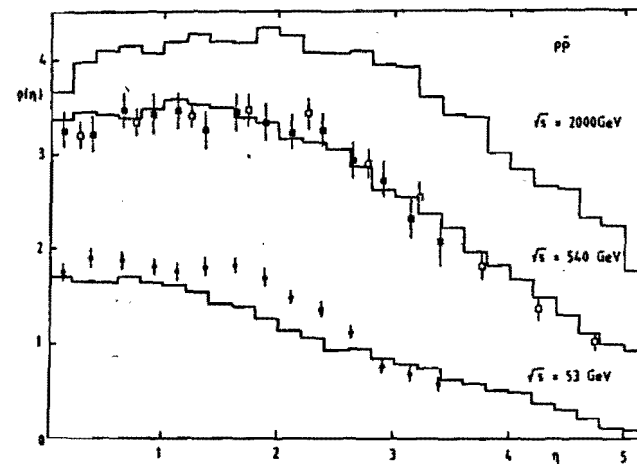


Figure 1.15:  $dN/d\eta$  from DPM and experiments. The lines (histograms) are the DPM calculations for  $\sqrt{s} = 53, 540$  and  $2000$  GeV. The agreement is good at  $\sqrt{s} = 540$  GeV.

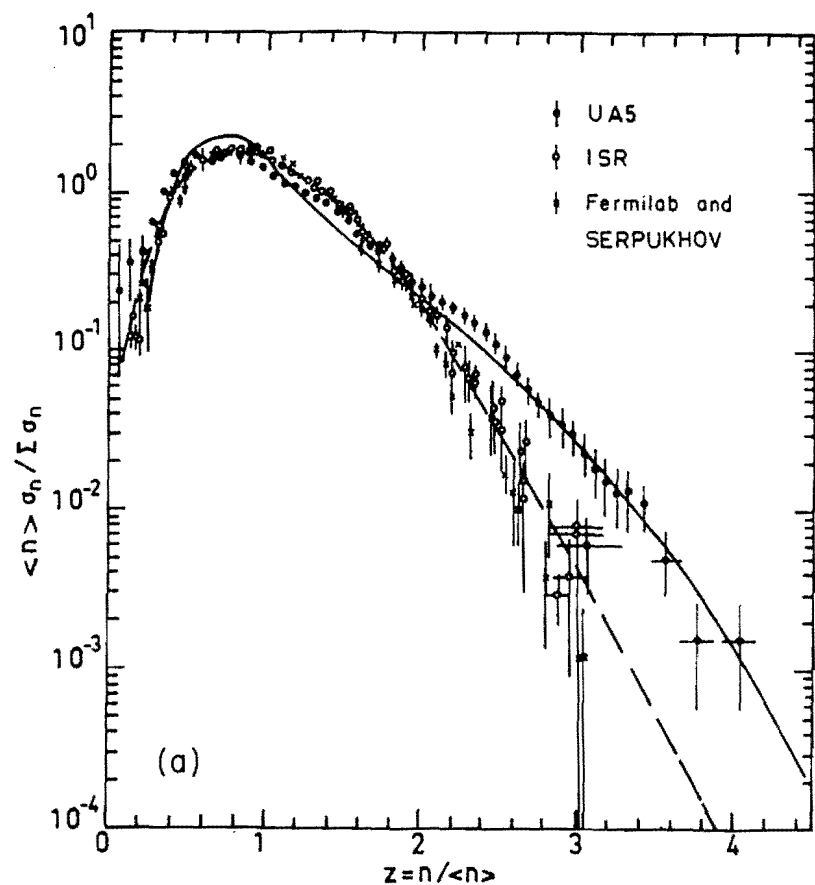


Figure 1.16: KNO distribution from DPM and experiments. The KNO  $\psi$  plots are shown for the ISR and SPS energy. The difference in the shape (at the larger multiplicity) shows the violation of the KNO scaling. The curves are the theoretical curves for these energies. The agreement between DPM and the experimental data is seen.

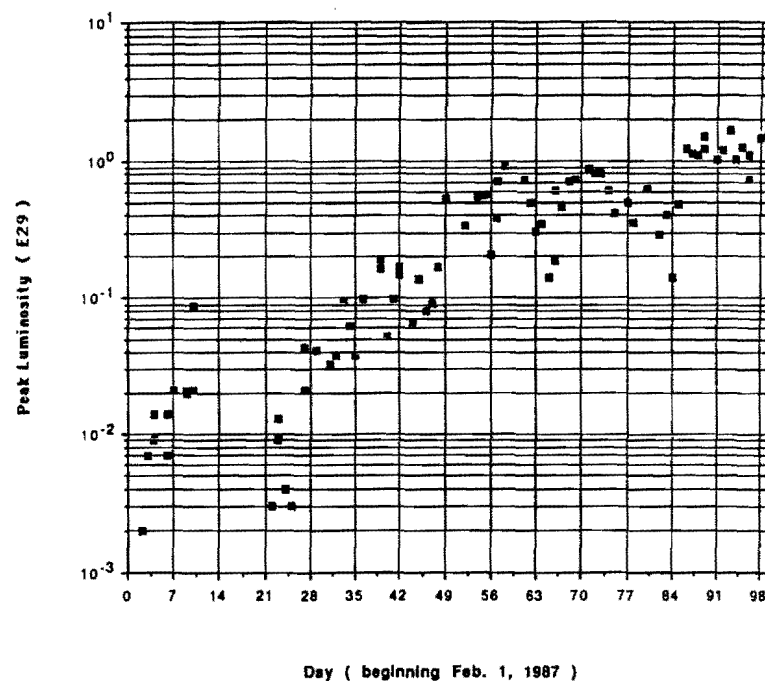


Figure 2.1: The Tevatron peak luminosity in unit of  $10^{29} \text{ cm}^{-2} \text{ sec}^{-1}$  is shown from February 1, 1987 to May 11, 1987. Each point represents a separate  $\bar{p}p$  store.

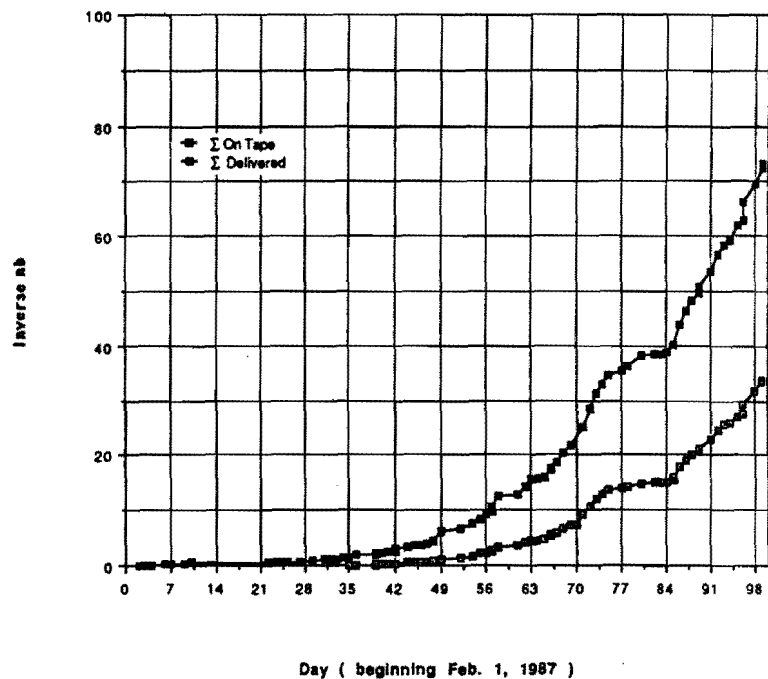


Figure 2.2: The integrated luminosity in unit of  $\text{nb}^{-1}$  is shown as a function of day. Solid squares represent the delivered luminosity and open squares represent the luminosity we took data with. The total integrated luminosity logged on tape was about  $34 \text{ nb}^{-1}$ .

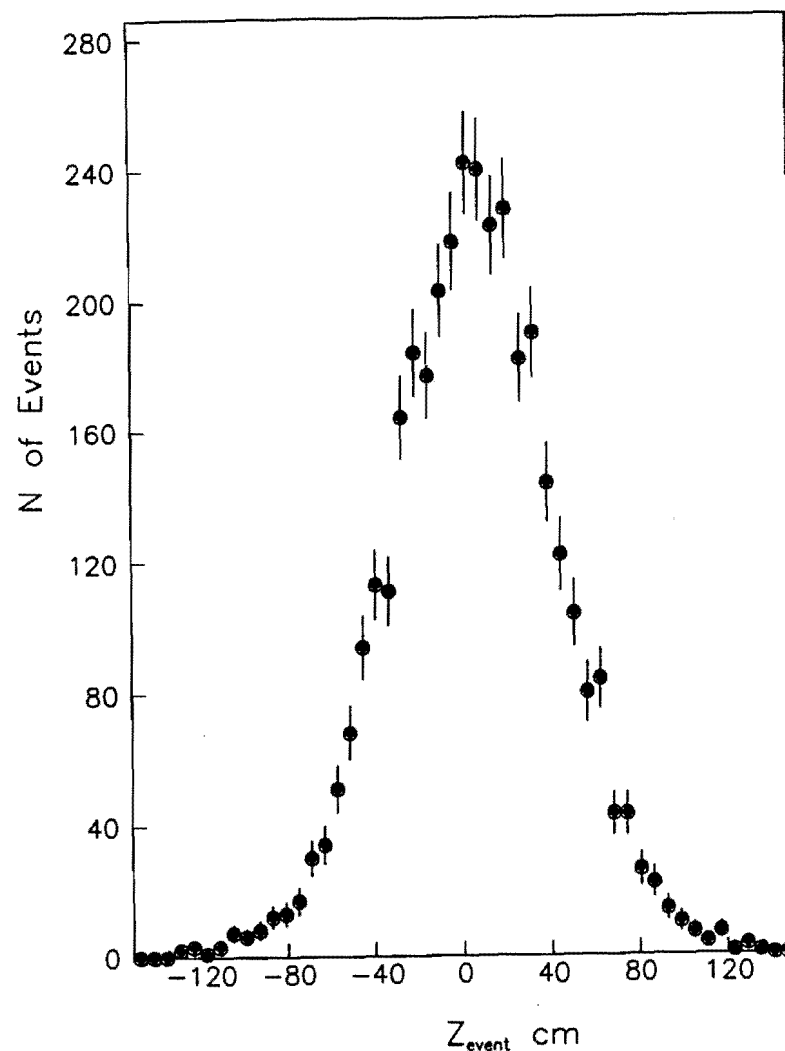


Figure 2.3: The distribution of the collision points. The collision point was smeared along the beam direction due to the finite length of the Tevatron beam. The collision point was determined by the VTPC on an event-by-event basis. This particular store has a smearing of 35 cm in rms.

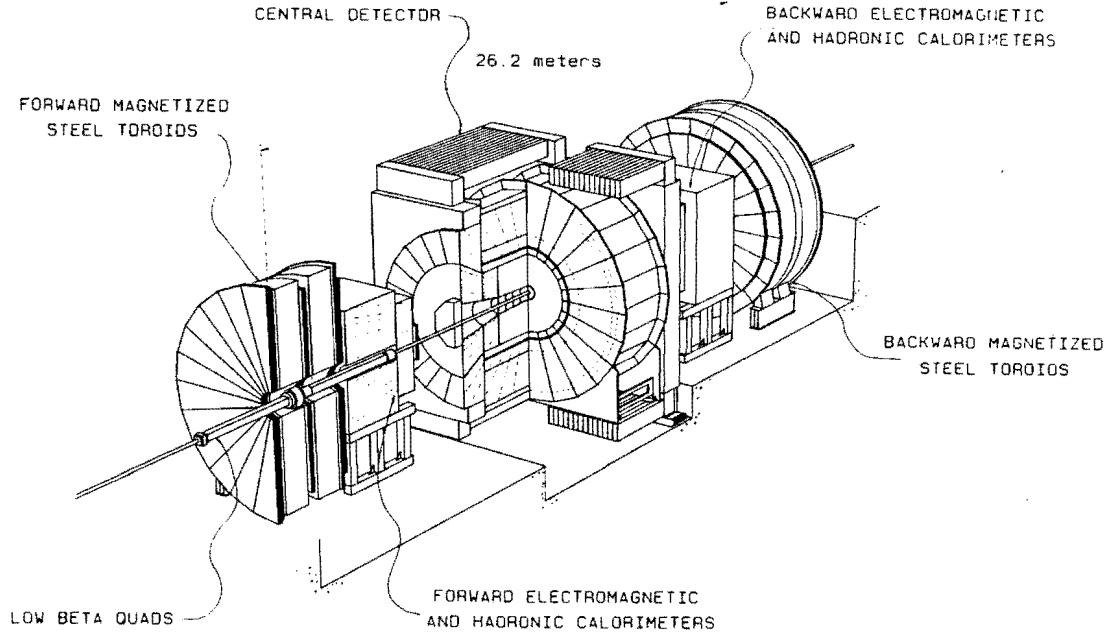


Figure 2.4: Isometric view of the Collider Detector at Fermilab (CDF). The forward/backward detector covers  $2^\circ \leq \theta \leq 10^\circ$  and  $170^\circ \leq \theta \leq 178^\circ$ . The central detector covers  $10^\circ \leq \theta \leq 170^\circ$ .

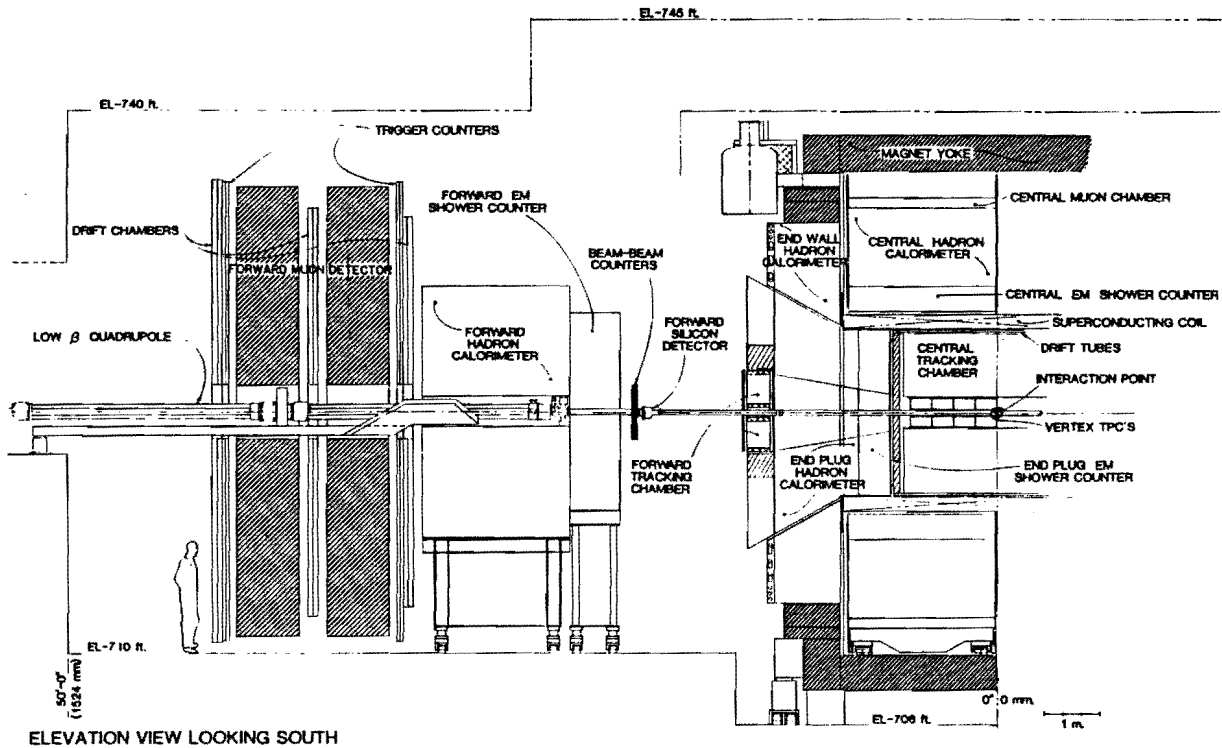


Figure 2.5: A vertical cut through one half of CDF. The forward detector is shown on the left side and a half of the central detector is shown in the right side. The nominal  $\bar{p}p$  collision point is indicated by  $\odot$ .

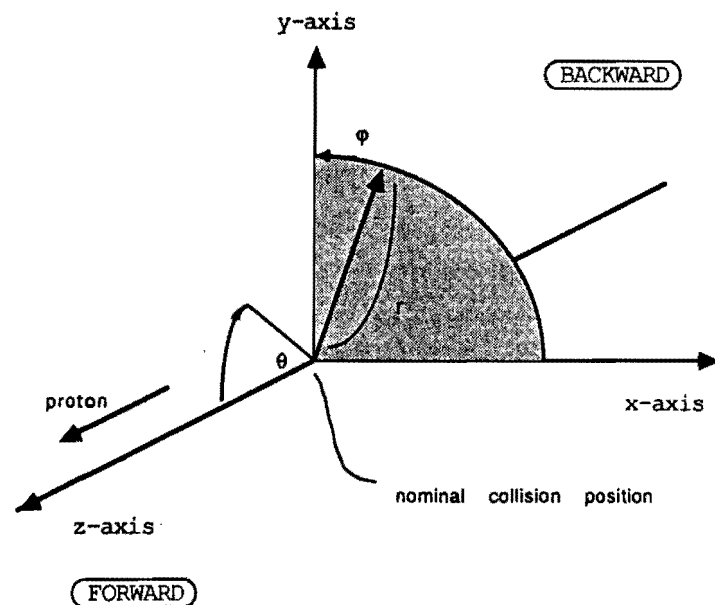


Figure 2.6: The CDF coordinate system. The  $z$  axis is along to the proton direction. The  $xy$  plane is perpendicular to the  $z$  axis, together forming a right-handed coordinate. The nominal collision point is at  $x = y = z = 0$ .  $\theta$  is the polar angle with respect to the  $z$  axis and  $\phi$  is the azimuthal angle around the  $z$  axis.

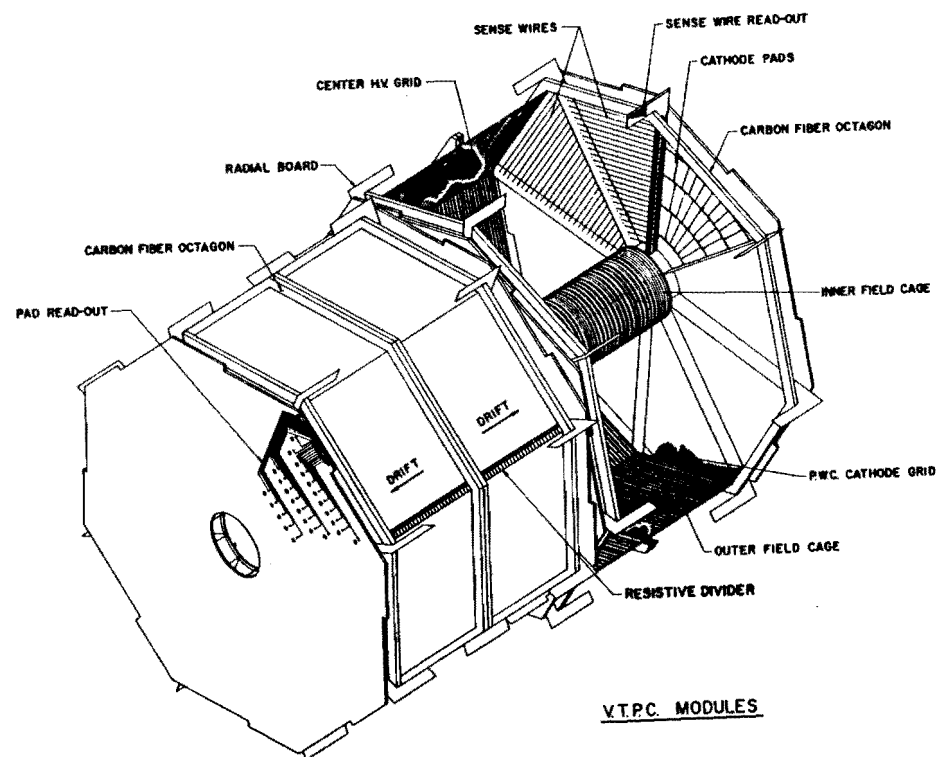


Figure 2.7: Two VTPC modules. Eight modules are mounted along the beam direction surrounding the beam pipe. Each module has two 15.25 cm long drift spaces and is divided into octants in  $\phi$ . One module is rotated to another by about ten degrees in  $\phi$  to prevent a charged particle totally missed due to the dead spaces near the octant boundaries.

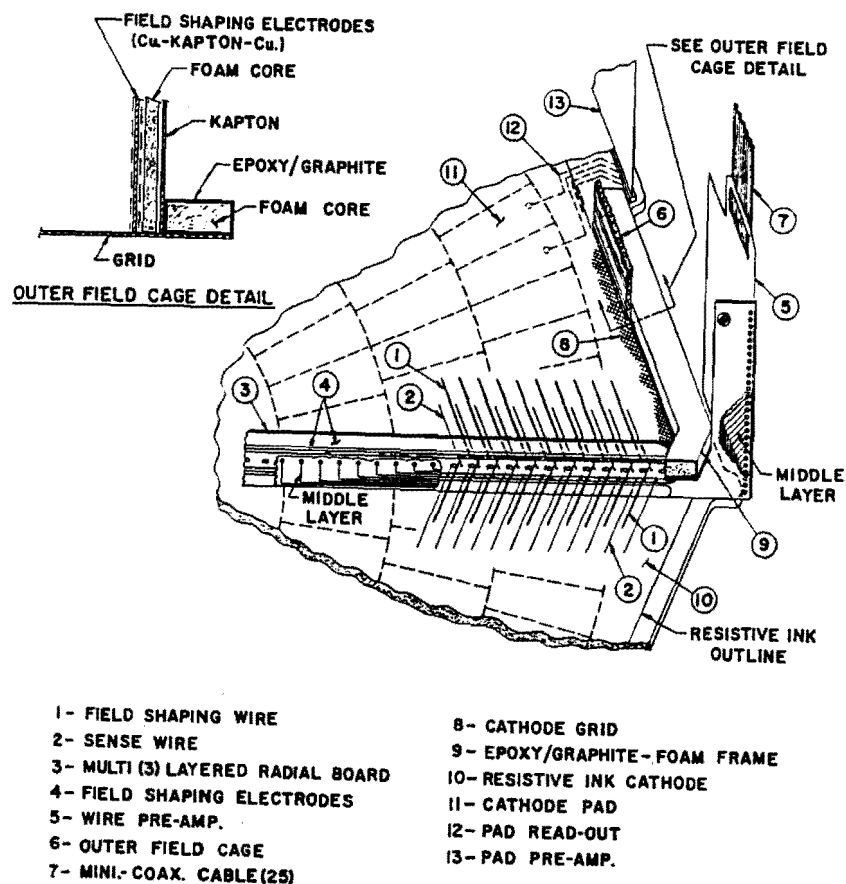


Figure 2.8: The construction detail of the endcap proportional chamber.

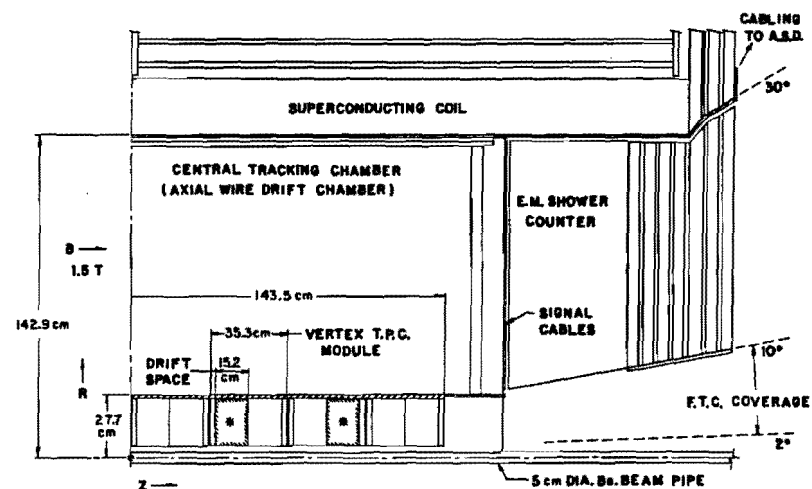


Figure 2.9: Flash ADC installation. The quarter of the CDF central detector is shown. The drift spaces marked with '\*' were instrumented for the pad and  $dE/dx$  readout with FADCs.

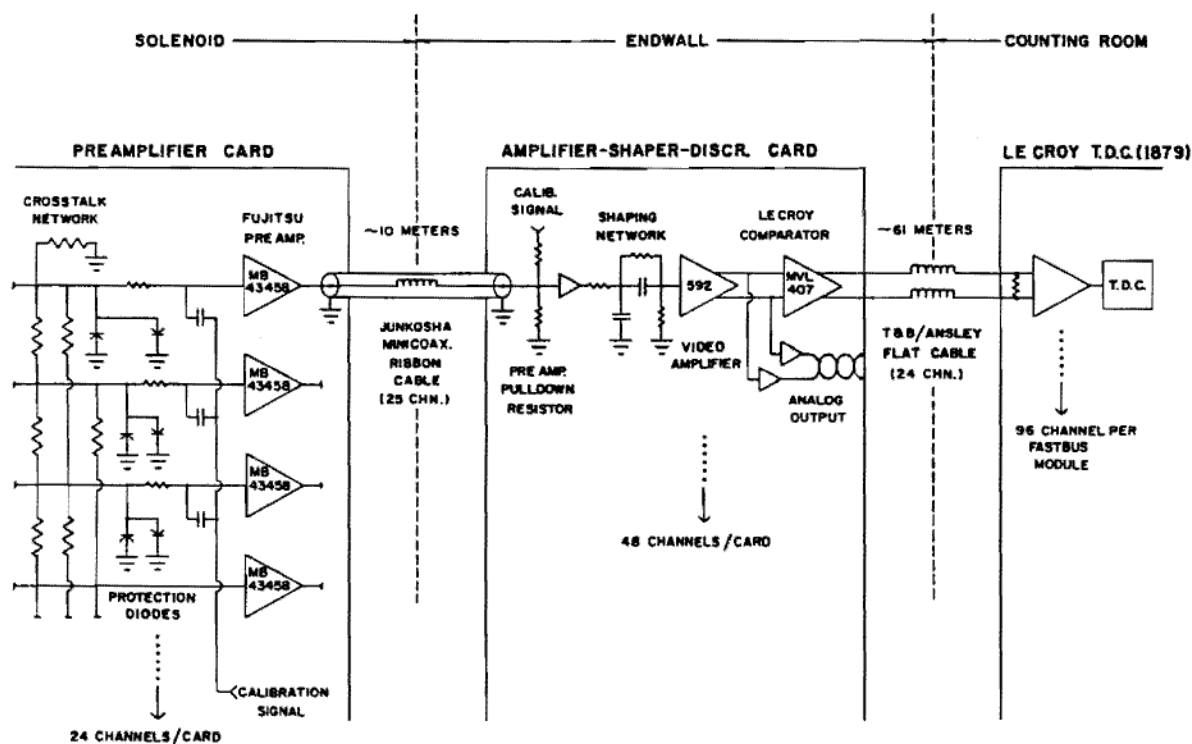


Figure 2.10: Simplified schematic of the wire electronics.

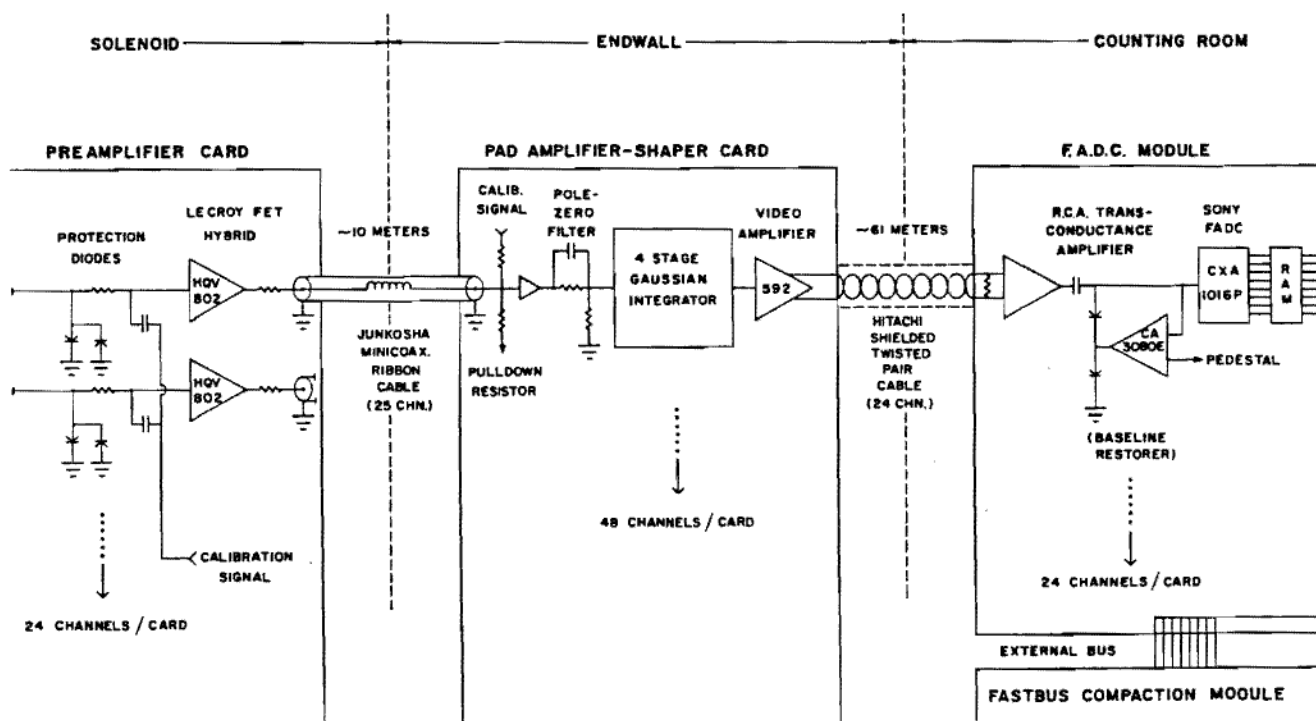


Figure 2.11: Simplified schematic of the pad electronics.



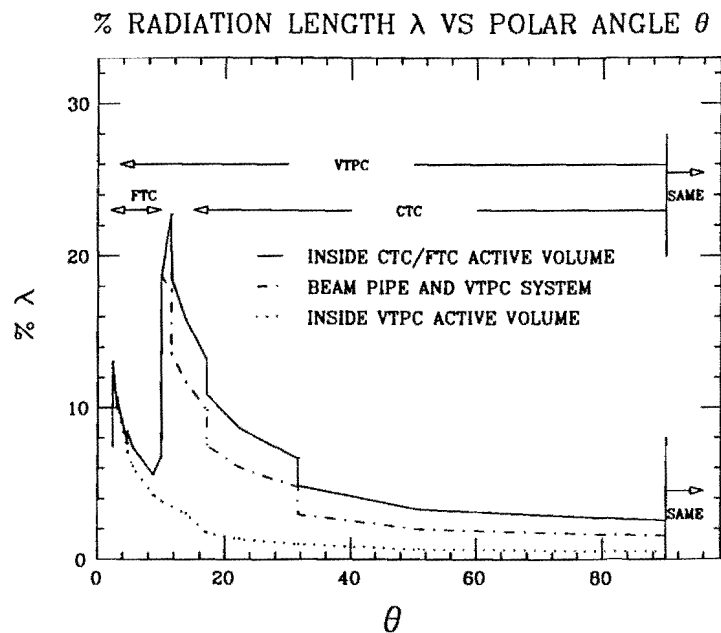


Figure 2.12: Material traversed (in % of radiation length) in the tracking system versus polar angle. The dotted line indicates material before entering the active VTPC volume. The dot-dashed line indicates the total amount crossed by a particle as it exits the VTPC system. The solid line indicates the average total material traversed before entering the active volume of the CTC and FTC.

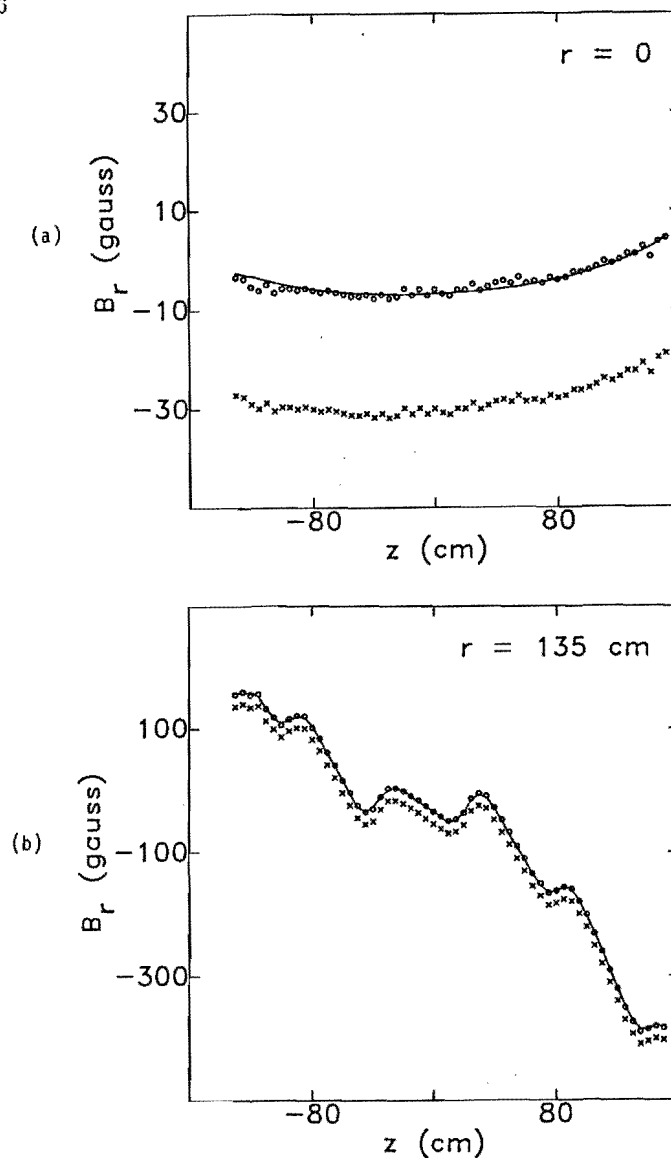


Figure 2.13: (a)  $z$ -dependence of the radial component of the magnetic field at  $r = 0$  cm, and (b)  $z$ -dependence of the radial component of the magnetic field at  $r = 135$  cm. The crosses are raw data and the open circles are after the alignment correction to the NMR probe. The curves are fittings based on the Maxwell equations.

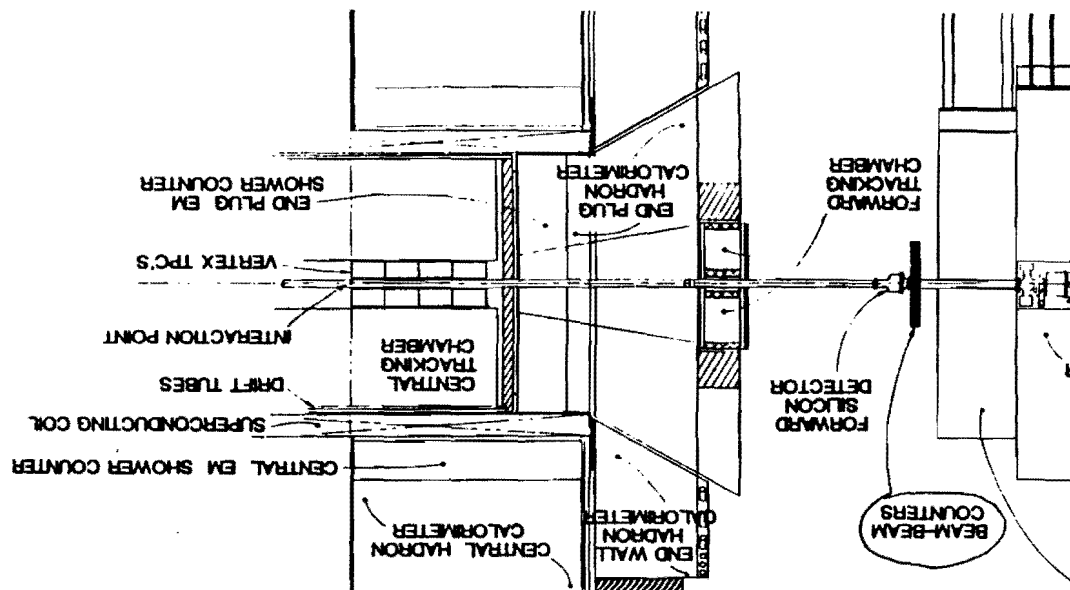


Figure 2.14: Location of the Beam-Beam Counters (the forward counters are shown). They were located at the forward position on the face of the forward calorimeter. The distance from the nominal collision point was 581 cm.

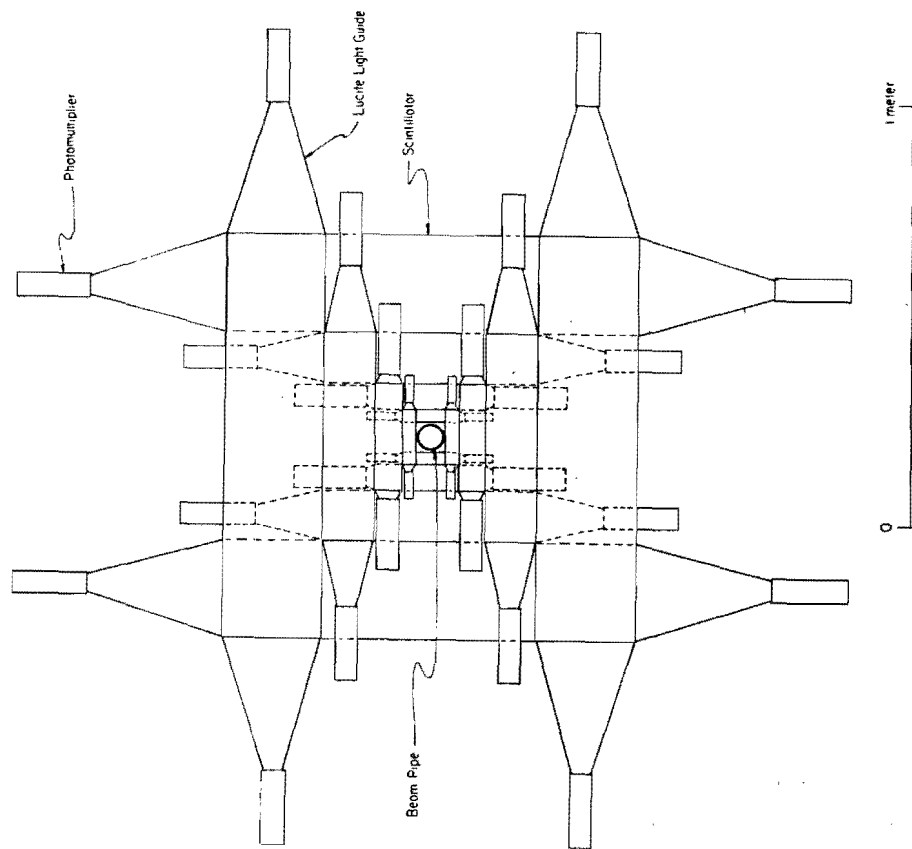


Figure 2.15: Arrangement of the BBC scintillation counters (the beam pipe is perpendicular to the counters). It consisted of 16 counters in each side. Both ends of each counter was attached to photomultiplier tubes to give a mean time.

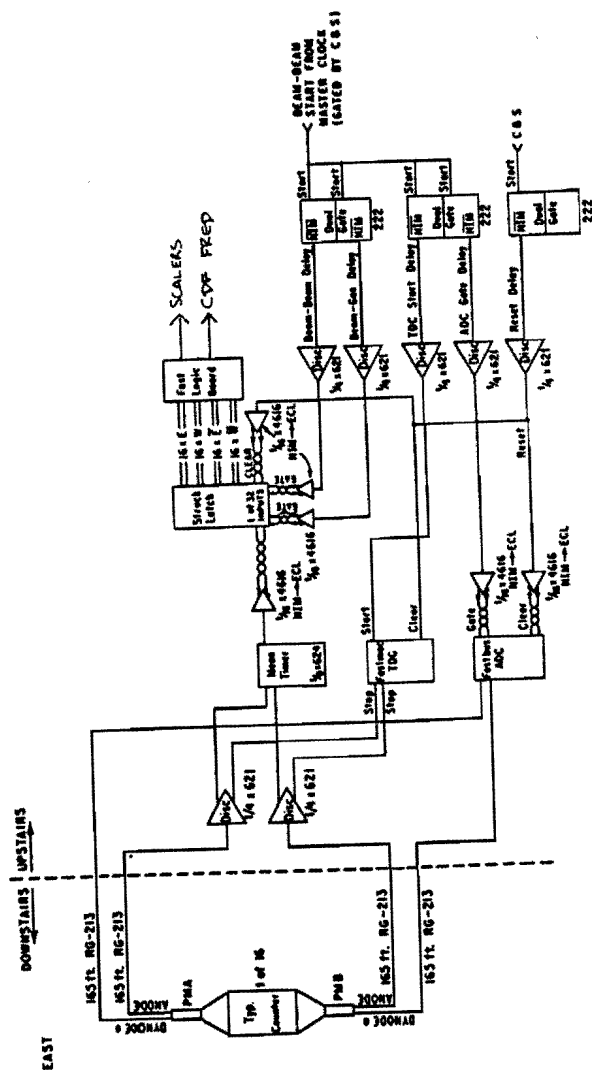


Figure 2.16: Block diagram of the BBC electronics.

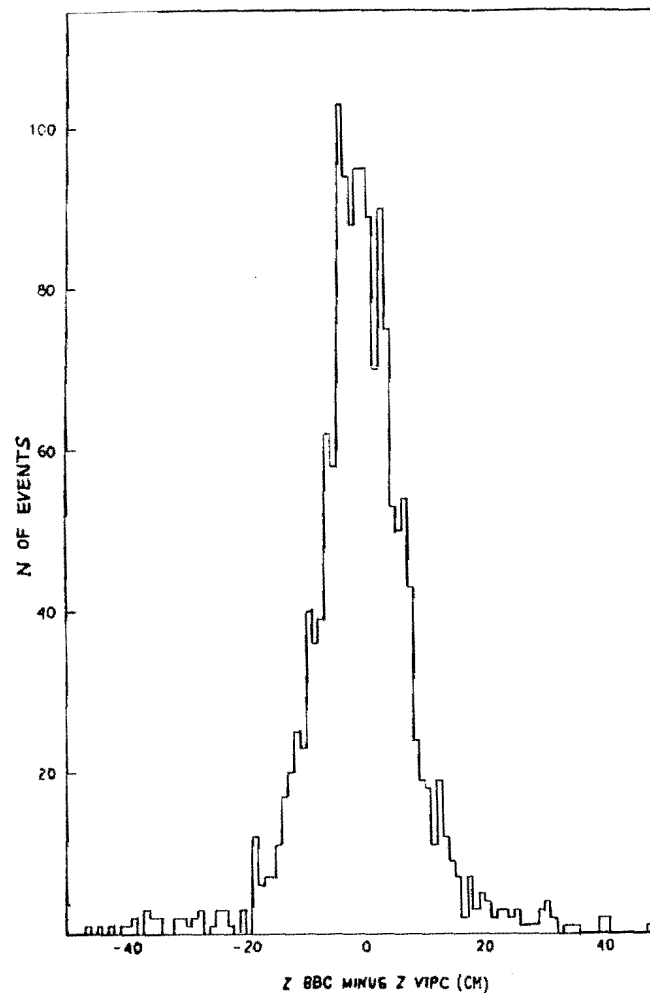


Figure 2.17: BBC  $z$  vertex - VTPC  $z$  vertex. The FWHM of the distribution is about 9 cm corresponding to a timing resolution of 300 psec in FWHM. The VTPC vertex resolution was better than 3 mm.

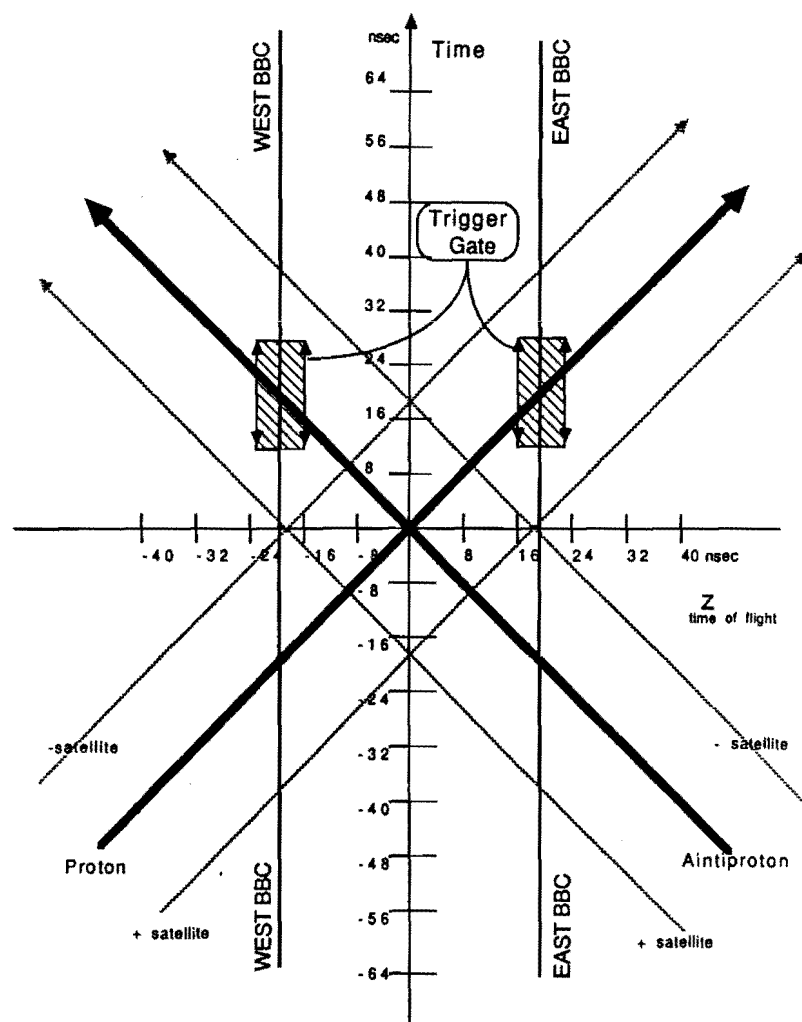


Figure 2.18: Timing diagram for the BBC trigger. The horizontal axis is the  $z$ -position in unit flight time (nsec) and the vertical axis is time in nsec. Two vertical lines at  $z = \pm 19.4$  nsec correspond to the BBC positions in the forward and backward direction. The diagonal bold lines correspond to proton and antiproton bunches. The four diagonal broken lines represent "satellites" in the proton or antiproton bunches. The hatched areas indicate a beam-beam gate with which we triggered  $pp$  collisions.

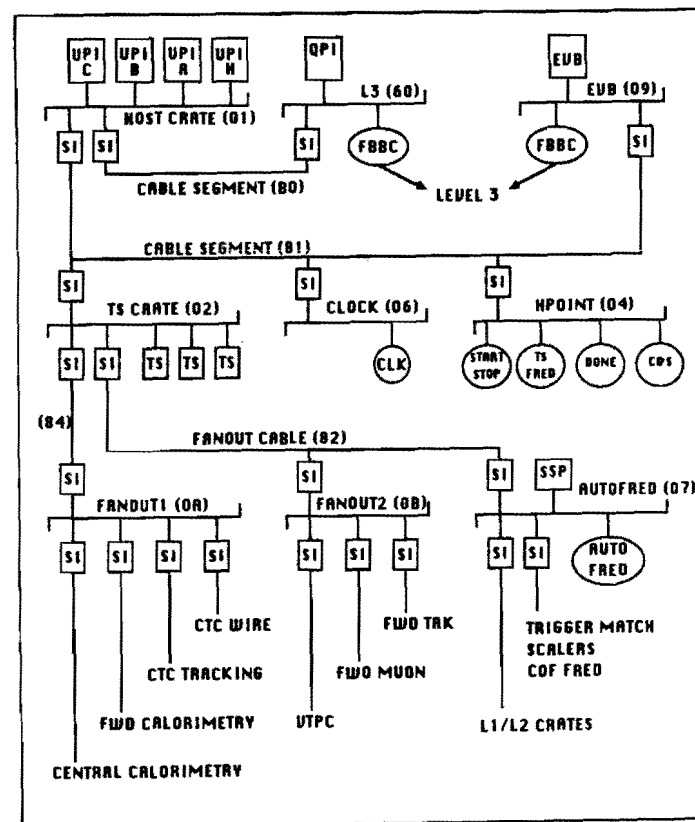


Figure 2.19: CDF data acquisition system.

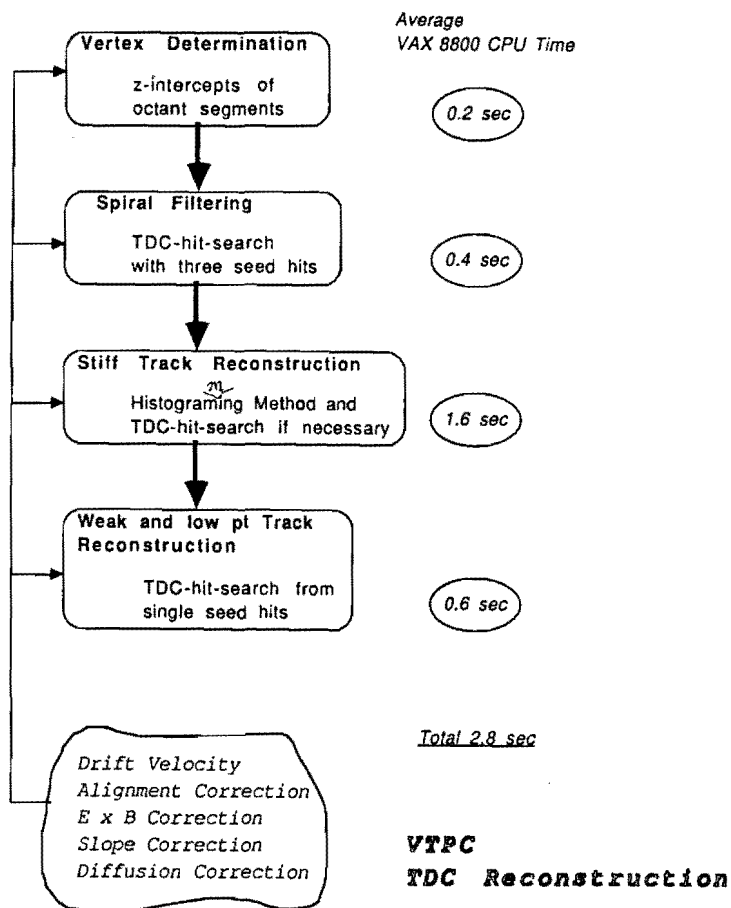


Figure 3.1: Steps of TDC data reconstruction.

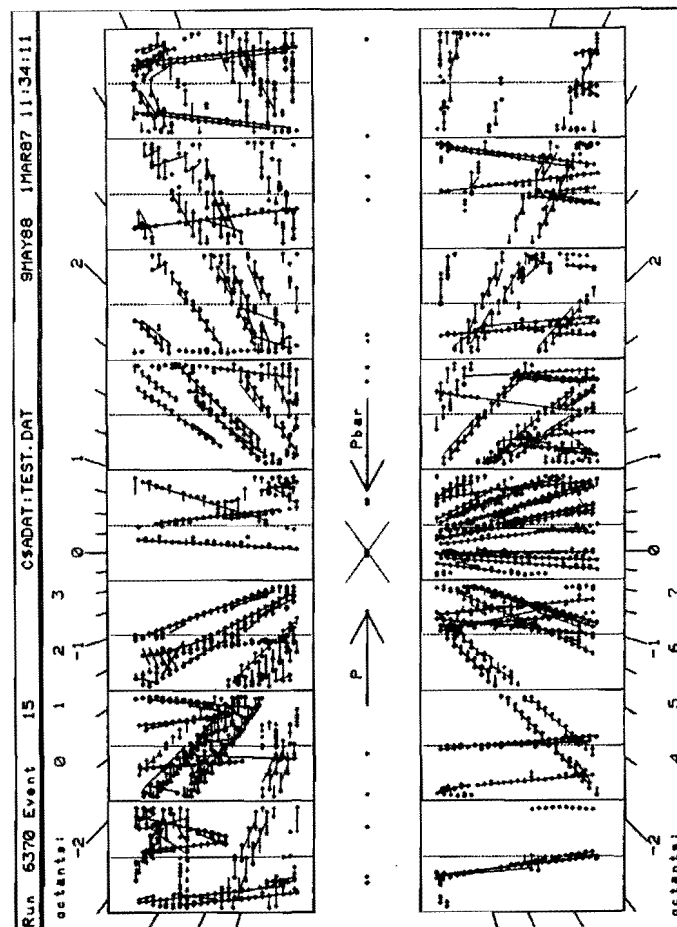


Figure 3.2: VTPC octant segments for vertex determination (rz view). The z axis or beam axis runs horizontally in the middle of the figure. The vertical axis is the position of the sense wires in each octant. The solid lines represent the VTPC module boundary. The dotted lines represent the high voltage screens. Four octants are shown in the upper half and other four octants in the lower half. Please note that the overall horizontal length and vertical length correspond to 2.8 m and 42 cm, respectively, in the real world. See next figure.

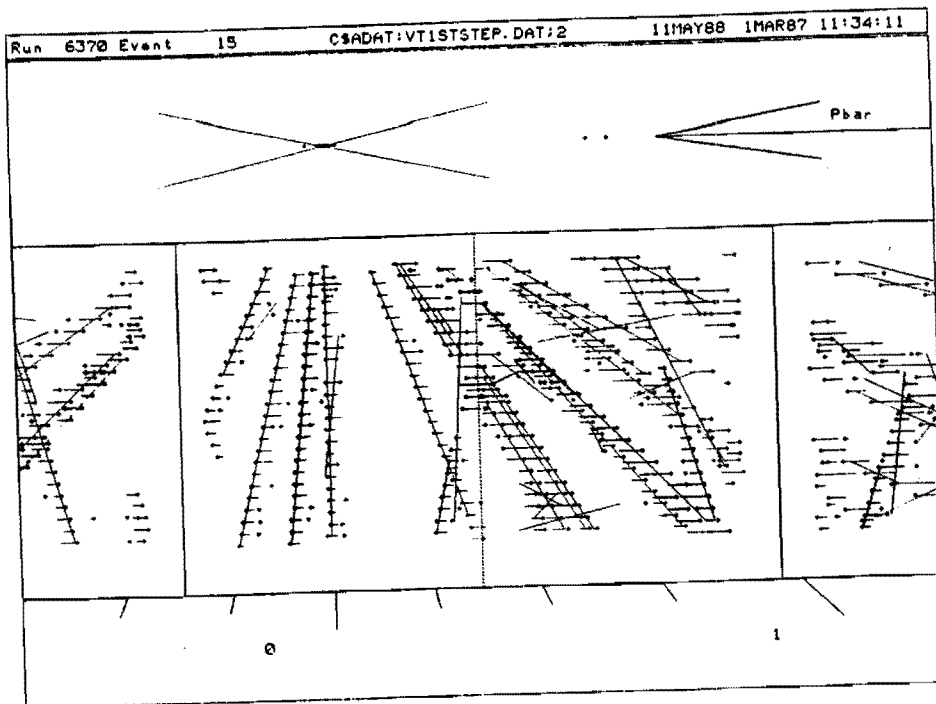


Figure 3.3: VTPC octant segment for vertex determination. This is a magnified portion of the previous figure and its aspect ratio is close to that in the real world. Each dot is the translated position of each TDC leading edge, followed a very short horizontal line indicating the pulse width obtained by the trailing-edge time minus the leading-edge time. The lines connecting the dots are the octant segments, whose  $z$  intercepts are plotted as dots on the beam axis. The vertex position (a large cross) is determined by finding a cluster of the  $z$  intercepts.

155

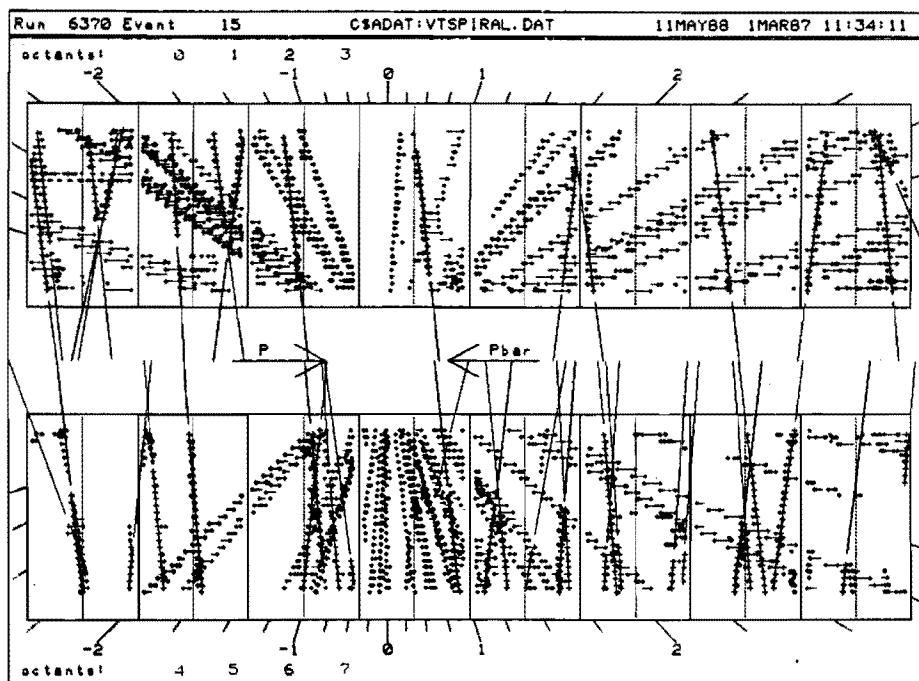


Figure 3.4: Reconstructed spiral tracks. The coordinate system is the same as figure 3.2 — the  $rz$  view of the VTPC. The TDC-leading-edge hits associated with spirals are indicated by +'. The lines are reconstructed spirals. The TDC hits associated with the spiral tracks were flagged and not used in the following steps of the reconstruction.

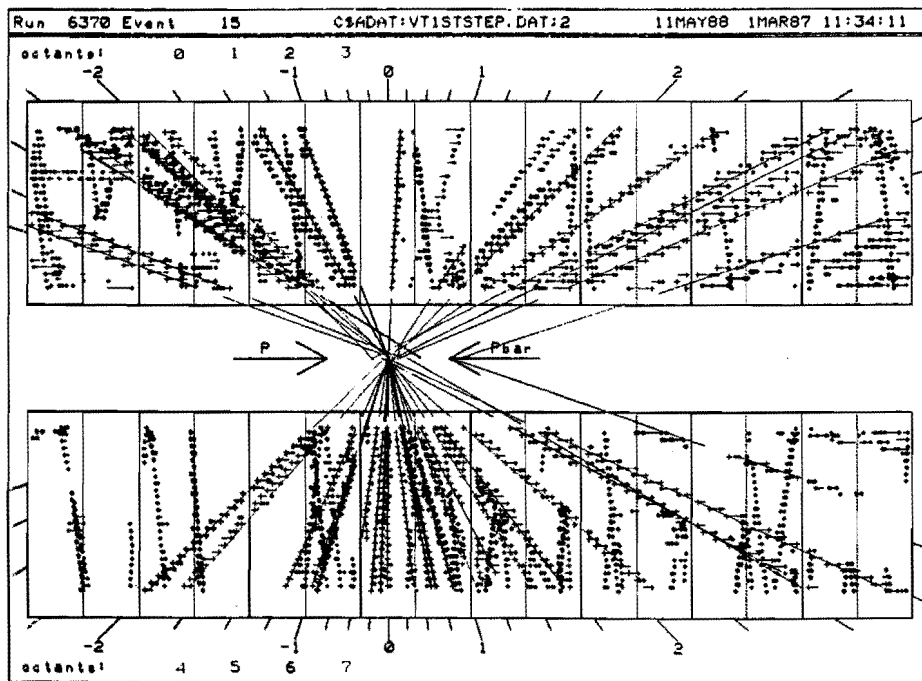


Figure 3.6: VTPC tracks reconstructed in the third step. The individual  $\phi$  slices can be seen in the next figure.

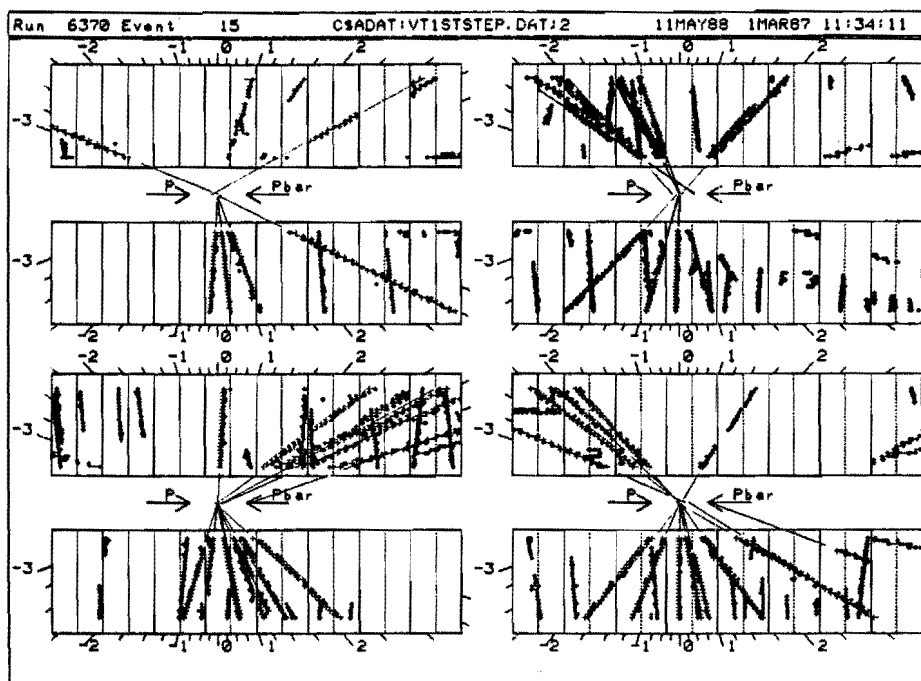


Figure 3.7: VTPC tracks reconstructed in the third step. The same event as the previous one is shown with each  $\phi$  slice separately.

159

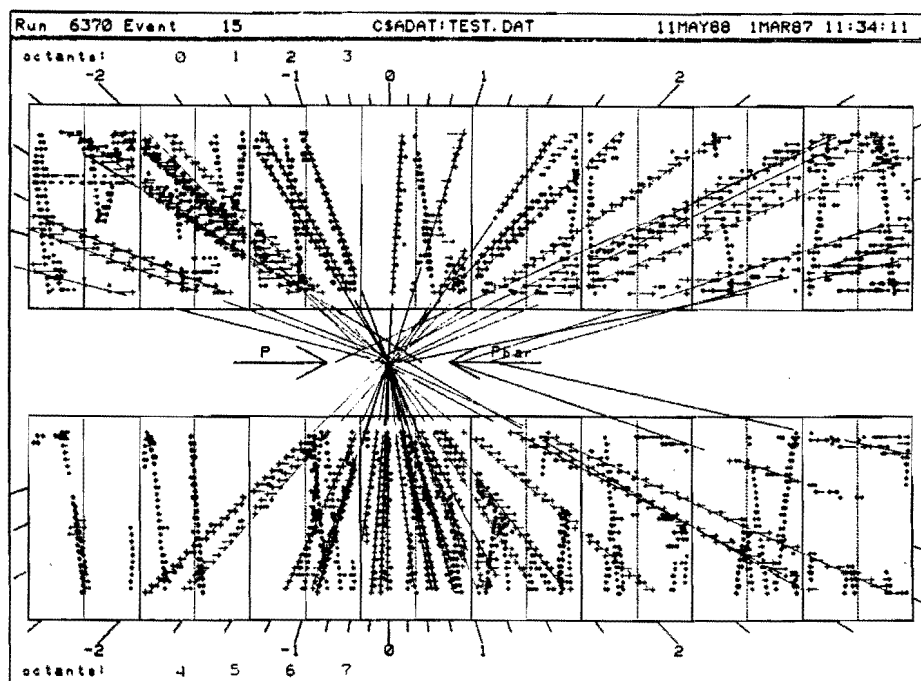


Figure 3.8: Fully reconstructed event. The individual  $\phi$  slices can be seen in the next figure.

160



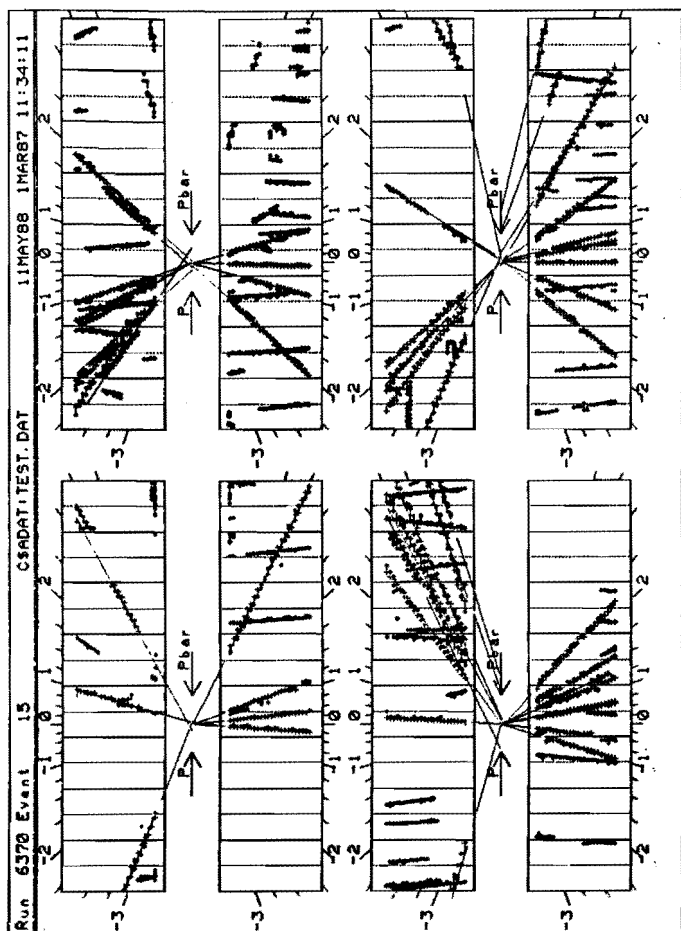


Figure 3.9: Fully reconstructed event. The same event as the previous figure with four  $\phi$  slices separately displayed.

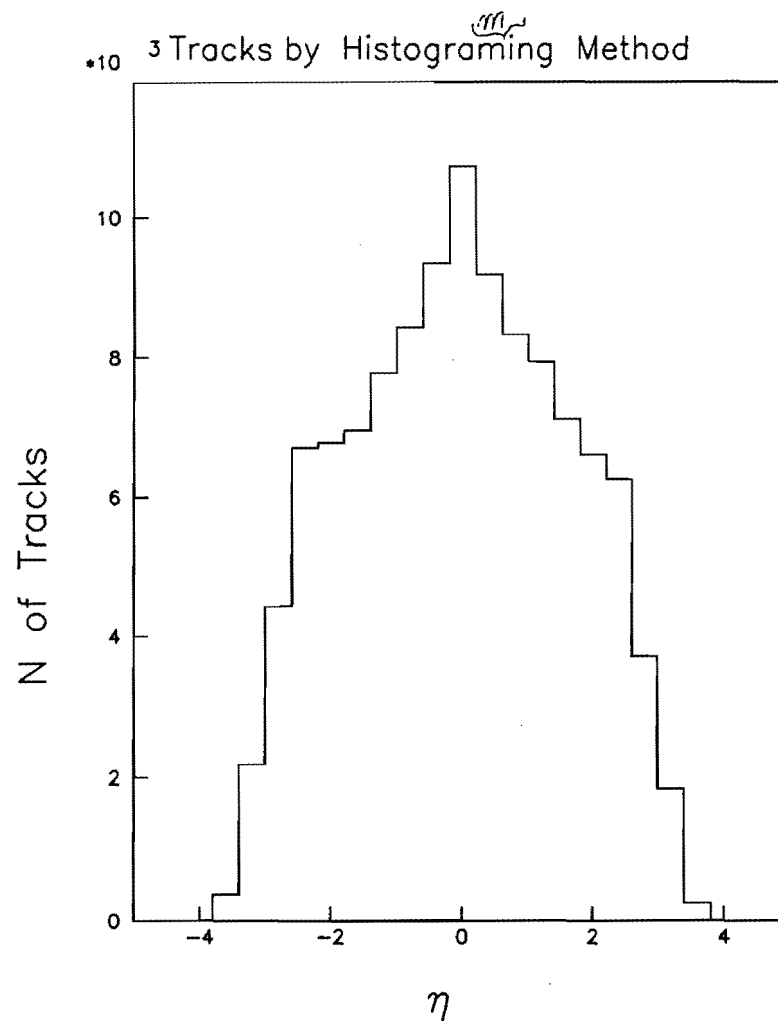


Figure 3.10:  $\eta$  distribution of tracks reconstructed by the histogramming method. This is with actual  $\bar{p}p$  data after the track selection. More tracks were found in the central region.

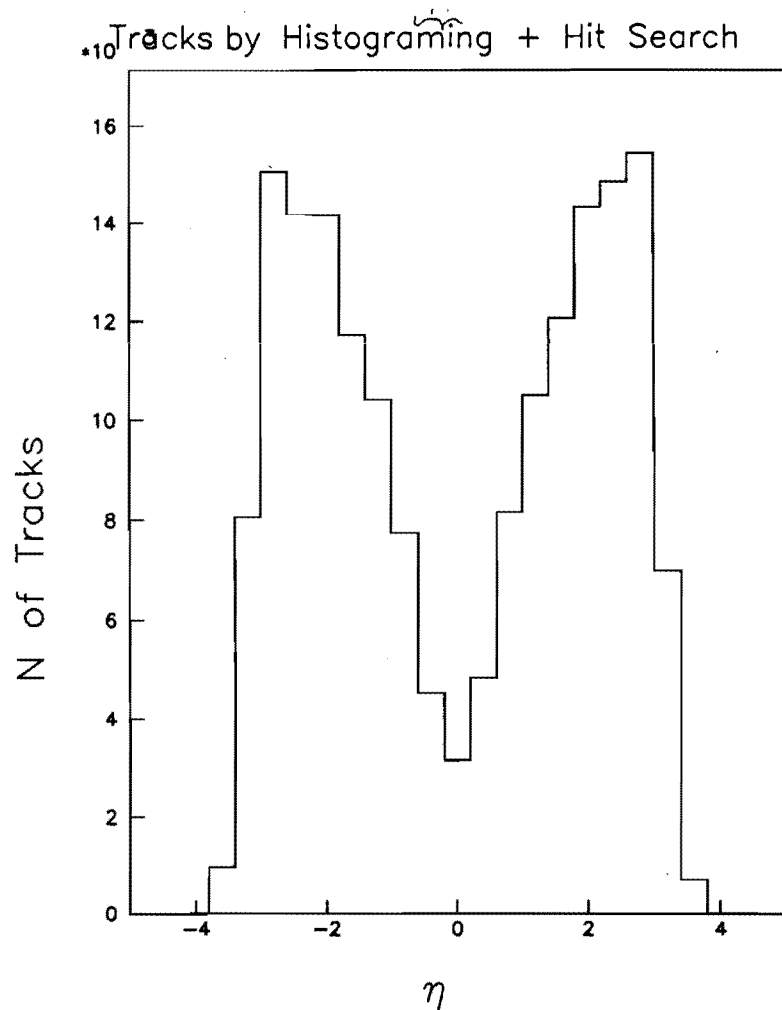


Figure 3.11:  $\eta$  distribution of tracks reconstructed by the histogramming method assisted by the hit-search method. This is with actual  $\bar{p}p$  data after the track selection. The more tracks were found in the forward region.

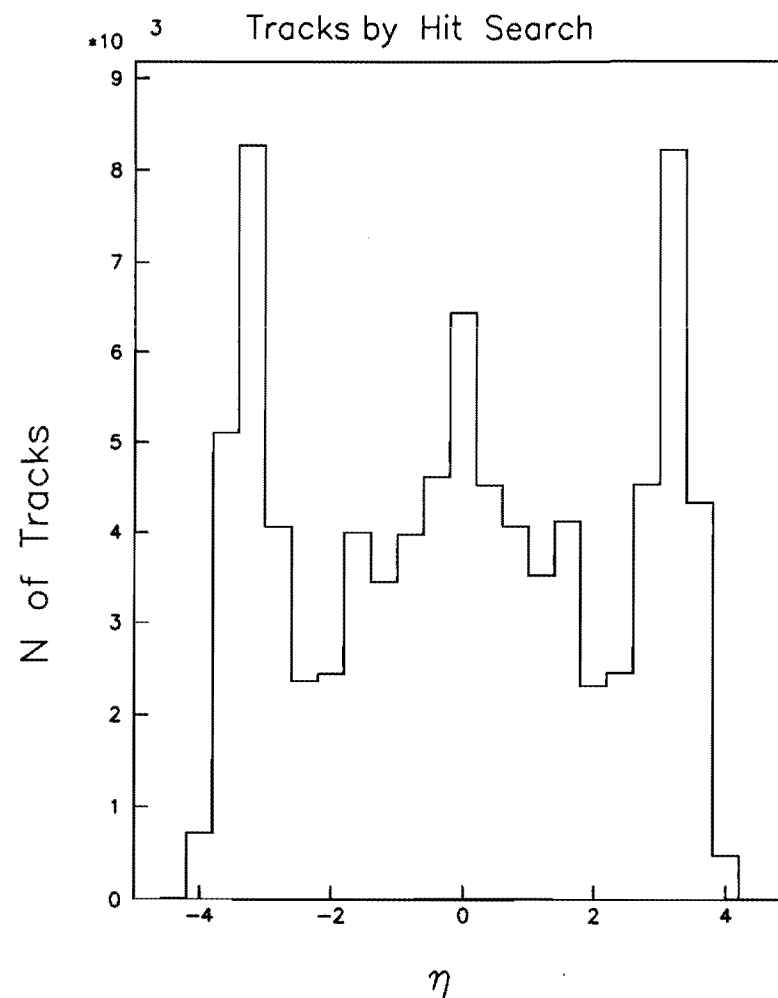


Figure 3.12:  $\eta$  distribution of tracks reconstructed by the hit-search method (the last reconstruction step). This is with actual  $\bar{p}p$  data after the track selection. Peaks are seen around  $|\eta| = 3.3$  where the maximum number of sense wires which particles go through is limited to 4-10.

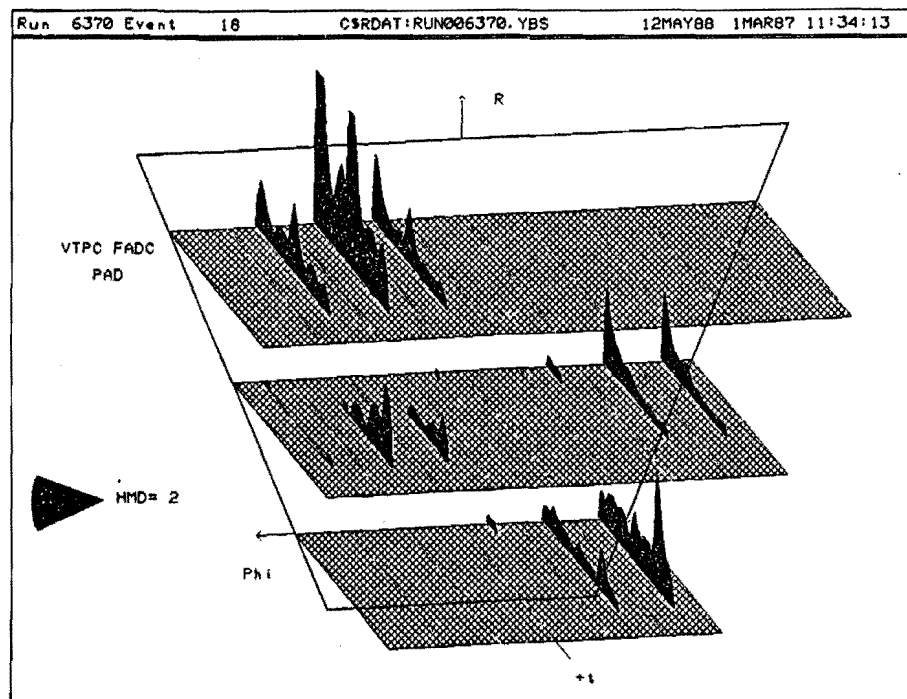
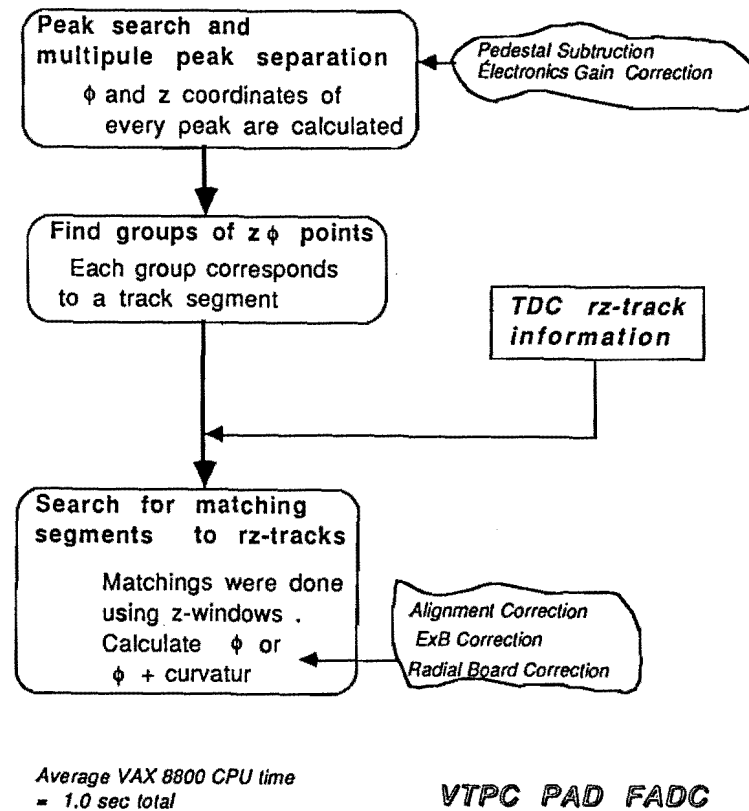


Figure 3.13: Pad FADC raw data. The horizontal axis is the radius  $r$  and  $\phi$  increase counter clockwise (right to left). The  $z$  or  $t$  axis is perpendicular to the plane of  $r\phi$ . Three pad rows are drawn at the inner, middle, and outer radius. Raw FADC data is shown on each pad as a function of  $t$ . The height corresponds to FADC counts.



**VTPC PAD FADC  
Reconstruction**

Figure 3.14: Flow chart of pad FADC reconstruction.

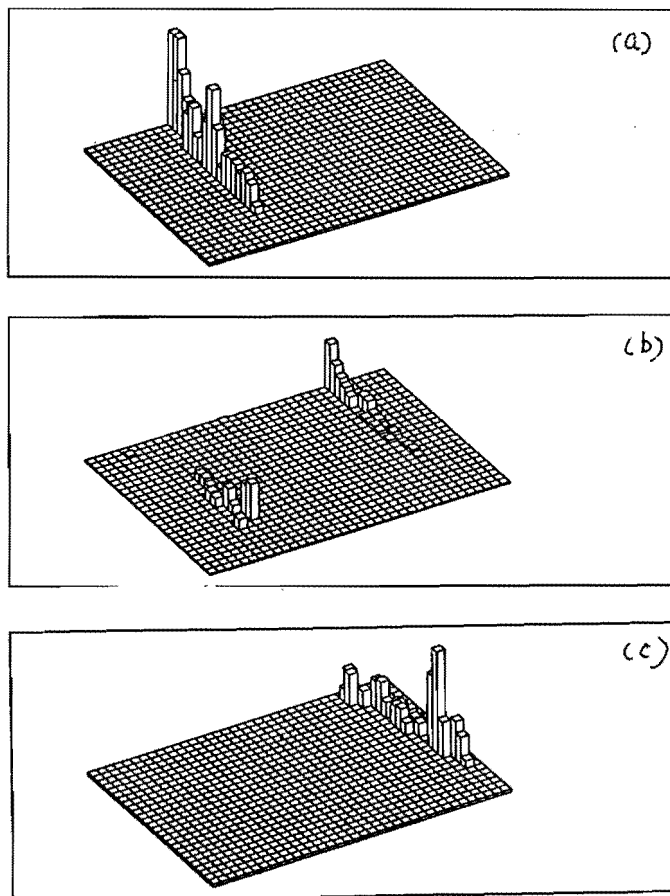


Figure 3.15: Example of two-dimensional histograms used to find  $z\phi$  segments; (a) is the outer row, (b) is the middle row, and (c) is the inner row. The  $z\phi$  points in the histograms are obtained from the data shown in figure 3.13. The three-dimensional prospect are roughly the same for figures here and figure 3.13. The points in the histograms are weighted by the peak heights of the induced charge distribution.

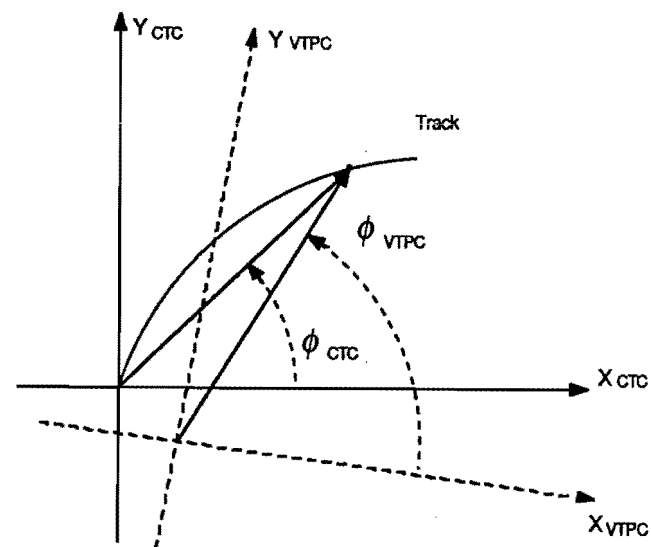


Figure 3.16: Definitions of  $\phi_{VTPC}$  and  $\phi_{CTC}$ . The nominal coordinate defined by the CTC is indicated by  $x_{CTC}$  and  $y_{CTC}$  axes. The VTPC coordinate, which is possibly misaligned, is indicated by  $x_{VTPC}$  and  $y_{VTPC}$  axes.

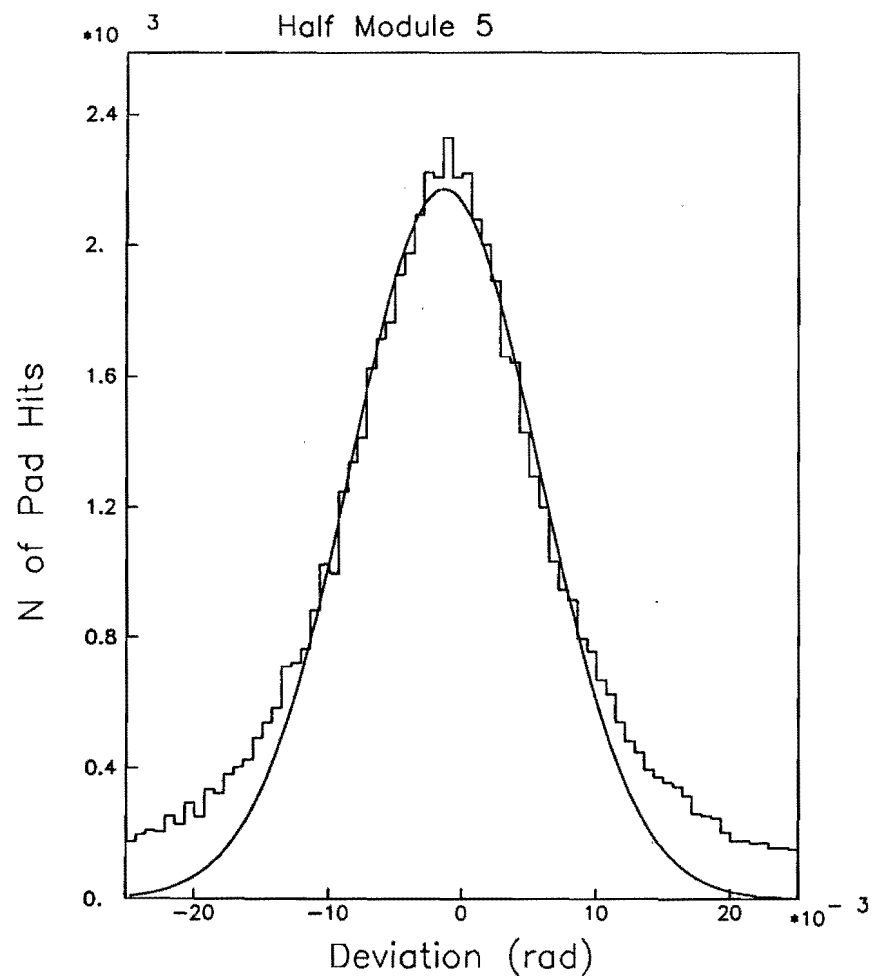


Figure 3.17: Distribution of deviation (radian) of VTPC  $\phi$  from CTC tracks, Module 2. The shift of the peak position is the  $\phi$  misalignment between the VTPC modules and the CTC. The curve is a fit to a Gaussian which has a peak position at  $-1.4$  mrad, indicating a good alignment.

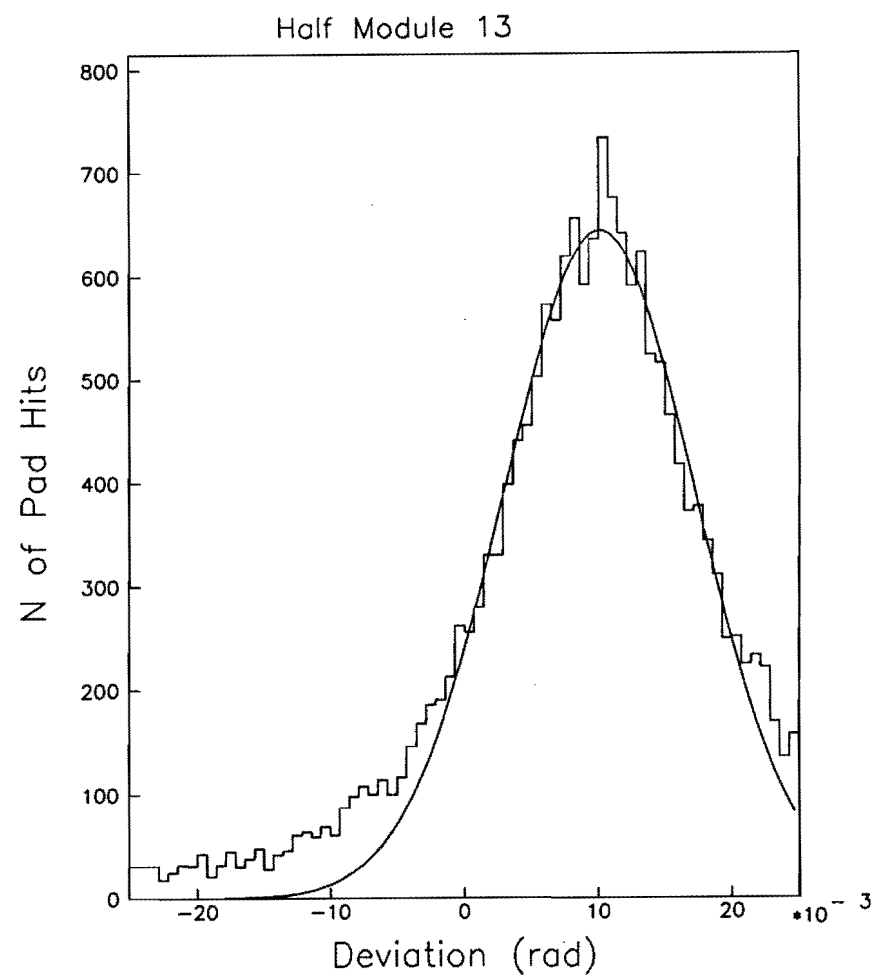


Figure 3.18: Distribution of deviation of VTPC  $\phi$  from CTC tracks, Module 5. The shift of the peak position indicates that this module is misaligned by 12 mrad.

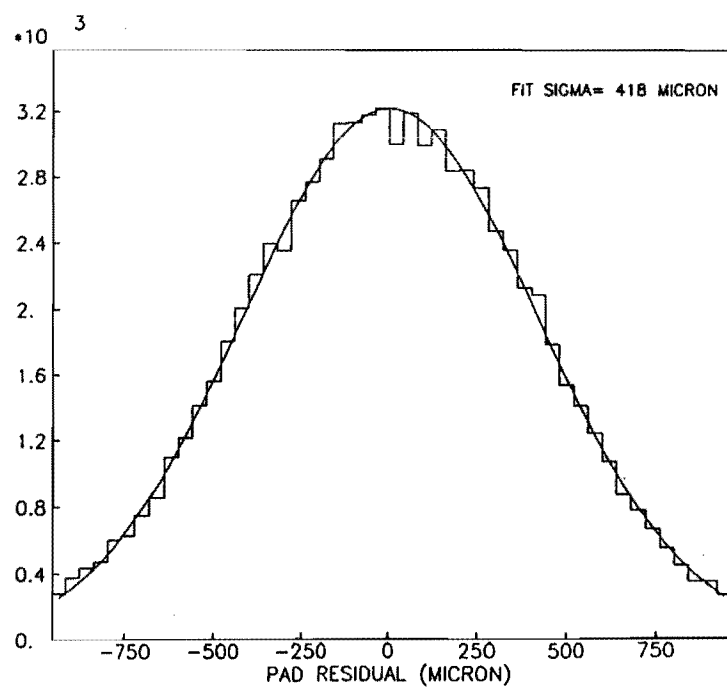
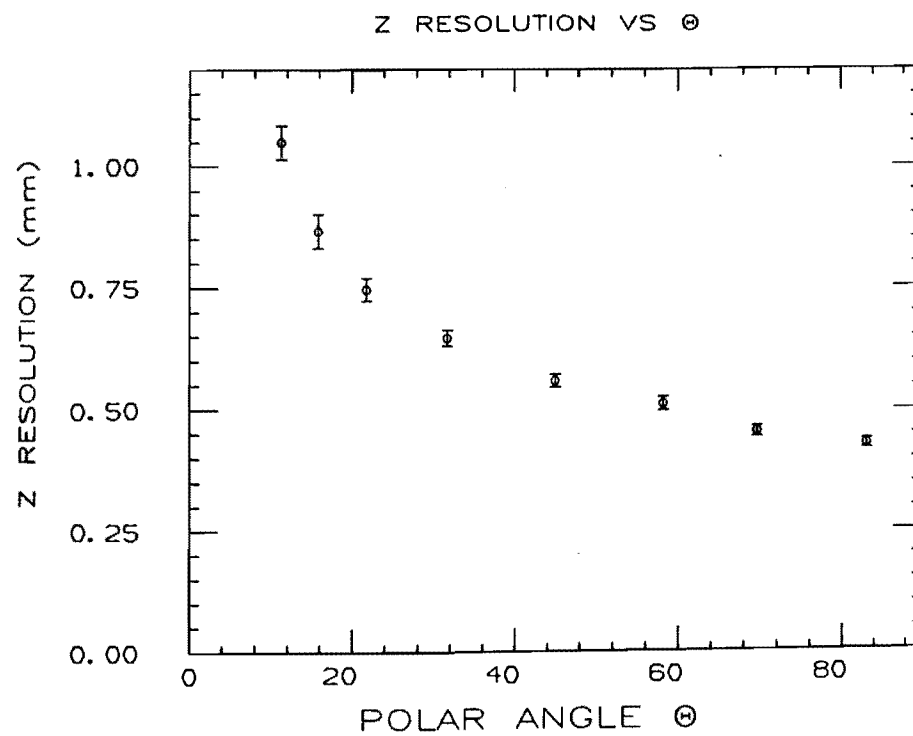
Figure 3.19: VTPC pad  $\phi$  residual.

Figure 3.20: VTPC Z spatial resolution v.s. track angle.

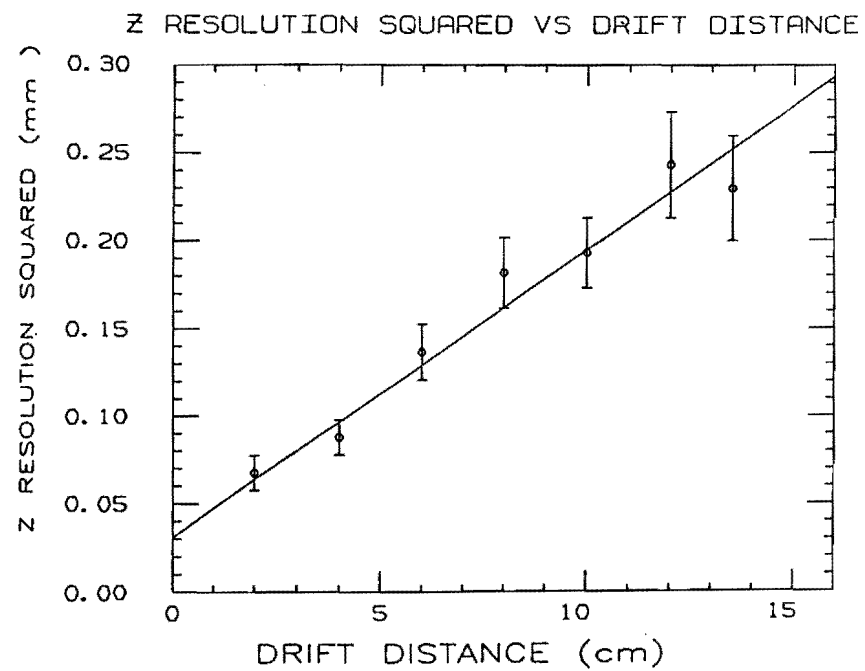


Figure 3.21: VTPC Z spatial resolution v.s. drift distance.

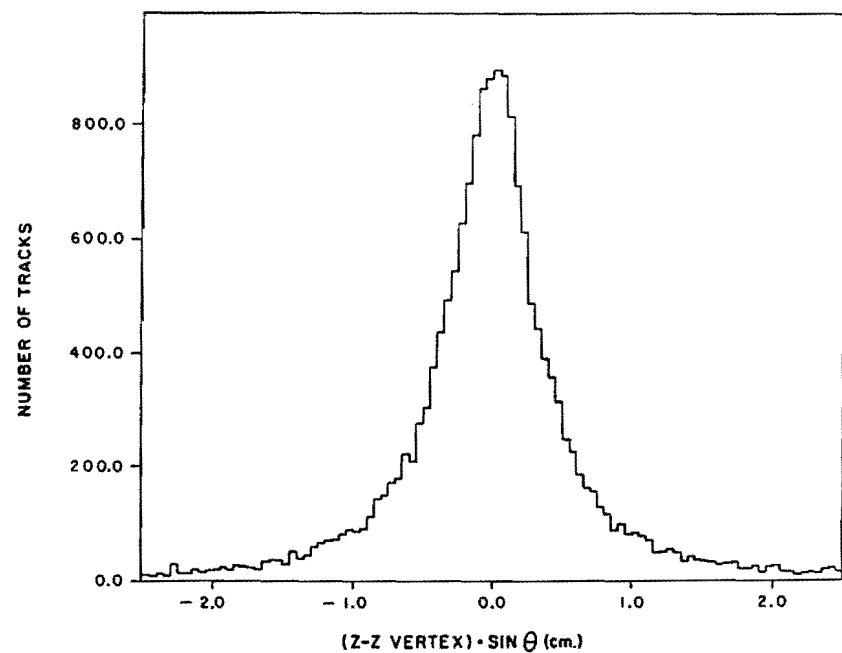
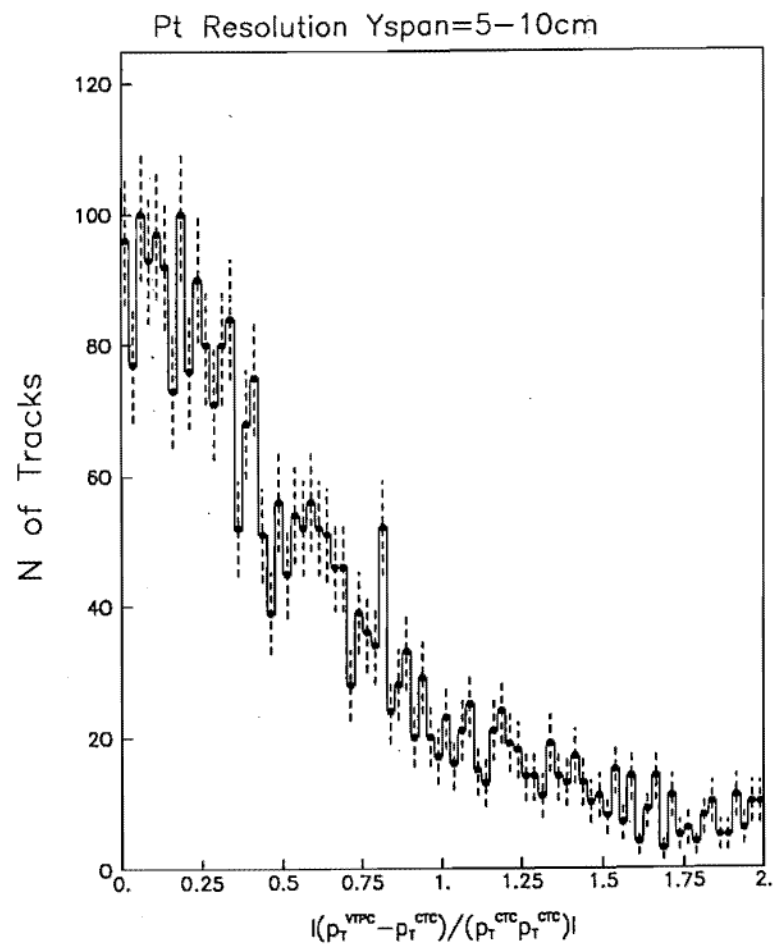
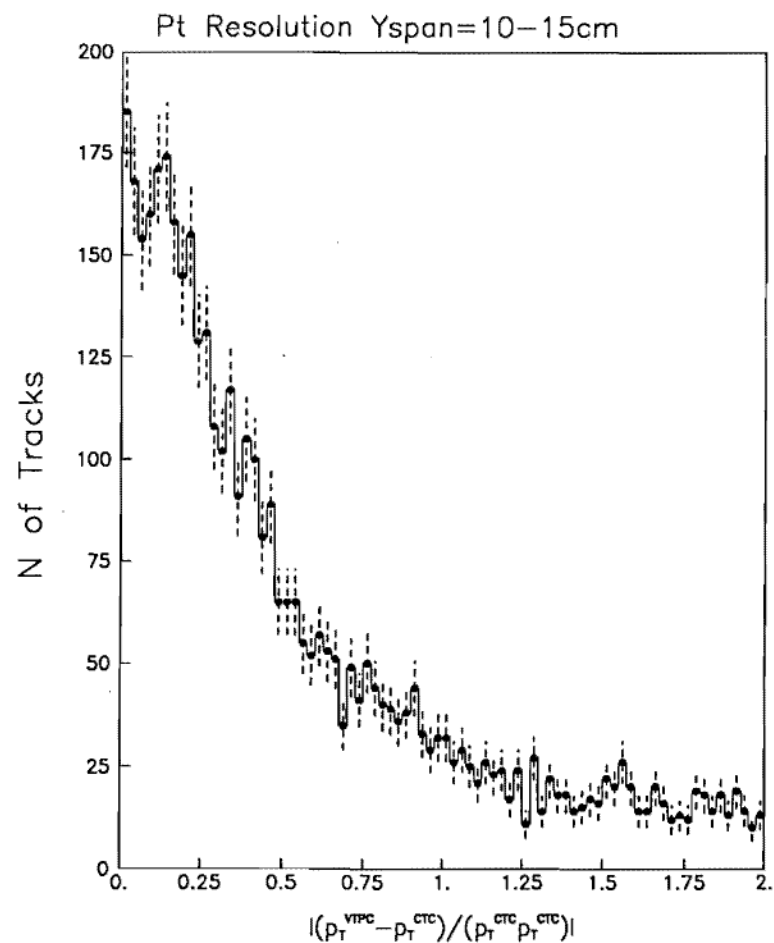


Figure 3.22: VTPC vertex impact parameter distribution.

Figure 3.23: VTPC  $p_t$  resolution  $(\text{GeV}/c)^{-1}$  for a radial span= 5.0 to 10 cm.Figure 3.24: VTPC  $p_t$  resolution  $(\text{GeV}/c)^{-1}$  for a radial span= 10 to 15 cm.



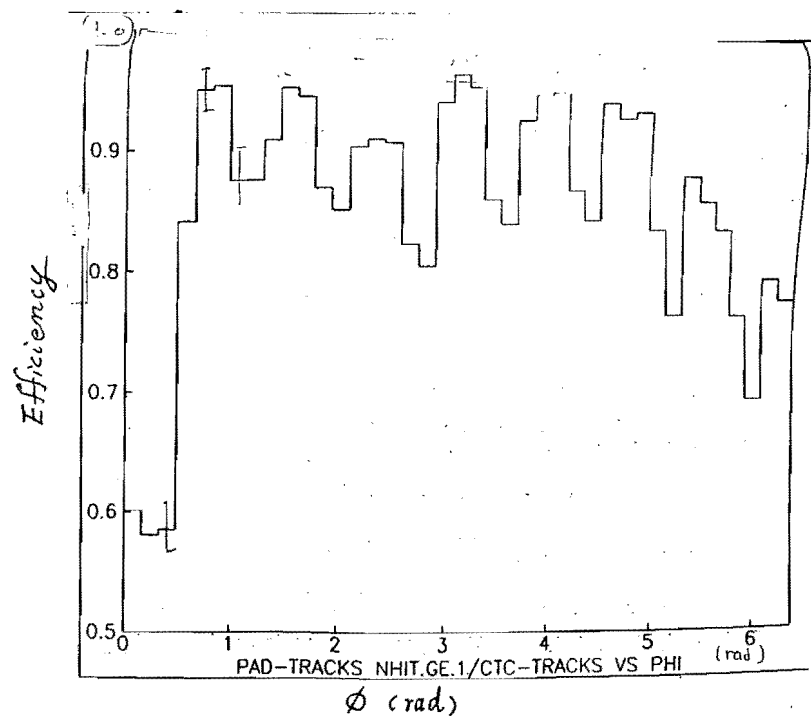


Figure 3.25: Pad efficiency with at least one FADC sampling is shown as a function of  $\phi$ .

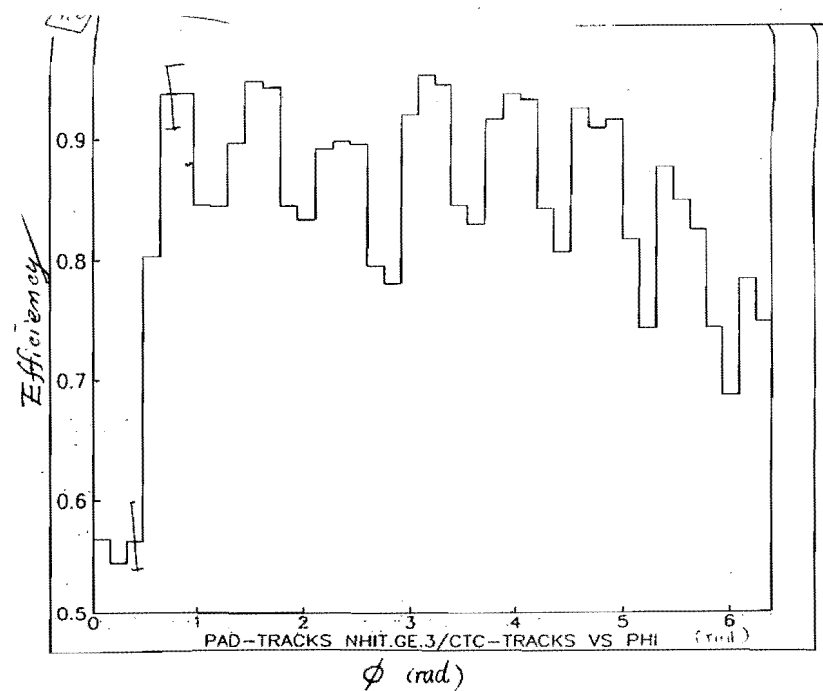


Figure 3.26: Pad efficiency with at least three FADC samplings is shown as a function of  $\phi$ .

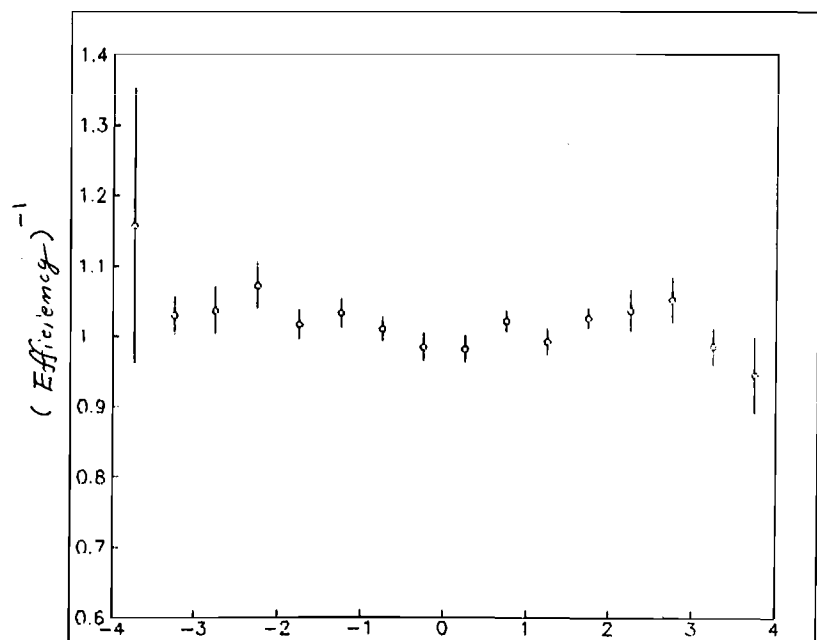


Figure 3.27: Reconstruction (efficiency)<sup>-1</sup> obtained by the hand-scan is shown as a function of  $\eta$ .

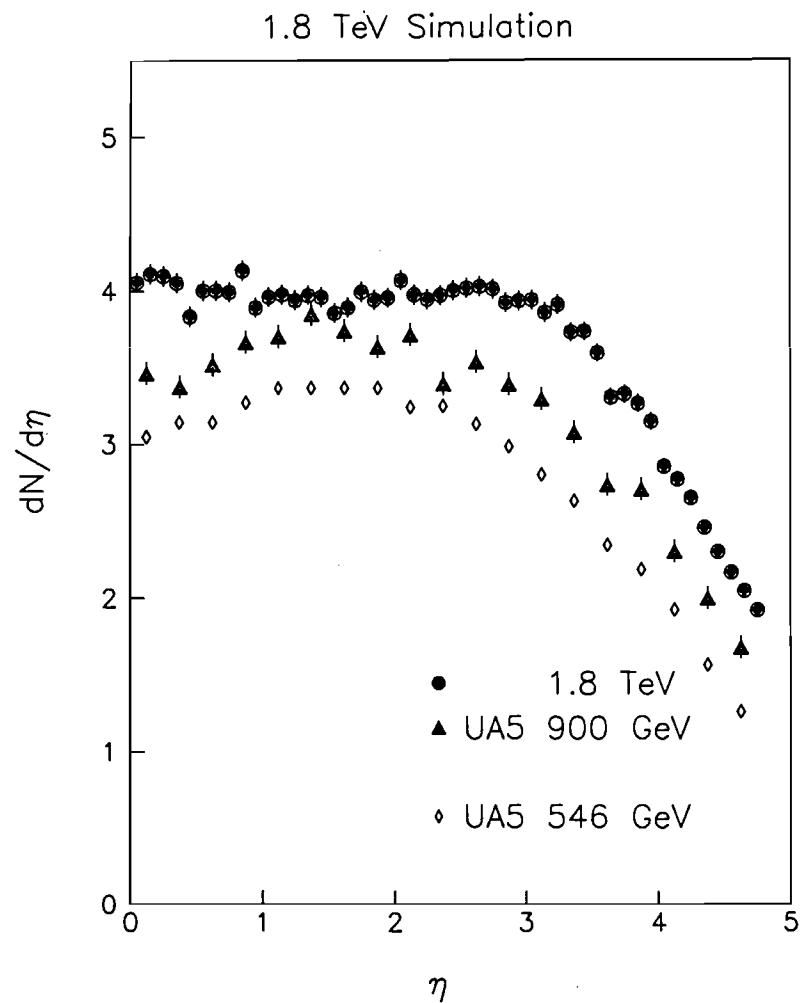


Figure 4.1:  $dN/d\eta$  by the Monte Carlo event simulation at  $\sqrt{s} = 1.8$  TeV. The UA5 data at  $\sqrt{s} = 546$  and 900 GeV are taken from reference [14]. The simulated data at roots = 1.8 TeV is flatter than the read data.

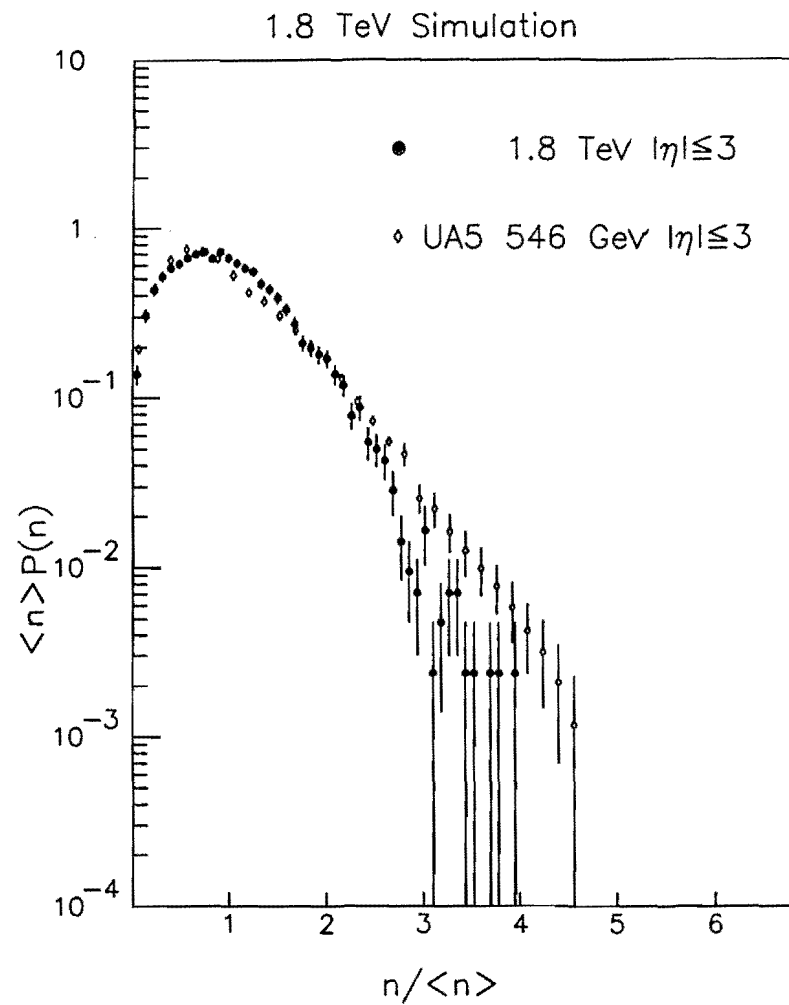


Figure 4.2: KNO  $\psi$  distribution by the Monte Carlo event simulation at  $\sqrt{s} = 1.8$  TeV. The Monte Carlo simulation uses the fixed distribution for all  $\eta$  range but the actual  $\psi$  distribution slightly differs for different  $\eta$  range, resulting in a slight disagreement with UA5 data for  $|\eta| \leq 3$  [1].

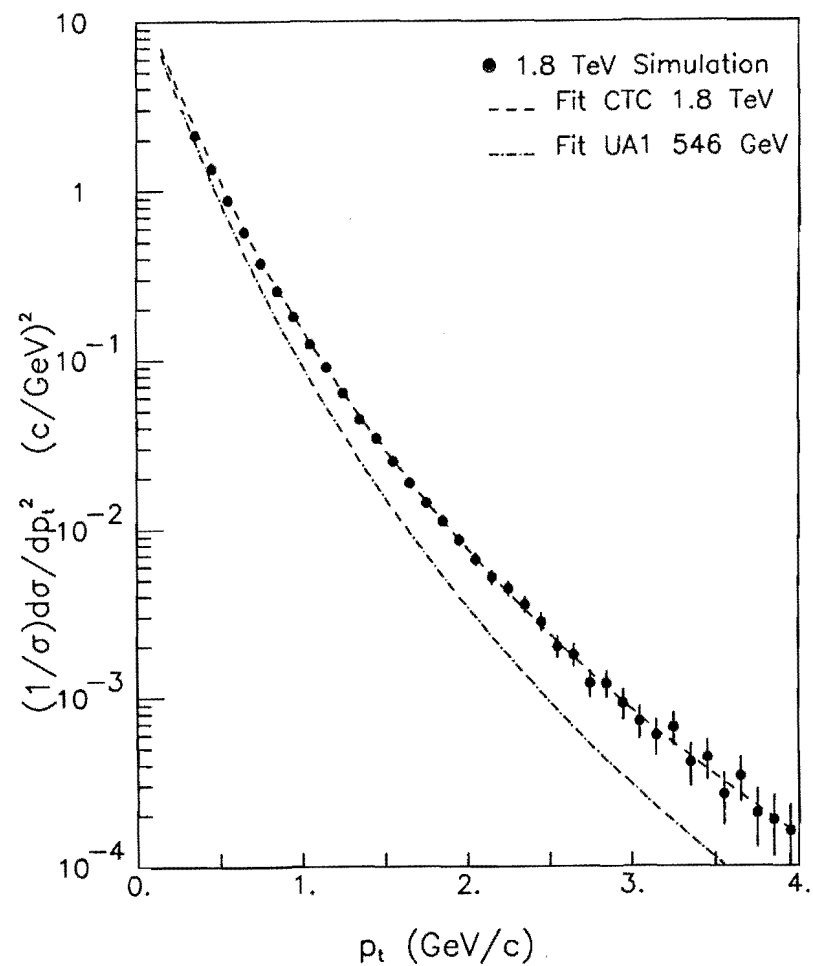


Figure 4.3:  $p_t$  spectrum with Monte Carlo simulation. The circles are the simulated data at  $\sqrt{s} = 1.8$  TeV, the dashed line is a fit to the actual CTC measurement at  $\sqrt{s} = 1.8$  TeV [86], and a dotted line is a fit to UA1 data at  $\sqrt{s} = 546$  GeV [87].

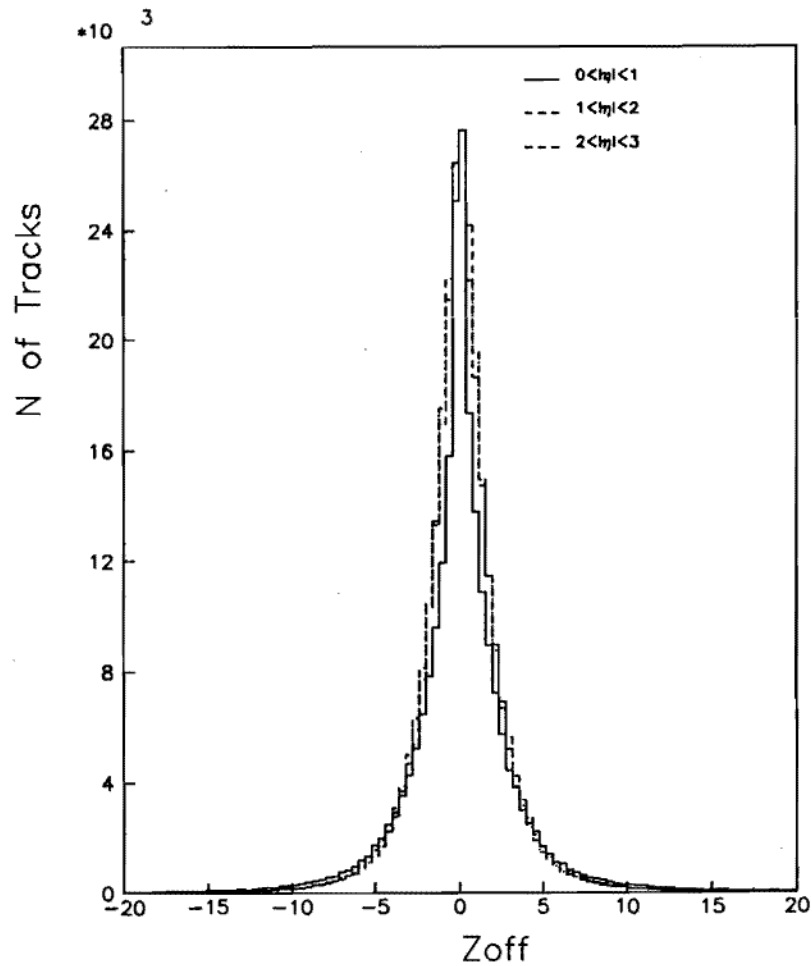


Figure 4.4:  $Z_{off}$  distributions for real data at  $\sqrt{s} = 1.8$  TeV. The solid line is for  $0 < |\eta| < 1$ , the dashed line is for  $1 < |\eta| < 2$ , and the dot-dashed line is for  $2 < |\eta| < 3$ . There are no significant differences for different  $\eta$  ranges, indicating our track selection would not distort the  $dN/d\eta$  distribution. The width of the distribution is approximately 2.4 in FWHM.

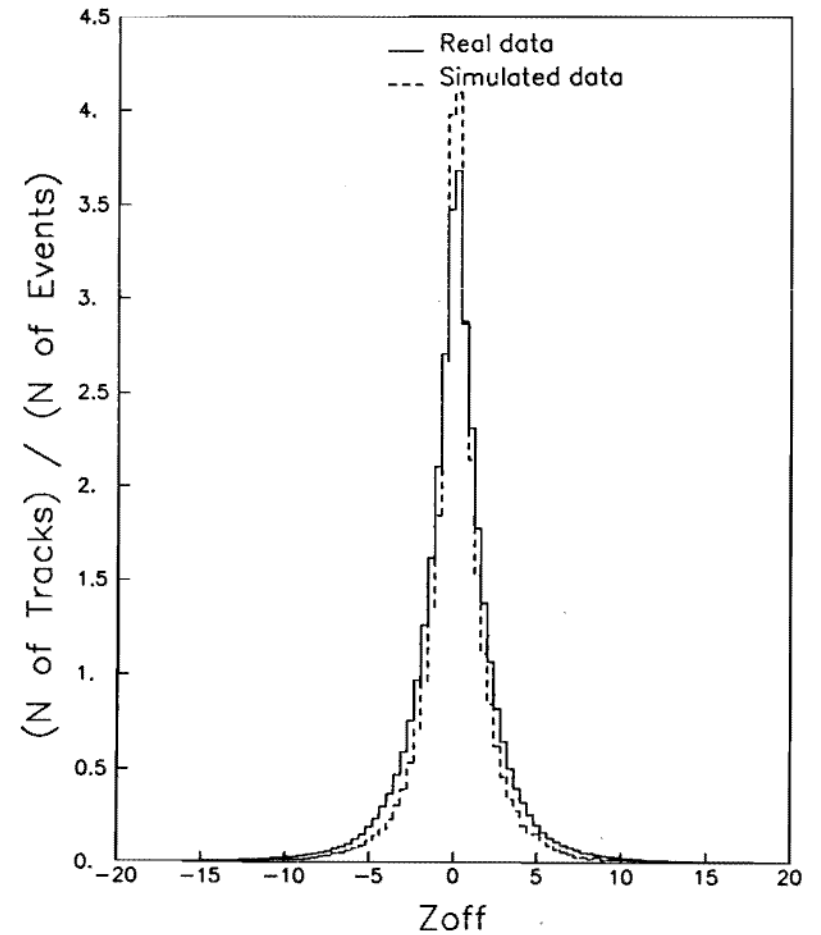


Figure 4.5:  $Z_{off}$  distributions for real and simulated data. The solid line is for real data. The dashed line is for the simulation including the material effects and decays. Both are normalized by the number of events.

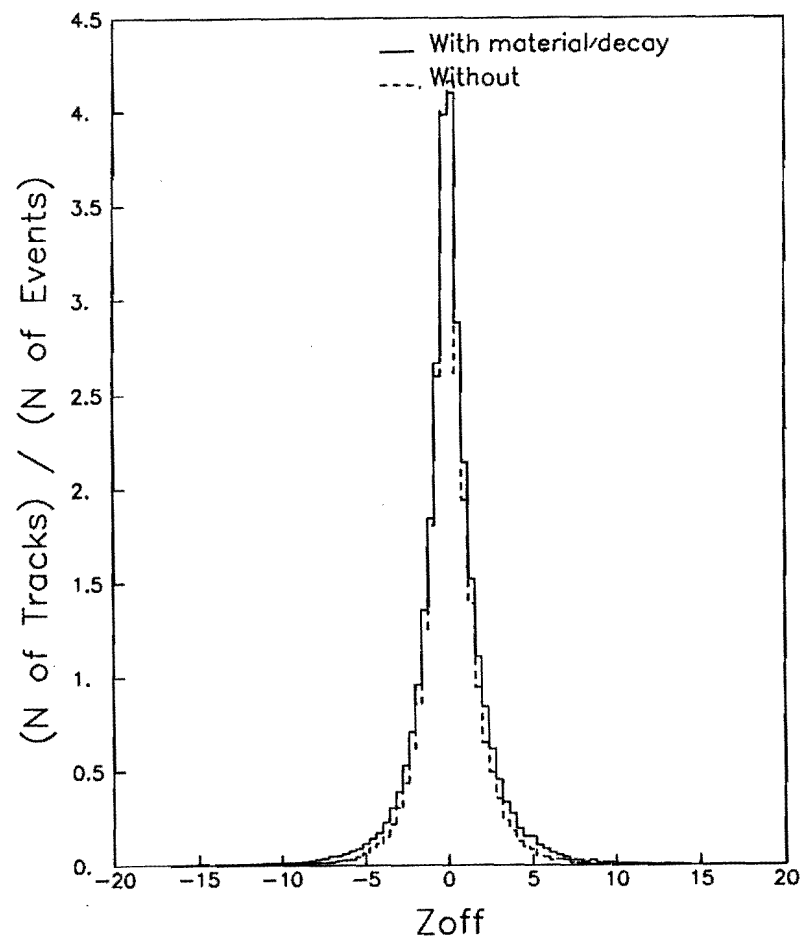


Figure 4.6:  $Z_{off}$  distributions with (solid line) and without (dashed line) the material/decay. The histograms are normalized by the number of events.

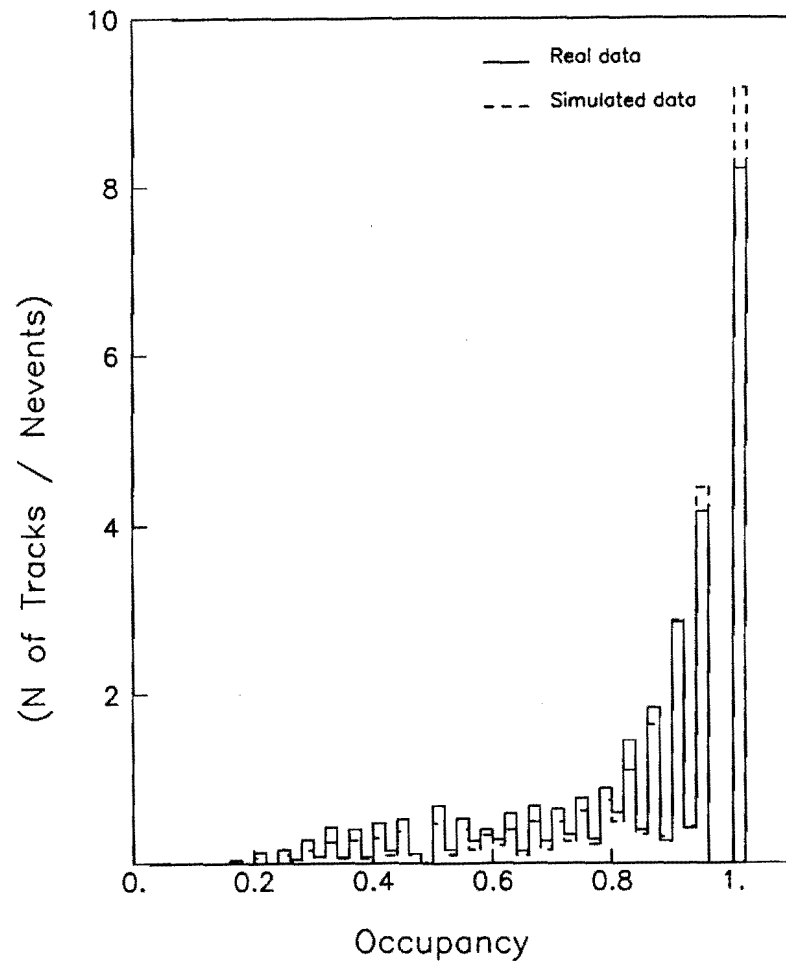


Figure 4.7: Occupancy distributions for real (solid line) and simulation (dashed line) data. The both histograms are normalized by the number of events. The statistical error of histogram contents is smaller than the line width. Both are after the track selection applied. Multiple peaks are seen because the maximum number of wire is 24.

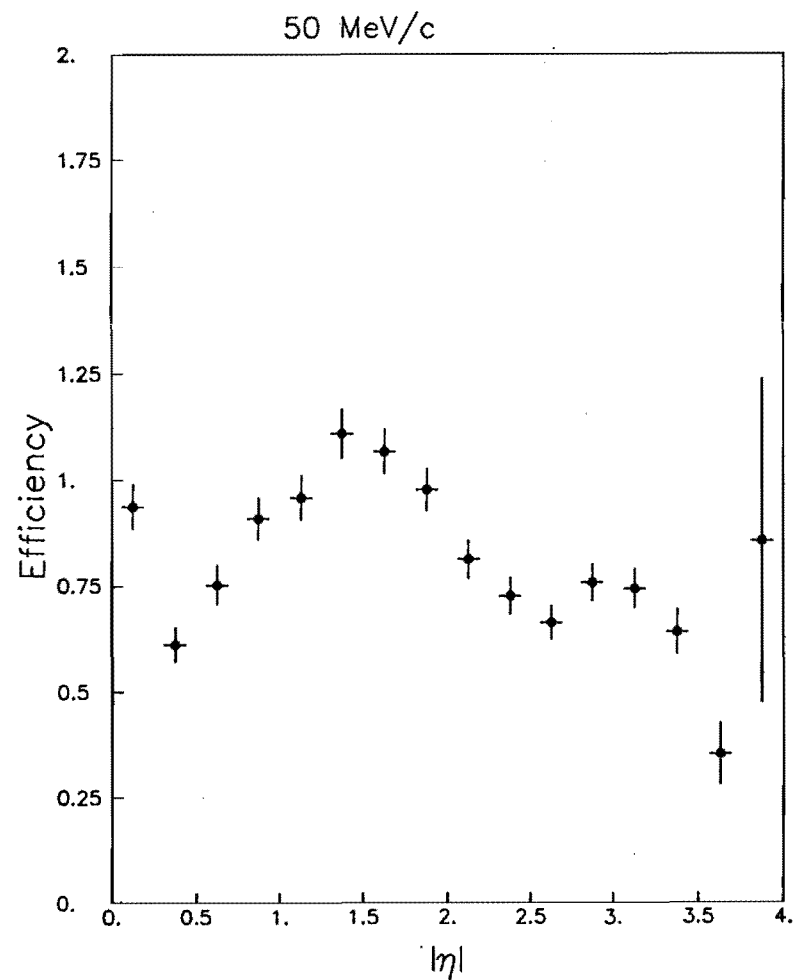


Figure 4.8: Efficiency for low  $p_t$  tracks ( $p_t = 50$  MeV/c). The ratio of  $dN/d\eta$  for  $p_t = 50$  MeV/c to the reference  $dN/d\eta$  which is for  $p_t = 9$  GeV/c is plotted versus  $|\eta|$ .

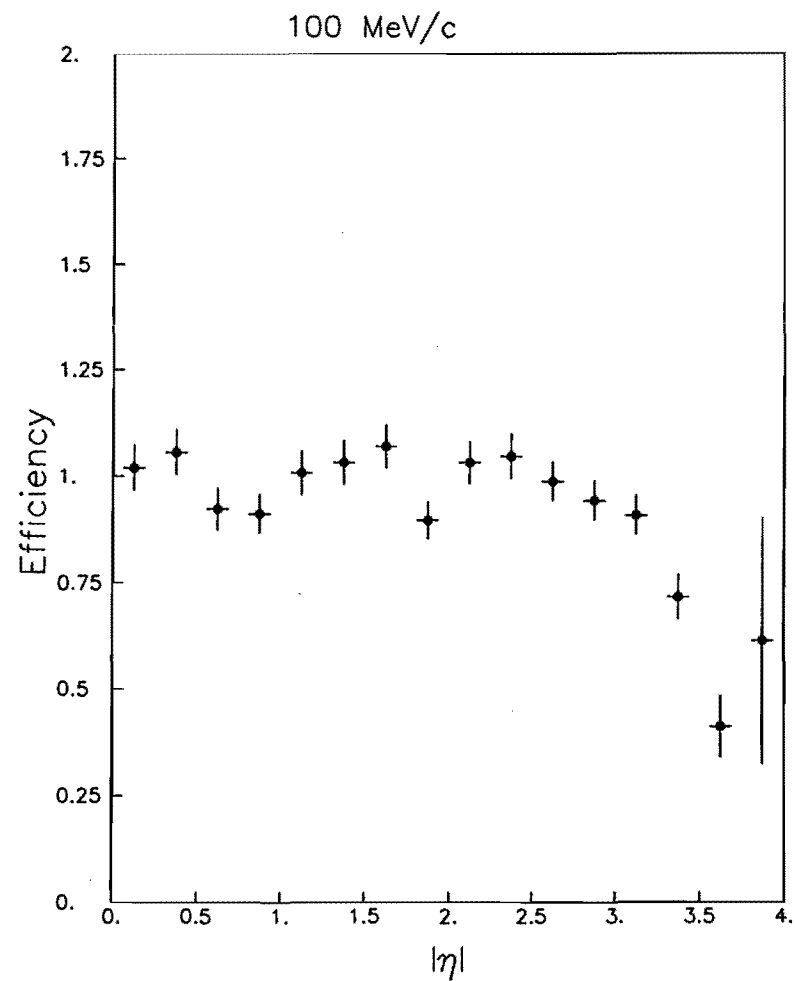


Figure 4.9: Efficiency for low  $p_t$  tracks ( $p_t = 100$  MeV/c). The ratio of  $dN/d\eta$  for  $p_t = 100$  MeV/c to the reference  $dN/d\eta$  which is for  $p_t = 9$  GeV/c is plotted versus  $|\eta|$ .

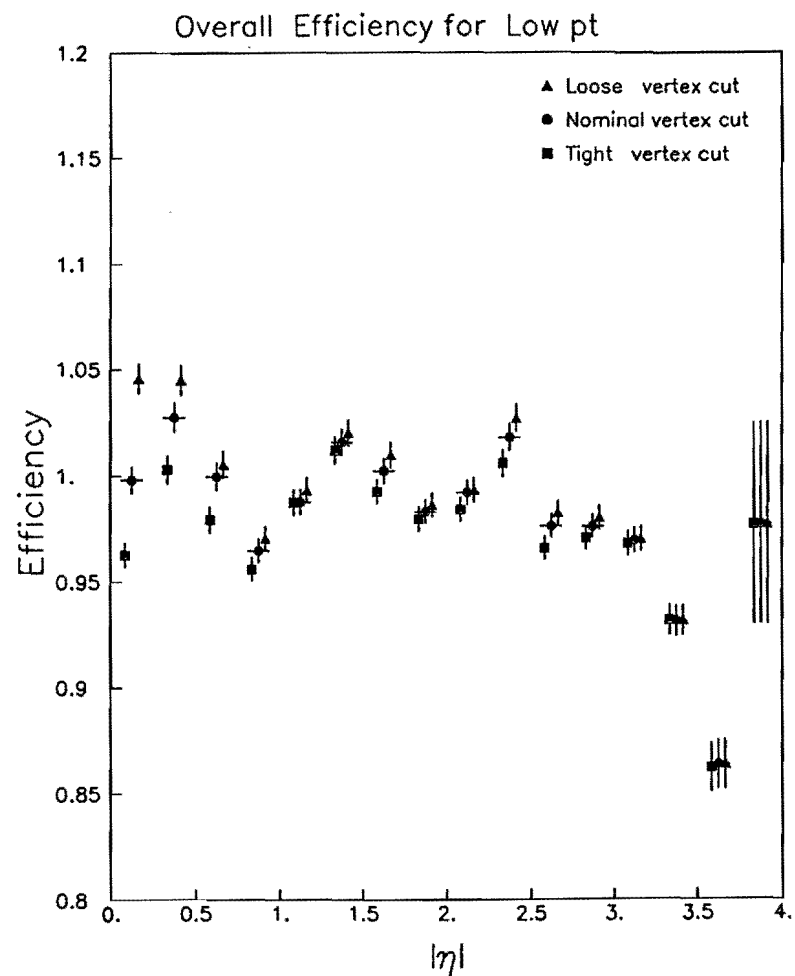


Figure 4.10: Net effects of low  $p_t$  tracks to  $dN/d\eta$ . The efficiencies for  $p_t = 50$  to 300 MeV/c are summed with weights calculated by the UA1  $p_t$  spectrum. The maximum loss is about 5% in  $|\eta| < 0.5$ , while there are some over-efficiencies (2-3%) in larger  $|\eta|$  because the reconstruction occasionally splits a low  $p_t$  track into two segments.

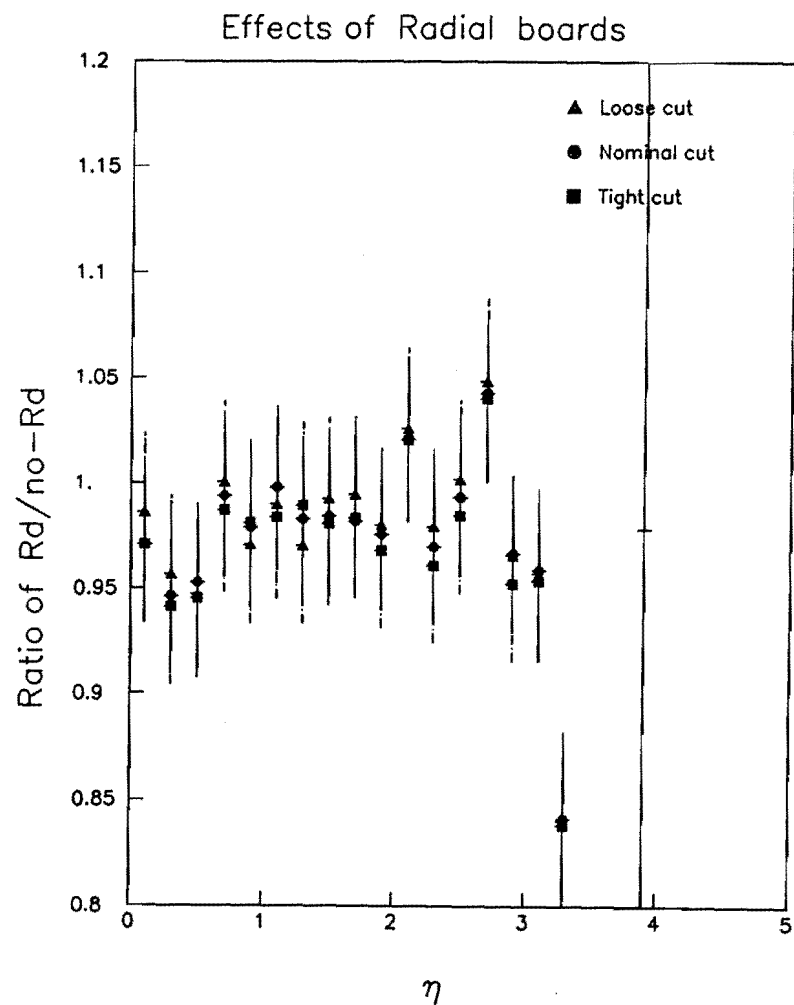


Figure 4.11: Effects of the chamber inefficiency near the radial boards. The figure shows the ratios of  $dN/d\eta$  with the radial board effects turned on to that with the effects turned off. The loss is about 2% in  $|\eta| > 1$  where a particle goes more than one VTPC module, taking an advantage of the  $\phi$  rotation between modules. In  $|\eta| < 1$ , the loss increase to 5%.

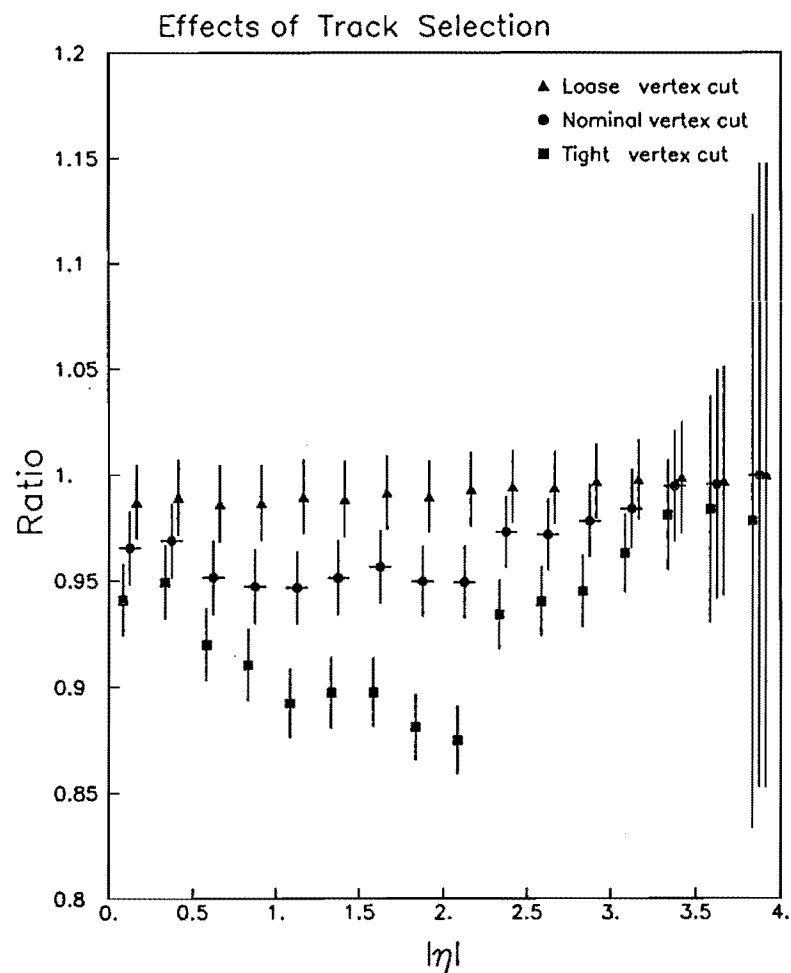


Figure 4.12: Loss of tracks by the track selection.  $\Delta$ 's are the ratio of  $dN/d\eta$  with the loose cut to  $dN/d\eta$  with the very loose cut. The loss is about 1%. The loss by the nominal cut ( $\bullet$ 's) is 4% in  $|\eta| < 1.5$  and 1-2% for larger  $|\eta|$ . The maximum loss by the tight cut ( $\square$ 's) goes up to 8%.

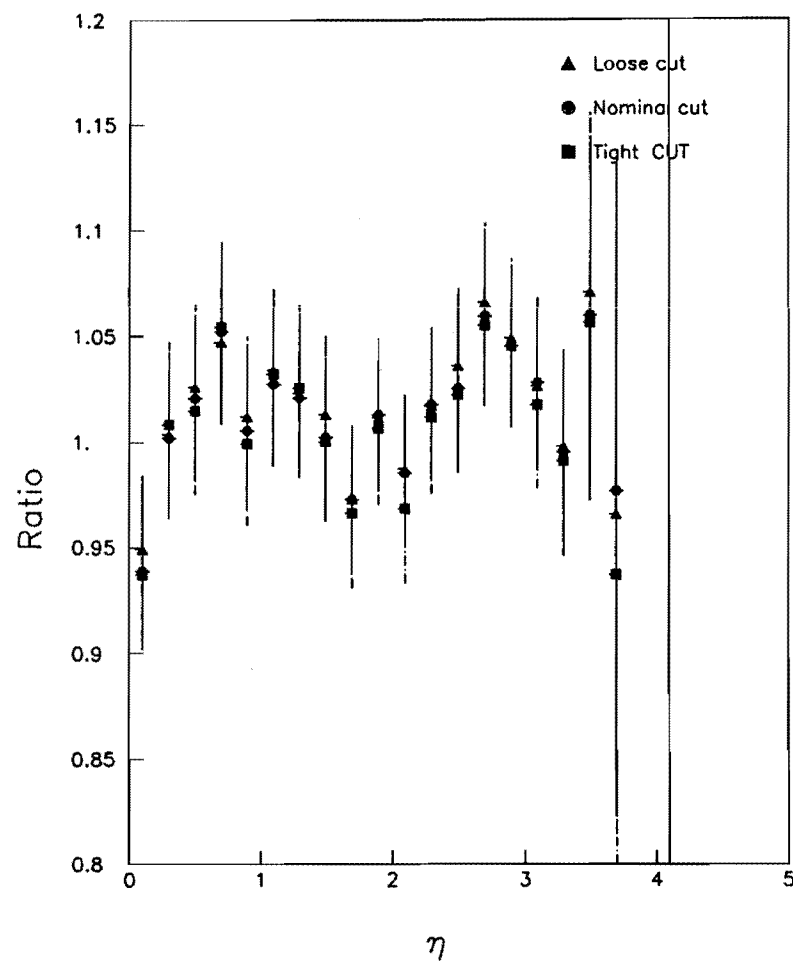


Figure 4.13: Effects of materials. The figure shows the ratios of  $dN/d\eta$  with the effects turned on to that without the effects for the various vertex cuts. The maximum increase due to the effects is about 5%.



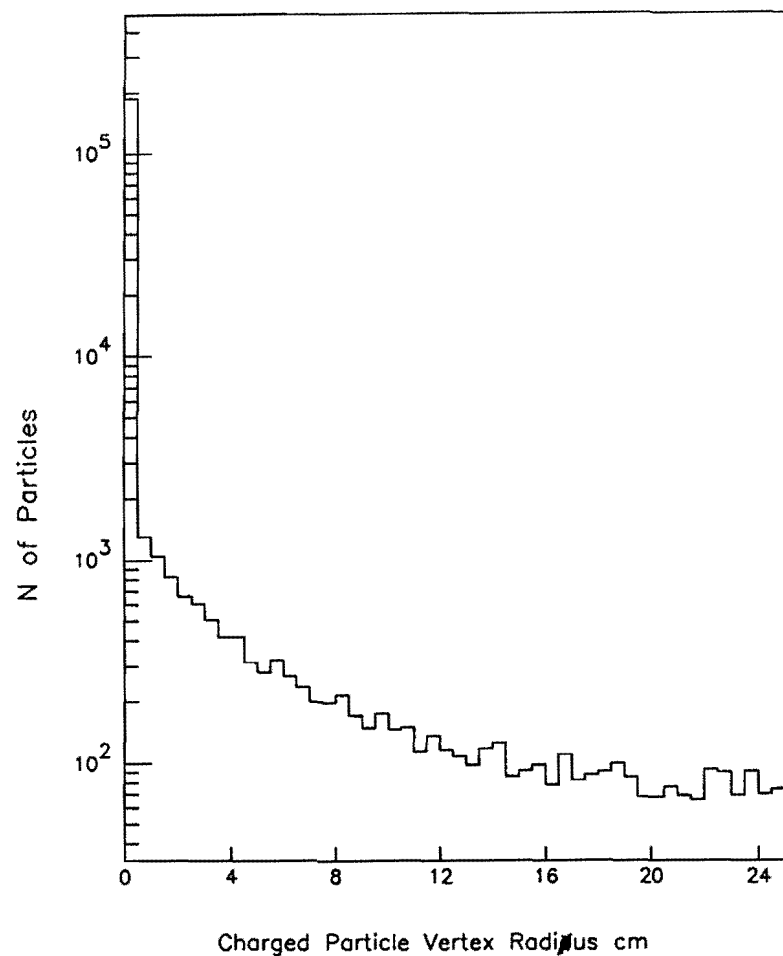


Figure 4.14: Simulated distribution of radius  $r$  (cm) of charged particle production vertex. Primary particles make a large peak at  $r=0$  and decay particles make a tail in the distribution. The VTPC extends from 6.5 cm to 21 cm.

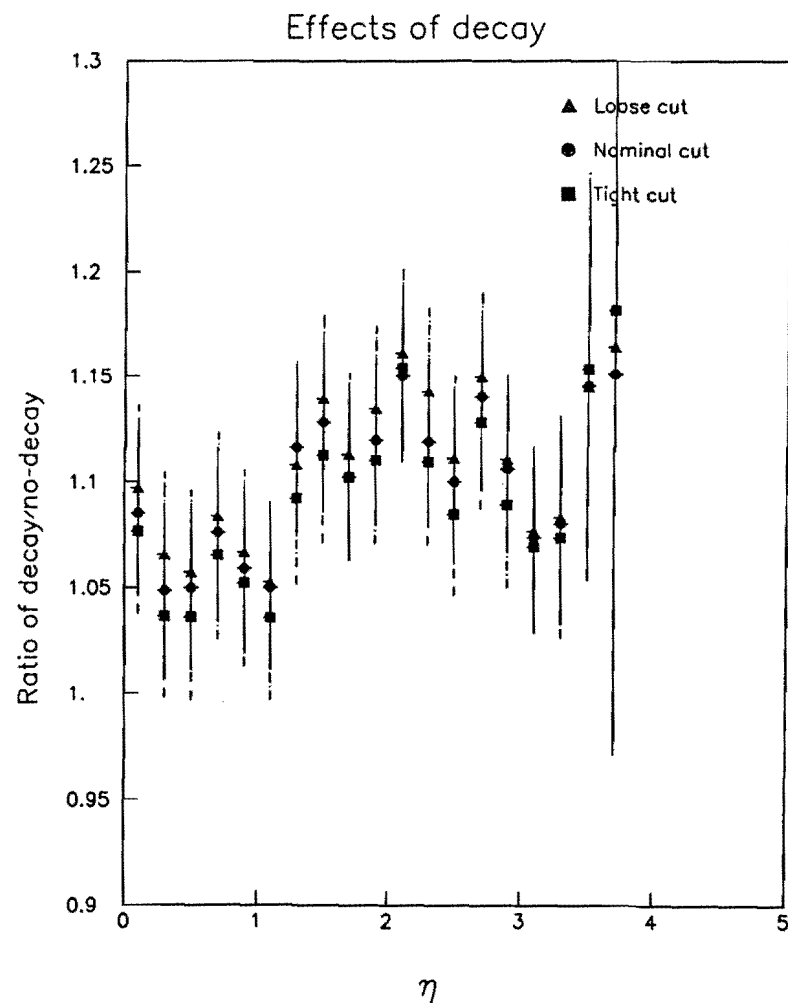


Figure 4.15: Effect of particle decays versus  $\eta$ . The figure shows the ratio of  $dN/d\eta$  with decays turned on to that without decays. The effect is the largest at  $|\eta| \sim 2$  (12-15%) and smallest in  $|\eta| < 1$  (5%).

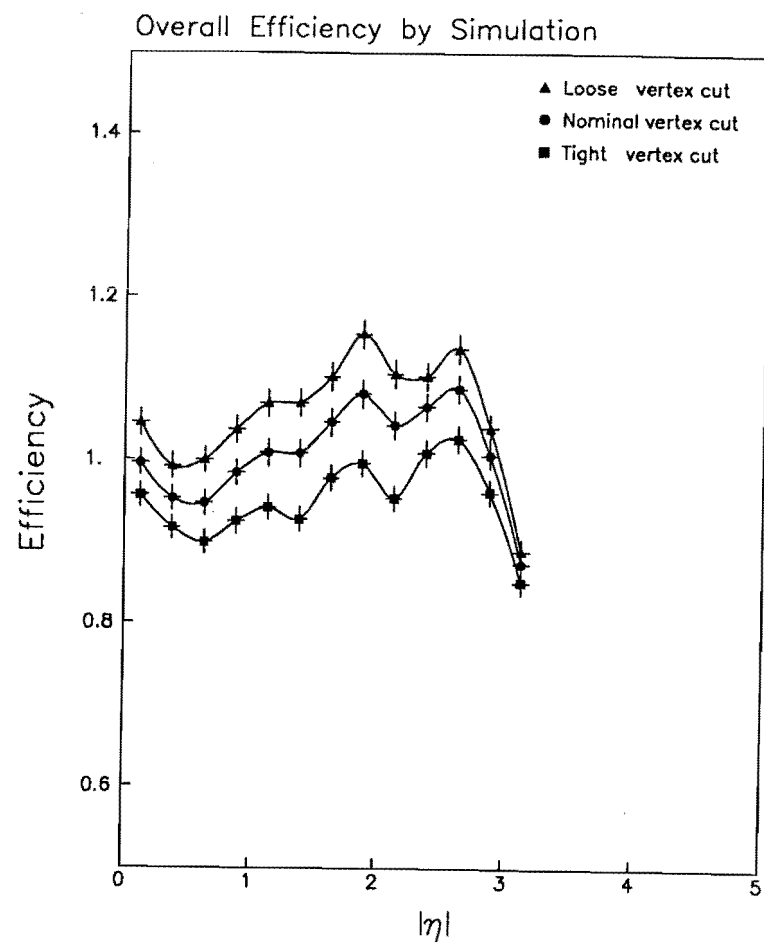


Figure 4.16: Overall efficiencies versus  $\eta$  for three vertex cuts. The efficiency is the reconstructed  $dN/d\eta$  of the simulated data with all possible effects described in this chapter divided by the  $dN/d\eta$  put into the Monte Carlo, therefore also including the reconstruction efficiency. The curves are computer-drawn smoothed curves connecting data points.

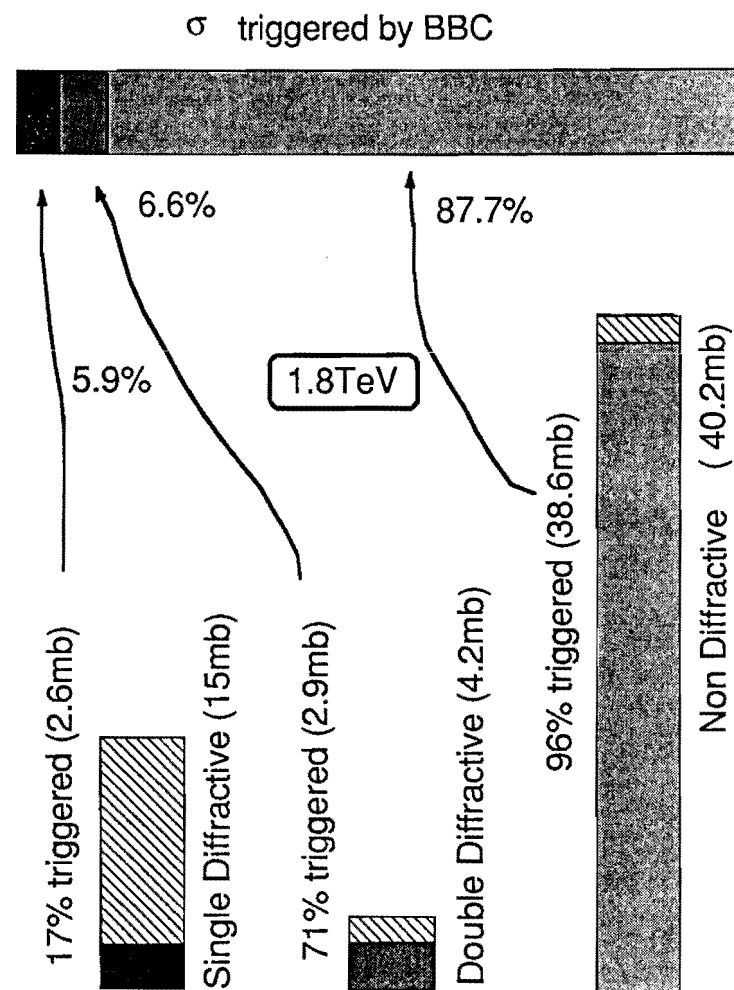


Figure 4.17: Illustration of the BBC acceptance and triggering cross section at  $\sqrt{s} = 1.8$  TeV.

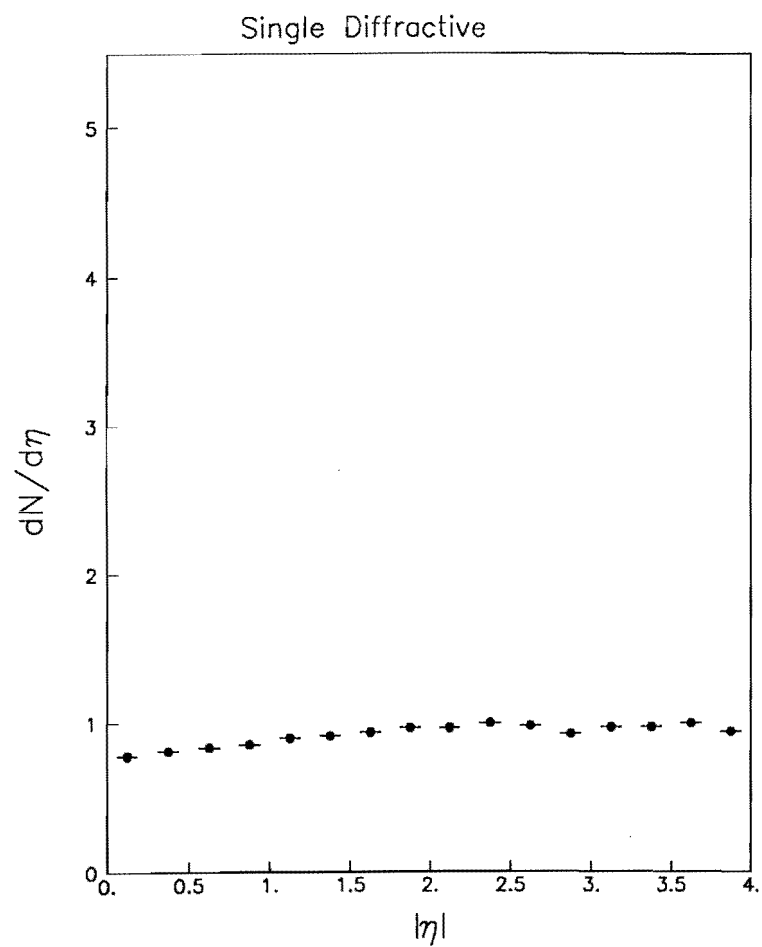


Figure 4.18: Simulated  $dN/d\eta$  for 1.8 TeV single diffractive events.

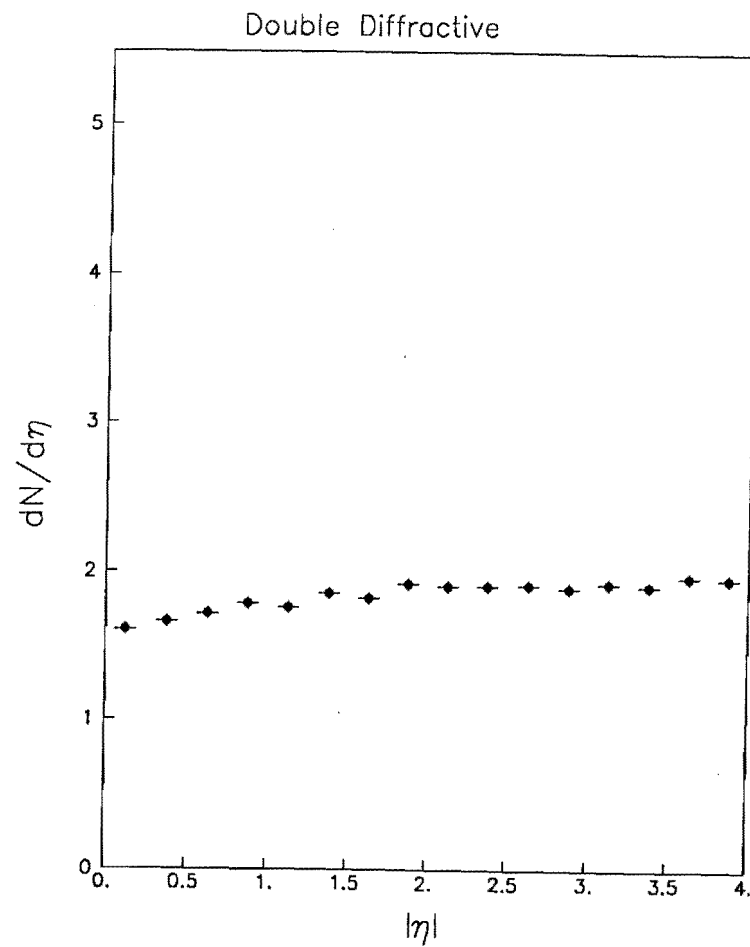


Figure 4.19: Simulated  $dN/d\eta$  for 1.8 TeV double diffractive events.

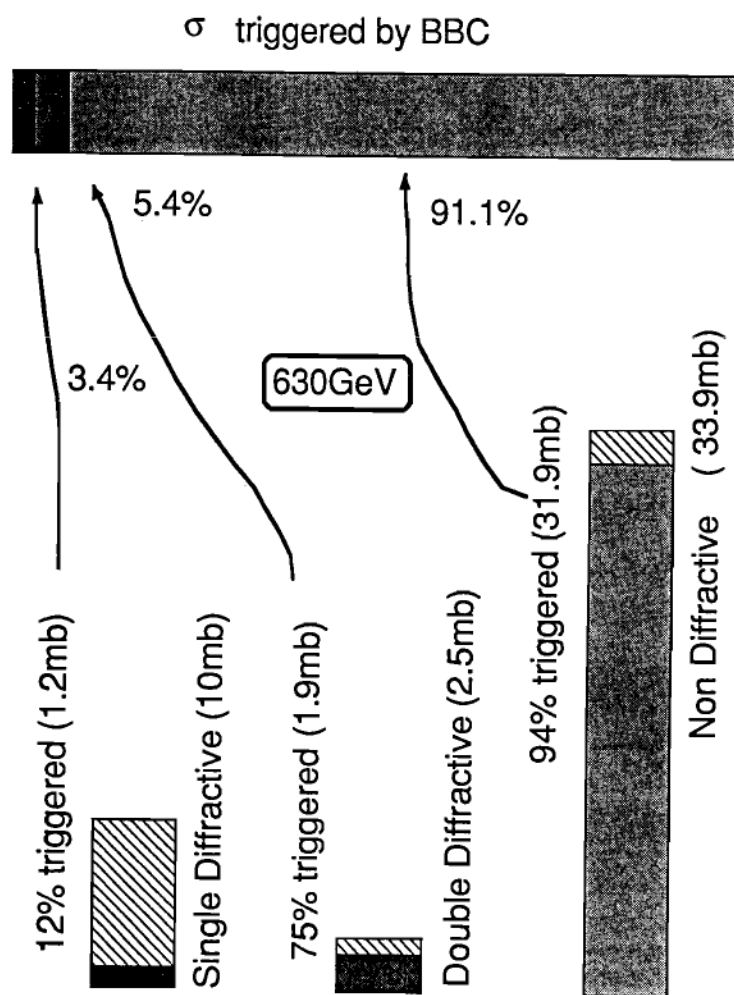


Figure 4.20: Illustration of the BBC acceptance and triggering cross section at  $\sqrt{s} = 630$  GeV.

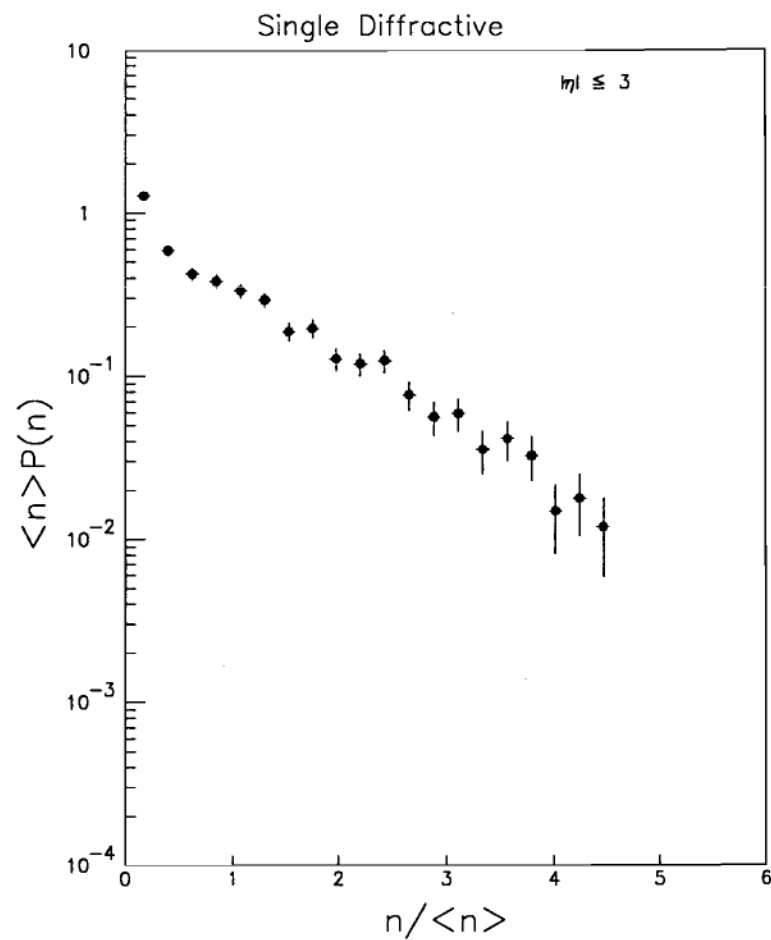


Figure 4.21: KNO  $\psi$  plot for the simulated single diffractive events at  $\sqrt{s} = 1.8$  TeV.

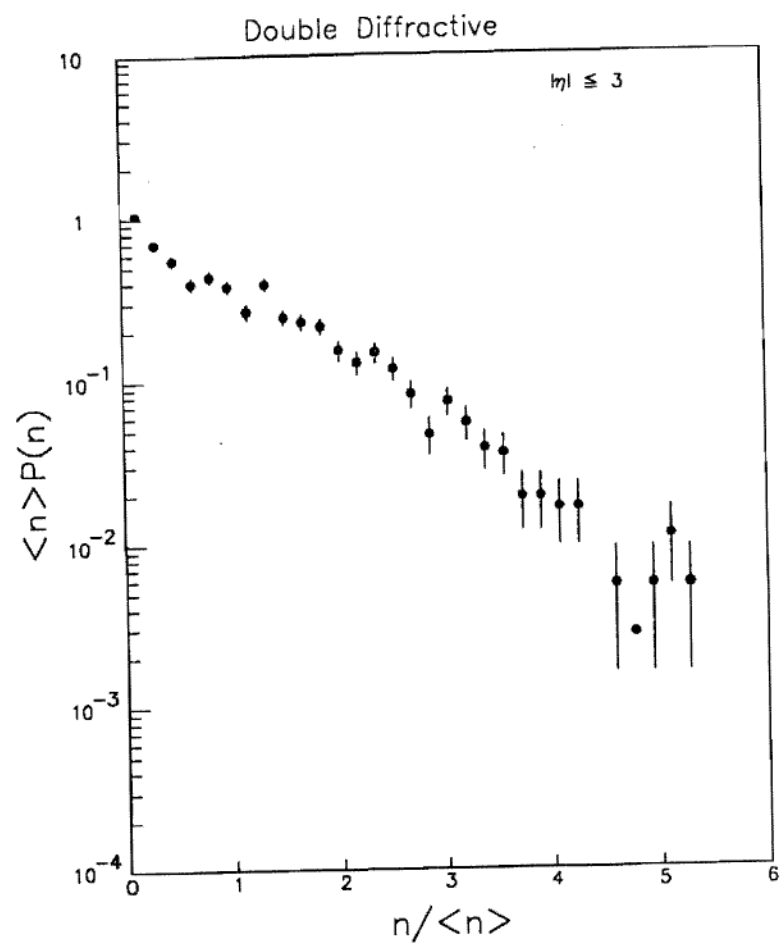


Figure 4.22: KNO  $\psi$  plot for the simulated double diffractive events at  $\sqrt{s} = 1.8$  TeV.

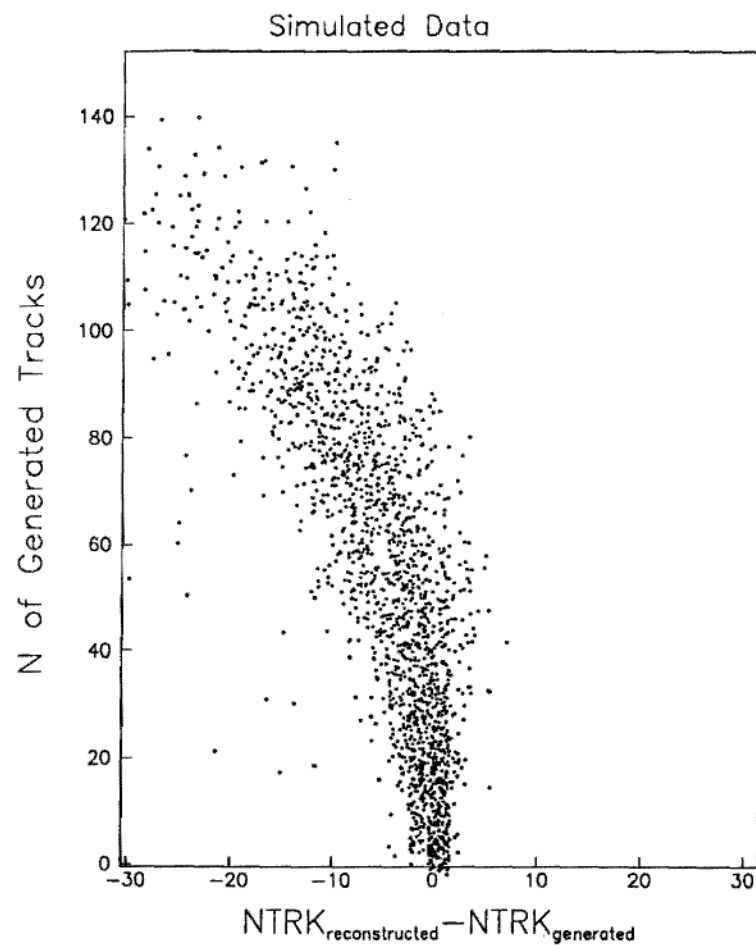


Figure 4.23: The number of generated tracks in the simulation is plotted against (the number of reconstructed tracks - the number of generated tracks). The  $|\eta|$  range was less than 3.0. The simulation had a uniform multiplicity from 0 to 150. The number of reconstructed tracks is after applying the track selection.

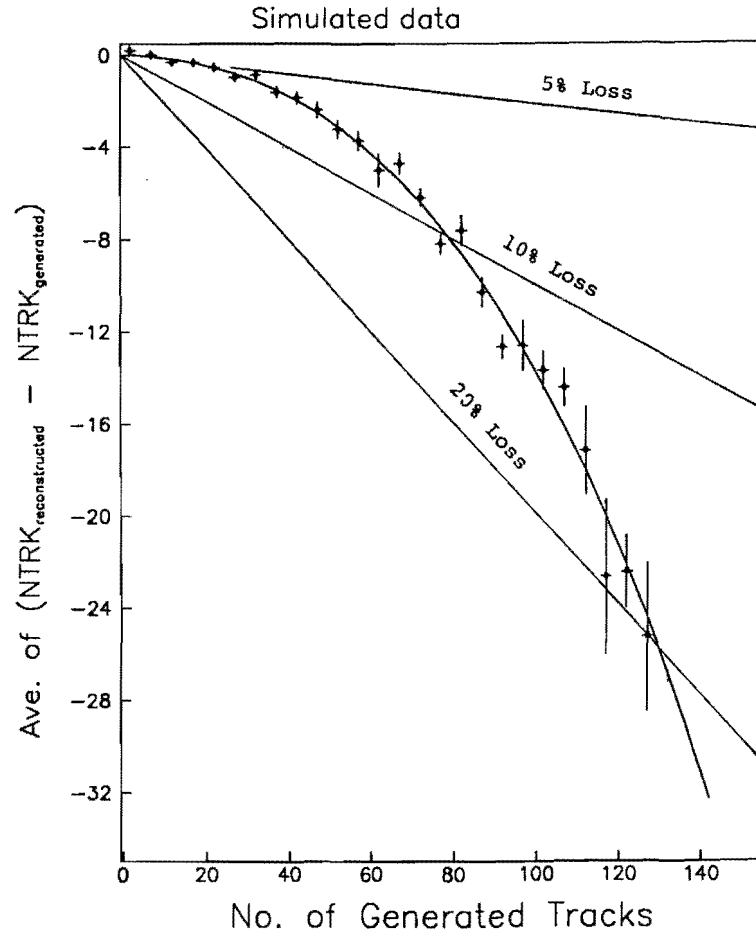


Figure 4.24: Average of  $\Delta N_{trk}$  versus  $N_{gen}$ . The error bars are statistical ones. The curve is a fit to  $p1 \cdot N_{gen} + p2 \cdot N_{gen}^2 + p3 \cdot N_{gen}^3$ , where the values of  $p1$ ,  $p2$ , and  $p3$  are shown in the text. The loss in the number of tracks at constant rates of 5%, 10% and 20% are indicated by the three straight lines.

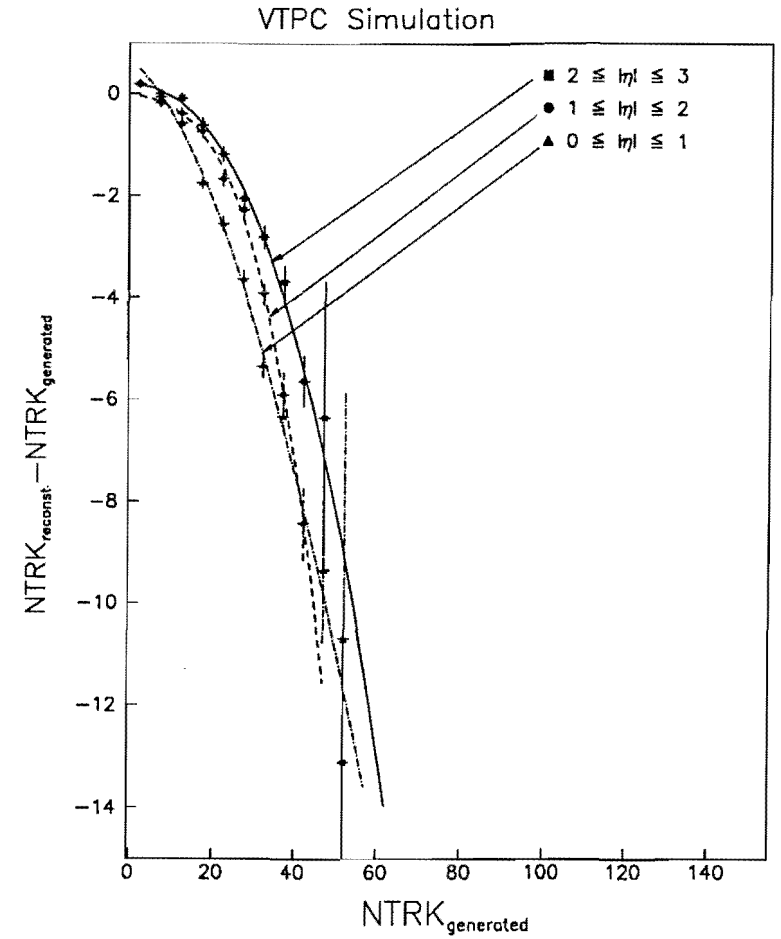


Figure 4.25: Average of  $\Delta N_{trk}$  versus  $N_{gen}$  for three  $\eta$  regions. The error bars are statistical. The curves are fits to  $p1 \cdot N_{gen} + p2 \cdot N_{gen}^2 + p3 \cdot N_{gen}^3$ .

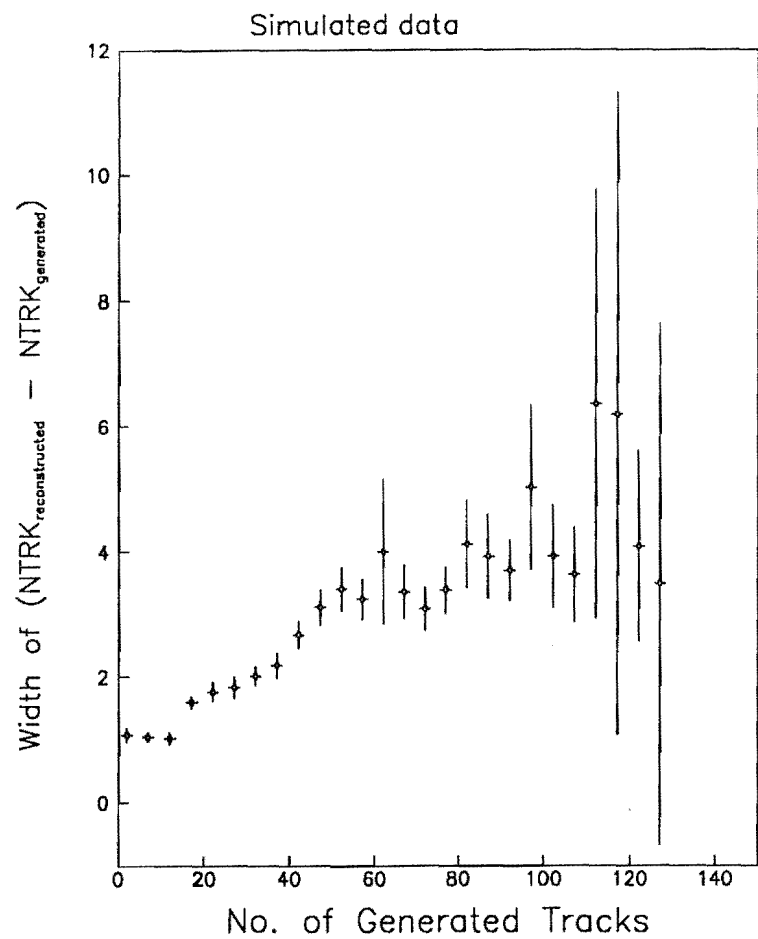


Figure 4.26: Rms width of  $\Delta N_{trk}$  versus  $N_{gen}$ . The error bars are statistical.

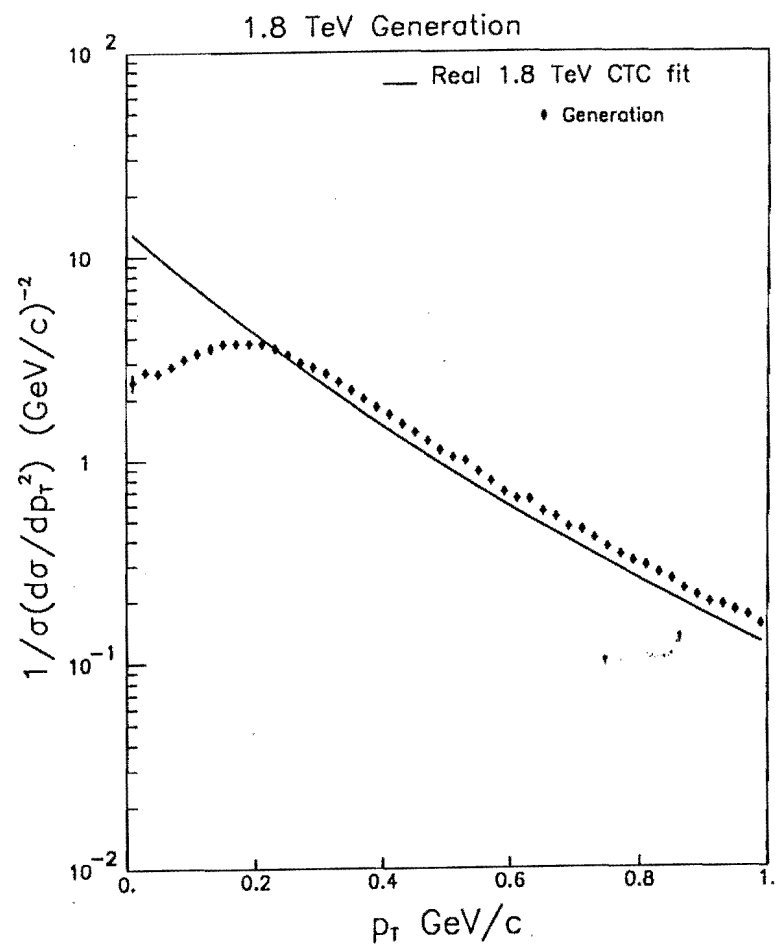


Figure 4.27:  $p_T$  spectrum put into the Monte Carlo simulation. The <sup>vertical</sup> ~~horizontal~~ axis is the normalized invariant cross section. The errors are purely statistical.

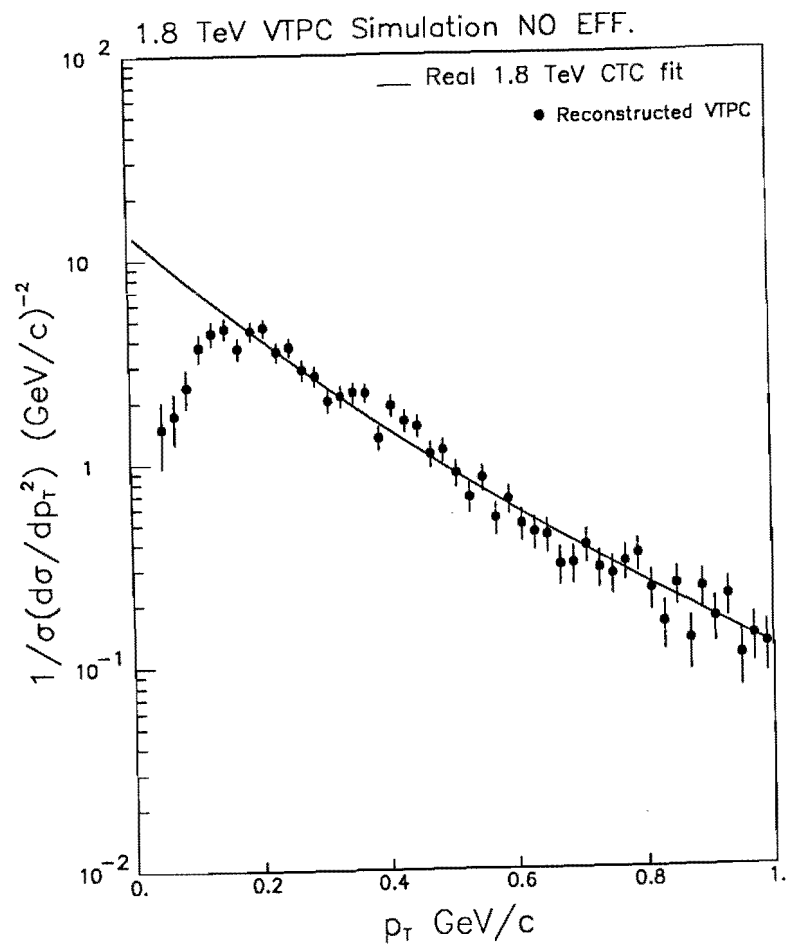


Figure 4.28:  $p_T$  spectrum with the VTPC pad for the simulation without any effects such as the particle decay and conversions. The vertical axis is the normalized invariant cross section. The errors are purely statistical.

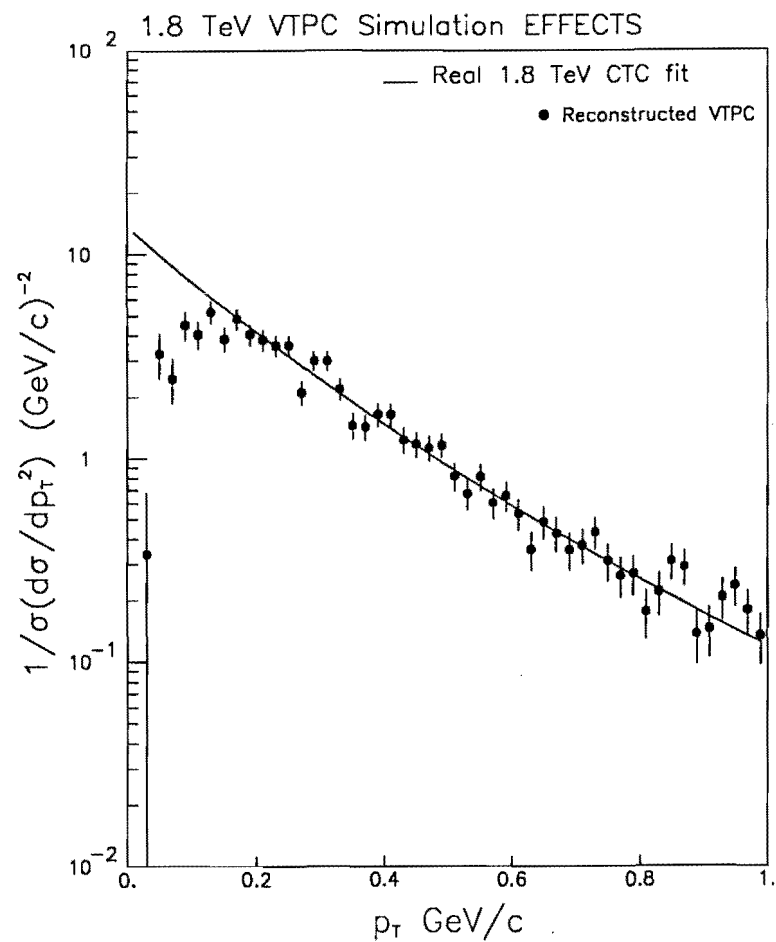


Figure 4.29:  $p_T$  spectrum with the VTPC pad for the simulation with all effects such as the particle decay and conversions. The vertical axis is the normalized invariant cross section. The errors are purely statistical.



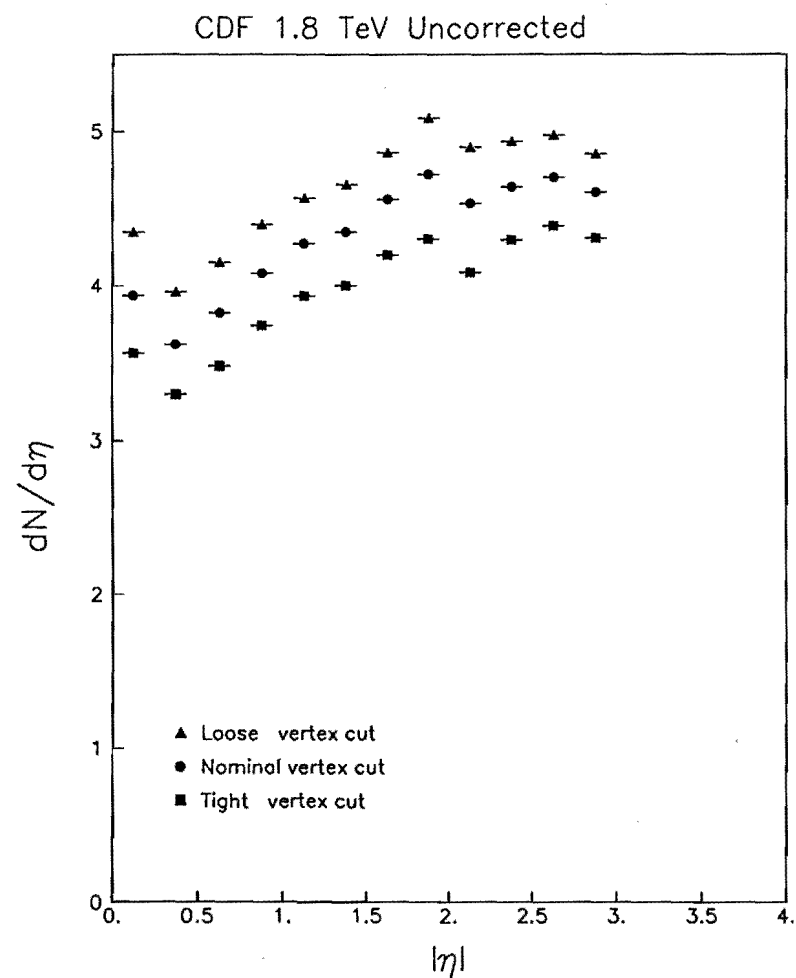


Figure 5.1: Uncorrected  $dN/d\eta$  at  $\sqrt{s} = 1.8$  TeV with three different track selections (the vertex cuts). The tight cut is  $|Z_{off}| \leq 3.0$ , the nominal cut is  $|Z_{off}| \leq 4.0$ , and the loose cut is  $|Z_{off}| \leq 6.0$ . The error bars are statistical.

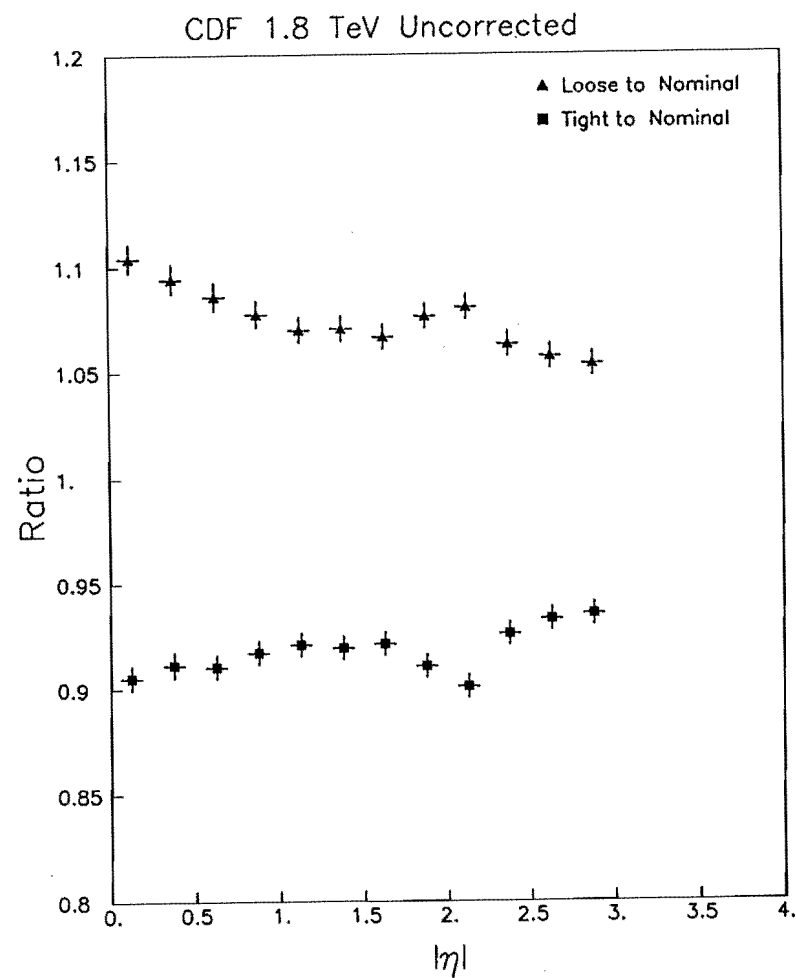


Figure 5.2: Ratio of  $dN/d\eta$  with the tight and loose cut to  $dN/d\eta$  with the nominal cut. (1.8 TeV) The difference in the vertex cut results in about 5-6 % of changes in  $dN/d\eta$ . The error bars are statistical.

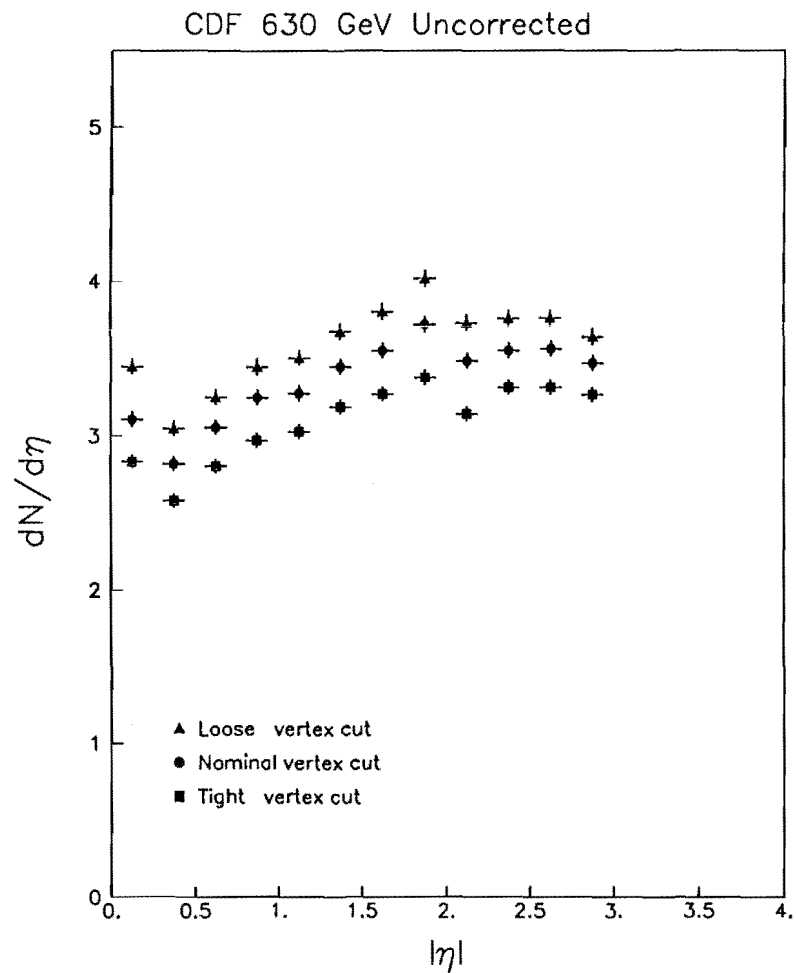


Figure 5.3: Uncorrected  $dN/d\eta$  at  $\sqrt{s} = 630$  GeV with three different vertex cuts. The error bars are statistical.

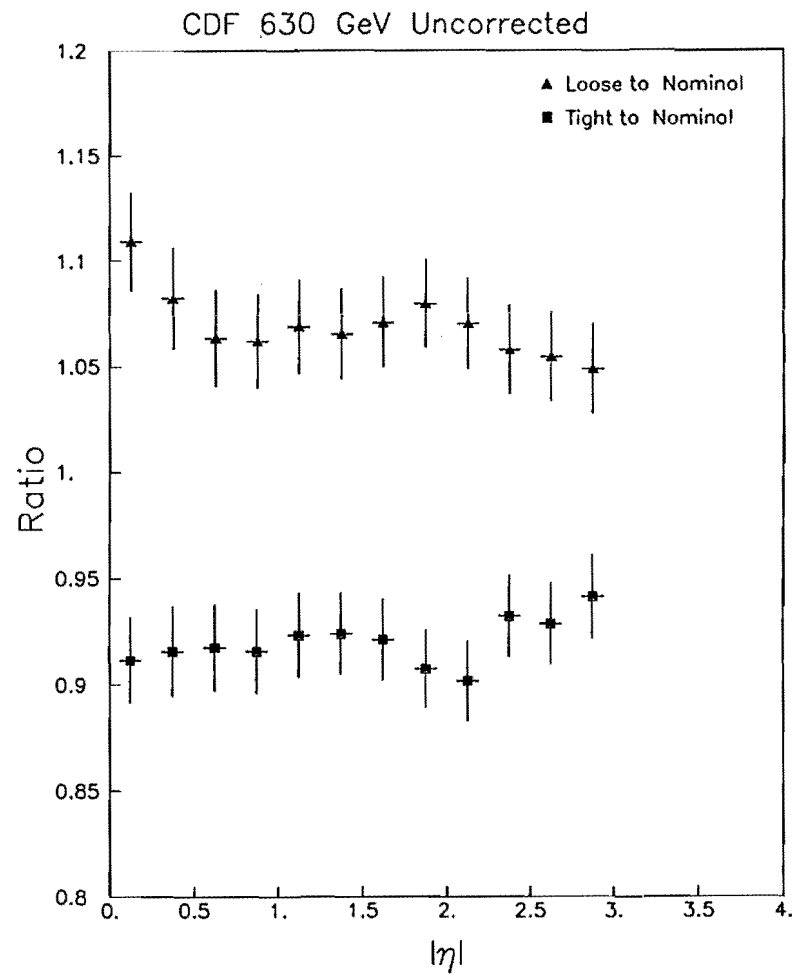


Figure 5.4: Ratio of  $dN/d\eta$  with the tight and loose cut to  $dN/d\eta$  with the nominal cut (630 GeV). The error bars are statistical. The ratios at  $\sqrt{s} = 630$  GeV are identical to those at 1.8 TeV (figure 5.2) within errors.

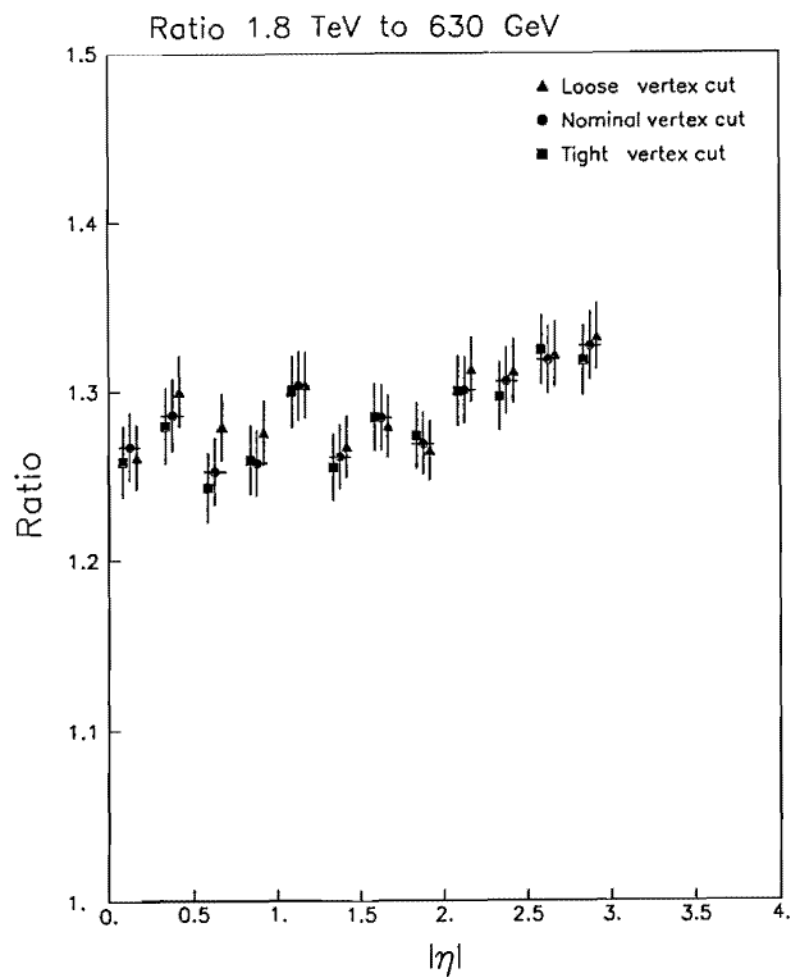


Figure 5.5: Ratio of  $dN/d\eta$  at  $\sqrt{s} = 1.8$  TeV to  $dN/d\eta$  at  $\sqrt{s} = 630$  GeV. The ratio changes by 1-2% for different  $\eta$ . The error bars are statistical (2%) + systematic (2%).

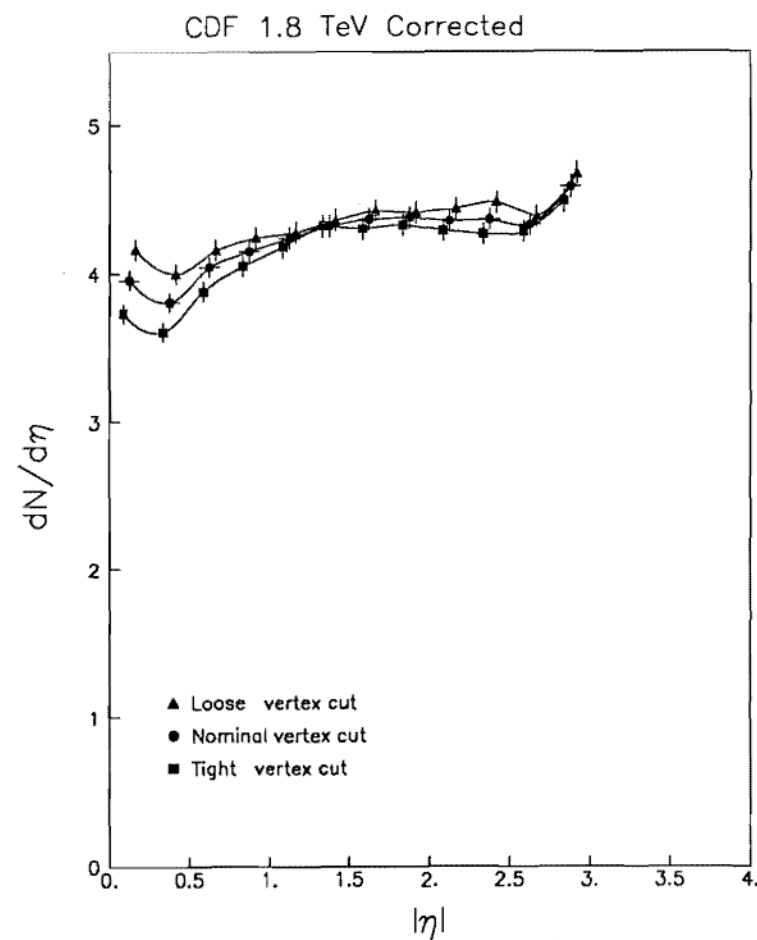


Figure 5.6:  $dN/d\eta$  at  $\sqrt{s} = 1.8$  TeV with all corrections. The error bars are purely statistical. The difference by the vertex cut is 1-2%.

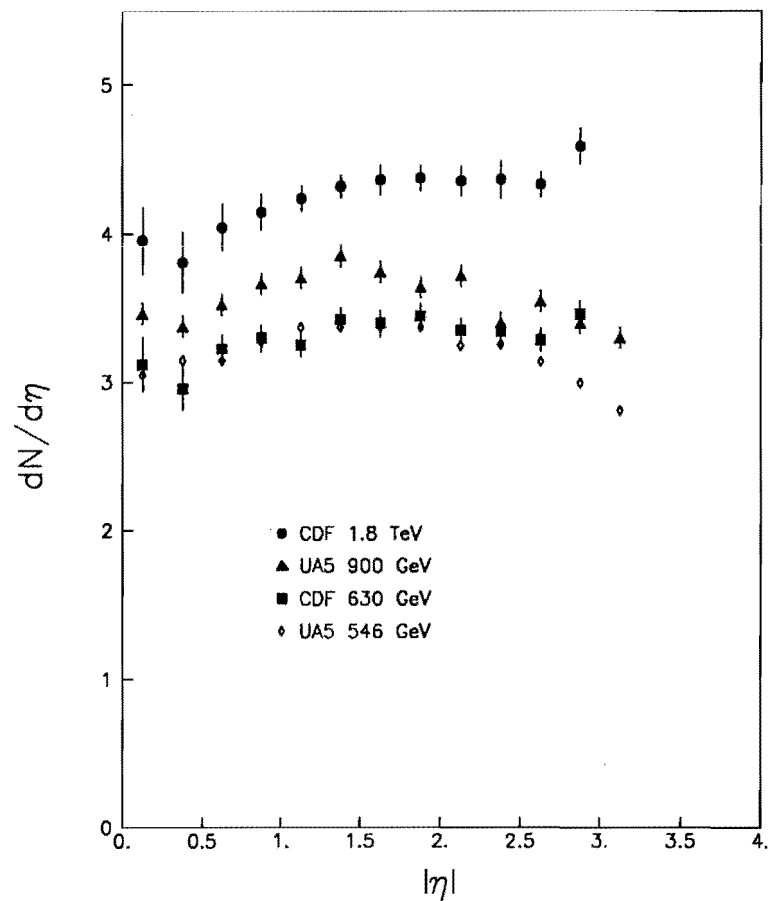


Figure 5.7:  $dN/d\eta$ 's at  $\sqrt{s} = 630$  GeV and 1.8 TeV. The error bars include the systematic errors as well as the statistical ones. The UA5 data at  $\sqrt{s} = 546$  GeV and 900 GeV are also shown [14].

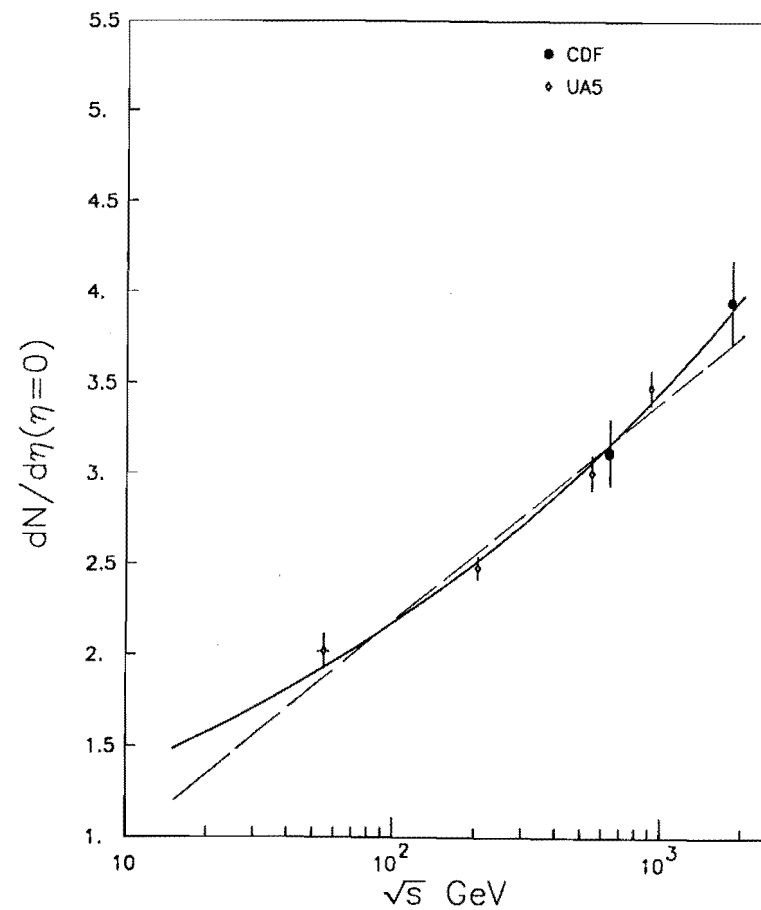


Figure 5.8:  $dN/d\eta(\eta=0)$  is plotted as a function of  $\sqrt{s}$  with the UA5 NSD data taken from ref. [14]. The errors are statistical and systematical. The dashed line is  $dN/d\eta(\eta=0) = -0.145 + 0.254 \ln s$  and the solid line is  $dN/d\eta(\eta=0) = 0.902s^{0.0962}$ .

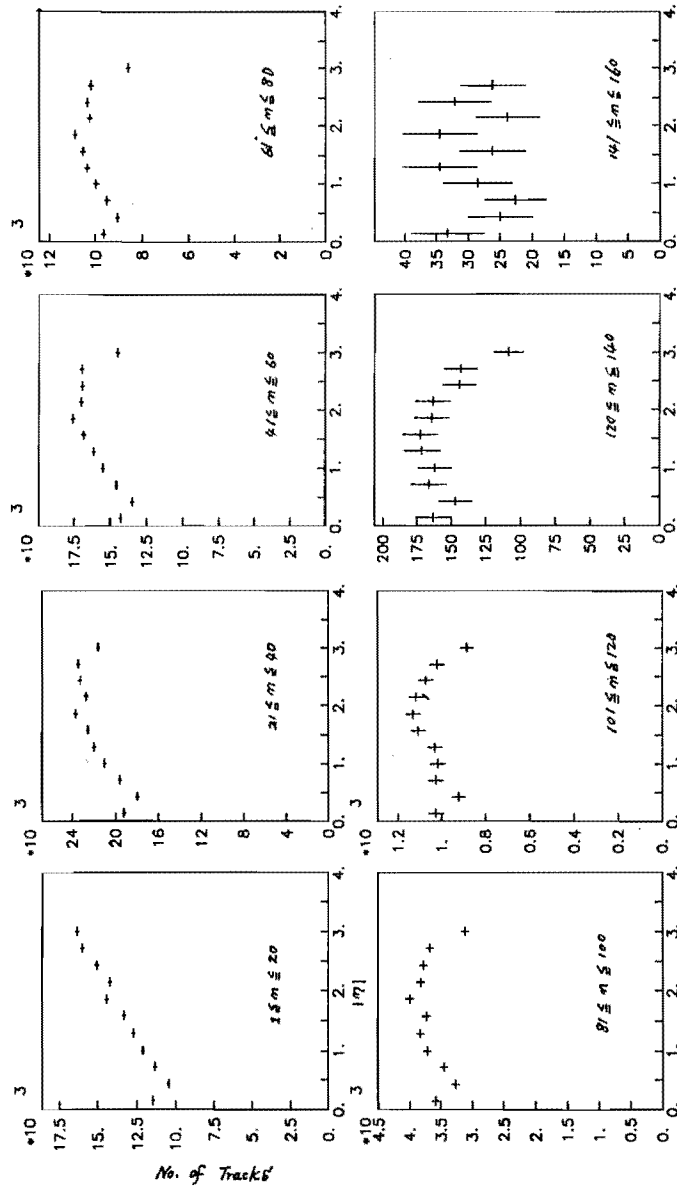


Figure 5.9: Pseudorapidity distributions of charged particles for various multiplicity ranges at  $\sqrt{s} = 1.8$  TeV. The multiplicity is for  $|\eta| \leq 3.0$ . The contribution from the central region (smaller  $|\eta|$ ) increases as the multiplicity increases.

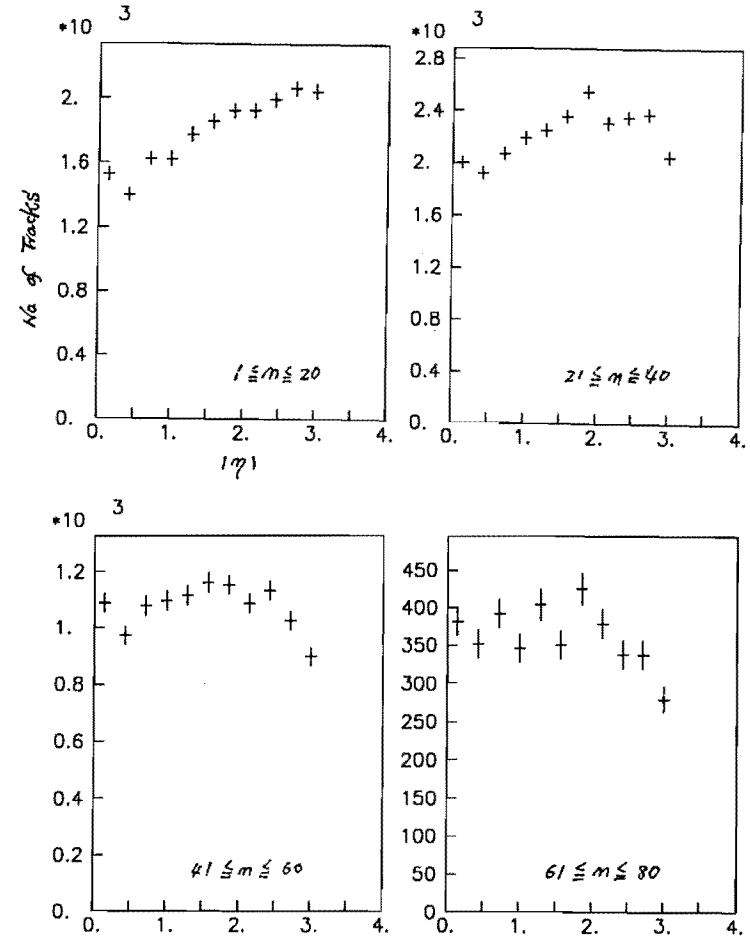


Figure 5.10: Pseudorapidity distributions of charged particles for various multiplicity ranges at  $\sqrt{s} = 630$  GeV. The multiplicity is for  $|\eta| \leq 3.0$ . Similarly to 1.8 TeV, the contribution from the central region (smaller  $|\eta|$ ) increases as the multiplicity increases.

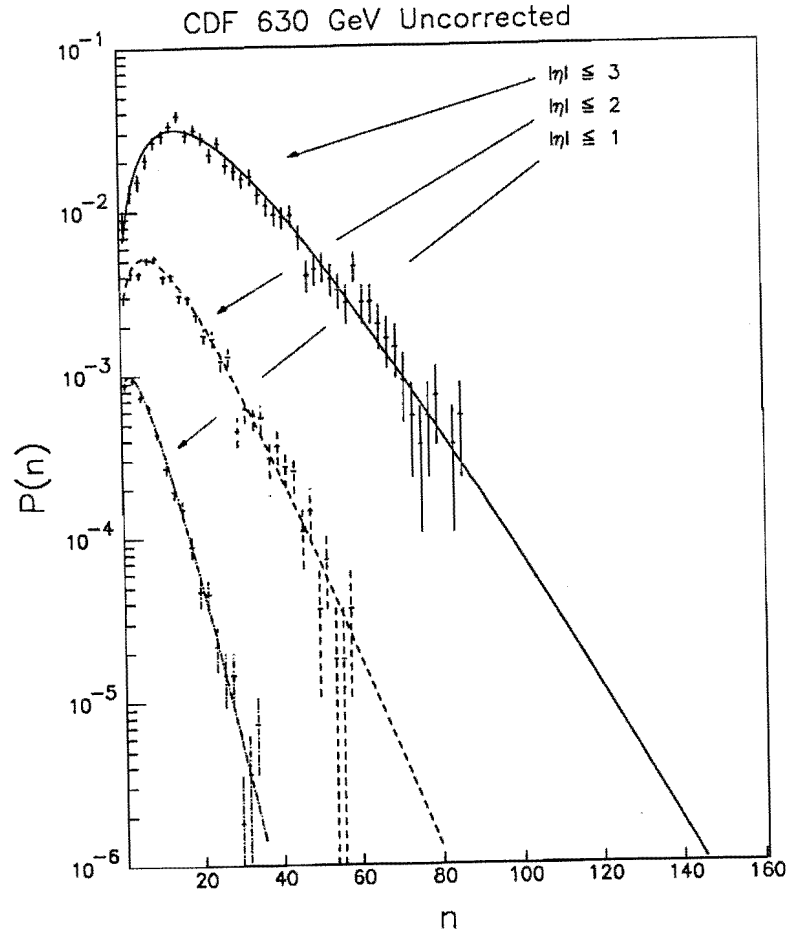


Figure 5.11: Charged particle multiplicities at  $\sqrt{s} = 630$  GeV for  $|\eta| \leq 1.0$ ,  $\leq 2.0$ , and  $\leq 3.0$ . The vertical axis is the probability density and multiplied by 0.1 for  $|\eta| \leq 2.0$  and by 0.01 for  $|\eta| \leq 1.0$ . The curves are the fitted negative binomial functions. The fit parameters are summarized in table 5.7.

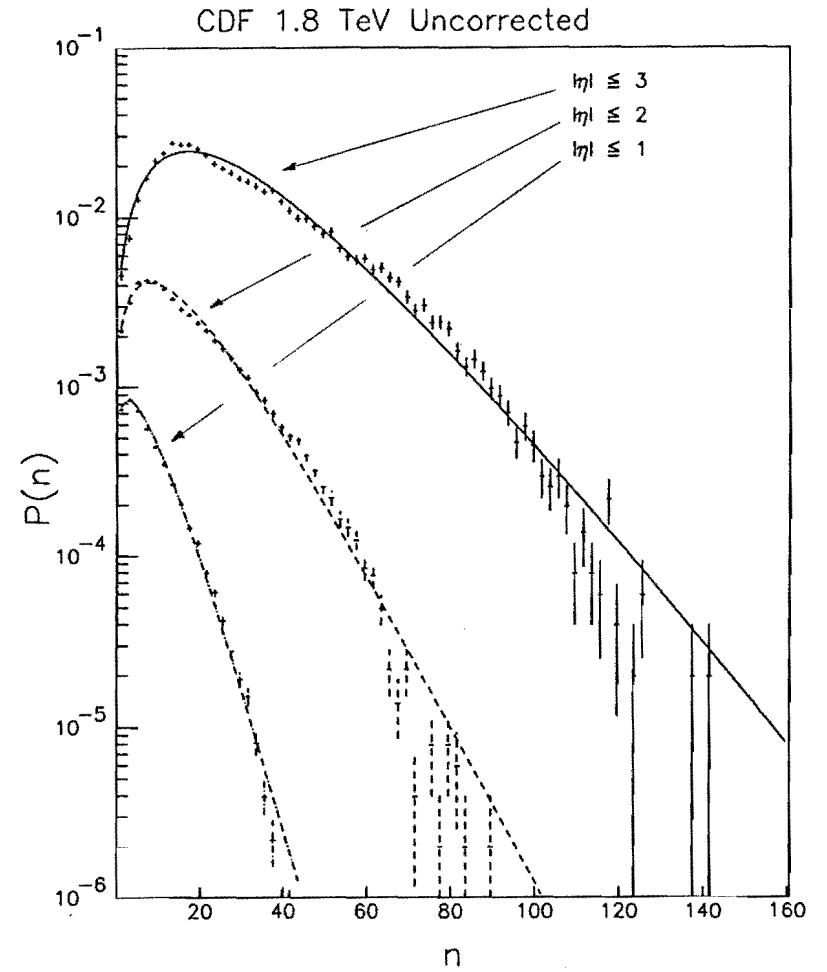


Figure 5.12: Charged particle multiplicities at  $\sqrt{s} = 1.8$  TeV for  $|\eta| \leq 1.0$ ,  $\leq 2.0$ , and  $\leq 3.0$ . The vertical axis is the probability density and multiplied by 0.1 for  $|\eta| \leq 2.0$  and by 0.01 for  $|\eta| \leq 1.0$ . The curves are the fitted negative binomial functions. The fit parameters are summarized in table 5.7.

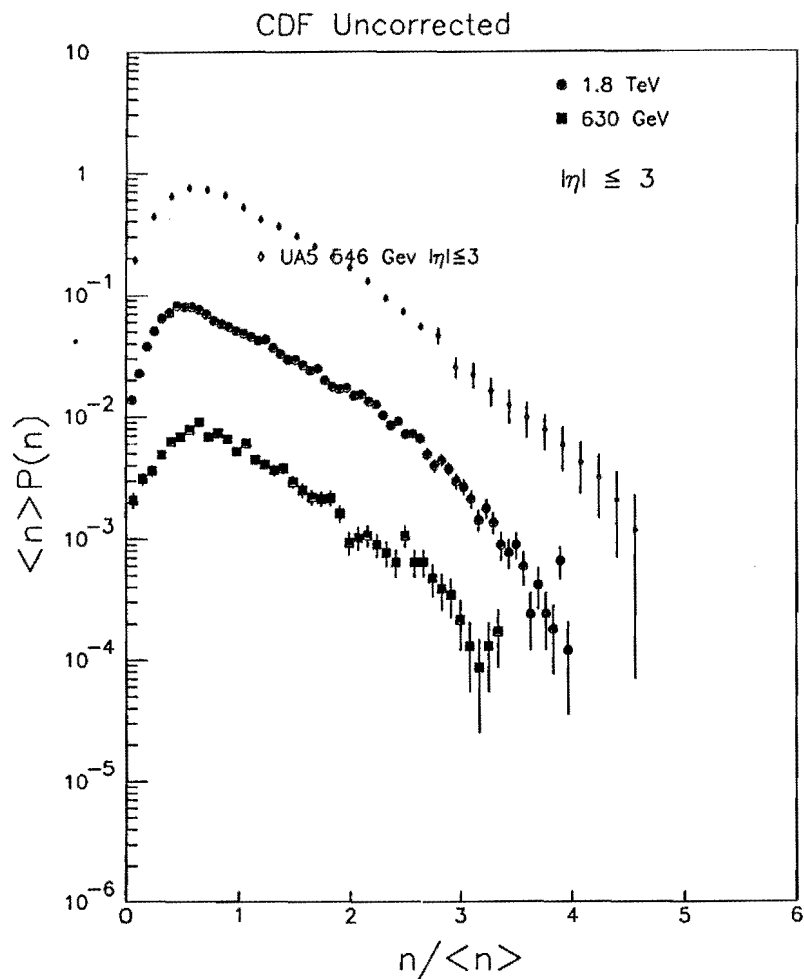


Figure 5.13: Comparison of uncorrected KNO distributions to UA5 KNO distribution. The vertical scale is multiplied by 0.1 and 0.01 for our 1.8 TeV data and 630 GeV data, respectively. The average multiplicities  $\langle n_{ch} \rangle$ 's are obtained from the fits to the negative binomial function.

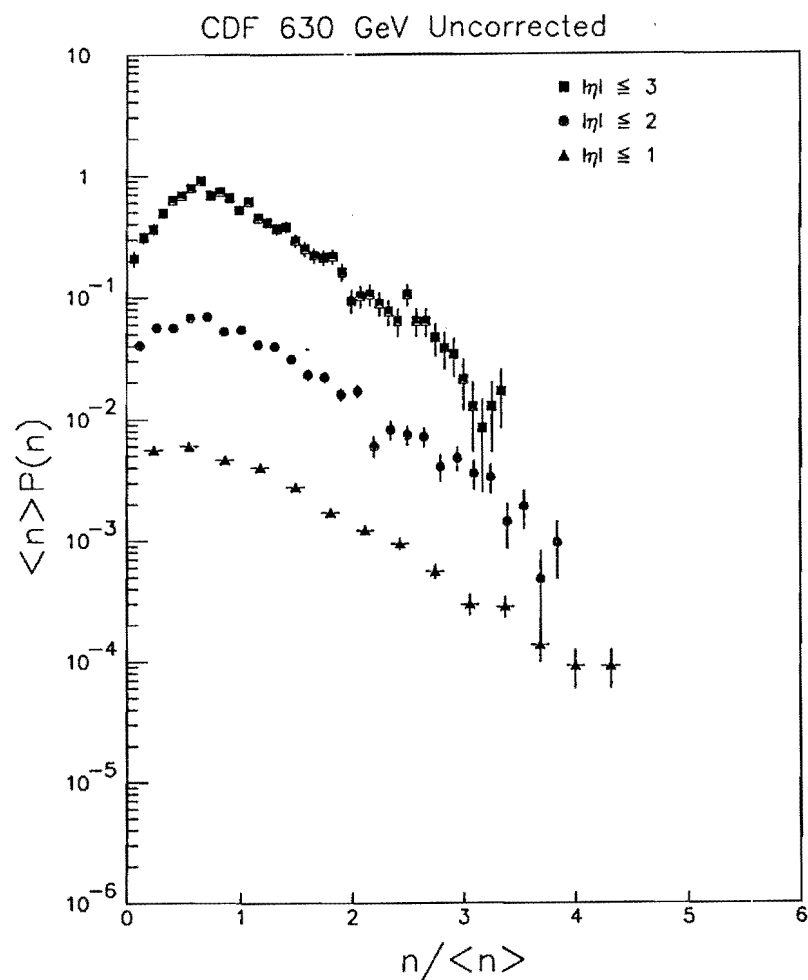


Figure 5.14: Uncorrected KNO distributions for  $|\eta| \leq 1.0$ ,  $\leq 2.0$ , and  $\leq 3.0$  at  $\sqrt{s} = 630$  GeV. The vertical scale is multiplied by 0.1 for  $|\eta| \leq 2.0$  and by 0.01 for  $|\eta| \leq 3.0$ .

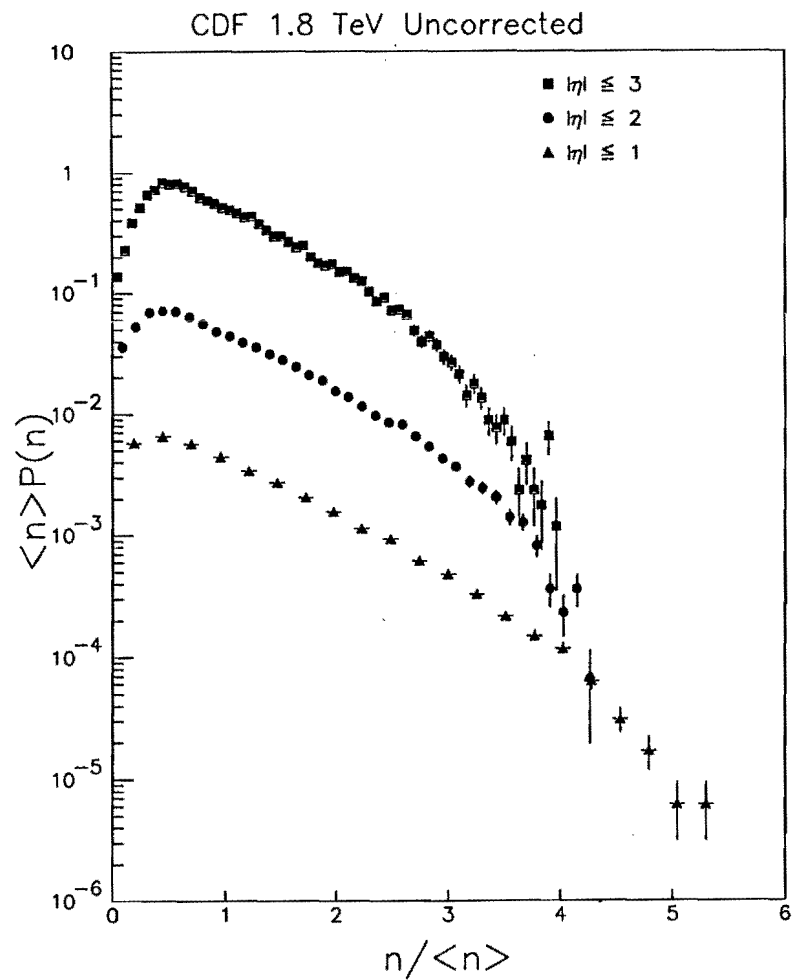


Figure 5.15: Uncorrected KNO distributions for  $|\eta| \leq 1.0$ ,  $\leq 2.0$ , and  $\leq 3.0$  at  $\sqrt{s} = 1.8$  TeV. The vertical scale is multiplied by 0.1 for  $|\eta| \leq 2.0$  and by 0.01 for  $|\eta| \leq 3.0$ .

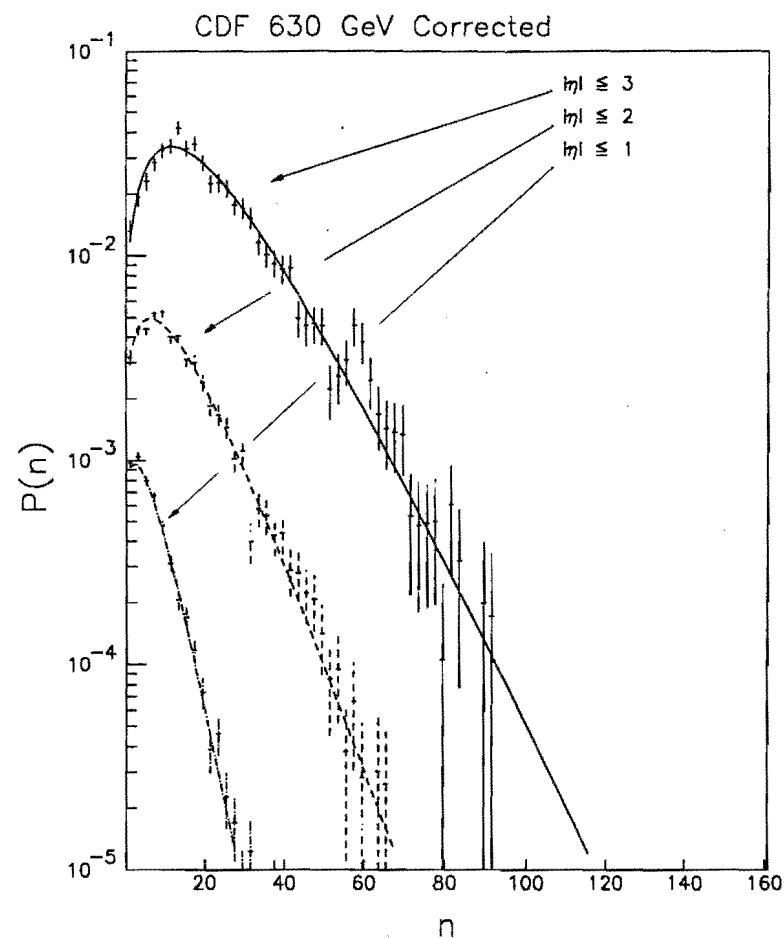


Figure 5.16: Multiplicity distribution at  $\sqrt{s} = 630$  GeV for  $|\eta| \leq 1.0$ ,  $\leq 2.0$ , and  $\leq 3.0$ . The vertical axis is the probability density (multiplied by 0.1 and 0.01 for  $\leq 2.0$ , and  $\leq 3.0$ , respectively) and the horizontal axis is the charged multiplicity. The curves are the fits to the negative binomial function.



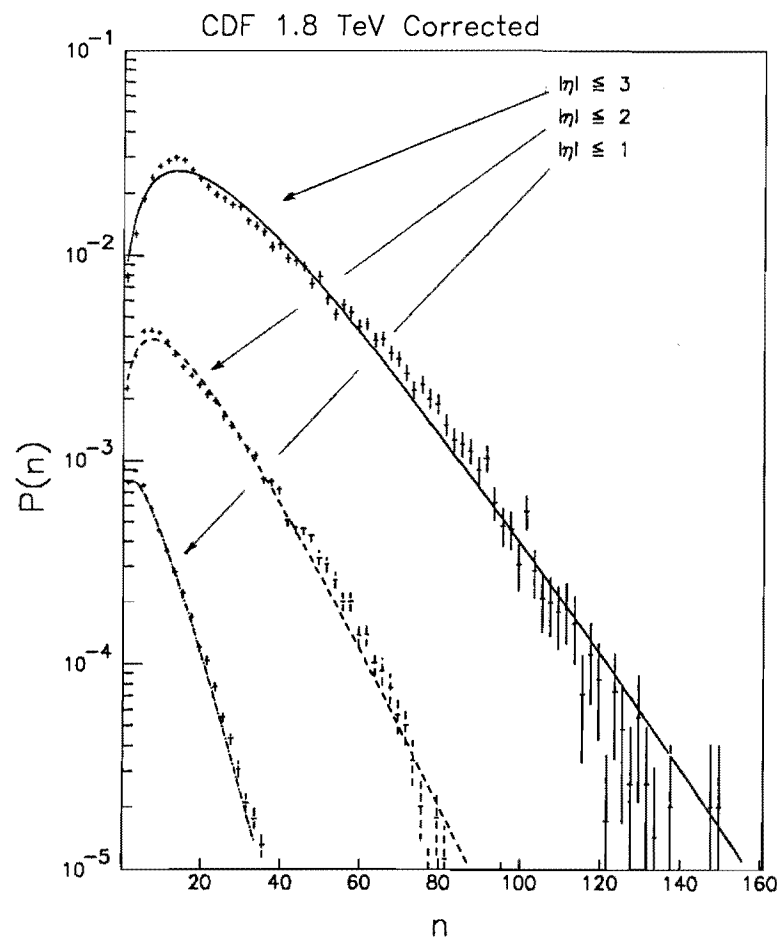


Figure 5.17: Multiplicity distributions at  $\sqrt{s} = 1.8$  TeV for  $|\eta| \leq 1.0$ ,  $1.0 < |\eta| \leq 2.0$ , and  $2.0 < |\eta| \leq 3.0$ . The vertical axis is the probability density (multiplied by 0.1 and 0.01 for  $1.0 \leq |\eta| \leq 2.0$  and  $2.0 \leq |\eta| \leq 3.0$ , respectively) and the horizontal axis is the charged multiplicity. The curves are the fits to the negative binomial function.

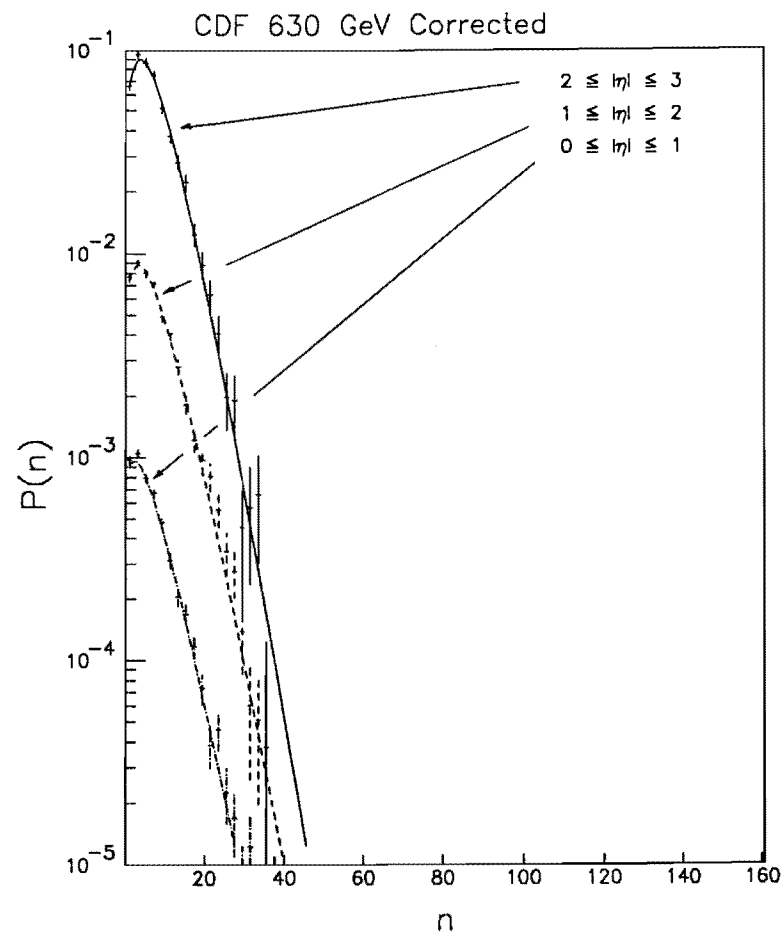


Figure 5.18: Multiplicity distributions at  $\sqrt{s} = 630$  GeV for  $0.0 \leq |\eta| \leq 1.0$ ,  $1.0 \leq |\eta| \leq 2.0$ , and  $2.0 \leq |\eta| \leq 3.0$ . The vertical axis is the probability density (multiplied by 0.1 and 0.01 for  $1.0 \leq |\eta| \leq 2.0$  and  $0.0 \leq |\eta| \leq 1.0$ , respectively) and the horizontal axis is the charged multiplicity. The curves are the fits to the negative binomial function.

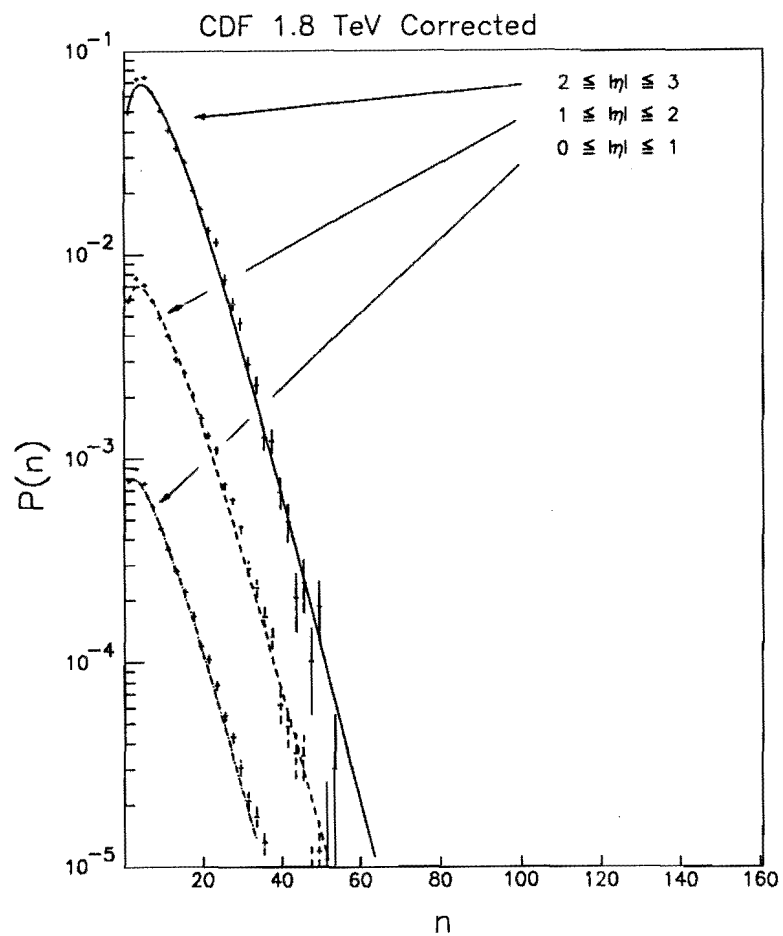


Figure 5.19: Multiplicity distribution at  $\sqrt{s} = 1.8$  TeV for  $0.0 \leq |\eta| \leq 1.0$ ,  $1.0 \leq |\eta| \leq 2.0$ , and  $2.0 \leq |\eta| \leq 3.0$ . The vertical axis is the probability density and the horizontal axis is the charged multiplicity. The curves are the fits to the negative binomial function.

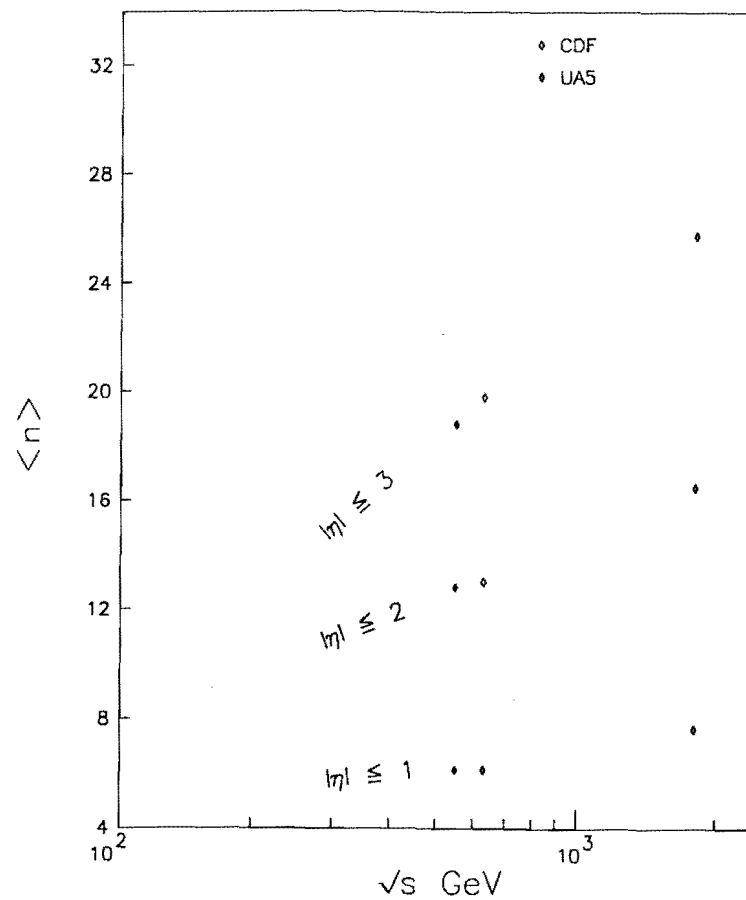


Figure 5.20: Average multiplicities obtained by the negative binomial fit versus  $\sqrt{s}$  for different  $|\eta|$  ranges. The UA5 data here are also obtained by the negative binomial fit.

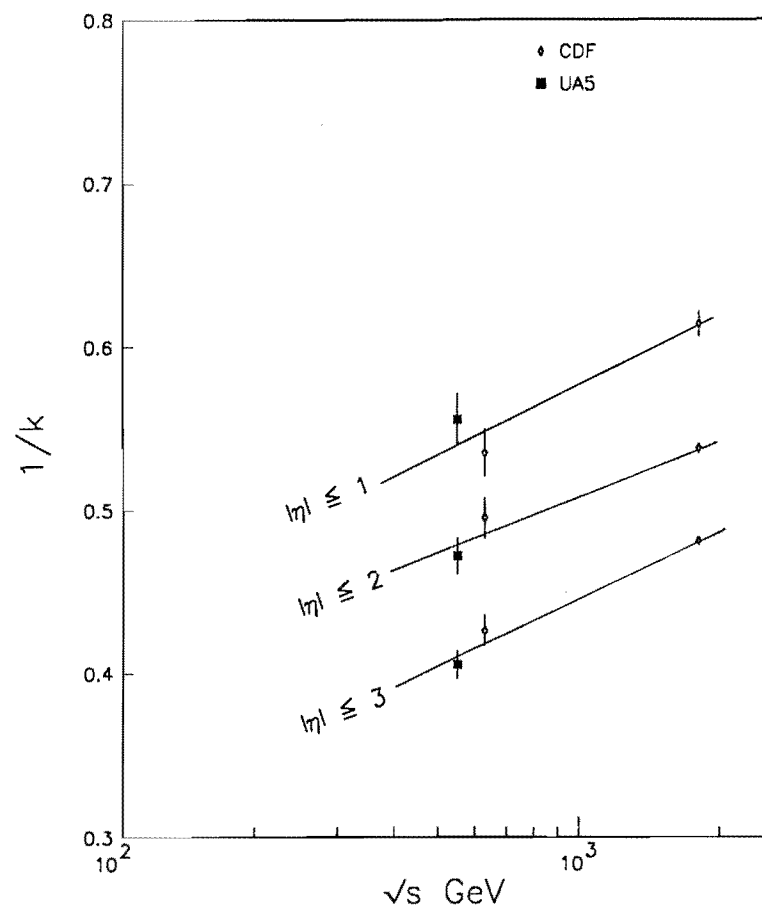


Figure 5.21:  $1/k$  versus  $\sqrt{s}$  for different  $|\eta|$  ranges. The lines are  $1/k = a + b \cdot \ln s$ . The values of  $a$  and  $b$  are shown in table 5.10.

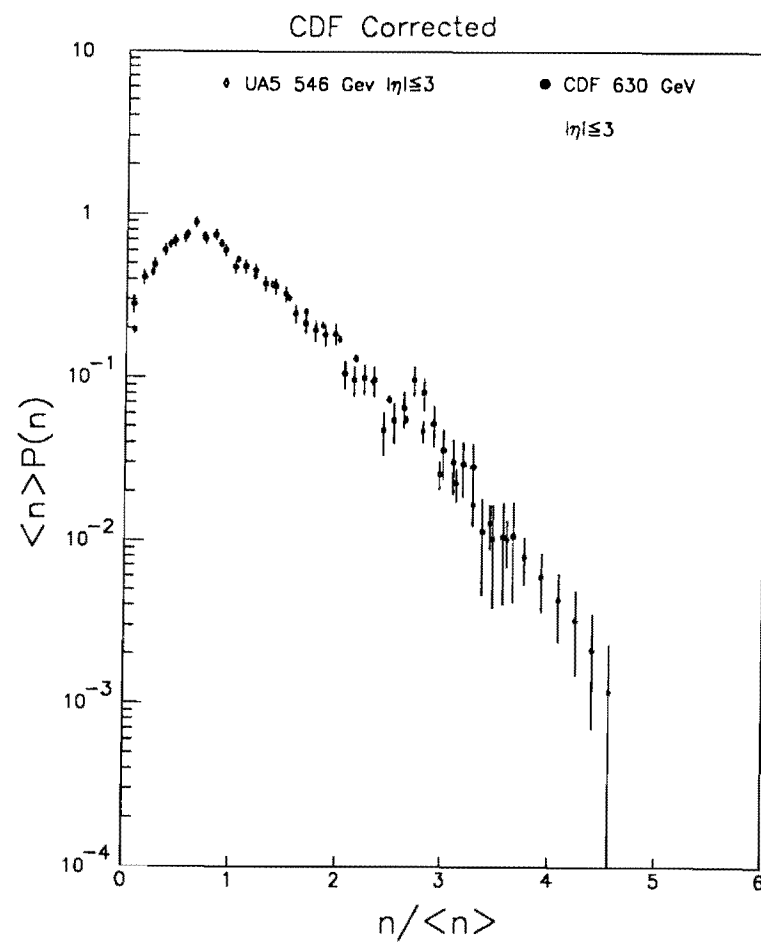


Figure 5.22: KNO  $\psi$  distribution at  $\sqrt{s} = 630$  GeV. The error bars are purely statistical. The UA5 data at  $\sqrt{s} = 546$  GeV are superimposed. Both agree very well.

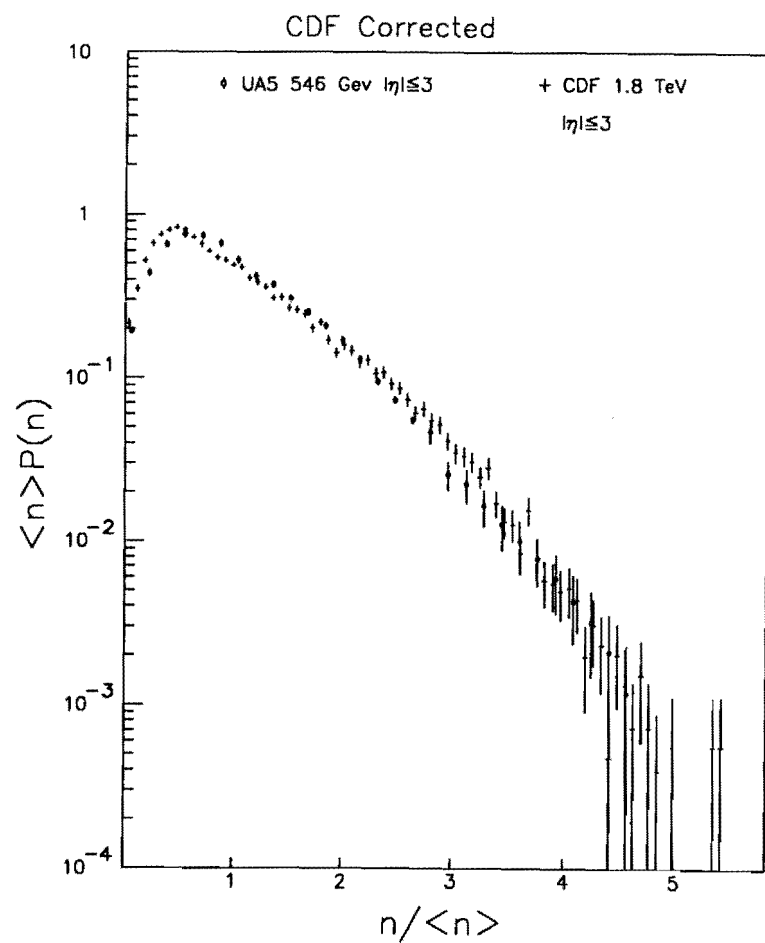


Figure 5.23: KNO  $\psi$  distribution at  $\sqrt{s} = 1.8$  TeV. The error bars are purely statistical. The UA5 data at  $\sqrt{s} = 546$  GeV are superimposed.

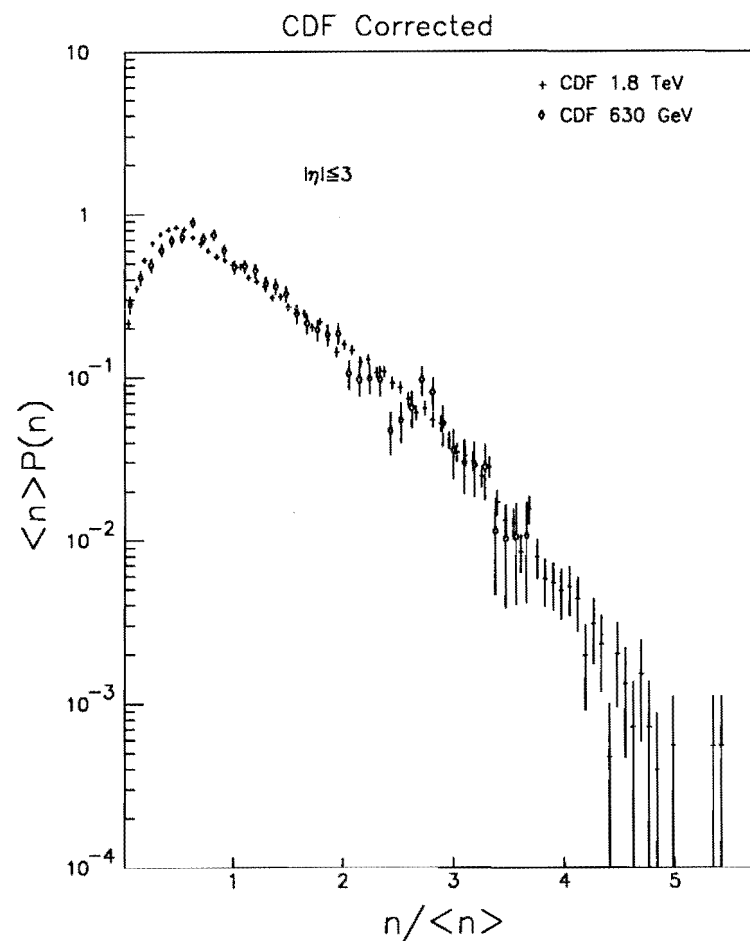


Figure 5.24: KNO  $\psi$  distribution at  $\sqrt{s} = 1.8$  TeV. The error bars are purely statistical. The CDF data at  $\sqrt{s} = 630$  GeV are superimposed.

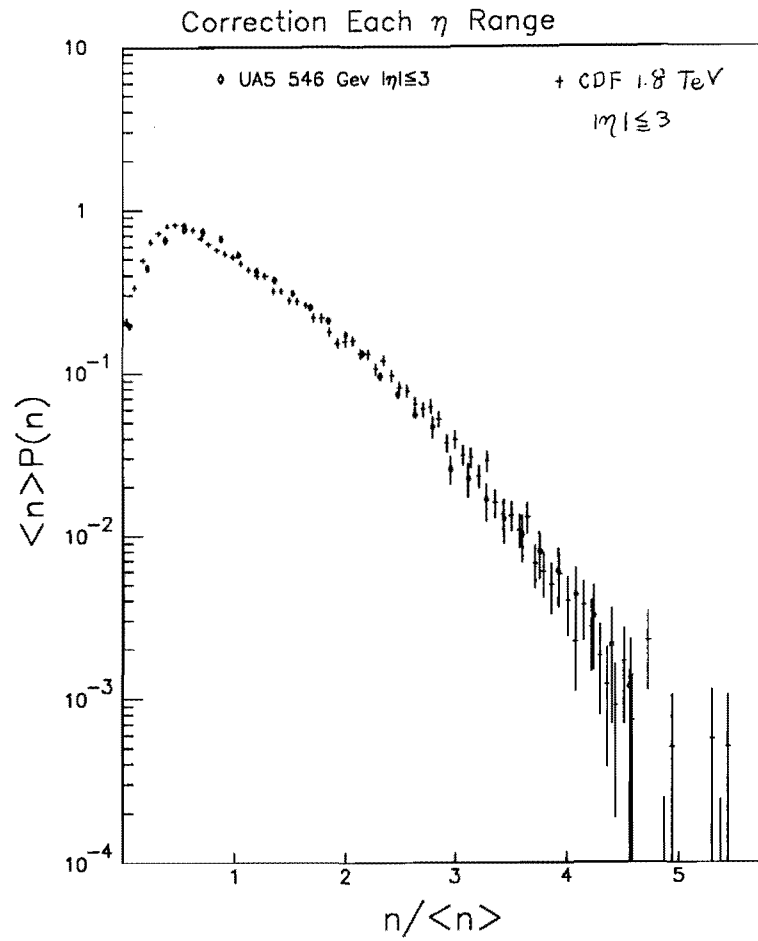


Figure : KNO distribution is shown <sup>with</sup> three  $|\eta|$  region at  $\sqrt{s}$  1.8 TeV.

independently corrected

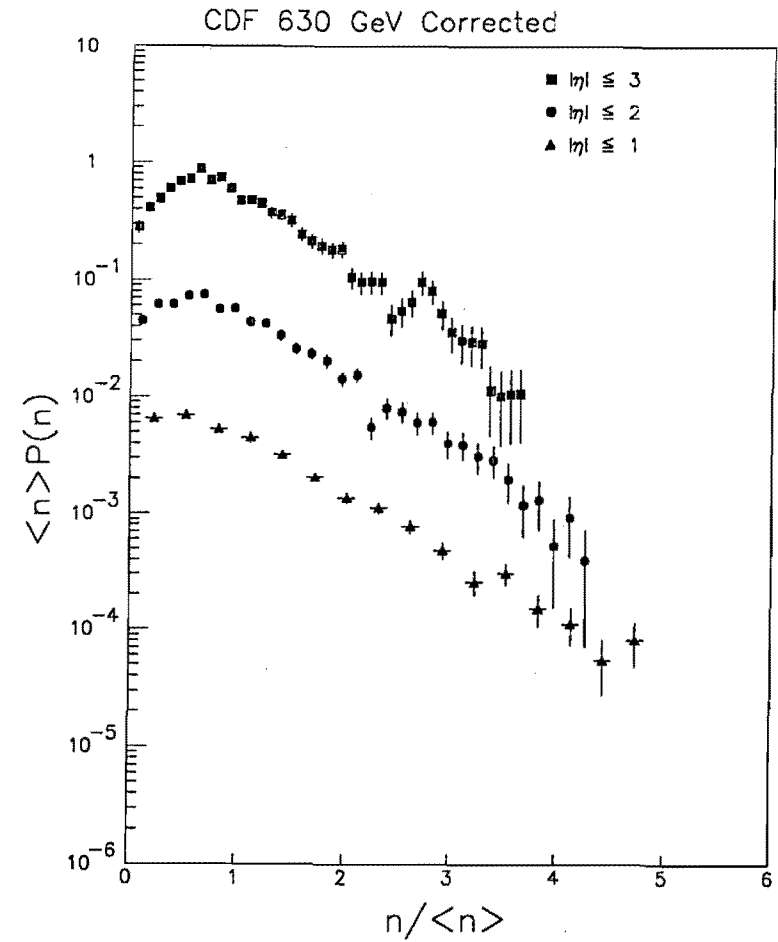


Figure 5.24: KNO distribution is shown for three  $|\eta|$  ranges at  $\sqrt{s} = 630$  GeV. The data for  $|\eta| \leq 2.0$  and  $|\eta| \leq 1.0$  are multiplied by 0.1 and 0.01, respectively.

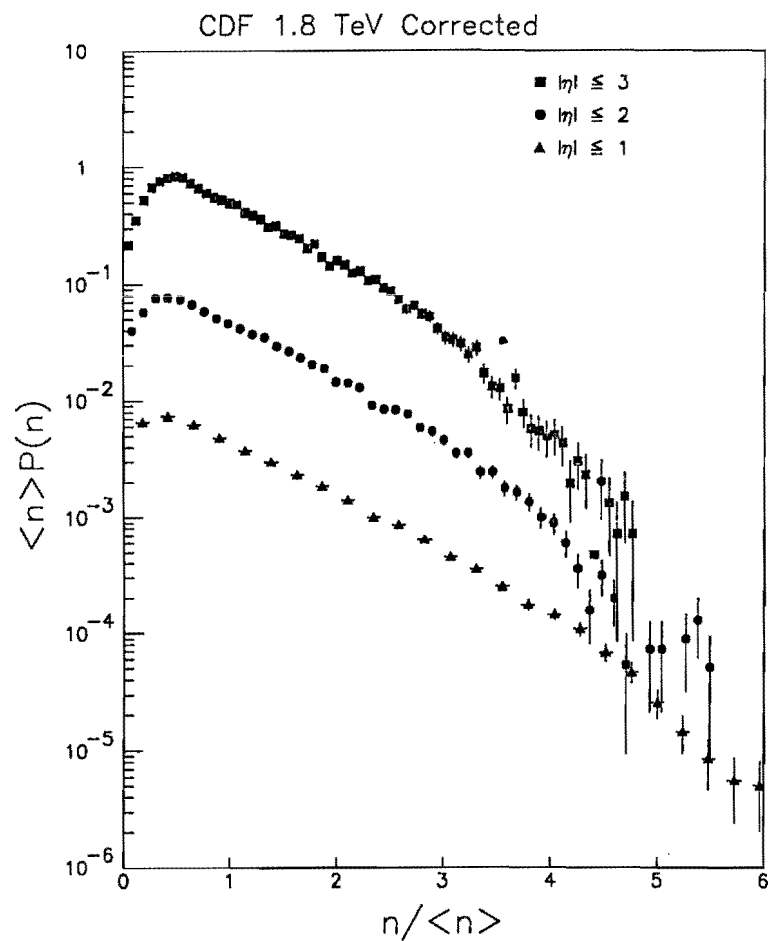


Figure 5.25: KNO distribution is shown for three  $|\eta|$  ranges at  $\sqrt{s} = 1.8$  TeV. The data for  $|\eta| \leq 2.0$  and  $|\eta| \leq 1.0$  are multiplied by 0.1 and 0.01, respectively.

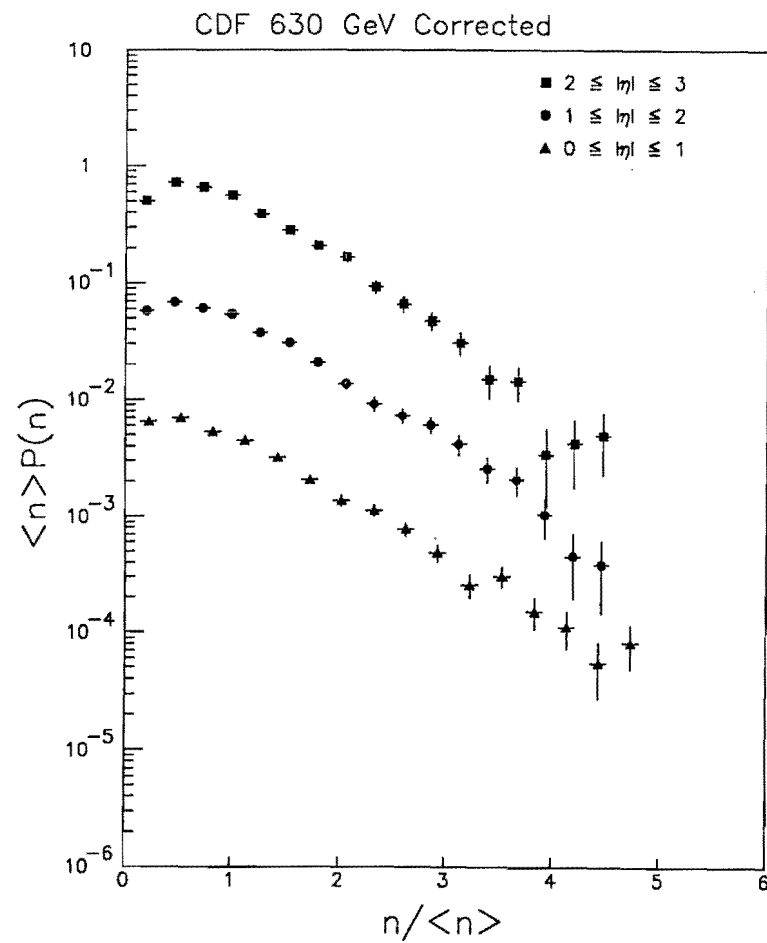


Figure 5.26: KNO distribution is shown for three  $|\eta|$  regions at  $\sqrt{s} = 630$  GeV. The data for  $1 \leq |\eta| \leq 2.0$  and  $0.0 \leq |\eta| \leq 1.0$  are multiplied by 0.1 and 0.01, respectively.

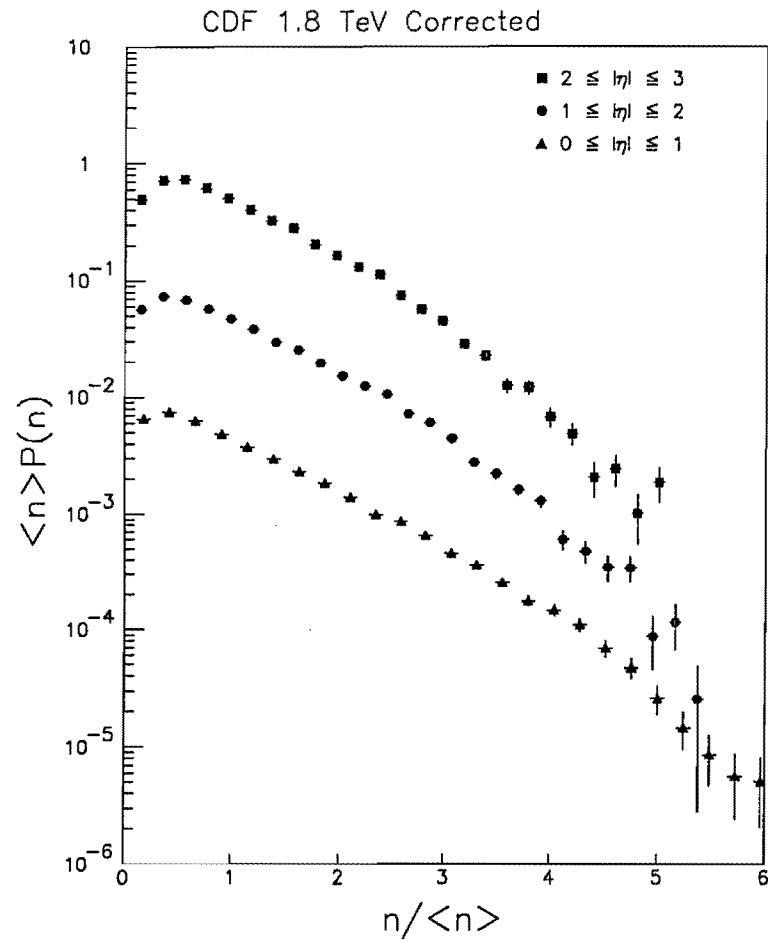


Figure 5.27: KNO distribution is shown for three  $|\eta|$  regions at  $\sqrt{s} = 1.8$  TeV. The data for  $1 \leq |\eta| \leq 2.0$  and  $0.0 \leq |\eta| \leq 1.0$  are multiplied by 0.1 and 0.01, respectively.

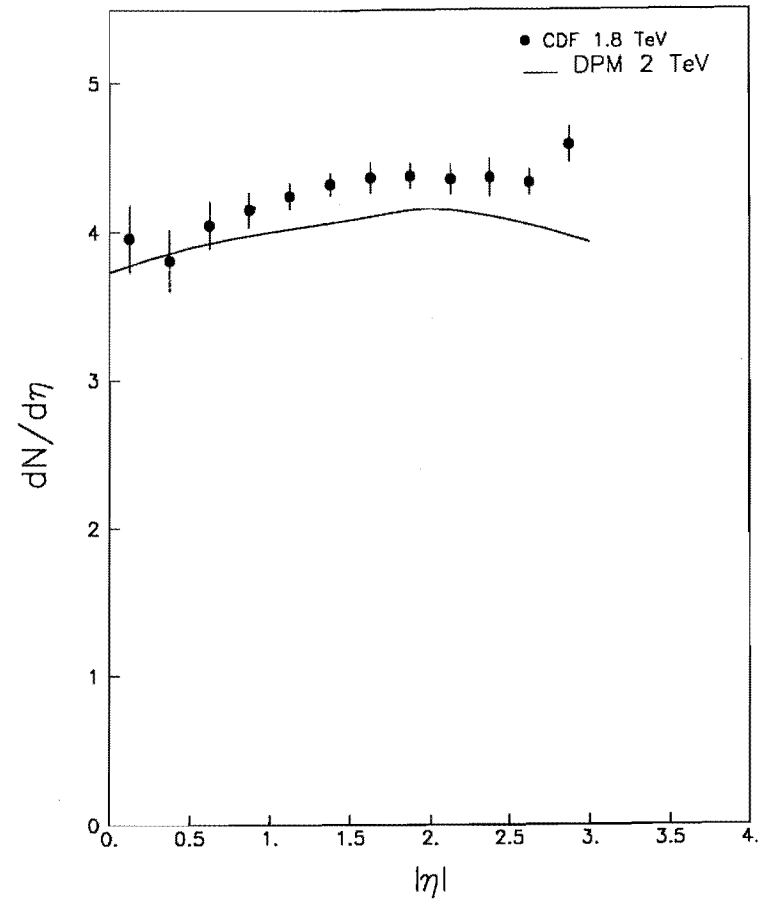


Figure 5.28: Comparison of the  $dN/d\eta$  at  $\sqrt{s} = 1.8$  TeV to the  $dN/d\eta$  at 2.0 TeV by the dual parton model [38].

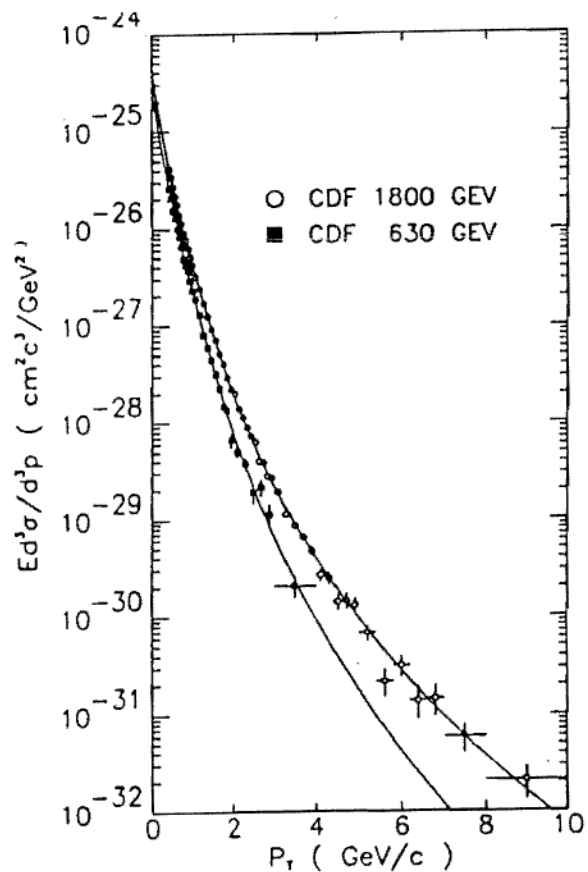


Figure 5.29: Inclusive cross sections for rapidity  $|Y| < 1.0$  measured with the CTC. The curves are the fits  $A p_o^n / (p_T + p_o)^n$  with  $p_o$  fixed at 1.3 GeV/c.

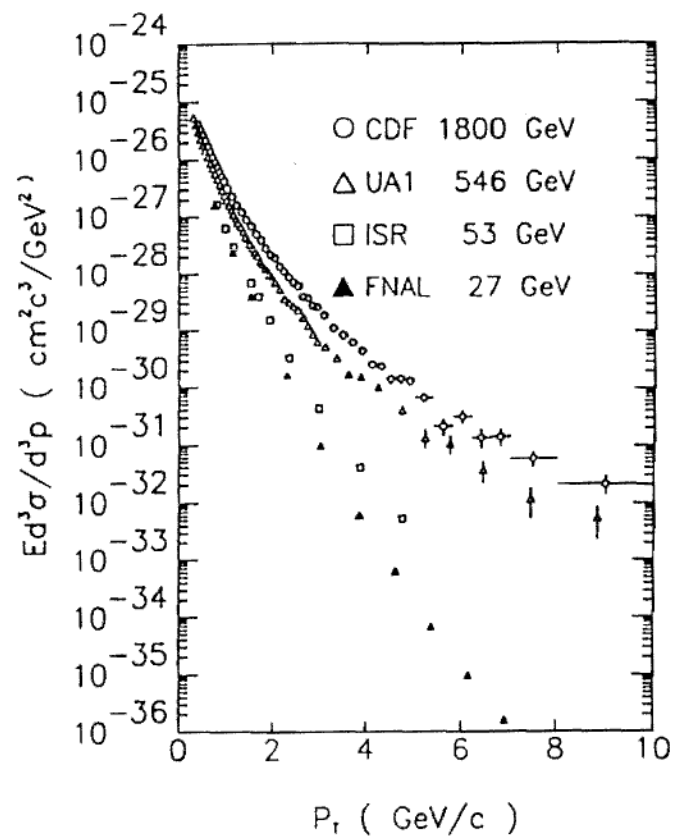


Figure 5.30: Energy Dependence of Inclusive Cross Sections. CP ( $Y=0$ ) Ref. [94], BS ( $Y=0$ ) Ref. [95], UA1 ( $|Y| < 2.5$ ) Ref. [87], and CDF CTC ( $|Y| < 1.0$ ).



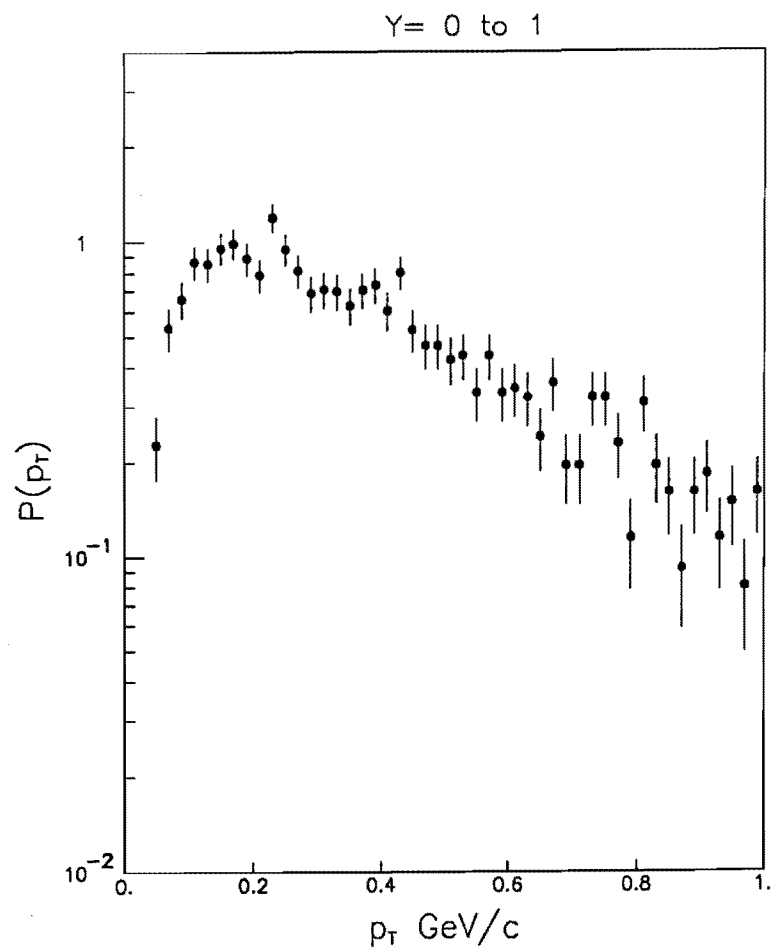


Figure 5.31:  $p_t$  spectrum measured with the VTPC pad for  $0.0 \leq |Y| \leq 1.0$  at  $\sqrt{s} = 1.8$  TeV. The vertical axis is the probability density of  $p_t$  in  $1/(\text{GeV}/c)$ . The errors are purely statistical.

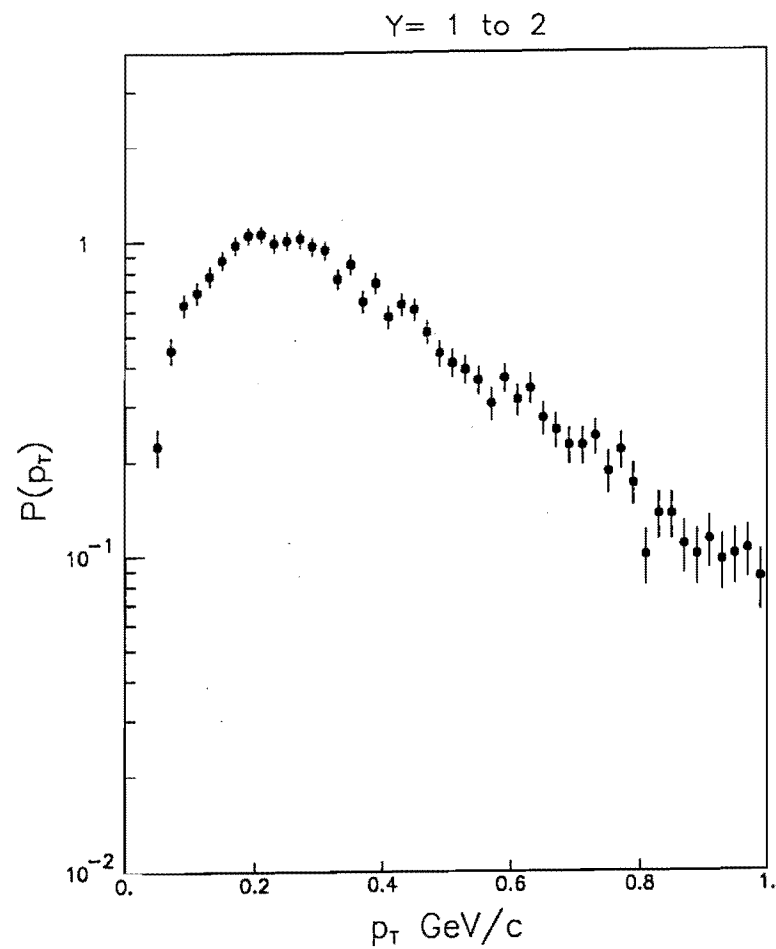


Figure 5.32:  $p_t$  spectrum measured with the VTPC pad for  $1.0 \leq |Y| \leq 2.0$  at  $\sqrt{s} = 1.8$  TeV. The vertical axis is the probability density of  $p_t$  in  $1/(\text{GeV}/c)$ . The errors are purely statistical.

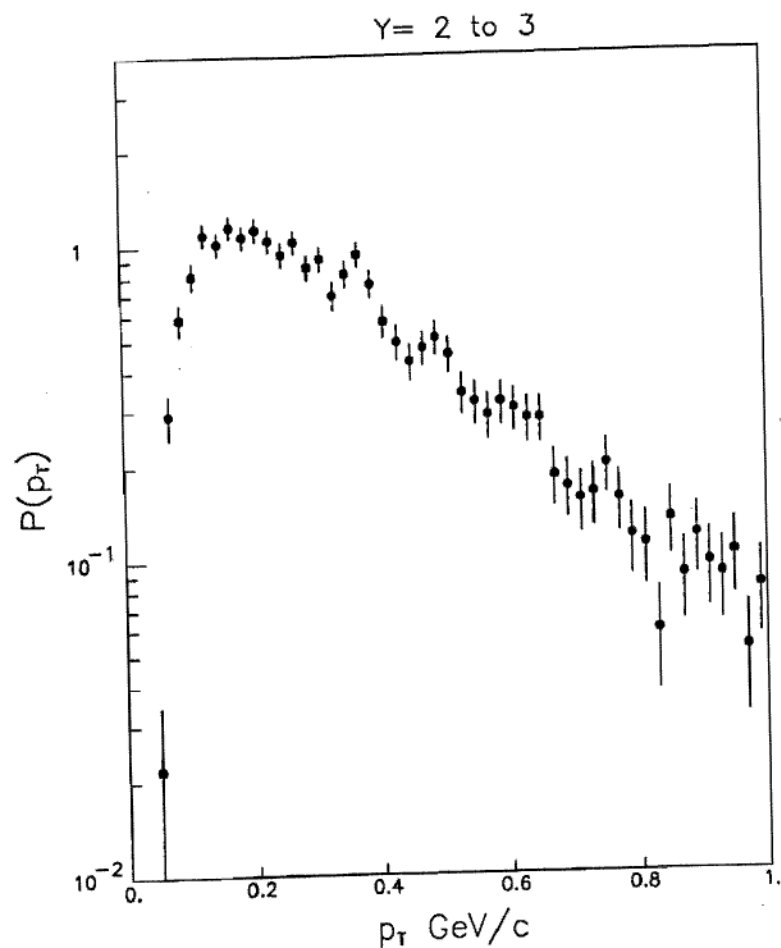


Figure 5.33:  $p_T$  spectrum measured with the VTPC pad for  $2.0 \leq |Y| \leq 3.0$  at  $\sqrt{s} = 1.8$  TeV. The vertical axis is the probability density of  $p_T$  in  $1/(\text{GeV}/c)$ . The errors are purely statistical.

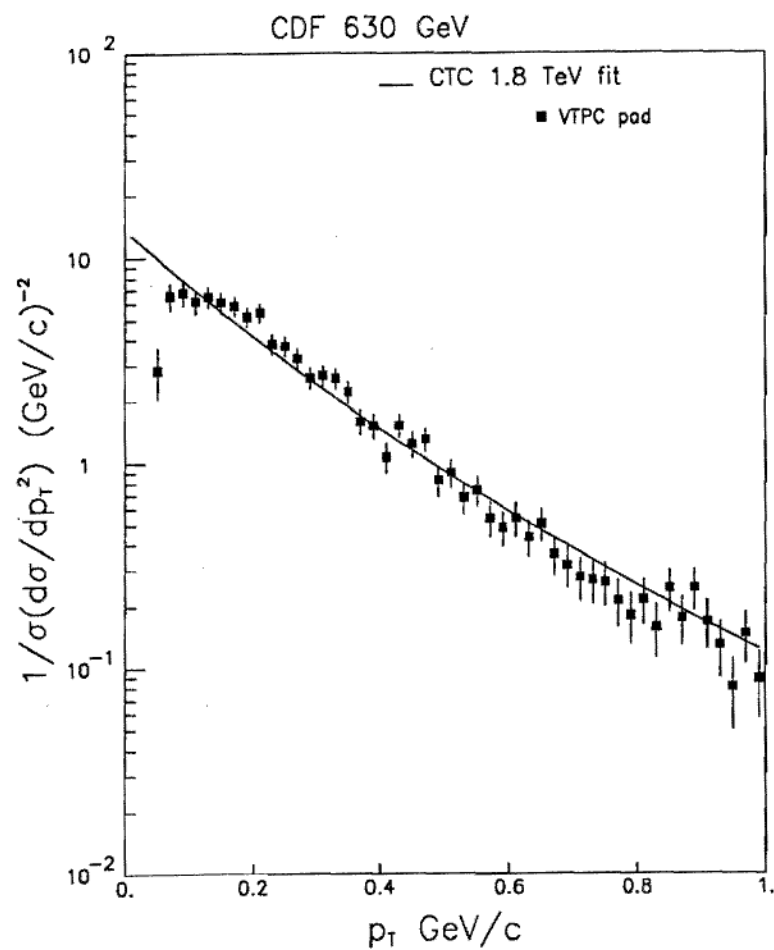


Figure 5.34:  $p_T$  spectrum measured with the VTPC pad for  $|Y| \leq 3.0$  at  $\sqrt{s} = 630$  GeV. The vertical axis is the invariant cross section normalized by the total cross section. The errors are purely statistical. The curve is the fit  $1/(p_T/p_0 + 1)^n$  to the CTC data above  $0.5 \text{ GeV}/c$ .

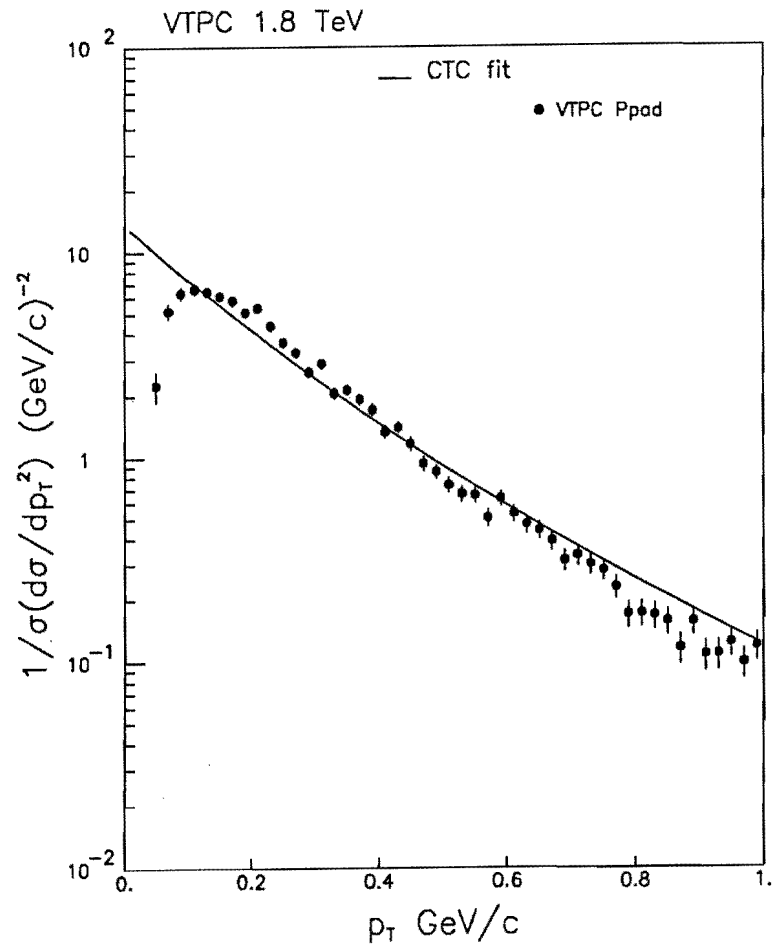


Figure 5.35:  $p_T$  spectrum with the VTPC pad for  $|Y| \leq 3.0$  at  $\sqrt{s} = 1.8$  TeV. The vertical axis is the invariant cross section normalized by the total cross section. The errors are purely statistical. The curve is the fit  $1/(p_T/p_0 + 1)^n$  to the CTC data above 0.5 GeV/c.

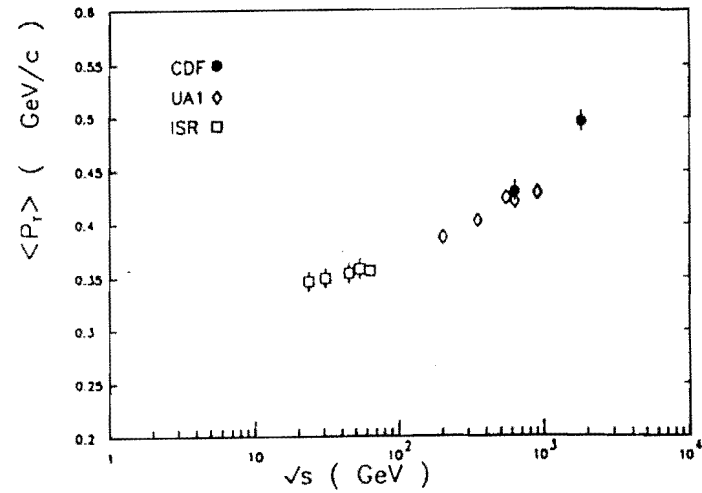


Figure 5.36: Energy dependence of  $\langle p_T \rangle$ .

## The CDF Collaboration

F.Abe<sup>a</sup>, D.Amadei<sup>c</sup>, G.Apollinari<sup>k</sup>, G.Ascoli<sup>a</sup>, M.Atac<sup>d</sup>, P.Auchincloss<sup>n</sup>, A.R.Baden<sup>f</sup>,  
 A. Barbaro-Galtieri<sup>i</sup>, V.E.Barnes<sup>f</sup>, E.Barsotti<sup>d</sup>, F.Bedeschi<sup>k</sup>, S.Belforte<sup>k</sup>,  
 G.Bellettini<sup>k</sup>, J.Bellinger<sup>a</sup>, J.Bensinger<sup>b</sup>, A.Beretvas<sup>n</sup>, P.Berge<sup>d</sup>, S.Bertolucci<sup>e</sup>,  
 S.Bhadra<sup>a</sup>, M.Binkley<sup>d</sup>, R.Blair<sup>a</sup>, C.Blocker<sup>b</sup>, J.Bofill<sup>d</sup>, A.W.Booth<sup>d</sup>, G.Brandenburg<sup>f</sup>,  
 A.Brenner<sup>d</sup>, D.Brown<sup>f</sup>, A.Byon<sup>f</sup>, K.L.Byrum<sup>a</sup>, M.Campbell<sup>c</sup>, R.Carey<sup>f</sup>, W.Carithers<sup>i</sup>,  
 D.Carlsmith<sup>a</sup>, J.T.Carroll<sup>d</sup>, R.Cashmore<sup>l</sup>, F.Cervelli<sup>k</sup>, K.Chadwick<sup>l,d</sup>, T.Chapin<sup>m</sup>,  
 G.Chiarelli<sup>k</sup>, W.Chinowsky<sup>i</sup>, S.Cihangir<sup>a</sup>, D.Cline<sup>a</sup>, D.Connor<sup>a</sup>, M. Contreras<sup>b</sup>, J.Cooper<sup>d</sup>,  
 M.Cordelli<sup>k</sup>, M.Curatolo<sup>a</sup>, C.Day<sup>d</sup>, R.DelFabbro<sup>k</sup>, M.Dell'Orso<sup>k</sup>, L.DeMortier<sup>b</sup>, T.Devlin<sup>n</sup>,  
 D.DiBitonto<sup>a</sup>, R.Diebold<sup>a</sup>, F.Dittus<sup>d</sup>, A.DiVirgilio<sup>k</sup>, R.Downing<sup>a</sup>, G. Drake<sup>d</sup>, T.Droege<sup>d</sup>,  
 M.Eaton<sup>f</sup>, J.E.Elias<sup>d</sup>, R.Ely<sup>i</sup>, S.Errede<sup>a</sup>, B.Esposito<sup>c</sup>, A.Feldman<sup>f</sup>, B.Flaugher<sup>n</sup>, E.Focardi<sup>k</sup>,  
 G.W.Foster<sup>d</sup>, M.Franklin<sup>f,a</sup>, J.Freeman<sup>c</sup>, H.Frisch<sup>c</sup>, Y.Fukui<sup>k</sup>, S.Galeotti<sup>k</sup>, I.Gaines<sup>d</sup>, A.F.Garfinkel<sup>i</sup>,  
 P.Giannetti<sup>k</sup>, N.Giokaris<sup>m</sup>, P.Giromini<sup>e</sup>, L.Gladney<sup>j</sup>, M.Gold<sup>i</sup>, K.Goulianos<sup>m</sup>, J.Grimson<sup>d</sup>,  
 C.Grosso-Pilcher<sup>c</sup>, C.Haber<sup>l</sup>, S.R.Hahn<sup>a</sup>, R.Handler<sup>a</sup>, D.Hanssen<sup>d</sup>, R.M.Harris<sup>i</sup>, J.Hauser<sup>c</sup>,  
 Y.Hayashide<sup>a</sup>, T.Hessing<sup>a</sup>, R.Hollebeek<sup>j</sup>, L.Holloway<sup>a</sup>, P.Hu<sup>n</sup>, B.Hubbard<sup>i</sup>, P.Hurst<sup>a</sup>, J.Huth<sup>d</sup>,  
 M.Ito<sup>a</sup>, J.Jaske<sup>a</sup>, H.Jensen<sup>d</sup>, R.P.Johnson<sup>d</sup>, U.Joshi<sup>n</sup>, R.W.Kadel<sup>d</sup>, T.Kamon<sup>a</sup>, S.Kanda<sup>a</sup>,  
 I.Karliner<sup>a</sup>, H.Kautzky<sup>d</sup>, K.Kazlauskis<sup>n</sup>, E.Kearns<sup>f</sup>, R.Kephart<sup>d</sup>, P.Kesten<sup>b</sup>, H.Keutelian<sup>a</sup>,  
 Y.Kikuchi<sup>a</sup>, S.Kim<sup>a</sup>, L.Kirsch<sup>b</sup>, S.Kobayashi<sup>2</sup>, K.Kondo<sup>a</sup>, U.Kruse<sup>a</sup>, S.E.Kuhlmann<sup>i</sup>, A.T.Laasanen<sup>i</sup>,  
 W.Li<sup>a</sup>, T.Liss<sup>c</sup>, N.Lockyer<sup>j</sup>, F.Marchetto<sup>a</sup>, R.Markeloff<sup>a</sup>, L.A. Markosky<sup>a</sup>, M.Masuzawa<sup>a</sup>,  
 P.McIntyre<sup>a</sup>, A.Menzione<sup>k</sup>, T.Meyer<sup>a</sup>, S.Mikamo<sup>k</sup>, M.Miller<sup>j</sup>, T.Mimashi<sup>a</sup>, S.Miscetti<sup>a</sup>,  
 M.Mishina<sup>k</sup>, S.Miyashita<sup>a</sup>, H.Miyata<sup>a</sup>, N.Mondal<sup>a</sup>, S.Mori<sup>a</sup>, Y.Morita<sup>a</sup>, A.Mukherjee<sup>d</sup>,  
 A.Murakami<sup>2</sup>, Y.Muraki<sup>3</sup>, C.Nelson<sup>d</sup>, C.Newman-Holmes<sup>d</sup>, L.Nodulman<sup>a</sup>, J.O'Meara<sup>d</sup>,  
 G.Ott<sup>a</sup>, T.Ozaki<sup>a</sup>, S.Palanque<sup>4</sup>, R.Paoletti<sup>k</sup>, A.Para<sup>d</sup>, D.Passuello<sup>k</sup>, J.Patrick<sup>d</sup>, R.Perchonok<sup>d</sup>,  
 T.J.Phillips<sup>f</sup>, H.Piekarz<sup>b</sup>, R.Plunkett<sup>m</sup>, L.Pondrom<sup>a</sup>, J.Proudfoot<sup>a</sup>, G.Punzi<sup>k</sup>, D.Quarrie<sup>d</sup>, K.Ragan<sup>j</sup>,  
 G.Redlinger<sup>c</sup>, R.Rezmer<sup>a</sup>, J.Rhoades<sup>a</sup>, L.Ristori<sup>k</sup>, T.Rohaly<sup>j</sup>, A.Roodman<sup>c</sup>, H.Sanders<sup>c</sup>,  
 A.Sanson<sup>i</sup>, R.Sard<sup>a</sup>, V.Scarpine<sup>a</sup>, P.Schlabach<sup>a</sup>, E.E.Schmidt<sup>d</sup>, P.Schoessow<sup>a</sup>,  
 M.H.Schub<sup>i</sup>, R.Schwitters<sup>f</sup>, A.Scribano<sup>k</sup>, S.Segler<sup>d</sup>, M.Sekiguchi<sup>a</sup>, P.Sestini<sup>k</sup>, M.Shapiro<sup>f</sup>,  
 M.Sheaff<sup>a</sup>, M.Shibata<sup>a</sup>, M.Shochet<sup>c</sup>, J.Siegrist<sup>i</sup>, V.Simaitis<sup>j</sup>, J.K.Simmons<sup>i</sup>, P.Sinervo<sup>j</sup>,  
 M.Sivertz<sup>b</sup>, J.Skarha<sup>a</sup>, D.A.Smith<sup>a</sup>, R.Snider<sup>c</sup>, L.Spencer<sup>b</sup>, R.St.Denis<sup>f</sup>, A.Stefanini<sup>k</sup>,  
 Y.Takaiwa<sup>a</sup>, K.Takikawa<sup>a</sup>, S.Tarem<sup>b</sup>, D.Theriot<sup>d</sup>, J.Ting<sup>c</sup>, A.Tollestrup<sup>d</sup>, G.Tonelli<sup>k</sup>,  
 W.Trischuk<sup>f</sup>, Y.Tsay<sup>c</sup>, K.Turner<sup>d</sup>, F.Ukegawa<sup>a</sup>, D.Underwood<sup>a</sup>, C.vanIngen<sup>d</sup>, R.VanBerg<sup>j</sup>,  
 R.Vidal<sup>d</sup>, R.G.Wagner<sup>a</sup>, R.L.Wagner<sup>d</sup>, J.Walsh<sup>j</sup>, T.Watts<sup>n</sup>, R.Webb<sup>a</sup>, T.Westhusing<sup>a</sup>,  
 S.White<sup>m</sup>, V.White<sup>d</sup>, A.Wicklund<sup>a</sup>, H.H.Williams<sup>j</sup>, T.Winch<sup>a</sup>, R.Yamada<sup>d</sup>,  
 T.Yamanouchi<sup>d</sup>, A.Yamashita<sup>a</sup>, K.Yasuoka<sup>a</sup>, G.P.Yeh<sup>d</sup>, J.Yoh<sup>d</sup>, F.Zetti<sup>k</sup>

## CDF Member Institutions

<sup>a</sup> Argonne National Laboratory- <sup>b</sup> Brandeis University- <sup>c</sup> University of Chicago  
<sup>d</sup> Fermi National Accelerator Laboratory- <sup>e</sup> INFN, Laboratori Nazionali di Frascati, Italy  
<sup>f</sup> Harvard University- <sup>g</sup> University of Illinois- <sup>h</sup> KEK, Japan  
<sup>i</sup> Lawrence Berkeley Laboratory- <sup>j</sup> University of Pennsylvania  
<sup>k</sup> INFN, University and Scuola Normale Superiore of Pisa, Italy- <sup>l</sup> Purdue University  
<sup>m</sup> Rockefeller University- <sup>n</sup> Rutgers University- <sup>o</sup> Texas A&M University  
<sup>p</sup> University of Tsukuba, Japan- <sup>q</sup> University of Wisconsin

## Visitors

<sup>1</sup> Oxford University, England- <sup>2</sup> Saga University, Japan  
<sup>3</sup> ICRR, Tokyo University, Japan- <sup>4</sup> CEN, Saclay, France-  
<sup>5</sup> Haverford College, Haverford, PA.

and

$$q = \frac{\langle n \rangle / k}{1 + \langle n \rangle / k}. \quad (\text{B.6})$$

Inserting these two equations into equation B.2 leads to equation 1.7. One application of the negative binomial distribution would be a family plan. If a couple decides to keep making children until they have three girls, assuming 50% of both probability of either sex, they would end up with three boys and three girls on an average. Although mathematical meaning of the negative binomial distribution is clear, its physical meaning is not established in the multiparticle production in the hadron-hadron collision. At least three theoretical models which reach the negative binomial distribution have been proposed. These models are discussed in § 5.2.2.

## Appendix B

### Negative Binomial Distribution

The negative binomial distribution occurs when someone waits *until* he/she finds  $k$  successes in the Bernoulli trial in which the results of a trial is either *success* or *failure*. Let the probabilities of *success* and *failure* to be  $p$  and  $q = 1 - p$ , respectively. The probability of having  $k - 1$  successes and  $n$  failures at  $(n + k - 1)$ th trial is:

$$P = \binom{n + k - 1}{n} \cdot p^{k-1} q^n. \quad (\text{B.1})$$

The probability of having the  $k$ th success in next trial is:

$$\begin{aligned} P_k(n) &= \binom{n + k - 1}{n} \cdot p^k q^n \\ &= \frac{(n + k - 1)(n + k - 2) \cdots (k + 1)(k)}{n!} \cdot p^k q^n \\ &= (-1)^n \frac{(-k)(-k - 1) \cdots (-k - n + 2)(-k - n + 1)}{n!} \cdot p^k q^n \\ &= \binom{-k}{n} \cdot p^k (-q)^n. \end{aligned} \quad (\text{B.2}) \quad (\text{B.3})$$

$P_k(n)$  is called the negative binomial distribution. The average value of  $n$  is given by:

$$\langle n \rangle = \frac{kq}{p} = \frac{k(1 - p)}{p}. \quad (\text{B.4})$$

Solving by  $p$  gives:

$$p = \frac{1}{1 + \langle n \rangle / k}, \quad (\text{B.5})$$

Using these equations:

$$\frac{\sqrt{V_x^2 + V_y^2}}{V_z} = \frac{\tan \alpha}{\sqrt{1 + (\omega\tau)^2}}, \quad (\text{D.4})$$

where  $\omega\tau$ , which depends on the magnetic field and the gas, is estimated to be 2 for the VTPC.

## Appendix D

### $E \times B$ effect on the drift direction

The drifting electrons receive the radial forces due to the  $E \times B$  effects in the drift region. This can change the apparent  $xy$  (or  $\phi$ ) of reconstructed tracks. Under the  $E \times B$  effect, the three components of drift velocity are given by:

$$V_x = +(e/m) f(E) \sin \alpha \tau / (1 + (\omega\tau)^2), \quad (\text{D.1})$$

$$V_y = -(e/m) f(E) \sin \alpha \omega\tau^2 / (1 + (\omega\tau)^2), \quad (\text{D.2})$$

$$V_z = +(e/m) f(E) \cos \alpha \tau, \quad (\text{D.3})$$

where

$V_x$  :  $x$  component of the drift velocity,

$V_y$  :  $y$  component of the drift velocity,

$V_z$  :  $z$  component of the drift velocity,

$e$  : electron charge,

$m$  : electron mass,

$f(E)$  : a function of the strength of the electric field,

$\alpha$  : angle between the electric field and the magnetic field,

$\tau$  : mean free path in the gas,

$\omega$  :  $= (e/m)$  times the magnetic field  $B$ .

systematics and is the following function of  $dz/dy$ :

$$corr_{sys} = 0.95 \cdot (\Delta y_{wire}/2) \cdot (\sqrt{(dz/dy)^2 - 1} - 1) \cdot (1 - 0.024 |dz/dy|), \quad (E.2)$$

where  $\Delta y_{wire}$  is the sense wire spacing.  $diff(dz/dy)$  is a Gaussian with a width of:

$$400\sqrt{((dz/dy)^2 + 1)} \mu m. \quad (E.3)$$

The TDC count is calculated as:

$$TDC = z_{app}/v_{drift} + t_0 + t_{PC}, \quad (E.4)$$

where  $v_{drift}$  is the drift velocity,  $t_0$  is the offset TDC count,  $t_{PC}$  is the total drift time in the proportional chamber region.

## Pulse height simulation

We generate and store the minimum ionizing  $dE/dx$  distribution along a track for 2000 TDC time slices ( $2000 \times 8$  nsec). The distribution has been chosen such that it reproduces the  $dE/dx$  distribution obtained by an experiment with 1.5 cm thick Argon(50%)/Ethane(50%) gas <sup>1</sup>, as shown in figure E.1.

We then integrate the original  $dE/dx$  distributions, where  $x$  is along the track, to obtain  $dE/dt$  (or  $dE/dz$ ) distributions for ten different ranges of  $\cot \theta$  each for the ASD/TDC and PAS/FADC data. The time constant  $\tau$  is 60 nsec in FWHM for the ASD and 200 nsec in FWHM for the PAS. The time slice is 8 nsec for the TDC and 94 nsec for the FADC. The integration at a certain time slice  $i_t$  is calculated by:

$$\frac{dE}{dt}(i_t) = \sum_{i_x=i_t-\tau_x}^{i_t+\tau_x} a(i_x) \cdot \frac{dE}{dx}(i_x), \quad (E.5)$$

where

---

<sup>1</sup>F.Harris et al., Nucl. Instrum. Methods A, 107 (1973) 413

## Appendix E

### VTPC detector simulation

We have two independent simulations, one for the TDC leading edge simulation and the other for the pulse-height related simulation such as the TDC trailing, TDC multiple hit, and FADC simulation. This is because the TDC leading edge simulation requires the accurate TDC time, while the other part does not require good timing resolution but realistic pulse-height simulation. It would result in a complex code and a large amount of CPU time if we try to attain both good timing and pulse-height accuracy with a single simulation.

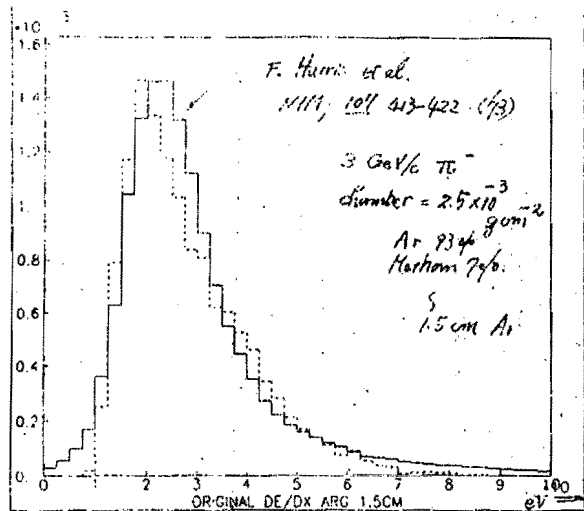
Prior to the TDC and FADC simulation, all necessary information on a track at each sense wire is calculated. This information includes the velocity of the particle, the  $z$ -coordinate, the slope in the  $xy$  plan, and the slope in the  $rz$  plan.

### TDC leading edge simulation

The TDC leading edge is simulated exactly in the reverse way of obtaining the  $z$ -coordinates from the read data as follows:

$$z_{app} = z_{track} + corr_{sys}(dz/dy) + diff(dz/dy), \quad (E.1)$$

where  $z_{app}$  is the apparent  $z$  distance between the cathode screen and a track,  $z_{track}$  is the track  $z$  coordinate,  $corr_{sys}(dz/dy)$  is the systematic correction, and  $diff(dz/dy)$  is the diffusion fluctuation.  $corr_{sys}$  is obtained by studying the chamber



255

Figure E.1: Reproduced  $dE/dx$  distribution by the simulation (the solid line) and the  $dE/dx$  measured experimentally (the dashed line). Both are for 1.5 cm thick gas.

- $\frac{dE}{dt}(i_t)$  : the  $dE/dt$  value at the time slice  $i_t$ ,
- $\tau_x$  : the integration time constant projected on the track,
- $a(i_x)$  : a triangle shaped integration weight with a width  $\tau_x$ ,
- $\frac{dE}{dx}(i_x)$  : the  $dE/dx$  value at the  $x$  slice  $i_x$  along the track

For a given track slope, one of the ten translated  $dE/dt$  samples is chosen and where to start in the sample is determined by a random number every time. The entire  $dE/dx$  and  $dE/dt$  samples are regenerated once every 20000 TDC hits to randomize the data.

With the velocity of the generated particle, the minimum ionizing  $dE/dt$  is changed into nominal  $dE/dt$  by the the Bethe-Block formula. We apply the correction for non-zero  $dx/dy$  and the chamber gain which has a dependence on both the octant  $\phi$  and the radial location of the sense wire. The latter has been obtained by studying the minimum ionizing as a function of the local  $\phi$  and the wire location using the wire FADC data. The decay time constant<sup>2</sup> in the ASD is not negligible

<sup>2</sup>This is due to the capacitive couplings in the ASD circuit. The decay time constant in the PAS

256

## APPENDIX E. VTPC DETECTOR SIMULATION

and a decay factor is applied to  $dE/dt$  assuming that the signals decay as  $e^{-t/\tau}$ , where  $\tau$  is approximately 4  $\mu$ sec. The time-over-threshold is applied to the selected and corrected sample of the  $dE/dt$  in order to simulate the TDC trailing edge and multiple TDC hits.

has been chosen to be more than 1.4 msec.



## Appendix F

### VTPC wire systematics

The long drift lengths, ExB forces on drifting electrons, and the wide range of track polar angles seen by the VTPC result in several important systematic effects which require correction. Proper treatment of these effects is important to ensure good tracking efficiency when linking tracks across chamber boundaries. The two largest systematic effects are:

- Variations in drift velocity due to variations in pressure, temperature and gas composition.
- Apparent shifts in track position as a function of the polar production angle.

The chamber is sensitive to small changes in gas conditions which result in variations in drift velocity. This is because the VTPCs operate at a value of  $E/p$  of 256 V/cm at one atmosphere, well below that necessary to saturate the drift velocity in Argon-Ethane<sup>1</sup>. At 256 V/cm the variation in drift velocity with  $E/p$  is roughly  $5 \times 10^{-3}$  cm/ $\mu$ s (V/cm)<sup>-1</sup> atm. This corresponds to about 1% change in drift velocity for a change in operating pressure of 25 torr. Variation of as much as 2% in  $v_d$  over a period of days is possible. This corresponds to about a 3 mm shift in the apparent position of electrons drifting from near the central grid. Clearly it is important to carefully monitor the drift velocity as a function of time. A technique (described below) has been developed for doing this directly from the data.

<sup>1</sup>Ma et al., MIT Technical reports 129 and 130 (1982).

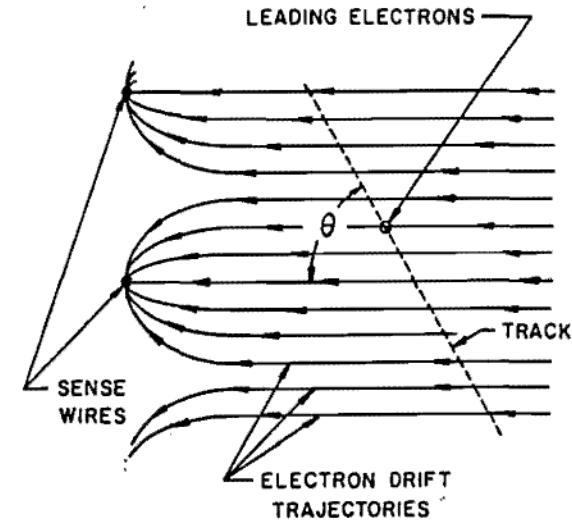


Figure F.1: Leading electron effect due to track polar angle  $\theta$ . The first electrons arriving at the sense wire come from different radial regions in the cell and follow different drift trajectories, depending on track polar angle  $\theta$ .

The second major systematic effect is due to the use of leading edge TDC timing to determine track locations in the chamber. The leading electrons contributing to the wire signal arrive from different radial positions within a cell, depending upon the inclination angle of the track relative to the sense wire plane (see Figure F.1).

For example, the leading electron from a 90° track will arrive from the center of the cell, whereas the leading electron from a 10° track will arrive from the edge of the sense wire cell. This results in an apparent shift in the  $r$  position of the wire, or equivalently in the  $z$  position of the track. This effect can be quite large for tracks at small polar angles. The corrections for this effect depend on the details of the electric field near the sense wire, diffusion, and ExB forces. These effects have been modeled analytically, but better estimates of these corrections are obtained directly from the data.

Two constraints are useful in determining these corrections. First, tracks crossing the center high voltage grid of the chamber must be continuous. If track segments measured in each half of the same module are not aligned, deviations are

assumed to be the result of drift velocity variations and the inclination angle effect mentioned above. The second constraint is that the vast majority of tracks originate from the primary vertex. Using both of these constraints, the drift velocity and the polar angle corrections are extracted from  $\bar{p}p$  collision data. This procedure uses a vertex constrained fit which forces track segments to be continuous across the central high voltage grid. The drift velocity, the parameterization of the polar angle correction, the TDC time offset, and the  $z$  position of the vertex are fit for each event. Only tracks which are isolated in a single octant and found on both sides of the high voltage grid in a single module are used in the fit. Each measured time  $t_i$  on a track corresponds to a location  $z_i$  parameterized as:

$$z_i = z_s \pm (v_d(t_i - t_o) + f(\theta)) \quad (\text{F.1})$$

where

$z_s$  is the position of the sense wire plane for that particular hit

$v_d$  is the drift velocity

$t_i$  is the leading edge time from wire  $i$

$t_o$  is a global time offset related to the difference between the actual interaction time and the TDC stop time.

$f(\theta)$  is the polar angle correction

The "+" in eq. 1 corresponds to tracks drifting towards smaller values of  $z$ , while "-" refers to tracks drifting in the opposite direction. An event  $\chi^2$  is formed by forcing the vertex  $z$  position to be the intercept for all the tracks. By minimizing this  $\chi^2$  with respect to the event vertex,  $v_d$ ,  $t_o$  and the parameters for  $f(\theta)$ , one can derive these constants on an event-by-event basis. Figure F.2 shows the wire hits and the track fits used to determine these constants for a typical event.

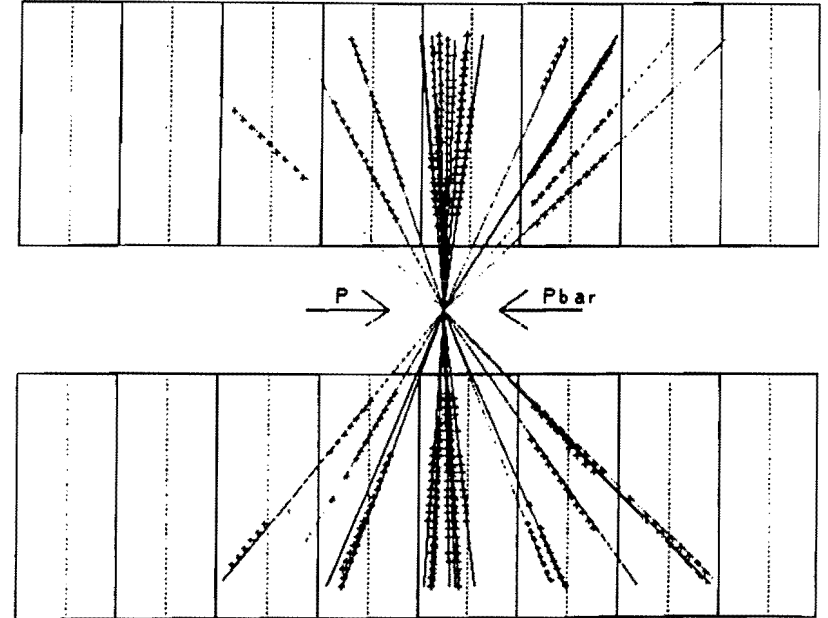


Figure F.2: The  $r$ - $z$  projection of a typical event used in determining the VTPC reconstruction constants. Shown are the track fits constrained to a common vertex, and the wire hits used in these fits.

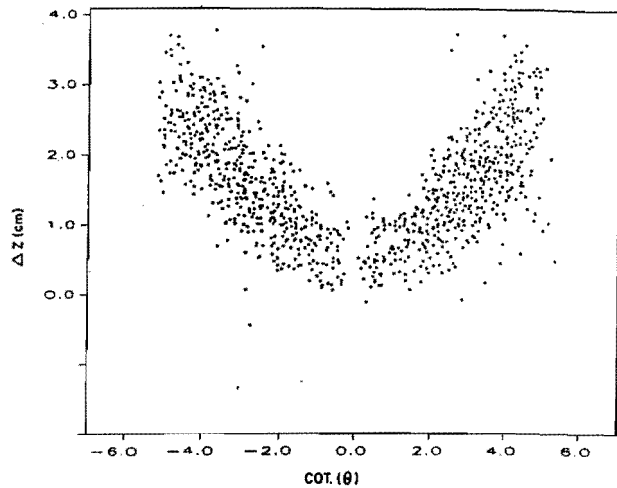


Figure F.3: Scatterplot of the mismatch in  $z$  for tracks crossing the center grid as a function of  $\cot \theta$ .

The results of these fits yield a measurement of drift velocity for each event. When averaged over only a few events, a value accurate to  $< 0.5\%$  can be obtained. For the majority of runs, the drift velocity is found to be about  $4.2 \text{ cm}/\mu\text{s}$ . The polar angle correction is approximated by quadratic splines for dip angles between  $30^\circ$  and  $120^\circ$ , and is assumed linear for lower angles. The asymptotic form of this correction has a slope which is equal to half the cell spacing. This agrees with expectations based upon purely geometric grounds since for small polar angles the earliest arriving electrons are those drifting from near the edge of the sense wire cell. Figure F.3 shows a scatterplot of the track mismatch ( $\Delta z$ ) as a function of  $\cot(\theta)$ .

## Appendix G

### VTPC pad systematics

The systematic effects on the pad data have been studied making use of the real  $\bar{p}p$  events. We have used CTC tracks as references because they had good uniform  $\phi$  precision ( $\sim 250 \mu\text{m}$ ) with small systematic effects and misalignment [50]. We selected relatively high quality CTC tracks which had at least 30 axial layer hits and 12 stereo layer hits with  $p_t \geq 0.8 \text{ GeV}/c$ . Expected positions of pad hits were calculated from CTC track parameters. Using the pad FADC data, The center of gravity of an induced charge distribution was calculated by fitting to a Gaussian as in the normal pad reconstruction. The FADC time bin numbers were translated into the  $z$  coordinates. If the pad hits were found within one pad width ( $4.5^\circ$ - $7.5^\circ$  in  $\phi$  depending on the row number) and if they were near the expected  $z$  positions, the hits were used to calculate the deviations from the CTC tracks. We did not use the pad hits which had the maximum induced charge on the closest pads to octant boundaries. We defined the deviation as:

$$\Delta_\phi = \phi_{VTPC} - \phi_{CTC}, \quad (\text{G.1})$$

or

$$\Delta_{r\phi} = r \cdot (\phi_{VTPC} - \phi_{CTC}), \quad (\text{G.2})$$

where  $r$  is a radius calculated from the CTC track parameters,  $\phi_{VTPC}$  is the  $\phi$  position of each pad hit, and  $\phi_{CTC}$  is the expected  $\phi$  position of tracks at  $r$  calculated from the CTC track parameters (See figure G.1).

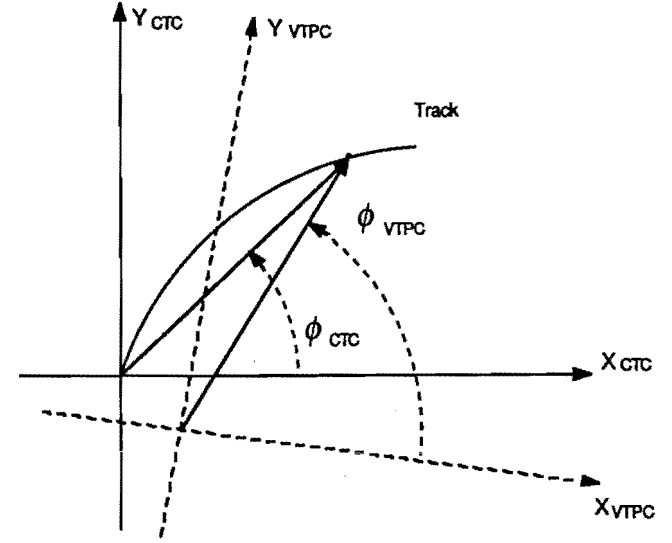


Figure G.1: Definitions of  $\phi_{VTPC}$  and  $\phi_{CTC}$ . The nominal coordinate defined by the CTC is indicated by  $x_{CTC}$  and  $y_{CTC}$  axes. The VTPC coordinate, which is possibly misaligned, is indicated by  $x_{VTPC}$  and  $y_{VTPC}$  axes.

We observed the systematics by looking at the distribution of  $\Delta_\phi$  or  $\Delta_{r\phi}$ . We have observed the following systematic effects on the pad FADC data:

1. Chamber misalignment in  $\phi$ ,
2. Chamber misalignment on  $xy$  plan,
3.  $E \times B$  effects due to the misalignment in  $\theta$ ,
4. Apparent shift of  $\phi$  positions near octant boundaries,
5. Deviation of induced charge distribution from a Gaussian.

The following sections describes each systematics. Although each systematics is relatively independent of each other, we used an iteration process to separate each systematics completely as described in § G.

### Chamber misalignment in $\phi$

The chamber misalignment in  $\phi$  is observed as an overall shift of the  $\Delta_\phi$  distribution. The other systematics does not shift the overall distribution but widen the distribution when  $\Delta_\phi$  is calculated for the all  $\phi$  direction. Figures G.2a, b, c, and d show the  $\Delta_\phi$  distributions using the real  $\bar{p}p$  events for the VTPC half module 2, 5, 10, and 13, respectively. The  $\Delta_\phi$  is calculated with corrections to all other systematics.

The curves in the figures are fittings to a Gaussian. The amount of the misalignment in  $\phi$  is obtained by  $-1$  times the peak position<sup>1</sup>, which are summarized in table G.1 with the  $\phi$  misalignment obtained by an optical survey. The values obtained by this study are consistent with those obtained by the survey. The maximum shift of  $+10$  mrad is observed for the half module 13.

VTPC half module#	$\phi$ rotation by $\Delta_\phi$	$\phi$ rotation by survey
2	+3.5 mrad	+3.2 mrad
5	+1.4 mrad	-3.0 mrad
10	-2.6 mrad	-5.6 mrad
13	-9.9 mrad	-11.6 mrad

Table G.1: Misalignment in  $\phi$  obtained from  $\Delta_\phi$ . The results from the optical survey are also shown. The accuracy of the survey is 2-3 mrad.

### Chamber misalignment on $xy$ plan

The chamber misalignment on the  $xy$  plan is observed as the sineoidal behavior of  $\Delta_{r\phi}$  when plotted as a function of  $\phi$ . The  $\phi$  misalignment in  $\phi$  does not affect the amplitude and phase of the sine curve. The other systematics are averaged over

<sup>1</sup>See figure G.1. Rotating the VTPC coordinate in negative  $\phi$  results in a positive  $\Delta_\phi = \phi_{VTPC} - \phi_{CTC}$ .

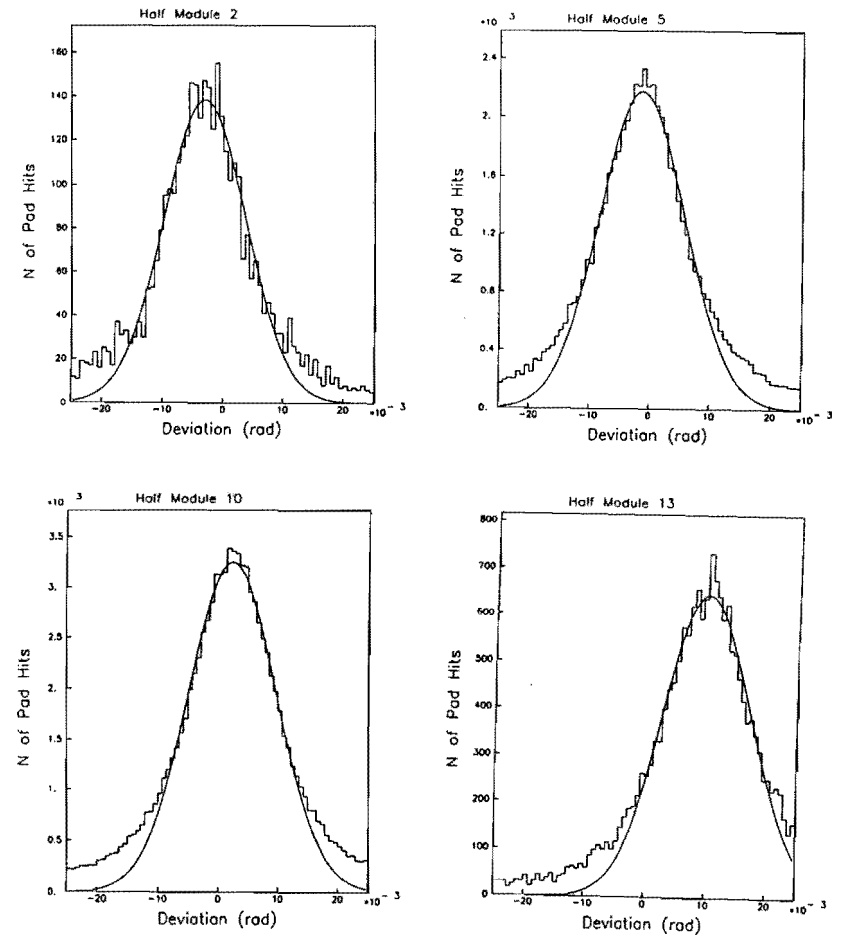


Figure G.2: Distributions of  $\Delta_\phi = \phi_{VTPC} - \phi_{CTC}$ .  $\Delta_\phi$  is calculated with corrections to all other systematics. The curves are fittings to a Gaussian. The peak positions is  $-3.5$ ,  $-1.4$ ,  $+2.6$ , and  $+9.9$  mrad from the half module 2 to 13.

and only make the distribution wider. The  $\Delta_{r\phi}$  is plotted against  $\phi$  in figure G.3a, b, c, and d for the VTPC half module 2, 5, 10, and 13, respectively. These are with corrections to all other systematics. The difference in the number of entries for the different half modules is due to the availability of the  $\bar{p}p$  events whose vertex position is under the particular half module. Less population at the octant boundaries is due to the fact that we did not use the pad hits very close to octant boundaries.

From these plots, the average of  $\Delta_{r\phi}$  are obtained as a function of  $\phi$  as shown in figure G.4. The curves are fitting to a sine function:

$$\langle \Delta_{r\phi} \rangle = A \cdot \sin(\phi + \rho). \quad (\text{G.3})$$

The amplitude  $A$  and phase  $\rho$  obtained by the fit is shown in table G.2. The maximum misalignment (the maximum amplitude) of 1.5 mm has been observed for the half module 13. The corrections to the other systematics have been chosen such that the amplitude and phase obtained here corresponds to the  $xy$  misalignment of the VTPC proportional chamber (not the center of VTPC module).

VTPC half module#	$A$	$\rho$
2	1.3 mm	+0.79 rad
5	0.5 mm	+0.14 rad
10	0.5 mm	-0.18 rad
13	1.5 mm	+1.20 rad

Table G.2: The amplitude ( $A$ ) and phase  $\rho$  obtained by fitting to  $\langle \Delta_{r\phi} \rangle = A \cdot \sin(\phi + \rho)$ .

The misalignment for the half module 13 is illustrated in figure G.5. The origin ( $x = y = 0$ ) of the half module 13 is located in the third quadrant and 1.5 mm away from the beam axis.

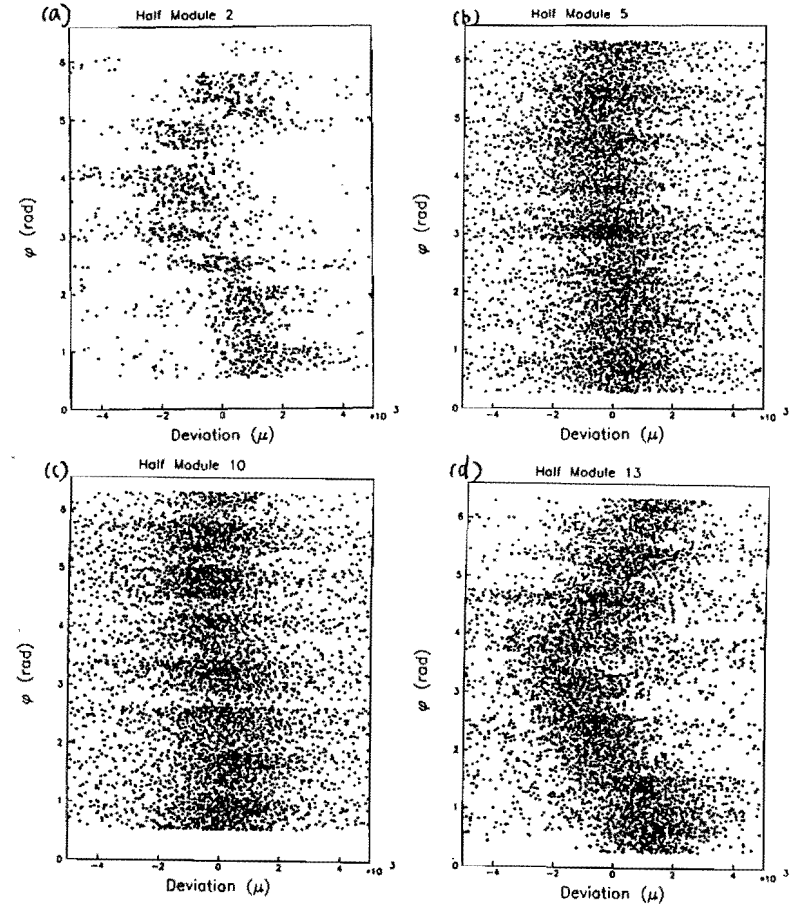


Figure G.3:  $\Delta_{r\phi}$  plotted against  $\phi$  for the VTPC half module 2 (a), 5 (b), 10 (c), and 13 (d).

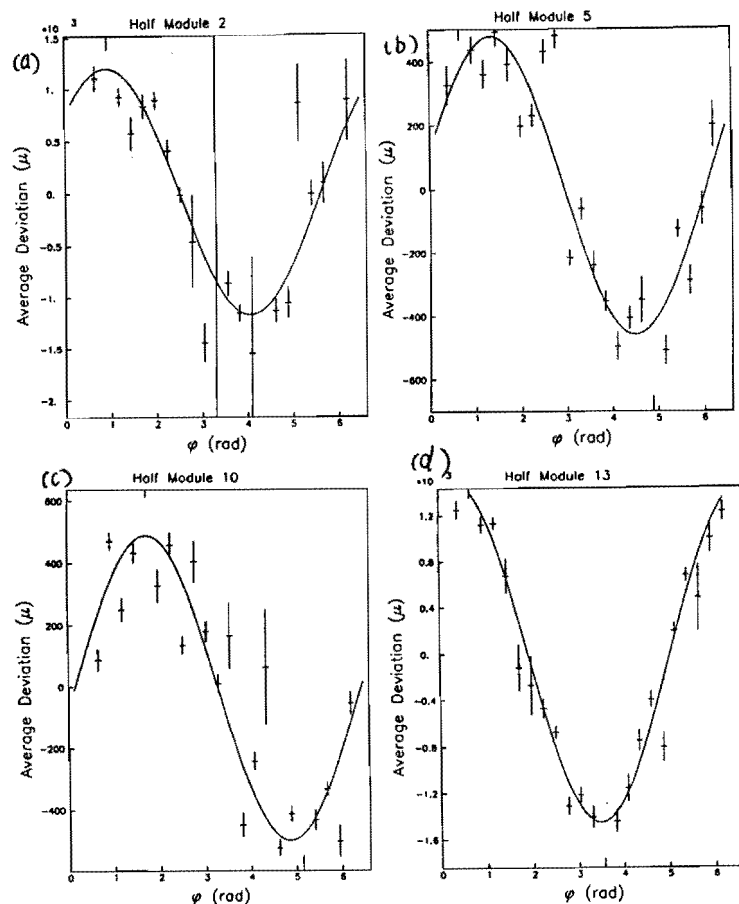


Figure G.4: Average of  $\Delta_{r\phi}$  is shown as a function of  $\phi$  for the VTPC half module 2 (a), 5 (b), 10 (c), and 13 (d). The curves are fitting to a sine function.

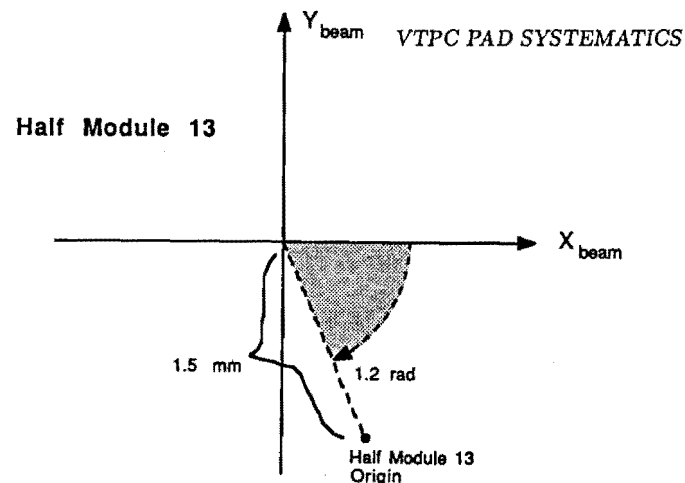


Figure G.5: Illustration of the misalignment for the half module 13. The maximum positive  $\Delta_{r\phi}$  occurs at  $\phi = \pi/2 - \rho$ . The direction of misalignment offset from the beam axis is  $-\rho$ .

### $E \times B$ effects

The  $E \times B$  effects are caused by the misalignment of the VTPC modules in  $\theta$  with respect to the axis of the magnetic field. The drifting electrons receive the  $E \times B$  force in a certain direction perpendicular to the longitudinal drift direction (figures G.6a and b).

Since the net effects are proportional to the drift distance, we have studied a quantity:

$$\Delta_{r\phi}^{E \times B} = \Delta_{r\phi}^{Late} - \Delta_{r\phi}^{Early}, \quad (G.4)$$

as a function of  $\phi$ , where  $\Delta_{r\phi}^{Late}$  is  $\Delta_{r\phi}$  averaged in late drift time (7.62-15.25 cm in drift distance) and  $\Delta_{r\phi}^{Early}$  is  $\Delta_{r\phi}$  averaged in early drift time (0-7.62 cm in drift distance). Figure G.7 shows the mean  $\Delta_{r\phi}^{E \times B}$  as a function of  $\phi$ . The curves are fittings to a sine function. The half module 2 does not shown the sine... behavior in  $\Delta_{r\phi}^{E \times B}$  possibly due to the lack of the statistics. Table G.3 shows the results of the fitting — the amount of the shift for the maximum drift distance and the direction of the force. The effects have been observed to be largest for the half module 13.

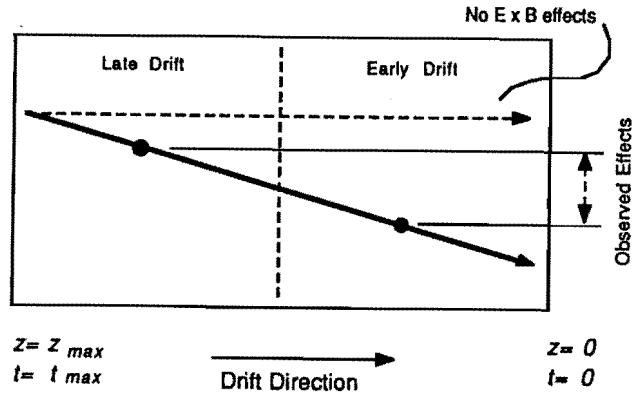


Figure G.6: Effects of the  $E \times B$  force is illustrated. The direction of the force is unique on the  $xy$  plan (a), and the net effects are proportional to the drift time (b).

### Effects of the radial boards

If a sense wire hit is close to the radial board, a fraction of the induced charge appears on the electroads of the radial board losing the necessary induced charge on the closest pad to calculate the correct hit position in  $\phi$ . (See figure G.8.)

Fitting such a distorted induced charge distribution to a Gaussian results in a apparent shift of the hit position toward the cent of an octant. We have studied this effect by plotting mean  $\Delta_{r\phi}$  as a function of octant  $\phi$  ( $-\pi/8$  to  $+\pi/8$ ), as shown in figures G.9a, b, and c. The effects are seen at the octant  $\phi$  close to  $\pm\pi/8$ . The effects have been well corrected when we multiplied the charge on the closest pad to the radial board by a factor of 1.14.

### Shape of the induced charge distribution

We have studied mean  $\Delta_{r\phi}$  as a function of the pad  $\phi$ . If the shape of the induced charge distribution is not an exact Gaussian, some periodic behavior must be seen with certain boundary conditions. The  $\Delta_{r\phi}$  should be zero on average at pad center

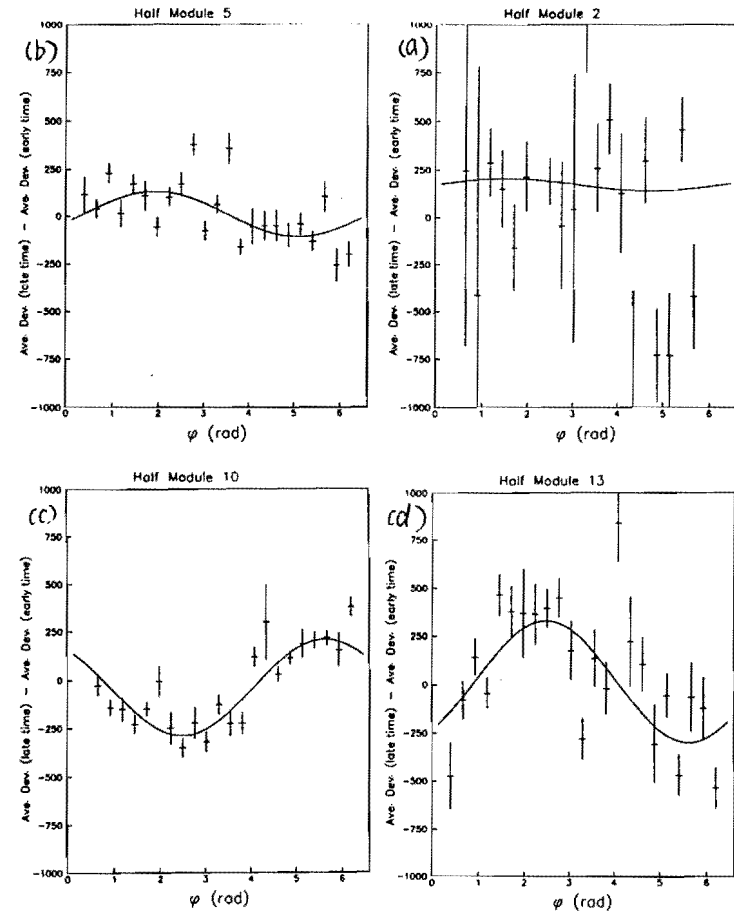


Figure G.7: Mean  $\Delta_{r\phi}^{E \times B}$  versus  $\phi$  for the VTPC half module 2 (a), 5 (b), 10 (c), and 13 (d). The curves are the fitting to a sine function. The half module 2 does not have enough statistics.



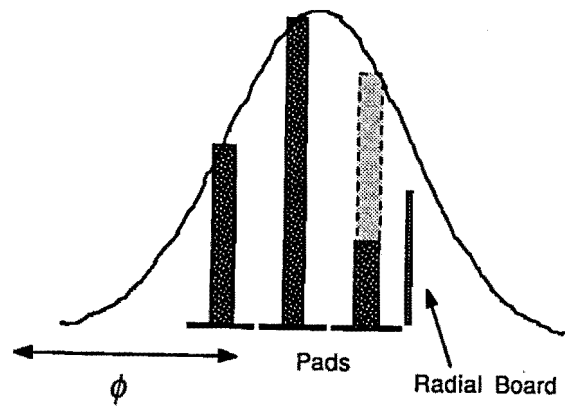


Figure G.8: Effects of the radial board is illustrated. Since some pads are next to the radial boards which have high voltage electroads, a fraction of the charge is taken by the them.

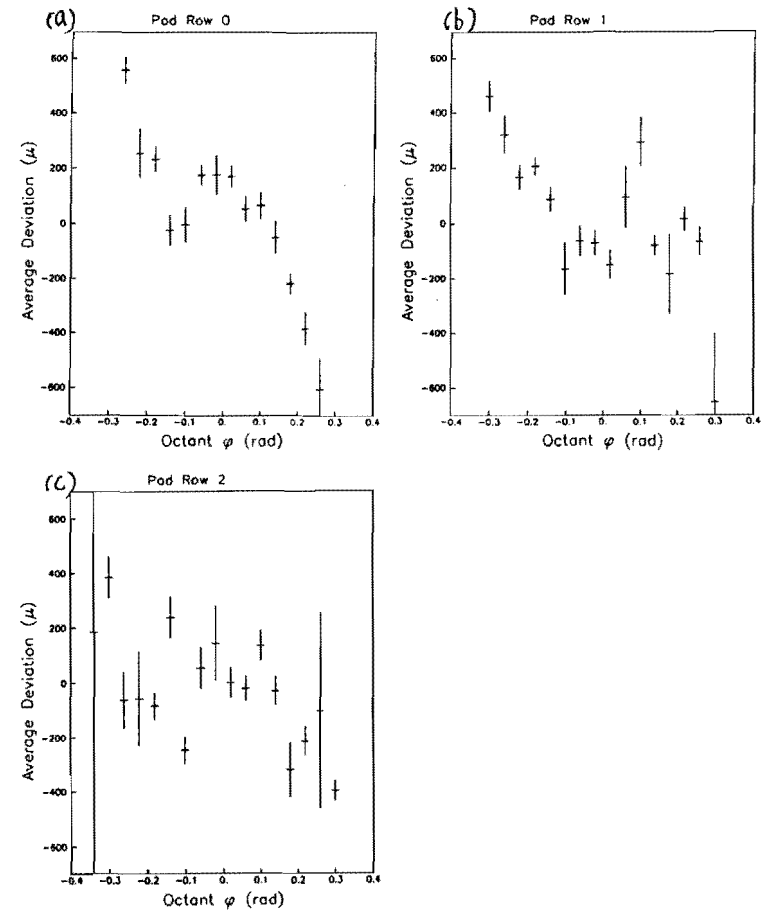


Figure G.9: Mean  $\Delta_{r\phi}$  is plotted as a function of the octant  $\phi$  for the pad row number 0 (a), 1 (b), and 2 (c).

(pad  $\phi = 0.5$  in pad width) because the charge distribution is symmetric in this case and the shape of the distribution is not important. The  $\Delta_{r\phi}$  at the pad  $\phi = 0.0$  should be the same as that at the pad  $\phi = 1.0$  because these two location are identical. Figures G.10a, b, and c show the actual mean  $\Delta_{r\phi}$  versus the pad  $\phi$  (in unit pad width) for the pad row number 0, 1, and 2, respectively.

The periodic behavior is seen only for the row 0, which is the innermost pad row. The behavior is approximately fitted to a sine function with a zero phase and an amplitude of  $100 \mu\text{m}$ . The mean  $\Delta_{r\phi}$  for the other two outer rows is consistent with a straight line within an error of  $\sim 50 \mu\text{m}$ . Such a difference for the pad rows might be due to the fact that the shape of a pad in the innermost row is fan-shaped but that in the other two rows is closer to the rectangle.

### Improvement by corrections

As already described, each systematics is relatively independent of others. We have done, however, an iteration process in order to obtain the best corrections. We first started with obtaining the alignment corrections which are the largest ones. With these first approximated corrections, the smaller systematic effects are obtained. We repeated this process 5-6 times. When studying a certain systematic effects, the corrections to the all other systematic effects are applied.

The rms width of  $\Delta_{r\phi}$  are plotted against the  $p_t$  of the CTC track is in figures G.11 *without* any corrections and in figure G.12 *with* all correction. In the both cases, the width is smaller for larger  $p_t$ . This is because (1) the multiple scattering due the the material between the VTPC and CTC and (2) the finite time resolution of the FADC data. The latter is significant when the  $\phi$  of a track changes (low  $p_t$  track) largely for a given time slice. For the high  $p_t$ , the with is approximately more than  $800 \mu\text{m}$  without the correction, improved to be less than  $600 \mu\text{m}$  with the corrections.

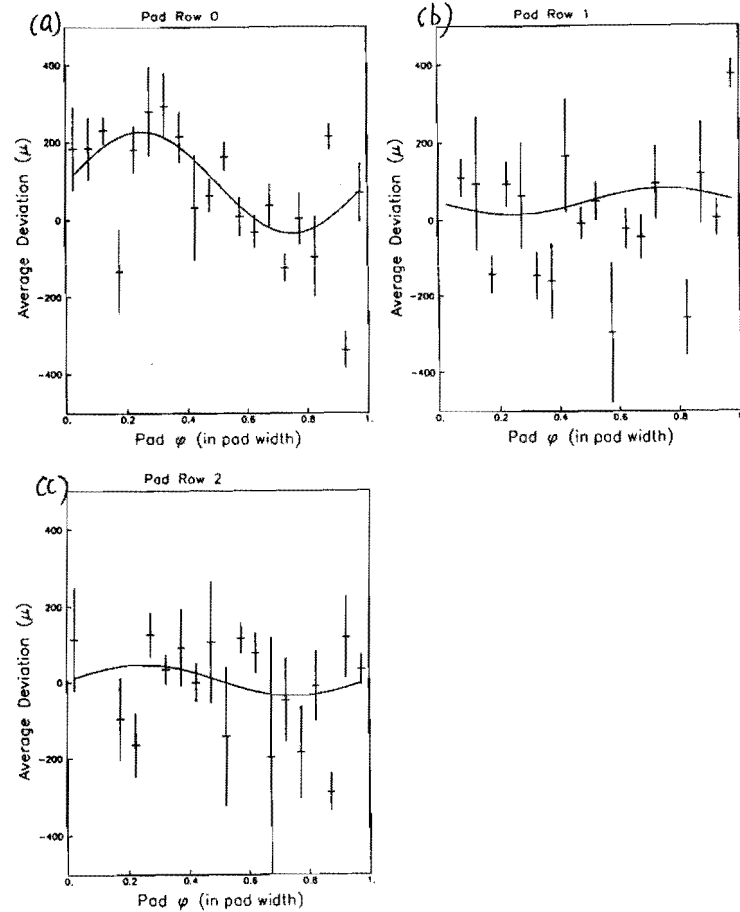


Figure G.10: Mean  $\Delta_{r\phi}$  is shown as a function of the pad  $\phi$  in unit pad width for the pad row 0 (a), 1 (b), and 2 (c).

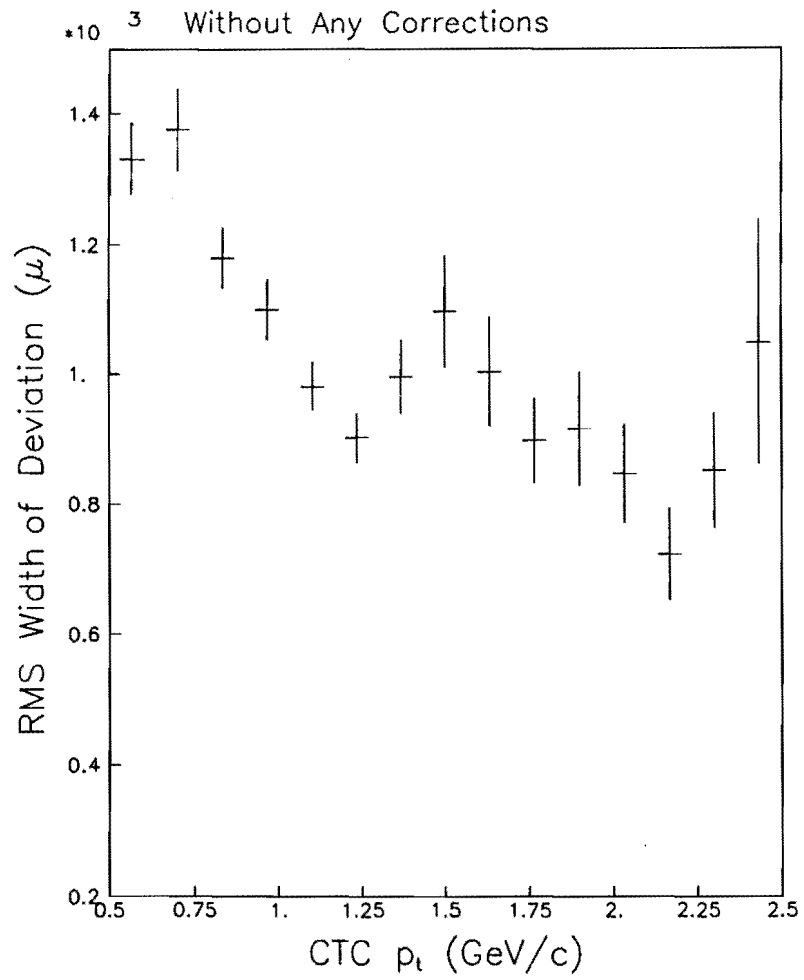


Figure G.11: Rms width of  $\Delta_{r\phi}$  versus  $p_t$  of CTC tracks without any systematic corrections.

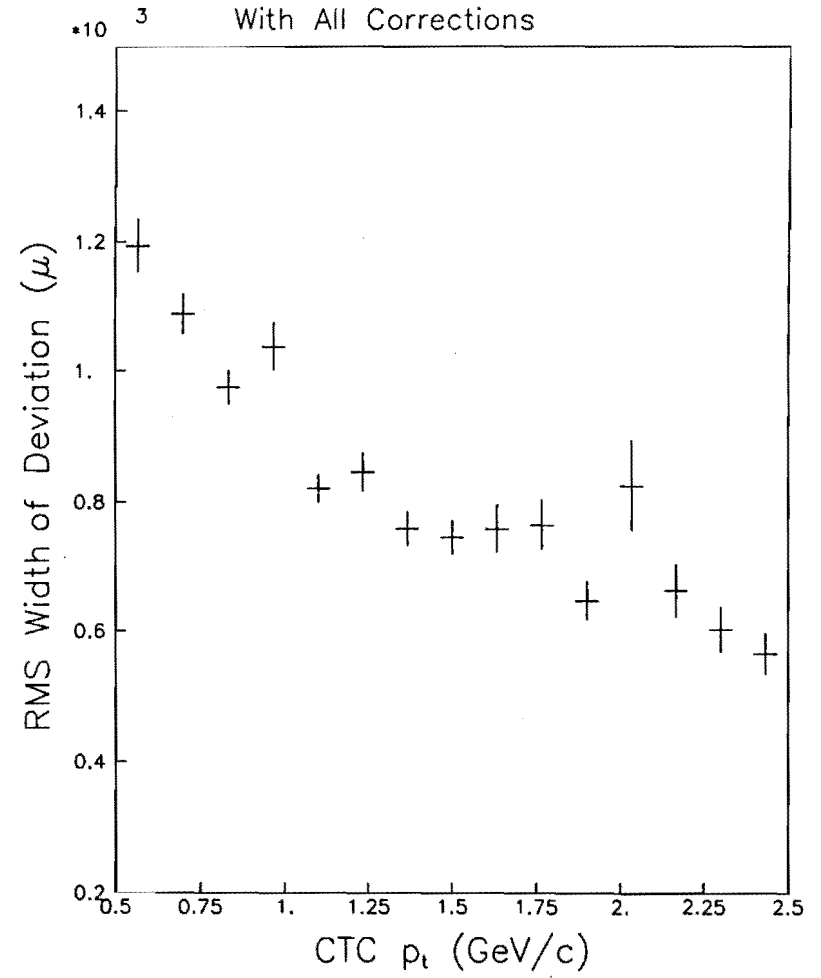


Figure G.12: Rms width of  $\Delta_{r\phi}$  versus  $p_t$  of CTC tracks with all systematic corrections.

VTPC half module#	Maximum shift	Direction
2		
5	174 $\mu\text{m}$	187°
10	512 $\mu\text{m}$	49°
13	764 $\mu\text{m}$	244°

Table G.3: Amounts and directions of  $E \times B$  forces. The half module 2 does not have enough statistics to determine. The maximum shift is the apparent shift of the drifting electrons for the maximum drift distance.

## Appendix H

### Trajectory of charged particle

The trajectory of a charged particle in an uniform magnetic field is a helix. Here, we derive some formula which are useful for studying charged particles. The coordinate system is the same as the CDF coordinate system; the  $z$  axis is the beam axis and parallel to the magnetic field,  $\phi$  is the azimuthal angle around the  $z$  axis, and the  $xy$  plane is perpendicular to the  $z$  axis forming the right handed coordinate.

#### Trajectory in $xy$ plane

Figure H.1 shows the projection of the trajectory on the  $xy$  plain. A charged particle starts with  $\phi = \phi_0$  with the transverse velocity of  $v_t$ . The projected trajectory is a circle centered at  $O'$  with a radius of  $\rho$  (a curvature radius). In the Gaussian cgs unit, the curvature radius  $\rho$  is determined by<sup>1</sup>:

$$\rho = \frac{p_t}{eB_z} \quad (\text{H.1})$$

where  $\rho$  is in cm,  $p_t$  is the transverse momentum of a particle in erg/c,  $e$  is an unit electric charge  $= 4.803 \times 10^{-10}$  esu, and  $B_z$  is the strength of magnetic field (Gauss). Using  $B_z = 15\text{K Gauss}$  for the CDF and  $p_t$  (erg/c)  $= 1.602 \times 10^{-3} \times p_t$  (GeV/c), we have:

$$2\rho = 444 \cdot p_t \quad (\text{H.2})$$

<sup>1</sup>L. D. Landau and E. M. Lifshitz, §21, Course of Theoretical Physics Vol. 2 (Field Theory), Pergamon, New York, 1959

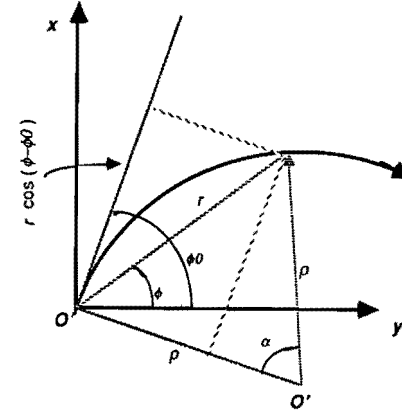


Figure H.1: Trajectory of a charged particle on  $xy$  plane. An uniform field is perpendicular to the  $xy$  plane and parallel to the  $z$  axis.

where  $p_t$  is in GeV/c. The transverse momenta for which the diameter ( $2\rho$ ) of the circle equals to the VTPC outer radius (21 cm) and inner radius (6.5 cm) are 50 MeV/c and 15 MeV/c, respectively.

It is useful to know how much the particle changes  $\phi$  as a function of  $p_t$  and the radius  $r$ . From the geometrical relations (see figure H.1), we have:

$$r \cos(\phi - \phi_0) = \rho \sin \alpha \quad (\text{H.3})$$

and

$$r = 2\rho \sin \frac{\alpha}{2} \quad (\text{H.4})$$

where  $\alpha$  is the angle between the beam position  $O$  and the particle looking from the helix origin  $O'$ . Using these relations, the change in  $\phi$  is:

$$\begin{aligned} \phi - \phi_0 &= \arccos \left( \frac{\sin \alpha}{2 \sin \frac{\alpha}{2}} \right) \\ &= \arccos \left( \frac{2 \sin \frac{\alpha}{2} \cos \frac{\alpha}{2}}{2 \sin \frac{\alpha}{2}} \right) \\ &= \frac{\alpha}{2} \end{aligned} \quad (\text{H.5})$$

$p_t$ (GeV/c)	Changes in $\phi$ from $r = 6.5$ cm to 21 cm
1.000	1.9°
0.400	4.7°
0.200	9.5°
0.100	19.8°

Table H.1: Changes in  $\phi$  within the VTPC volume for various transverse momenta

By using equation H.4, this becomes:

$$\phi - \phi_0 = \arcsin\left(\frac{r}{2\rho}\right) \quad (\text{H.6})$$

For the case of the CDF, with equation H.2, the changes in  $\phi$  is written as:

$$\phi - \phi_0 = \arcsin\left(\frac{r}{444 \cdot p_t}\right) \quad (\text{H.7})$$

where  $p_t$  is in GeV/c and  $r$  is in cm. Using this result, the changes in  $\phi$  within the VTPC volume (the radius from 6.5 cm to 21 cm) are summarized in table H.1 for various transverse momenta.

## Trajectory in $rz$ plane

The trajectory projected on the  $rz$  plane is a sine curve. Since the motion of the particle in the  $z$  direction is not affected by the magnetic field, the change in the  $z$  coordinate of the particle is:

$$z - z_0 = v_z \cdot t \quad (\text{H.8})$$

where  $z_0$  is the vertex position and  $t$  is the time passed after the collision. With the transverse velocity  $v_t$ , the angle  $\alpha$  defined in the previous section is (see figure H.1):

$$\alpha = \frac{v_t t}{\rho} \quad (\text{H.9})$$

With equation H.8, this can be written as:

$$\alpha = \frac{v_t \cdot (z - z_0)}{v_z \rho} \quad (\text{H.10})$$

$$= \frac{z - z_0}{\cot \theta \cdot \rho} \quad (\text{H.11})$$

where  $\theta$  is the polar angle with respect to the  $z$  axis. By inserting this relation in to equation H.4, we have a trajectory on  $rz$  the plane as:

$$r = 2\rho \sin\left(\frac{z - z_0}{\cot \theta \cdot 2\rho}\right) \quad (\text{H.12})$$

or

$$z = z_0 + 2\rho \cot \theta \arcsin\left(\frac{r}{2\rho}\right) \quad (\text{H.13})$$

$$= z_0 + 444 \cdot p_t \cot \theta \arcsin\left(\frac{r}{444 \cdot p_t}\right) \quad (\text{H.14})$$

## Trajectory in $z\phi$ space

From equations H.6 and H.12, the trajectory in the  $z\phi$  space is:

$$\phi - \phi_0 = \frac{z - z_0}{\cot \theta \cdot 2\rho} \quad (\text{H.15})$$

$$= \frac{z - z_0}{\cot \theta \cdot 444 \cdot p_t} \quad (\text{H.16})$$

The trajectory of the charged particle in the  $z\phi$  space is there a straight line, although this is true only for primary particles. In the forward region ( $|\cot \theta| > 1$ ), the slope of the line is quite small. For  $p_t = 0.400$  GeV/c, for instance, the slope is  $1/(178 \cdot \cot \theta)$ . Figure H.2 illustrates the typical  $z\phi$  trajectories in the VTPC.

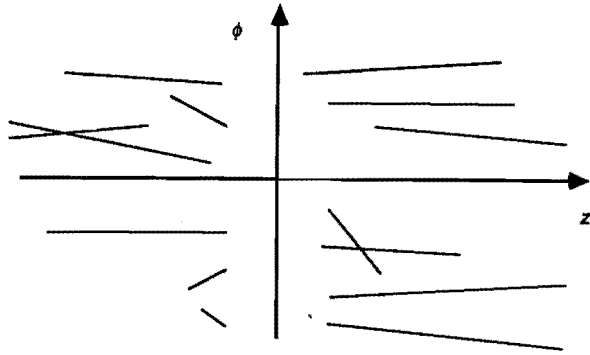


Figure H.2: Illustration of typical  $z\phi$  trajectories in VTPC. The horizontal axis is the  $z$  axis and the vertical axis is the  $\phi$  coordinate. Each line represents a trajectory. A collision occurs at the center. A certain particle enters the VTPC volume with a certain  $z$  and  $\phi$ . The long lines are the tracks with large  $\cot \theta$  and the short lines are the tracks with small  $\cot \theta$ .

## Appendix I

### Statistical hydrodynamic model

Attempts to understand the multiparticle productions in the hadron-hadron (or nucleon-nucleon) collisions started with the statistical model of Fermi [26] followed by the significant improvements by Pomeranchuk and Landau [27][28][29] in 1950's, stimulated by the results from the cosmic ray experiments. In the modernized Landau's model, called the statistical (relativistic) hydrodynamic model, a hadron-hadron collision is described as follows:

1. When two high energy hadrons collide, a system (mostly consisted of gluons) is formed with the energy  $E$ :

$$E = K\sqrt{s} \quad (I.1)$$

where  $K$  is the inelasticity — the fraction of energy remained after the leading partons fly away (with an energy of  $(1 - K)\sqrt{s}$ ). In the center-of-mass frame, the energy  $E$  is released in a very small volume followed by the excitation of many strongly interacting gluons and pairs of quark-antiquark (See figures 1.8a-c.) The collision mean free path in such a system is small compared to its dimension — the establishment of statistical equilibrium.

2. This strongly interacting multiparticle system expands according to the relativistic hydrodynamic equation [30]:

$$\partial_\mu T^{\mu\nu} = 0 \quad (I.2)$$

where

$$T^{\mu\nu} = (\epsilon + p)u^\mu u^\nu - pg^{\mu\nu} \quad (I.3)$$

is the energy-momentum tensor (or stress tensor) of an ideal relativistic fluid,  $\epsilon$  is the energy density,  $p$  is the pressure,  $u_\mu$  is the four-velocity of the fluid and  $g^{\mu\nu}$  is the metric tensor.

3. With the expansion of the system, the mean free path increases. When the mean free path becomes comparable with the dimension of the system, the break-up (hadronization) takes place at a temperature of  $m_\pi c^2$ , where  $m_\pi$  is the pion mass.

The advantage of such a statistical approach is that the detail of the underlying dynamics can be ignored except that one has to know the relation between  $\epsilon$  and  $p$  in the above equation (Landau chose  $p = \epsilon/3$ ). The modern refinements of the statistical hydrodynamic model (SHM) [31][32][33] show the good agreements with the experimental data at  $\sqrt{s} = 60\text{--}540$  GeV in the average charged multiplicity (table 1.1), the average  $p_t$  [34] (figure 1.9) and the pseudorapidity distribution [35] (figure 1.10).

Is there no connection between SHM and QCD? Figure 1.10 shows that the best fit is obtained with a sound velocity in the equilibrium system of  $1/\sqrt{3} \times c$ . The independent QCD calculation [36] for the gluon-quark plasma suggests that the sound velocity at high energy limit is  $1/\sqrt{3} \times c$ . This is an indication that SHM and QCD are not exclusive but complementary.



## Appendix J

### Dual parton model

Until recently there were no theories which gave quantitative explanation of the multiparticle production using the Quantum Chromo-Dynamics (QCD). However the most successful theory developed in recent several years can explain the multiparticle production quantitatively from ISR to SPS energy. This theory, called Dual Parton Model (DPM) [37], is based on the constituent quark-parton model and the non-perturbative QCD. According to DPM, a hadron-hadron interaction takes place in two steps. First, one of the valence quarks (quarks carrying a part of the quantum numbers of a hadron) is separated from an incident hadron leaving rest of quarks as a diquark. This process is called "knock" (figure 1.11). Since the knocked (di)quarks are not color singlet, they are called colored system. As second step, two of the colored system (one from each hadron) produce particle fragmentations and result in final hadrons. Each fragmentation is called "a chain". Figure 1.11 shows two chains are produced. (Figure 1.12 shows the corresponding perturbative Feynman diagram. This is not far from the view of gluon plasma in SHM.) Each chain is assumed to be independent of other chains. Figure 1.13 shows DPM diagrams with the sea quark contribution which becomes important at  $\sqrt{s} > \sim 500$  GeV. DPM has some basic assumptions in order to calculate physics quantity:

1. The momentum distribution of knocked (di)quark is given by Regge singularities [39].
2. The fragmentation (particle yield) of each chain does not depend on the momentum transfer of the process. Therefore the fragmentation function from  $e^+/e^-$  collision (hadronic events), the LUND model [41] or the Feynman-Field model [42] are applicable.
3. The contribution from the multiple chains is determined by the eikonal theory [40].

These assumptions leave no free parameters to tune. Figure 1.14 shows DPM result [43] on  $\langle n_{ch} \rangle$  with experimental data. There is a good agreement between the theory and experimental data from  $\sqrt{s} = 10 - 540$  GeV. Figure 1.15 shows the  $dN/d\eta$  at  $\sqrt{s} = 53$  and 540 GeV with the DPM calculations [38]. DPM also gives the normalized charged multiplicity distribution (KNO distribution  $\psi(z)$  described in next section) as shown in figure 1.16 for ISR energy and SPS energy [44]. An agreement between DPM and ISR data can be seen. Moreover the broadening of  $\psi(z)$  in SPS data known as the KNO scaling violation is well reproduced by DPM. Later on, We will compare our data to DPM prediction for  $\sqrt{s} = 1.8$  TeV.

## Appendix K

### Feynman scaling

The Feynman scaling is Feynman's inductive estimation of some physics quantities at a limit of  $\sqrt{s} \rightarrow \infty$  in the hadron-hadron collisions. According to his paper [45]:

In a high energy hadron-hadron collision, because of the Lorentz contraction, the energy of the field is distributed in a  $\delta$ -function in  $z$  (the direction of the beam) and therefore the field energy is uniform in the  $z$ -component of the momentum ( $p_z$ ). If the distribution of the field energy to the various kind of particles does not depend on  $\sqrt{s}$ , the probability of finding a particle of kind  $i$ , transverse momentum  $Q_i$  and mass  $m_i$  is the form of:

$$\frac{f(Q_i, x_i) dp_{zi} d^2 Q_i}{E_i} \quad (\text{K.1})$$

where  $E_i$  is the particle energy:

$$E_i = \sqrt{m_i^2 + Q_i^2 + p_{zi}^2} \quad (\text{K.2})$$

$x_i$  is the Feynman scaling variable:

$$x_i = 2p_{zi}/\sqrt{s} \quad (\text{K.3})$$

and  $f(Q_i, x_i)$  is the energy distribution (independent of  $\sqrt{s}$ ) and has a limit  $F(Q_i)$  for small  $x_i$ .

Using the Feynman scaling, Koba, Nielsen and Olesen (KNO) [46] derived a conclusion (KNO scaling):

If we define a normalized charged distribution  $\psi$  as:

$$\psi(z) = \langle n_{ch} \rangle P(n_{ch}) \quad (\text{K.4})$$

$$z = n_{ch} / \langle n_{ch} \rangle \quad (\text{K.5})$$

where  $P(n_{ch})$  is the probability that an event have  $n_{ch}$ , the distribution  $\psi(z)$  is independent of  $\sqrt{s}$ .

The KNO scaling was thought to be correct up to  $\sqrt{s} = 60$  GeV. At the higher energy, however, the  $\psi(z)$  distribution was found to be broader (Figure 1.16 shows  $\psi(z)$  for different energies [1]) and this is known as the violation of the KNO scaling and thus the violation of the Feynman scaling. It remains still useful to express the experimental data in terms of  $\psi(z)$  since the  $\psi(z)$  distribution is still "relatively" independent of the energy.